

Winter 2016

# A BIOLOGICAL BASED MODEL OF THE HUMAN VISUAL SYSTEM INCORPORATING LATERAL SUBTRACTIVE INHIBITION WITH NON-UNIFORM SAMPLING AND MULTIPLE SPATIAL FREQUENCY FILTERS

Nisreen Hanoon Radhi  
*University of New Hampshire, Durham*

Follow this and additional works at: <https://scholars.unh.edu/thesis>

---

## Recommended Citation

Radhi, Nisreen Hanoon, "A BIOLOGICAL BASED MODEL OF THE HUMAN VISUAL SYSTEM INCORPORATING LATERAL SUBTRACTIVE INHIBITION WITH NON-UNIFORM SAMPLING AND MULTIPLE SPATIAL FREQUENCY FILTERS" (2016). *Master's Theses and Capstones*. 1094.  
<https://scholars.unh.edu/thesis/1094>

This Thesis is brought to you for free and open access by the Student Scholarship at University of New Hampshire Scholars' Repository. It has been accepted for inclusion in Master's Theses and Capstones by an authorized administrator of University of New Hampshire Scholars' Repository. For more information, please contact [nicole.hentz@unh.edu](mailto:nicole.hentz@unh.edu).

**A BIOLOGICAL BASED MODEL OF THE HUMAN VISUAL  
SYSTEM INCORPORATING LATERAL SUBTRACTIVE  
INHIBITION WITH NON-UNIFORM SAMPLING AND  
MULTIPLE SPATIAL FREQUENCY FILTERS**

BY

Nisreen Radhi

B.S., University of Technology (2009)

THESIS

Submitted to the University of New Hampshire  
in partial fulfillment of  
the requirements for the degree of

Master of Science

in

Electrical and Computer Engineering

December 2016



ALL RIGHTS RESERVED

©2016

Nisreen Radhi

This thesis has been examined and approved in partial fulfillment of the requirements for the degree of Master of Science in Electrical Engineering by:

Thesis Director, Richard A. Messner, Ph.D.  
Associated Professor  
Department of Electrical & Computer Engineering

John R. LaCourse, Ph.D.  
Associate Professor  
Department of Electrical & Computer Engineering

Wayne J. Smith, Ph.D.  
Senior Lecturer  
Department of Electrical & Computer Engineering

On December, 2016

Original approval signatures are on file with the University of New Hampshire Graduate School.

# Acknowledgments

I would like to express my gratitude to my research adviser Dr. Richard Messner whose stimulating suggestions helped me out in the research for this thesis. Who was always gave me great encouragements that made me more confident in overcoming difficulties and making improvements. The research experience in the Synthetic Vision and Pattern Analysis Lab is a precious wealth for all my life.

Many thanks to the Department of Electrical Engineering for giving me one year and a half of Teaching Assistantship position which made my master study here possible, I would like to thank my thesis committee members, Dr. John LaCourse and Dr. Wayne Smith for their careful review of my thesis document. I also would like to acknowledge Dr. Kent Chamberlin for giving me his full support during my graduate journey at UNH.

I want to thank University of Technology of Electro-Optics Engineering for giving me an excellent undergraduate education . Thank you to my good friend from the UNH and from my home country Iraq, for all their continuous support, help and valuable suggestions both on academic and my everyday life.

Special thank to my family, my husband who always stands by my side and encourages me to keep going. Thanks to my girls who were my motivation and strength. Thanks to my dad, mom, brother and my sister. Many thanks to all of you, I could not have done without you.

# Table of Contents

Acknowledgments . . . . .	iii
Abstract . . . . .	xxviii
<b>1 The Human Visual System (HVS)</b>	<b>1</b>
1.1 Basic Model of the HVS as an Information Processing System . . . . .	2
1.2 Phenomenon, Evidence and Explanation of Lateral Inhibition . . . . .	3
1.3 Lateral Inhibition Applications . . . . .	7
<b>2 Lateral Inhibition</b>	<b>8</b>
2.1 What is Lateral Inhibition ? . . . . .	8
2.2 Historical Background of Lateral Inhibition . . . . .	9
2.2.1 Horseshoe Crab (Limulus Polyphemus) . . . . .	9
2.2.2 Horseshoe Crab Vision and Lateral Inhibition . . . . .	11
2.3 The Effect of Lateral Inhibition . . . . .	13
2.3.1 The Human Visual System . . . . .	13
2.3.2 The Eye . . . . .	14
2.3.3 The Retina . . . . .	15
2.4 Mathematical Formulation of Lateral Inhibition . . . . .	17
2.4.1 One Dimensional Matrix . . . . .	17
2.4.2 Two Dimensional Matrix . . . . .	19
2.4.3 The Exponential Model to Generate the Coupling Coefficients Matrix . . . . .	21
<b>3 Effect of Lateral Inhibition within Two Different Image Mapping Models</b>	<b>23</b>
3.1 The Work Structure: . . . . .	26

3.2	The Non Uniform Mapping Model of the coupling coefficients matrix based on the Recurrent Lateral Inhibition Method . . . . .	27
3.2.1	Introduction to Log - Polar Transformation Mapping . . . . .	27
3.2.2	Background . . . . .	27
3.2.3	Mathematical Representation of Log-Polar Mapping Algorithm . . . . .	28
3.3	Non-Uniform Model And Lateral Subtractive Inhibition (LSI) Method . . . . .	31
3.4	The Contrast Sensitivity Function (CSF) of the Human Visual System (HVS) . . . .	34
3.4.1	Contrast Sensitivity . . . . .	35
3.4.2	Contrast Sensitivity Function . . . . .	36
3.5	Multiple-Spatial Frequency Channels . . . . .	39
3.5.1	The Link Between The Contrast Sensitivity Function and The Recurrent Lateral Inhibition of HVS . . . . .	39
3.5.2	Filtering Entirely In Spatial Domain: . . . . .	40
<b>4</b>	<b>The Simulation Output Images</b>	<b>45</b>
4.1	The Exponential Model's variables for the Uniform Mapping Image: . . . . .	47
4.1.1	The $\alpha$ Variable of the Exponential Model . . . . .	49
4.1.2	The $\beta$ Variable: . . . . .	59
4.2	The Simulation Results of the Uniform model via the LSI Method . . . . .	70
4.3	Filtering the Uniform Mapping Image via Multiple Spatial Frequency Channels (CSF)	80
4.3.1	The Simulation Results of The Filtration Process of The Uniform Model: . .	85
4.3.2	The Simulation Results of The Lateral Inhibition Method and the Multiple Spatial Frequency channels (CSF): . . . . .	90
4.3.3	The Simulation results of the Inverse Uniform Model Based on the Multiple Spatial Frequency Channels (MTF): . . . . .	98
4.4	The Non-Uniform Model . . . . .	106
4.5	The Exponential Model's variables for the NON-Uniform Mapping Image: . . . . .	112
4.5.1	Alpha ( $\alpha$ ) parameter for the NON-Uniform Model: . . . . .	114
4.5.2	Beta ( $\beta$ ) parameter for Non-Uniform Model: . . . . .	120

4.6	The Simulation Results of the Non-Uniform Model Based Lateral Inhibition . . . .	125
4.7	The Filtration Process of the Non-Uniform Model based on the Multiple Spatial Frequency Channels (CSF): . . . . .	133
4.7.1	The Simulation results of the Inverse Non-Uniform Model . . . . .	141
4.8	The Comparison Between The Uniform Model and The Non-Uniform Model: . . . .	146
<b>5</b>	<b>Conclusions</b>	<b>150</b>
<b>6</b>	<b>Future Work</b>	<b>165</b>

# List of Tables

- 4.1 The Root Mean Square Error Numerical Results Regarding The Uniform Model . . 149
- 4.2 The Root Mean Square Error Numerical Results Regarding The Non-Uniform Model 149

# List of Figures

1-1	Basic Model Showing Mapping from External Sensory World to Internal Memory World . . . . .	3
1-2	Illustrate The Mach Band Effect Experiment [1]. . . . .	4
1-3	(A):The Input Image.(B)The Cross Section Profile of the Image . . . . .	5
1-4	(A):The Output Image Based on The LSI.(B)The Cross Section Profile of the Image	6
1-5	(A):The Colored Version of Output Image Based on The LSI.(B)The Cross Section Profile of the Image . . . . .	6
2-1	Defines a set of sensors with lateral inhibition mechanism. The arrows are indicating the inhibitory effect of each sensory on the neighbor's sensors which are represented by "B". each individual input that is designated by "x" and each drives down the output "y" of its neighbors which are connected to it at black arrow end. The ratio between the amount of sensory output which is driven by neighbors and the amount of output is called the degree of lateral inhibition [2]. . . . .	9
2-2	Dorsal and ventral view of Horseshoe Crab [2] . . . . .	10
2-3	Illustration of Compound Eye Consist of Ommatidia [2] . . . . .	11
2-4	Compound Eye of Horseshoe Crab. (a) Real Photo of Compound Eye (b) Close Up View of Compound Eye of Horseshoe Crab [2] . . . . .	12
2-5	Schematic Demonstration of Optical and Neural Mechanism of Ommatidium [3] . . .	12
2-6	Contrast Enhancement [4] . . . . .	13
2-7	Major Parts of Human Eye [5] . . . . .	14
2-8	Neural Pathway of Visual Stimulus in The Retina [6] . . . . .	16
2-9	The Effects of Lateral Inhibition on Edge Enhancement . . . . .	17
2-10	Image With Two Intensity level . . . . .	18



3-1	This figure Illustrates the Uniform Model of the Recurrent Lateral Inhibition, with neural network size $[3 \times 3]$ . . . . .	25
3-2	The Work Structure Of this Thesis. . . . .	26
3-3	The conversion of the Uniform space to the Non-Uniform plane $(r, \theta)$ in (a). Illustration the transformation of the Non-Uniform Plane to Uniform $(u, v)$ space (b) [7]. . . . .	29
3-4	The Log-Polar Mapping Applied to Regular Patterns (Concentric Circles and Radial Lines in The Image Plane). . . . .	30
3-5	the human retina cone-rods distribution. . . . .	32
3-6	Illustrate The Non-Uniform Distribution of the Receptors: Inter-connection Distance Calculation of the Receptors and the inhibition Impact. . . . .	33
3-7	Illustration of the Cartesian plane and the Log-Polar plane with non-uniform distance between two radii [8]. . . . .	34
3-8	three different spatial frequency ranges $[2 \text{ cycles/mm}, 4 \text{ cycles/mm}$ and $16 \text{ cycles/mm}$ . . . . .	36
3-9	Contrast Sensitivity Function Envelope Curve (CSF). . . . .	37
3-10	Sweep Grating . . . . .	38
3-11	The two models of the neurons receptive fields of the HVS. . . . .	40
3-12	Demonstration the Relationship Between the Second Sigma $\sigma_2$ to the First one $\sigma_1$ . . . . .	42
3-13	The contrast sensitivity function (dashed line) and its underlying spatial frequency channels (solid line). These channels, each of which is sensitive to specific range of frequencies each corresponding to a different size of the receptive fields, by adding up these three channels the Contrast Sensitivity Function envelope curve can be obtained which is the black dashed curve of this figure. . . . .	43
3-14	Input Image and The Filtered Image based a Three Different Spatial Frequency Bands . . . . .	44
4-1	Demonstration the Work Procedures of this chapter for both models . . . . .	46
4-2	(A)Input Synthetic Image. (B)Cross Section Profile . . . . .	48
4-3	(A)Lateral Inhibition Uniform Mapping Image. (B)Cross Section Profile . . . . .	48

4-4	(A) The Cross Section Profile of The LSI Image. (B) The LSI Image With $\alpha=0.03$ and $\beta=0.5$ . . . . .	49
4-5	(A) The Cross Section Profile of The LSI Image. (B) The LSI Image With $\alpha=0.05$ and $\beta=0.5$ . . . . .	50
4-6	(A) The Cross Section Profile of The LSI Image. (B) The LSI Image With $\alpha=0.08$ and $\beta=0.5$ . . . . .	50
4-7	(A) The Cross Section Profile of The LSI Image. (B) The LSI Image With $\alpha=0.1$ and $\beta=0.5$ . . . . .	51
4-8	(A) The Cross Section Profile of The LSI Image. (B) The LSI Image With $\alpha=0.2$ and $\beta=0.5$ . . . . .	51
4-9	(A) The Cross Section Profile of The LSI Image. (B) The LSI Image With $\alpha=0.3$ and $\beta=0.5$ . . . . .	52
4-10	(A) The Cross Section Profile of The LSI Image. (B) The LSI Image With $\alpha=0.4$ and $\beta=0.5$ . . . . .	52
4-11	(A) The Cross Section Profile of The LSI Image. (B) The LSI Image With $\alpha=0.5$ and $\beta=0.5$ . . . . .	53
4-12	(A) The Cross Section Profile of The LSI Image. (B) The LSI Image With $\alpha=0.6$ and $\beta=0.5$ . . . . .	53
4-13	(A) The Cross Section Profile of The LSI Image. (B) The LSI Image With $\alpha=0.7$ and $\beta=0.5$ . . . . .	54
4-14	(A) The Cross Section Profile of The LSI Image. (B) The LSI Image With $\alpha=0.8$ and $\beta=0.5$ . . . . .	54
4-15	(A) The Cross Section Profile of The LSI Image. (B) The LSI Image With $\alpha=0.9$ and $\beta=0.5$ . . . . .	55
4-16	(A) The Cross Section Profile of The LSI Image. (B) The LSI Image With $\alpha=1$ and $\beta=0.5$ . . . . .	55
4-17	(A) The Cross Section Profile of The LSI Image. (B) The LSI Image With $\alpha=1.1$ and $\beta=0.5$ . . . . .	56

4-18 (A) The Cross Section Profile of The LSI Image. (B) The LSI Image With $\alpha=1.2$ and $\beta=0.5$ . . . . .	56
4-19 Illustrates the relationship between the overshooting edges of the lateral inhibition image and <i>alpha</i> parameter. when alpha $\alpha$ changes from $[0.08 - 1.2]$ , while beta $\beta$ $=0.5$ . . . . .	57
4-20 Represents the Impact of $\alpha$ Parameter on the Differential of The Intensities of the Resultant Output Image. . . . .	58
4-21 (A) The Cross Section Profile of The LSI Image. (B) The LSI Image With $\beta=0.1$ and $\alpha=0.5$ . . . . .	59
4-22 (A) The Cross Section Profile of The LSI Image. (B) The LSI Image With $\beta=0.2$ and $\alpha=0.5$ . . . . .	60
4-23 (A) The Cross Section Profile of The LSI Image. (B) The LSI Image With $\beta=0.3$ and $\alpha=0.5$ . . . . .	60
4-24 (A) The Cross Section Profile of The LSI Image. (B) The LSI Image With $\beta=0.4$ and $\alpha=0.5$ . . . . .	61
4-25 (A) The Cross Section Profile of The LSI Image. (B) The LSI Image With $\beta=0.5$ and $\alpha=0.5$ . . . . .	61
4-26 (A) The Cross Section Profile of The LSI Image. (B) The LSI Image With $\beta=0.6$ and $\alpha=0.5$ . . . . .	62
4-27 (A) The Cross Section Profile of The LSI Image. (B) The LSI Image With $\beta=0.7$ and $\alpha=0.5$ . . . . .	62
4-28 (A) The Cross Section Profile of The LSI Image. (B) The LSI Image With $\beta=0.8$ and $\alpha=0.5$ . . . . .	63
4-29 (A) The Cross Section Profile of The LSI Image. (B) The LSI Image With $\beta=0.9$ and $\alpha=0.5$ . . . . .	63
4-30 (A) The Cross Section Profile of The LSI Image. (B) The LSI Image With $\beta=1$ and $\alpha=0.5$ . . . . .	64

4-31 (A) The Cross Section Profile of The LSI Image. (B) The LSI Image With $\beta=1.1$ and $\alpha=0.5$ . . . . .	64
4-32 (A) The Cross Section Profile of The LSI Image. (B) The LSI Image With $\beta=1.2$ and $\alpha=0.5$ . . . . .	65
4-33 (A) The Cross Section Profile of The LSI Image. (B) The LSI Image With $\beta=1.3$ and $\alpha=0.5$ . . . . .	65
4-34 (A) The Cross Section Profile of The LSI Image. (B) The LSI Image With $\beta=1.5$ and $\alpha=0.5$ . . . . .	66
4-35 Illustration The Impact of Beta parameter $\beta$ on the Overshooting Peak of the LSI Image . . . . .	67
4-36 The Relationship between the separation Distance between the Overshooting and the Undershooting and the beta $\beta$ parameter of LSI Image . . . . .	67
4-37 Different Cases of Alpha from [0.08 to 1] While Beta =0.5. . . . .	68
4-38 Different Cases of Beta from [0.08 to 1] While Alpha =0.5. . . . .	69
4-39 (A):A Stripped Image with Size [100x100]. (B)A Synthetic Staircase Images with size [100x100] . . . . .	71
4-40 The Input Real images with size [100x100] with Four Different Types: (A): Flower. (B):Butterfly. (C):Jet. (D): Word. . . . .	71
4-41 Circular Pattern To inverse the Uniform Mapped Image with size [100 ring x 100 wedge] . . . . .	72
4-42 (A)The Synthetic Input Image. (B)The Lateral Inhibition Image with $\alpha = 0.5$ and $\beta = 1$ . . . . .	73
4-43 (A)The LSI of Synthetic Input Image.(B) the LSI Wrapped Back Image with $\alpha = 0.5$ and $\beta = 1$ . . . . .	73
4-44 (A)The Synthetic Mach Bands Input Image. (B) the Lateral Inhibition Image with $\alpha = 0.5$ and $\beta = 1$ . . . . .	74
4-45 (A)The Colored Version of the Synthetic Mach Bands Input image. (B)The Colored Version of the Lateral Inhibition Image. . . . .	74

4-46	(A)The Colored Version of the Synthetic Mach Bands Input image. (B)The Colored Version Wrapped Back LSI Image with $\alpha = 0.5$ and $\beta = 1$ .	75
4-47	(A)The Real Image with Size [100x100]. (B)The Lateral Inhibition Image with alpha $\alpha=0.5$ and beta $\beta=1$ .	76
4-48	(A)The Inverse of Real Image with Size [100x100]. (B)The Lateral Inhibition Image with alpha $\alpha=0.5$ and beta $\beta=1$ .	76
4-49	(A)The Real Image with Size [100x100]. (B)The Lateral Inhibition Image with alpha $\alpha=0.5$ and beta $\beta=1$ .	77
4-50	The Inverse Real Image with Size [100x100] and the Lateral Inhibition Image with alpha $\alpha=0.5$ and beta $\beta=1$	77
4-51	(A)The Real Image with Size [100x100]. (B) The Lateral Inhibition Image with alpha $\alpha=0.5$ and beta $\beta=1$ .	78
4-52	(A)The Inverse Real Image with Size [100x100] (B) The Lateral Inhibition Image with alpha $\alpha=0.5$ and beta $\beta=1$ .	78
4-53	(A)The Real Image with Size [100x100]. (B)The Lateral Inhibition Image with alpha $\alpha=0.5$ and beta $\beta=1$ .	79
4-54	(A)The Inverse Real Image with Size [100x100].(B)The Lateral Inhibition Image with alpha $\alpha=0.5$ and beta $\beta=1$ .	79
4-55	Difference of Gaussian Filter (DOG) acts like Low-Pass Filter where: (A) First Gaussian with $\mu = 0$ and $\sigma = 2$ . (B)First Gaussian with $\mu = 0$ and $\sigma = 11.2$ . (C)The Difference-of-Gaussian Filter. (D)Profile of The First Low-Pass Gaussian Filter. (E)Profile of The Second Low-Pass Gaussian Filter. (F)Profile of The Difference of Gaussian Filter.	82
4-56	Difference of Gaussian Filter (DOG) acts like Band-Pass Filter where: (A) First Gaussian with $\mu = 0$ and $\sigma = 3$ . (B)First Gaussian with $\mu = 0$ and $\sigma = 16.8$ . (C)The Difference-of-Gaussian Filter. (D)Profile of The First Low-Pass Gaussian Filter. (E)Profile of The Second Low-Pass Gaussian Filter. (F)Profile of The Difference of Gaussian Filter.	83

4-57	Difference of Gaussian Filter (DOG) acts like High-Pass Filter where: (A) First Gaussian with $\mu = 0$ and $\sigma = 5$ . (B)First Gaussian with $\mu = 0$ and $\sigma = 28$ . (C)The Difference-of-Gaussian Filter. (D)Profile of The First Low-Pass Gaussian Filter. (E)Profile of The Second Low-Pass Gaussian Filter. (F)Profile of The Difference of Gaussian Filter. . . . .	83
4-58	The Composite Envelop Figure Which Represents The Result of Summing Up All The Three Channels Above. . . . .	84
4-59	(A)Butterfly Image in Gray scale. (B)Butterfly Image After DOG-LPF. (C)Butterfly Image After DOG-BPF.(D)Butterfly Image After DOG-HPF. . . . .	85
4-60	This Figure is Representing the Gray Scale Image and The Color Space Version of Lena Image. . . . .	86
4-61	(A)Butterfly Image in Color Space. (B)Butterfly Image After DOG-LPF. (C)Butterfly Image After DOG-BPF.(D)Butterfly Image After DOG-HPF. . . . .	86
4-62	(A)Jet Image in Grayscale. (B)Jet Image After DOG-LPF. (C)Jet Image After DOG-BPF.(D)Jet Image After DOG-HPF. . . . .	87
4-63	(A)Jet Image in Color Space. (B)Jet Image After DOG-LPF. (C)Jet Image After DOG-BPF.(D)Jet Image After DOG-HPF. . . . .	87
4-64	(A)Word Image in Grayscale. (B)Word Image After DOG-LPF. (C)Word Image After DOG-BPF.(D)Word Image After DOG-HPF. . . . .	88
4-65	(A)Word Image in Color Space. (B)Word Image After DOG-LPF. (C)Word Image After DOG-BPF.(D)Word Image After DOG-HPF. . . . .	88
4-66	(A)Flower Image in Grayscale. (B)Flower Image After DOG-LPF. (C)Flower Image After DOG-BPF.(D)Flower Image After DOG-HPF. . . . .	89
4-67	(A)Flower Image in Color Space. (B)Flower Image After DOG-LPF. (C)Flower Image After DOG-BPF.(D)Flower Image After DOG-HPF. . . . .	89

4-68	The Comparison Between LSI Image to The Filtered image: (A)The Original Image.(B)The Lateral Inhibition Image with $[\alpha = 0.5$ and $\beta = 1]$ .(C)The Filtered Image via DOG-LPF.(D)The Filtered Image via DOG-BPF.(E)The Filtered Image via DOG-HPF. . . . .	91
4-69	The Comparison Between LSI Image to The Filtered image: (A)The Original Image.(B)The Lateral Inhibition Image with $[\alpha = 0.5$ and $\beta = 1]$ .(C)The Filtered Image via DOG-LPF.(D)The Filtered Image via DOG-BPF.(E)The Filtered Image via DOG-HPF. . . . .	91
4-70	The Comparison Between LSI Image to The Filtered image: (A)The Original Image.(B)The Lateral Inhibition Image with $[\alpha = 0.5$ and $\beta = 1]$ .(C)The Filtered Image via DOG-LPF.(D)The Filtered Image via DOG-BPF.(E)The Filtered Image via DOG-HPF. . . . .	92
4-71	The Comparison Between LSI Image to The Filtered image: (A)The Original Image.(B)The Lateral Inhibition Image with $[\alpha = 0.5$ and $\beta = 1]$ .(C)The Filtered Image via DOG-LPF.(D)The Filtered Image via DOG-BPF.(E)The Filtered Image via DOG-HPF. . . . .	92
4-72	The Comparison Between LSI Image to The Filtered image: (A)The Original Image.(B)The Lateral Inhibition Image with $[\alpha = 0.5$ and $\beta = 1]$ .(C)The Filtered Image via DOG-LPF.(D)The Filtered Image via DOG-BPF.(E)The Filtered Image via DOG-HPF. . . . .	93
4-73	The Comparison Between LSI Image to The Filtered image: (A)The Original Image.(B)The Lateral Inhibition Image with $[\alpha = 0.5$ and $\beta = 1]$ .(C)The Filtered Image via DOG-LPF.(D)The Filtered Image via DOG-BPF.(E)The Filtered Image via DOG-HPF. . . . .	93
4-74	The Comparison Between LSI Image to The Filtered image: (A)The Original Image.(B)The Lateral Inhibition Image with $[\alpha = 0.5$ and $\beta = 1]$ .(C)The Filtered Image via DOG-LPF.(D)The Filtered Image via DOG-BPF.(E)The Filtered Image via DOG-HPF. . . . .	94

4-75	The Comparison Between LSI Image to The Filtered image: (A)The Original Image.(B)The Lateral Inhibition Image with $[\alpha = 0.5 \text{ and } \beta = 1]$ .(C)The Filtered Image via DOG-LPF.(D)The Filtered Image via DOG-BPF.(E)The Filtered Image via DOG-HPF. . . . .	94
4-76	(A)The Flower original input image.(B) Lateral Inhibition image with $\alpha=0.5$ and $\beta=1$ (C) DOG-LPF Filtered image with $\mu=0$ and $\sigma=9.2$ .(D)The Test image $[LSI_{img} - LPF_{img}]$ . . . . .	95
4-77	(A)The Flower original input image.(B) Lateral Inhibition image with $\alpha=0.5$ and $\beta=1$ (C) DOG-LPF Filtered image with $\mu=0$ and $\sigma=9.2$ .(D)The Test image $[LSI_{img} - LPF_{img}]$ . . . . .	95
4-78	(A)The Flower original input image.(B) Lateral Inhibition image with $\alpha=0.5$ and $\beta=1$ (C) DOG-BPF Filtered image with $\mu=0$ and $\sigma=13.8$ .(D)The Test image $[LSI_{img} - BPF_{img}]$ . . . . .	96
4-79	(A)The Flower original input image.(B) Lateral Inhibition image with $\alpha=0.5$ and $\beta=1$ (C) DOG-BPF Filtered image with $\mu=0$ and $\sigma=13.8$ .(D)The Test image $[LSI_{img} - BPF_{img}]$ . . . . .	96
4-80	(A)The Flower original input image.(B) Lateral Inhibition image with $\alpha=0.5$ and $\beta=1$ (C) DOG-HPF Filtered image with $\mu=0$ and $\sigma=23$ .(D)The Test image $[LSI_{img} - HPF_{img}]$ . . . . .	97
4-81	(A)The Flower original input image.(B) Lateral Inhibition image with $\alpha=0.5$ and $\beta=1$ (C) DOG-HPF Filtered image with $\mu=0$ and $\sigma=23$ .(D)The Test image $[LSI_{img} - HPF_{img}]$ . . . . .	97
4-82	(A)The Original Image. (B) THE Wrapped Back Version of the Uniform Mapped Image with Size $[100 \times 100]$ . (C) LSI Image with $[\alpha = 0.5 \text{ and } \beta = 1]$ . (D)The Filtered Image via DOG-LPF.(E)The Filtered Image via DOG-BPF.(F)The Filtered Image via DOG-HPF. . . . .	98



4-83	(A)The Original Image. (B) The Wrapped Back Version of the Uniform Mapped Image with Size [100 x 100]. (C) LSI Image with [ $\alpha = 0.5$ and $\beta = 1$ ]. (D)The Filtered Image via DOG-LPF.(E)The Filtered Image via DOG-BPF.(F)The Filtered Image via DOG-HPF. . . . .	99
4-84	(A)The Original Image. (B) The Wrapped Back Version of the Uniform Mapped Image with Size [100 x 100]. (C) LSI Image with [ $\alpha = 0.5$ and $\beta = 1$ ]. (D)The Filtered Image via DOG-LPF.(E)The Filtered Image via DOG-BPF.(F)The Filtered Image via DOG-HPF. . . . .	100
4-85	(A)The Original Image. (B) The Wrapped Back Version of the Uniform Mapped Image with Size [100 x 100]. (C) LSI Image with [ $\alpha = 0.5$ and $\beta = 1$ ]. (D)The Filtered Image via DOG-LPF.(E)The Filtered Image via DOG-BPF.(F)The Filtered Image via DOG-HPF. . . . .	100
4-86	(A)The Original Image. (B) The Wrapped Back Version of the Uniform Mapped Image with Size [100 x 100]. (C) LSI Image with [ $\alpha = 0.5$ and $\beta = 1$ ]. (D)The Filtered Image via DOG-LPF.(E)The Filtered Image via DOG-BPF.(F)The Filtered Image via DOG-HPF. . . . .	101
4-87	(A)The Original Image. (B) The Wrapped Back Version of the Uniform Mapped Image with Size [100 x 100]. (C) LSI Image with [ $\alpha = 0.5$ and $\beta = 1$ ]. (D)The Filtered Image via DOG-LPF.(E)The Filtered Image via DOG-BPF.(F)The Filtered Image via DOG-HPF. . . . .	101
4-88	(A)The Original Image. (B) The Wrapped Back Version of the Uniform Mapped Image with Size [100 x 100]. (C) LSI Image with [ $\alpha = 0.5$ and $\beta = 1$ ]. (D)The Filtered Image via DOG-LPF.(E)The Filtered Image via DOG-BPF.(F)The Filtered Image via DOG-HPF. . . . .	102
4-89	(A)The Original Image. (B) The Wrapped Back Version of the Uniform Mapped Image with Size [100 x 100]. (C) LSI Image with [ $\alpha = 0.5$ and $\beta = 1$ ]. (D)The Filtered Image via DOG-LPF.(E)The Filtered Image via DOG-BPF.(F)The Filtered Image via DOG-HPF. . . . .	102

4-90	(A)The Flower original input image.(B) Lateral Inhibition image with $\alpha=0.5$ and $\beta=1$ (C) DOG-LPF Filtered image with $\mu=0$ and $\sigma=9.2$ .(D)The Test image [ $LSI_{img}-LPF_{img}$ ].	103
4-91	(A)The Flower original input image.(B) Lateral Inhibition image with $\alpha=0.5$ and $\beta=1$ (C) DOG-LPF Filtered image with $\mu=0$ and $\sigma=9.2$ .(D)The Test image [ $LSI_{img}-LPF_{img}$ ].	103
4-92	(A)The Flower original input image.(B) Lateral Inhibition image with $\alpha=0.5$ and $\beta=1$ (C) DOG-BPF Filtered image with $\mu=0$ and $\sigma=13.8$ .(D)The Test image [ $LSI_{img}-BPF_{img}$ ].	104
4-93	(A)The Flower original input image.(B) Lateral Inhibition image with $\alpha=0.5$ and $\beta=1$ (C) DOG-BPF Filtered image with $\mu=0$ and $\sigma=13.8$ .(D)The Test image [ $LSI_{img}-BPF_{img}$ ].	104
4-94	(A)The Flower original input image.(B) Lateral Inhibition image with $\alpha=0.5$ and $\beta=1$ (C) DOG-HPF Filtered image with $\mu=0$ and $\sigma=23$ .(D)The Test image [ $LSI_{img}-HPF_{img}$ ].	105
4-95	(A)The Flower original input image.(B) Lateral Inhibition image with $\alpha=0.5$ and $\beta=1$ (C) DOG-HPF Filtered image with $\mu=0$ and $\sigma=23$ .(D)The Test image [ $LSI_{img}-HPF_{img}$ ].	105
4-96	Illustration the Non-Uniform Circular Pattern with $NRXNW = 2X4$ .	107
4-97	Lena Image after assigning the center-points of each Sub-Circle of the Previous Pattern.	108
4-98	The Extracted Information from the Input Image based the Non-Uniform Mapping Model with size $[2x4]$ , Where, the Fovea Area has removed using equation 4.6	108
4-99	The Mean Value of each sub-circle has been calculated and placed on the exact position according to the Log-Polar Mapping Mathematical Representation see equations (3.1) and (3.2). The black part is representing the removed area of the nonuniform model (Fovea).	109
4-100	Illustration the distribution of the cone receptive fields along a concentric rings with different Radii in the HVS, [8].	109

4-101	The Non-uniform Model to Mimic the HVS with size= $[number\ of\ Rings \times number\ of\ angles = 32 \times 64]$ . . . . .	110
4-102	Representation of the relationship between the number of rings and the number of wedges $[NRXNW]$ to the fovea's radius depending upon the equation 4.6. . . . .	110
4-103	The Resultant output image with the Mean Values via the Non-Uniform Mapping, with size = $[128 \times 64]$ . . . . .	111
4-104	(A) The Cross Section Profile of The Original Image. (B) The Original Synthetic Image. . . . .	113
4-105	(A) The Cross Section Profile of The LSI Image. (B) The LSI Image. . . . .	113
4-106	(A) The Cross Section Profile of The LSI Image. (B) The LSI Image With $\beta=0.5$ and $\alpha=0.08$ . . . . .	114
4-107	(A) The Cross Section Profile of The LSI Image. (B) The LSI Image With $\beta=0.05$ and $\alpha=0.1$ . . . . .	115
4-108	(A) The Cross Section Profile of The LSI Image. (B) The LSI Image With $\beta=0.05$ and $\alpha=0.2$ . . . . .	115
4-109	(A) The Cross Section Profile of The LSI Image. (B) The LSI Image With $\beta=0.05$ and $\alpha=0.3$ . . . . .	116
4-110	(A) The Cross Section Profile of The LSI Image. (B) The LSI Image With $\beta=0.05$ and $\alpha=0.4$ . . . . .	116
4-111	(A) The Cross Section Profile of The LSI Image. (B) The LSI Image With $\beta=0.05$ and $\alpha=0.5$ . . . . .	116
4-112	(A) The Cross Section Profile of The LSI Image. (B) The LSI Image With $\beta=0.05$ and $\alpha=0.6$ . . . . .	117
4-113	(A) The Cross Section Profile of The LSI Image. (B) The LSI Image With $\beta=0.05$ and $\alpha=0.7$ . . . . .	117
4-114	(A) The Cross Section Profile of The LSI Image. (B) The LSI Image With $\beta=0.05$ and $\alpha=0.9$ . . . . .	118

4-115	Illustrating The Relationship Between an Alpha Parameter $\alpha$ to the Overshooting Peak Enhancement. When Beta $\beta=0.05$ and Alpha $\alpha$ is changing within the range of [0.1 - 0.7]. . . . .	119
4-116	Represents The Impact of $\alpha$ Parameter on the Differential of the Intensities of the Resultant Output Image with Changing Alpha [0.1-0.7]. . . . .	119
4-117	(A) The Cross Section Profile of The LSI Image. (B) The LSI Image With $\beta=0.1$ and $\alpha=0.3$ . . . . .	120
4-118	(A) The Cross Section Profile of The LSI Image. (B) The LSI Image With $\beta=0.08$ and $\alpha=0.3$ . . . . .	120
4-119	(A) The Cross Section Profile of The LSI Image. (B) The LSI Image With $\beta=0.05$ and $\alpha=0.3$ . . . . .	121
4-120	(A) The Cross Section Profile of The LSI Image. (B) The LSI Image With $\beta=0.03$ and $\alpha=0.3$ . . . . .	121
4-121	(A) The Cross Section Profile of The LSI Image. (B) The LSI Image With $\beta=0.01$ and $\alpha=0.3$ . . . . .	122
4-122	The Impact of Beta $\beta$ parameter on the Overshooting Peaks of the Lateral Inhibition Image when Alpha $\alpha = 0.3$ . . . . .	123
4-123	The Impact of Beta $\beta$ parameter on the Differential Intensities of the Lateral Inhibition Image when Alpha $\alpha=0.3$ . . . . .	123
4-124	Different Cases of Alpha from [0.1 to 0.6] While Beta = 0.05. . . . .	124
4-125	Different Cases of Beta While Alpha = 0.3. . . . .	124
4-126	(A)The Synthetic Input Image of Two Gray Intensity Levels with with Size [500 x 500]. (B) The Non-uniform Mapping Model via LPT Method with Size [64 x 128]. (C)The Uniform [UxV] Mapped Image via LPT Method. (D) The Lateral Inhibition Method with Alpha $\alpha=0.3$ and Beta $\beta=0.05$ . . . . .	126

4-127(A)The Synthetic Staircase grayscale Input Image with with Size [500 x 500]. (B) The Non-uniform Mapping Model via LPT Method with Size [64 x 128]. (C)The Uniform [UxV] Mapped Image via LPT Method. (D) The Lateral Inhibition Method with Alpha $\alpha=0.3$ and Beta $\beta=0.05$ . . . . .	127
4-128(A)The Colored Version of Synthetic Staircase grayscale Input Image with with Size [500 x 500]. (B) The Non-uniform Mapping Model via LPT Method with Size [64 x 128]. (C)The Uniform [UxV] Mapped Image via LPT Method. (D) The Lateral Inhibition Method with Alpha $\alpha=0.3$ and Beta $\beta=0.05$ . . . . .	127
4-129(A)The Image after Combining The non-uniform Mapping Model and The Original Image. (B).The Mean Value Image After Mapping The Original One with size [NRxNW]. (C) The Wrapped Back Image with The Mean Values From the [UxV] Mapped Image With The Same Size As The Non-uniform Circular Pattern. . . . .	128
4-130(A)The Wrapped Back Version of Synthetic Staircase Input Image. (B)The Lateral Inhibition Image of The Reverse Non-uniform Mapped image. . . . .	129
4-131(A)The Wrapped Back Version of Synthetic Staircase Input Image. (B)The Lateral Inhibition Image of The Reverse Non-uniform Mapped image. . . . .	129
4-132(A)The Flower Input Image with Size [500x500].(B) The [UxV] Mapped Image Based on Log-Polar Mapping Method.(C) The Wrapped Back Image with Size [500x500]. (D)The Non-Uniform Mapped Pattern with Dimension [128 x 64].(E)The Lateral Inhibition Method of the Forward Image with size [128x64]. (F)The Lateral Inhibition Image of the Reversed mapped image. . . . .	130
4-133(A)The Butterfly Input Image with Size [500x500].(B) The [UxV] Mapped Image Based on Log-Polar Mapping Method.(C) The Wrapped Back Image with Size [500x500]. (D)The Non-Uniform Mapped Pattern with Dimension [128 x 64].(E)The Lateral Inhibition Method of the Forward Image with size [128x64]. (F)The Lateral Inhibition Image of the Reversed mapped image. . . . .	131

4-134(A)The Jet Input Image with Size [500x500].(B) The $[UxV]$ Mapped Image Based on Log-Polar Mapping Method.(C) The Wrapped Back Image with Size [500x500].(D)The Non-Uniform Mapped Pattern with Dimension [128 x 64].(E)The Lateral Inhibition Method of the Forward Image with size [128x64]. (F)The Lateral Inhibition Image of the Reversed mapped image. . . . .	131
4-135(A)The Word Input Image with Size [500x500].(B) The $[UxV]$ Mapped Image Based on Log-Polar Mapping Method.(C) The Wrapped Back Image with Size [500x500].(D)The Non-Uniform Mapped Pattern with Dimension [128 x 64].(E)The Lateral Inhibition Method of the Forward Image with size [128x64]. (F)The Lateral Inhibition Image of the Reversed mapped image. . . . .	132
4-136(A)The Lena Input Image with Size [500x500].(B) The $[UxV]$ Mapped Image Based on Log-Polar Mapping Method.(C) The Wrapped Back Image with Size [500x500].(D)The Non-Uniform Mapped Pattern with Dimension [128 x 64].(E)The Lateral Inhibition Method of the Forward Image with size [128x64]. (F)The Lateral Inhibition Image of the Reversed mapped image. . . . .	132
4-137(A)The Original Input Image. (B) The Non-Uniform Sampling of Synthetic Staircase Image. (C) The Lateral Inhibition Synthetic Image with $[\alpha = 0.3 \text{ and } \beta = 0.05]$ .(D) The Filtered Image via DOG-LPF .(E)The Filtered Image via DOG-BPF.(F)The Filtered Image via DOG-HPF. . . . .	133
4-138(A)The Original Input Image. (B) The Non-Uniform Sampling of Synthetic Staircase Image. (C) The Lateral Inhibition Synthetic Image with $[\alpha = 0.3 \text{ and } \beta = 0.05]$ .(D) The Filtered Image via DOG-LPF .(E)The Filtered Image via DOG-BPF.(F)The Filtered Image via DOG-HPF. . . . .	134
4-139(A)The Original Input Image. (B) The Non-Uniform Sampling of Synthetic Staircase Image. (C) The Lateral Inhibition Synthetic Image with $[\alpha = 0.3 \text{ and } \beta = 0.05]$ .(D) The Filtered Image via DOG-LPF .(E)The Filtered Image via DOG-BPF.(F)The Filtered Image via DOG-HPF. . . . .	134

4-140(A)The Original Input Image. (B) The Non-Uniform Sampling of Butterfly Real Image. (C) The Lateral Inhibition Real Image with $[\alpha = 0.3 \text{ and } \beta = 0.05]$ . (D) The Filtered Image via DOG-LPF. (E) The Filtered Image via DOG-BPF. (F) The Filtered Image via DOG-HPF. . . . .	135
4-141(A)The Original Input Image. (B) The Non-Uniform Sampling of Butterfly Real Image. (C) The Lateral Inhibition Real Image with $[\alpha = 0.3 \text{ and } \beta = 0.05]$ . (D) The Filtered Image via DOG-LPF. (E) The Filtered Image via DOG-BPF. (F) The Filtered Image via DOG-HPF. . . . .	135
4-142(A)The Original Input Image. (B) The Non-Uniform Sampling of Jet Real Image. (C) The Lateral Inhibition Real Image with $[\alpha = 0.3 \text{ and } \beta = 0.05]$ . (D) The Filtered Image via DOG-LPF. (E) The Filtered Image via DOG-BPF. (F) The Filtered Image via DOG-HPF. . . . .	136
4-143(A)The Original Input Image. (B) The Non-Uniform Sampling of Jet Real Image. (C) The Lateral Inhibition Real Image with $[\alpha = 0.3 \text{ and } \beta = 0.05]$ . (D) The Filtered Image via DOG-LPF. (E) The Filtered Image via DOG-BPF. (F) The Filtered Image via DOG-HPF. . . . .	136
4-144(A)The Original Input Image. (B) The Non-Uniform Sampling of Word Real Image. (C) The Lateral Inhibition Real Image with $[\alpha = 0.3 \text{ and } \beta = 0.05]$ . (D) The Filtered Image via DOG-LPF. (E) The Filtered Image via DOG-BPF. (F) The Filtered Image via DOG-HPF. . . . .	137
4-145(A)The Original Input Image. (B) The Non-Uniform Sampling of Word Real Image. (C) The Lateral Inhibition Real Image with $[\alpha = 0.3 \text{ and } \beta = 0.05]$ . (D) The Filtered Image via DOG-LPF. (E) The Filtered Image via DOG-BPF. (F) The Filtered Image via DOG-HPF. . . . .	137
4-146(A)The Non-Uniform Mapping Flower original input image. (B) Lateral Inhibition image with $\alpha = 0.3 \text{ and } \beta = 0.05$ . (C) DOG-LPF Filtered image with $\mu = 0$ and $\sigma = 9.2$ . (D) The Test Image image $[LI_{img} - LPF_{img}]$ . . . . .	138

4-147(A)The Non-Uniform Mapping Flower original input image.(B)Lateral Inhibition image with $\alpha = 0.3$ and $\beta = 0.05$ .(C)DOG-LPF Filtered image with $\mu = 0$ and $\sigma = 9.2$ .(D) The Test Image image $[LI_{img} - LPF_{img}]$ . . . . .	138
4-148(A)The Non-Uniform Mapping Flower original input image.(B)Lateral Inhibition image with $\alpha = 0.3$ and $\beta = 0.05$ .(C)DOG-BPF Filtered image with $\mu = 0$ and $\sigma = 13.8$ .(D) The Test Image image $[LI_{img} - BPF_{img}]$ . . . . .	139
4-149(A)The Non-Uniform Mapping Flower original input image.(B)Lateral Inhibition image with $\alpha = 0.3$ and $\beta = 0.05$ .(C)DOG-BPF Filtered image with $\mu = 0$ and $\sigma = 13.8$ .(D) The Test Image image $[LI_{img} - BPF_{img}]$ . . . . .	139
4-150(A)The Non-Uniform Mapping Flower original input image.(B)Lateral Inhibition image with $\alpha = 0.3$ and $\beta = 0.05$ .(C)DOG-HPF Filtered image with $\mu = 0$ and $\sigma = 23$ .(D) The Test Image image $[LI_{img} - HPF_{img}]$ . . . . .	140
4-151(A)The Non-Uniform Mapping Flower original input image.(B)Lateral Inhibition image with $\alpha = 0.3$ and $\beta = 0.05$ .(C)DOG-HPF Filtered image with $\mu = 0$ and $\sigma = 23$ .(D) The Test Image image $[LI_{img} - HPF_{img}]$ . . . . .	140
4-152(A)The Flower Input Image with Size $[500 \times 500]$ . (B) The $[XxY]$ Wrapped Back Image Based on Log-Polar Mapping Method.(C) The LSI Wrapped Back Image. (D)The Wrapped Back Non-Uniform Filtered Image Based on DOG-LPF.(E)The Wrapped Back Non-Uniform Filtered Image Based on DOG-BPF. (F)The Wrapped Back Non-Uniform Filtered Image Based on DOG-HPF. . . . .	142
4-153(A)The Flower Input Image with Size $[500 \times 500]$ . (B) The $[XxY]$ Wrapped Back Image Based on Log-Polar Mapping Method.(C) The LSI Wrapped Back Image. (D)The Wrapped Back Non-Uniform Filtered Image Based on DOG-LPF.(E)The Wrapped Back Non-Uniform Filtered Image Based on DOG-BPF. (F)The Wrapped Back Non-Uniform Filtered Image Based on DOG-HPF. . . . .	143



4-154(A)The Butterfly Input Image with Size [500x500].(B) The [XxY] Wrapped Back Image Based on Log-Polar Mapping Method.(C) The LSI Wrapped Back Image. (D)The Wrapped Back Non-Uniform Filtered Image Based on DOG-LPF.(E)The Wrapped Back Non-Uniform Filtered Image Based on DOG-BPF. (F)The Wrapped Back Non-Uniform Filtered Image Based on DOG-HPF. . . . .	143
4-155(A)The Butterfly Input Image with Size [500x500].(B) The [XxY] Wrapped Back Image Based on Log-Polar Mapping Method.(C) The LSI Wrapped Back Image. (D)The Wrapped Back Non-Uniform Filtered Image Based on DOG-LPF.(E)The Wrapped Back Non-Uniform Filtered Image Based on DOG-BPF. (F)The Wrapped Back Non-Uniform Filtered Image Based on DOG-HPF. . . . .	144
4-156(A)The Jet Input Image with Size [500x500].(B) The [XxY] Wrapped Back Image Based on Log-Polar Mapping Method.(C) The LSI Wrapped Back Image. (D)The Wrapped Back Non-Uniform Filtered Image Based on DOG-LPF.(E)The Wrapped Back Non-Uniform Filtered Image Based on DOG-BPF. (F)The Wrapped Back Non-Uniform Filtered Image Based on DOG-HPF. . . . .	144
4-157(A)The Jet Input Image with Size [500x500].(B) The [XxY] Wrapped Back Image Based on Log-Polar Mapping Method.(C) The LSI Wrapped Back Image. (D)The Wrapped Back Non-Uniform Filtered Image Based on DOG-LPF.(E)The Wrapped Back Non-Uniform Filtered Image Based on DOG-BPF. (F)The Wrapped Back Non-Uniform Filtered Image Based on DOG-HPF. . . . .	145
4-158(A)The Word Input Image with Size [500x500].(B) The [XxY] Wrapped Back Image Based on Log-Polar Mapping Method.(C) The LSI Wrapped Back Image. (D)The Wrapped Back Non-Uniform Filtered Image Based on DOG-LPF.(E)The Wrapped Back Non-Uniform Filtered Image Based on DOG-BPF. (F)The Wrapped Back Non-Uniform Filtered Image Based on DOG-HPF. . . . .	145

4-159	(A)The Word Input Image with Size [500x500].(B) The [XxY] Wrapped Back Image Based on Log-Polar Mapping Method.(C) The LSI Wrapped Back Image. (D)The Wrapped Back Non-Uniform Filtered Image Based on DOG-LPF.(E)The Wrapped Back Non-Uniform Filtered Image Based on DOG-BPF. (F)The Wrapped Back Non-Uniform Filtered Image Based on DOG-HPF. . . . .	146
4-160	The Comparison Between the Uniform to the Non-uniform Model Regarding Time Required to Sample The Input Image within Different Image Sizes. . . . .	147
5-1	The Identification of the Mathematical Relationship Between an Alpha and Beta Variables [ $\alpha$ and $\beta$ ] for the Uniform Model: (A)The Original Image.(B)LSI Image When $\alpha=\beta$ (C)LSI Image When $\alpha=\frac{1}{2}*\beta$ (D) LSI Image When $\beta=\frac{1}{2}*\alpha$ . . . . .	152
5-2	The Identification of the Mathematical Relationship Between an Alpha and Beta Variables [ $\alpha$ and $\beta$ ] for the Uniform Model: (A)LSI Image When $\alpha=2*\beta$ (B)LSI Image When $\beta=2*\alpha$ (C)LSI Image When $\alpha=\frac{1}{3}*\beta$ (D) LSI Image When $\beta=\frac{1}{3}*\alpha$ . . . . .	153
5-3	The Identification of the Mathematical Relationship Between an Alpha and Beta Variables [ $\alpha$ and $\beta$ ] for the Uniform Model: (A)LSI Image When $\alpha=3*\beta$ (B)LSI Image When $\beta=3*\alpha$ (C)LSI Image When $\alpha=\frac{1}{\beta}$ (D) LSI Image When $\beta=\frac{1}{\alpha}$ . . . . .	154
5-4	Illustration the Best Expression of Alpha $\alpha$ parameter and Beta $\beta$ for the Uniform Model. (A)The Original Image (B)LSI Image $\beta = 1 * \alpha$ . (C)LSI Image $\beta = 2 * \alpha$ . (D)LSI Image $\beta = 3 * \alpha$ . . . . .	155
5-5	Illustration the Best Expression of Alpha $\alpha$ parameter and Beta $\beta$ for the Uniform Model. (A)LSI Image $\beta = 4 * \alpha$ (B)LSI Image $\beta = 5 * \alpha$ . (C)LSI Image $\beta = 6 * \alpha$ . (D)LSI Image $\beta = 7 * \alpha$ . . . . .	156
5-6	Illustration the Best Expression of Alpha $\alpha$ parameter and Beta $\beta$ for the Uniform Model. (A)LSI Image $\beta = 8 * \alpha$ (B)LSI Image $\beta = 9 * \alpha$ . (C)LSI Image $\beta = 10 * \alpha$ . . . . .	156
5-7	The Identification of the Mathematical Relationship Between Alpha and Beta Variables [ $\alpha$ and $\beta$ ] for the Non-uniform Model. (A) The Original Image. (B)LSI Image when $\alpha=\beta=0.3$ . (C)LSI Image when $\alpha=\frac{1}{2}*\beta$ . (D)LSI Image when $\beta=\frac{1}{2}*\alpha$ . . . . .	158

5-8	The Identification of the Mathematical Relationship Between Alpha and Beta Variables $[\alpha$ and $\beta]$ for the Non-uniform Model.(A)LSI Image when $\alpha=2*\beta$ . (B)LSI Image when $\beta=2*\alpha$ . (C)LSI Image when $\alpha=\frac{1}{3}*\beta$ .(D)LSI Image when $\beta=\frac{1}{3}*\alpha$ . . .	159
5-9	The Identification of the Mathematical Relationship Between Alpha and Beta Variables $[\alpha$ and $\beta]$ for the Non-uniform Model.(A)LSI Image when $\alpha=3*\beta$ . (B)LSI Image when $\beta=3*\alpha$ . (C)LSI Image when $\alpha=\frac{1}{\beta}$ .(D)LSI Image when $\beta=\frac{1}{\alpha}$ . . . . .	160
5-10	Illustration the Best Expression of Alpha $\alpha$ parameter and Beta $\beta$ for the Non-uniform Model. (A)The Original Image. (B)LSI Image when $\beta=\frac{1}{2}*\alpha$ .(C)LSI Image when $\beta=\frac{1}{3}*\alpha$ .(D)LSI Image when $\beta=\frac{1}{4}*\alpha$ . . . . .	161
5-11	Illustration the Best Expression of Alpha $\alpha$ parameter and Beta $\beta$ for the Non-uniform Model. (A)LSI Image when $\beta=\frac{1}{5}*\alpha$ .(B)LSI Image when $\beta=\frac{1}{6}*\alpha$ .(C)LSI Image when $\beta=\frac{1}{7}*\alpha$ . . . . .	162
5-12	Illustration the Best Expression of Alpha $\alpha$ parameter and Beta $\beta$ for the Non-uniform Model. (A)LSI Image when $\beta=\frac{1}{8}*\alpha$ .(B)LSI Image when $\beta=\frac{1}{9}*\alpha$ .(C)LSI Image when $\beta=\frac{1}{10}*\alpha$ . . . . .	162

**ABSTRACT**  
**A BIOLOGICAL BASED MODEL OF THE HUMAN VISUAL SYSTEM**  
**INCORPORATING LATERAL SUBTRACTIVE INHIBITION WITH**  
**NON-UNIFORM SAMPLING AND MULTIPLE SPATIAL FREQUENCY**  
**FILTERS**

by

Nisreen Radhi  
University of New Hampshire, December, 2016

The human visual system has been an interesting topic of scientific research for decades. It is known that the cone photo-receptors are arrayed in a non-linear fashion and that a lateral subtractive inhibitory process is occurring in the visual pathway. This thesis outlines for the first time how lateral subtractive inhibition manifests itself in the context of a non-uniform sensor distribution where the distance between cone photo-receptors, and size of the receptors, are varying in a log manner when moving radially away from the foveal area. Range limits on the parameters that control the non-uniform sampling and coupling coefficients are presented and optimal values are identified for specific image resolutions. The results of this analysis are then coupled to a proposed model of spatial frequency filtering to assist in subsequent studies of feature extraction and pattern analysis. The filters generated are based on three spatial-frequency channels that are designed to model the human eye contrast sensitivity curve. Simulated results are presented.

# Chapter 1

## The Human Visual System (HVS)

Humans can recognize a face, an apple or identify car keys with ease. This pattern recognition task is accomplished by processing the image information through the visual system, and then a cognitive evaluation of extracted information from that image is used to form a judgment on the particular models. An interesting question is raised here: how the Human Visual System (HVS) maps the captured visual information from the external sensory world into internal memory representation? The answer to this question would be of great benefit to some research areas. Such as an Artificial Intelligence and Neural Network aspects.

Artificial Intelligence is an interesting research topic that offers the capability to study and understand the information processing of the human intelligence system that underlies thinking and intelligent behavior. One of the most intriguing senses that many biological entities possess is a vision. The way in which human acquire, process and finally interpret visual information has been an interesting topic of scientific study for years. So the objective of this study reduces the gap between the biology and man-made machines so that our “smart computers” can sense, process and perform as well as human. A lot of efforts have been made to propose an adequate model with computationally efficient, biologically inspired, image processing framework suitable for pattern recognition purposes. That model is designed to satisfy two important properties of machine vision applications that already exist in the HVS. The first property is maintaining a large field of view while preserving the detailed information from the scene at the point of interest. The second feature is providing the capability to process the data at a very fast rate. The human visual system has a non-uniform sampling of visual input in the space domain. Non-uniform or space-variant factors including cortical magnification and receptive field scatter substantially affects human perception

from a visual scene. In this research work, the non-uniform distribution of the photo-receptor cells of the HVS will be investigated and explored to present the benefits of this biological-like pattern. Also, a comparison is made between the new biological-like model and the Uniform model where the receptors are organized in a uniform way. In other words, the spatial distance between the receptors is constant (more information regarding this model is providing in chapter three). The comparison is made depending on the resultant output images via each mapping model as well as the Root Mean Square Error quality metric. The justifications of using the HVS as a reference model can be summarized as follows:

1. The human visual system can be viewed as the most delicate, perfectly designed information processing system in many aspects such as real time, pattern recognition, feature exploiting, etc. Therefore, by using HVS characteristics, it may be possible to develop better recognition systems.
2. The finding or design an accurate model that precisely simulates the functionalities of the human visual system at a present time is not an easy task at all. Therefore, researchers usually start with assumptions about the mechanism associated with one or more aspects of the HVS. To investigate the HVS quantitatively, we resort to computers and mathematical models, even though these models are much simplified compared to the actual HVS models.

## 1.1 Basic Model of the HVS as an Information Processing System

The essential function of the human visual system is processing image data. Whereas, the first step of the processing is the image sampling (mapping) from the external sensory world into an internal memory representation. Figure 1-1, illustrates the concept of mapping. In which it is valid to assume that the image data processing occurs simultaneously with the image mapping task. From the same figure, the input information (projected image) in the retinal photo-receptors layer which is denoted by the matrix  $[E]$  corresponding to the two-dimensional nature of the picture data. On the other hand, the matrix  $[F]$  which represents the lower level electrochemical firing rate associated with the neural information transferred or with, the higher level output feature

vectors. The visual sampling task is accomplished by linear sensory mapping represented by the matrix  $[S]$ . The neural firing rate information  $[F]$  is then mapped into the internal memory world of the brain via associative memory mapping, represented by the matrix  $[M]$ . In this thesis work,

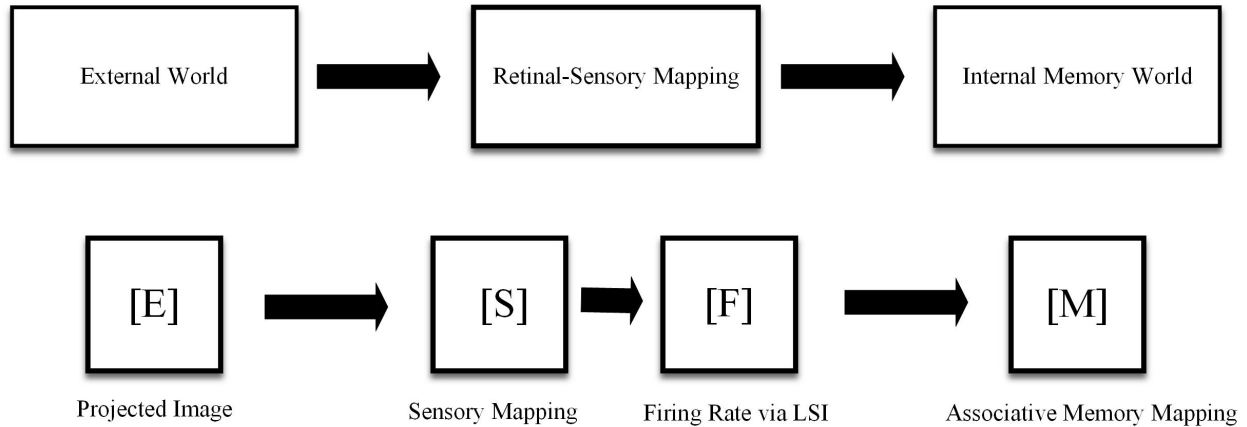


Figure 1-1: Basic Model Showing Mapping from External Sensory World to Internal Memory World

we have concentrated on a mapping matrix  $[S]$ . The associative memory mapping is a fascinating research topic in the neural network area, but it is beyond the scope of this study. Although the mapping are described in the context of Human Visual System (HVS), it is reasonable to believe that similar exist in other biological visual systems.

## 1.2 Phenomenon, Evidence and Explanation of Lateral Inhibition

Lateral inhibition of neurons is an interesting phenomenon found in biological sensory systems such as the human eye. This mechanism is discovered and verified by Hartline and his research team when they carried out an electro-physiology experiment on the Limulus' vision [9]. Every microphthalmia of Limulus' ommuleum is seen as a receptor. They found that a receptor is inhibited by its adjacent receptors and this inhibition effect is spatially summed. A certain receptor is more severely inhibited by the closer receptors rather than the farther ones. The inhibition among cells is mutual, every receptor is adjacent to its adjacent receptors and it tries to inhibit it's adjacent receptor. This is the final mode of nerve fiber activities. This inhibition effect has also been

observed in higher level animals' sensory systems through electro-physiological experiments on the retinas of cats and monkeys [10, 11]. It is greatly accepted that the lateral inhibition mechanism also exists in the human visual system [9]. The effectiveness of this mechanisms can be represented by some kinds of negative feed-back systems. The explanation of this representation is interpreted biologically. There are a finite number of ions available for neural firing rates which propagate the information from a local region of the retina to the corresponding cortex region. This local propagation procedure inhibitory influences among all the receptors in the neighborhood because they compete for those ions at the ganglion level. There will overabundance of ions accumulated on the bright side of a dark/bright boundary. This phenomenon enhances the contrast and the sharpness in the sensory field of receptors and neurons and this can cause two effects. Simultaneous contrast and Mach band effect [1]. Mach band phenomenon is a well-known phenomenon that was detected by the scientist, Ernst Mach, see figure 1-2. Then, the gratings with dark and white bars are honored his name. Center-surround receptive field interactions can explain these Mach bands. Where, the receptive fields are represented as a disk (+) and annulus (-). The center point of the disk is an excitatory area and the annulus an inhibitory area. The receptive field of the uniformly white and uniformly black areas received about the same stimulation in their excitatory center and inhibitory surrounds. Therefore, the center excitation area is in balance with surround inhibitions.

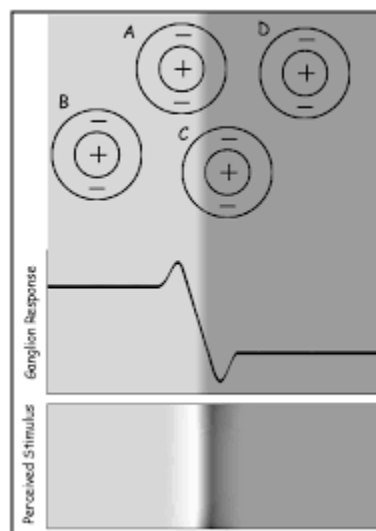


Figure 1-2: Illustrate The Mach Band Effect Experiment [1].



The neuron over the bright Mach band gives a stronger response in the center because part of surround is in the dark part of the grating. Therefore, it inhibits from the surround cells less than if it is in the bright area. This biological phenomenon can be representing in the following figures.

A typical experiment was performed with a gray level chart shown in figure 1-3. In figure 1-3 a bar chart image with a monotonic function of luminance has shown and its cross section profile to represent the constant transition between two adjacent bars within different intensity levels. However, the apparent brightness is not uniform along the width of each particular bar. Transitions between two adjacent bars appear brighter on the right hand side (where the darker luminance is to its left) and darker on the left side (where the brighter luminance is to its right hand side). Figure 1-4 demonstrates the perceived brightness that observed via the sensory field of receptors and neurons in the human visual system. Whereas, the overshooting and undershooting edges in figure 1-4 and 1-5, are characterizing the effect of this biological method in grayscale and color space, respectively.

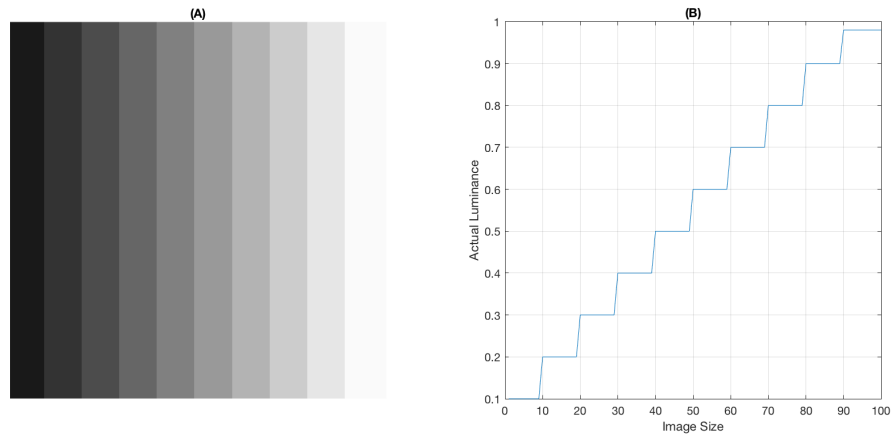


Figure 1-3: (A):The Input Image.(B)The Cross Section Profile of the Image

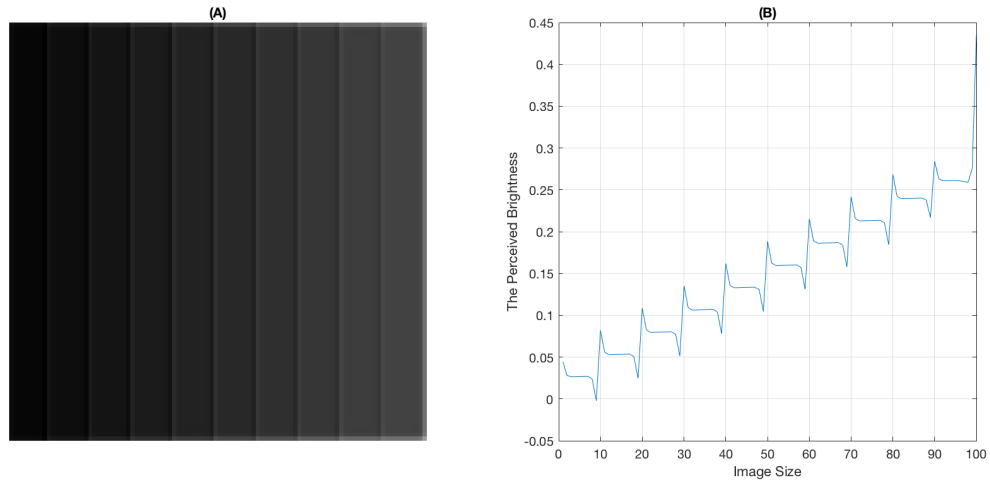


Figure 1-4: (A):The Output Image Based on The LSI.(B)The Cross Section Profile of the Image

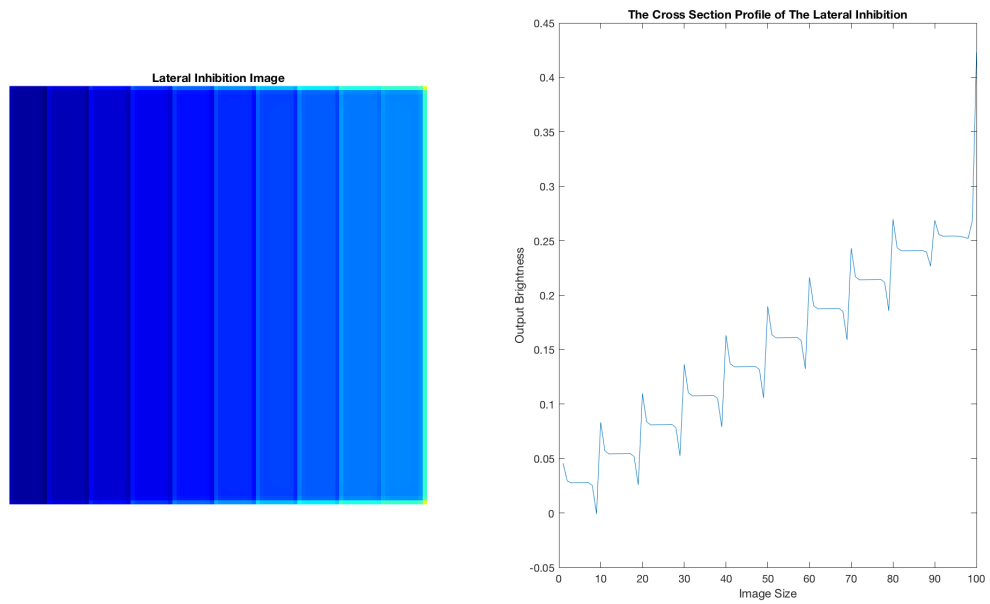


Figure 1-5: (A):The Colored Version of Output Image Based on The LSI.(B)The Cross Section Profile of the Image

### 1.3 Lateral Inhibition Applications

The contour of the image as the main feature of a picture has a strong stability, and therefore the image processing is necessary for the detection of contour information. In the field of defense technology and aerospace, demands have been proposed on the shape detection of the target, such as processing speed, lower memory consumption, positioning accuracy and better effects. Contour points are usually defined as a pixel location of abrupt gray-level change. The application of lateral inhibition mechanism is possibly a new way of looking at contour (edge) detection and enhancement problem. Although the lateral subtractive inhibition as an interesting biological phenomenon has been known for decades, the applications of algorithms based on that has not been investigated thoroughly. Few research results can be found in which precise model describing lateral subtractive inhibition is proposed. George G. Furman Proposed and compared four models about lateral inhibition in receptor-neuron fields in his paperback in 1965 [12]. He applied his model to one-dimensional sensory area to simulate this mechanism. His research represents the early efforts in investigating lateral inhibition based algorithms and their application quantitatively. Dr. Richard Messner 's dissertation about smart visual sensors for real-time image processing and pattern recognition based upon the human visual system characteristics explored this area further [13]. He proposed the quad-tree matrix inversion (QMI) algorithm which is useful in doing the calculation associated with certain models. His research provides the basis and motivation for this research work.

# Chapter 2

## Lateral Inhibition

### 2.1 What is Lateral Inhibition ?

Lateral Inhibition (L.I.) is an interaction between neurons in which the excitement of one neuron inhibits the excitability of neighboring neurons. The strength of this inter-connections are stable rather than changeable as well as they are organized as excitatory among nearby receptors and inhibitory among farther receptors. In other words, when any given receptor responds, the excitatory connections tend to increase its response while inhibitory connections try to decrease it.

All the receptors in the neural network receive a mixture of excitatory and inhibitory signals from other competitive receptors. As a result of the competitive network structure, a distinction between the receptor or a group of receptors which have the strongest output and the receptors with weaker output become larger. Weaker receptors might be suppressed. According to the value of excitatory and inhibitory coefficients and number of interconnected optimum coefficients, the receptor which has the strongest output contained all the other receptor outputs and this kind called “the winner takes all” type [14]. For a biological system, the lateral inhibition can be considered as a peripheral processing phenomenon. According to this study presented here [2] the lateral inhibition is commonplace in human nervous system, and it has been widely recognized as contrast detection and enhancement mechanism. It is also sometimes called on-center or off-surround architecture. These terms are mainly used for biological structures that operate in the same way.

Figure 2-1 illustrates the interconnection between the receptors in the neural network sensory field.

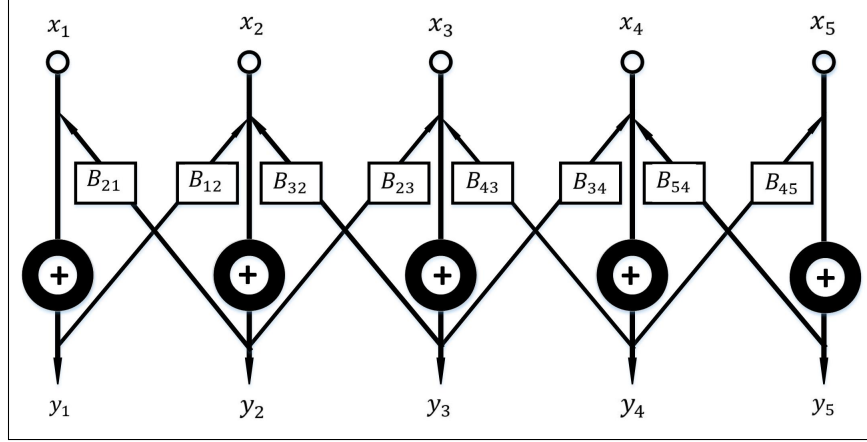


Figure 2-1: Defines a set of sensors with lateral inhibition mechanism. The arrows are indicating the inhibitory effect of each sensory on the neighbor's sensors which are represented by "B". each individual input that is designated by "x" and each drives down the output "y" of its neighbors which are connected to it at black arrow end. The ratio between the amount of sensory output which is driven by neighbors and the amount of output is called the degree of lateral inhibition [2].

## 2.2 Historical Background of Lateral Inhibition

Effects of lateral inhibition were first recognized in 1886 by the Austrian physicist Ernst Mach who ascertained that all knowledge was based on sensation and that scientific observations or measurements were dependent upon the observer's perception. H.K. Hartline in 1956 [15], has received Nobel prize for his work on a visual system of the horseshoe crab, which is a kind of arthropod from North America, see figure 2-2. The concept of lateral inhibition arose in the comprehensive experimental research of H.K. Hartline and his colleagues on the faceted compound eye horseshoe crab. This study proceeded the period of over fifty years and was an outstanding example of bringing quantitative mathematical methods of signal transmission.

In figure 2-2, illustrates the dorsal-ventral structure of a horseshoe creature.

### 2.2.1 Horseshoe Crab (Limulus Polyphemus)

Horseshoe crabs or Limulus are the oldest and an interesting creatures. They are estimated to be at least 300-million years old. This kind of creatures belongs to the large group of invertebrates

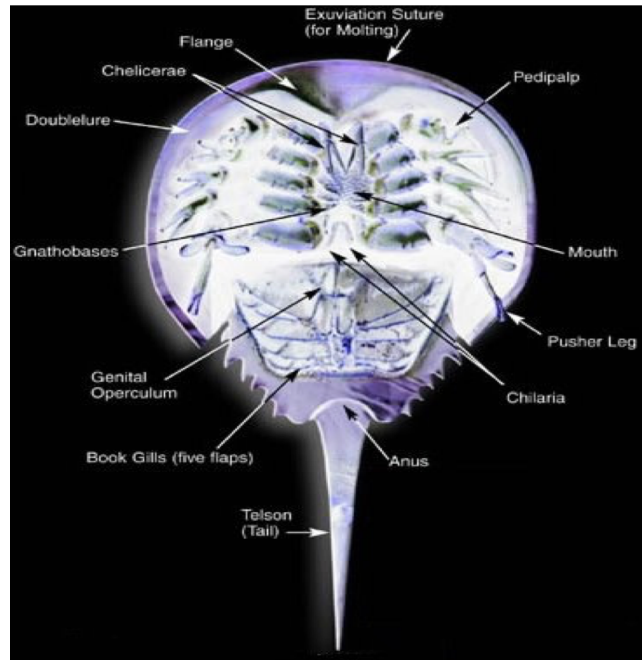


Figure 2-2: Dorsal and ventral view of Horseshoe Crab [2]

(animals without backbones) called Arthropods. The first generation of the horseshoe crab species was crawling around the earth's shallow coastal seas for at least 100-million years before even the dinosaurs arrived. People have used horseshoe crabs for different scientific purposes. Recently, these creatures have been instrumental in the scientific research, especially in biomedical fields.

The horseshoe crabs have been beneficial to the research world, and several Nobel prizes have been awarded to researchers based on their work on horseshoe crabs. The researchers have found that chitin, which makes up the horseshoe crab's shell, can reduce the healing time of wounds as well as it reduces the pain compared to other standard treatments. Chitin is now used to make dressing and sutures for burns, surface wounds, and skin graft donor sites. On previous fifty years, research on the compound eye of this creature has led to a better understanding of how human eyes function. The reasons for relying on the horseshoe's compound eye for scientific studies especially about the vision studies are: the compound eyes of Horseshoe crab are relatively large, horseshoe crab optic nerve, which connects the compound eyes to the brain is not very long; and last but not least, the horseshoe crab can be safely kept out of water for a relatively extended period.

### 2.2.2 Horseshoe Crab Vision and Lateral Inhibition

Horseshoe crab have about a ten eyes with sensing light, used for finding mates and feeding. The most bright eyes are the two lateral eyes which are used to find their mates during the spawning season. These eyes are also called the compound eyes. The compound eyes are included the smaller, simple eye units, called Ommatidia, see figure 2-3. Each compound eye has about 1,000 of light receptors or Ommatidia. Those receptors have the same structure as those in the human eyes. It's classified into Cones and Rods, except that they around 100 times larger in size than those in the human eye, figure 2-4.

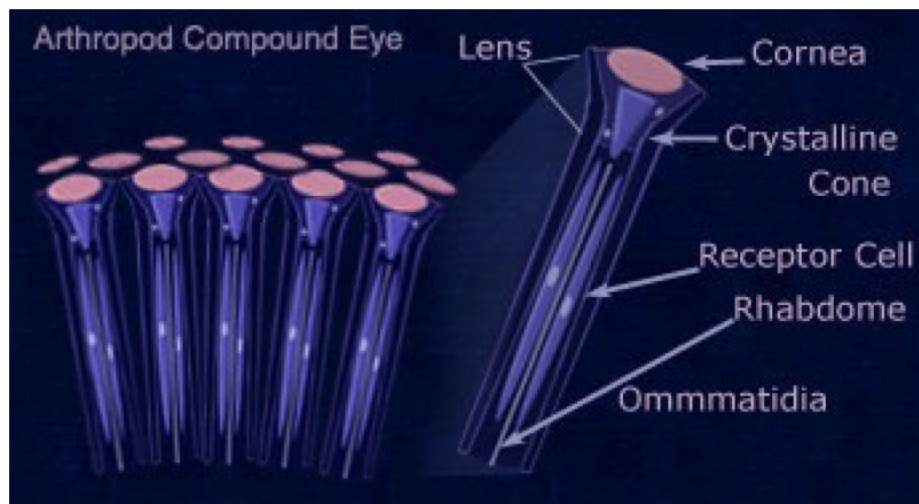


Figure 2-3: Illustration of Compound Eye Consist of Ommatidia [2]

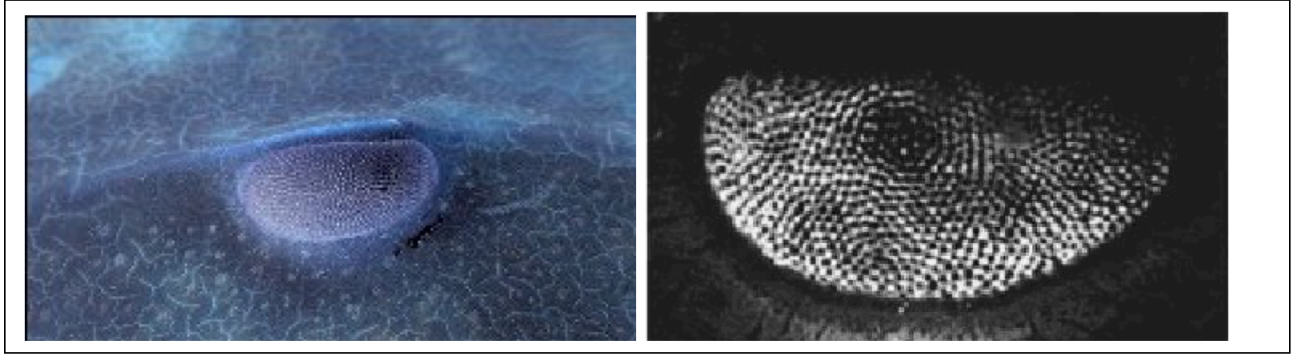


Figure 2-4: Compound Eye of Horseshoe Crab. (a) Real Photo of Compound Eye (b) Close Up View of Compound Eye of Horseshoe Crab [2]

The inhibitory and the excitatory currents are summed to produce the “Spike Generator.” This peak generator will be encoding as a train of action potentials. Then, the spike train propagates and forward along to the optic nerve to the brain to mediate behavior. The goal of the earlier experiment is to prove that the primary visual requirement of the horseshoe crab is contrast and the lateral inhibition mechanism to enhance the ability of horseshoe crab to distinguish contrast. This phenomenon can be seen in Figure 2-5 and it will be discussed in the following section of this chapter.

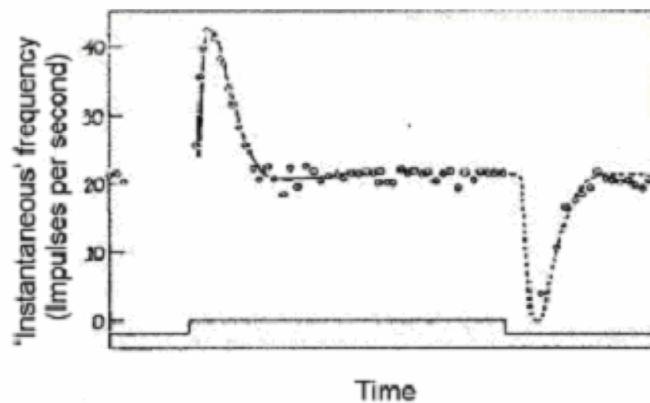


Figure 2-5: Schematic Demonstration of Optical and Neural Mechanism of Ommatidium [3]



## 2.3 The Effect of Lateral Inhibition

Lateral subtractive inhibition plays a significant role in contrast enhancement, see figure 2-6. This figure below illustrates the enhancement of the edge via the lateral inhibition effectiveness. Whereas, this figure represents a horizontal line for photo-receptors and the vertical line for the input light intensity. It can be seen that the edge or the discontinuity in the input is exaggerated in the output due to the lateral inhibition influence. In the visual system the contrast enhancement effect can be easily detect.

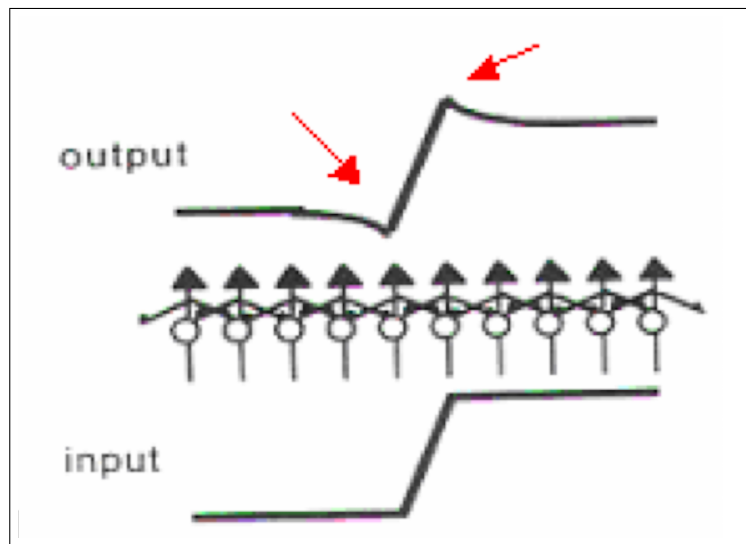


Figure 2-6: Contrast Enhancement [4]

### 2.3.1 The Human Visual System

The Human Visual System can be classified into two important parts, the eyes and the brain. Whereas, the eyes act as a camera to capture the light and transform it into signals which are then transmitted to image processing centers in the brain.

### 2.3.2 The Eye

The structure of the human eye is analogous to that of a camera. The basic structure of the eye is displayed in Figure 2-7.

- a. The cornea serves as a primary lens which performs the focusing task of the incoming light signal.
- b. A muscle which controls both the positioning and the shape of the eye's lens. The benefit of that is to obtain an excellent control over how the light entering the eye[?]
- c. The iris of the human eye is a muscle which, when contracted, covers all but a small central portion of the lens. Whereas an adaptive controlling the light entering the eye.
- d. The retina, where the contrast enhancement can be observed. This part of the human eye provides a photosensitive skin at the back side of the eye, where is the light converting into nerve signals.
- e. The fovea which is the central region of the retina is particularly sensitive, and it provides the highest resolution and is used for close inspection of objects in the visual field.

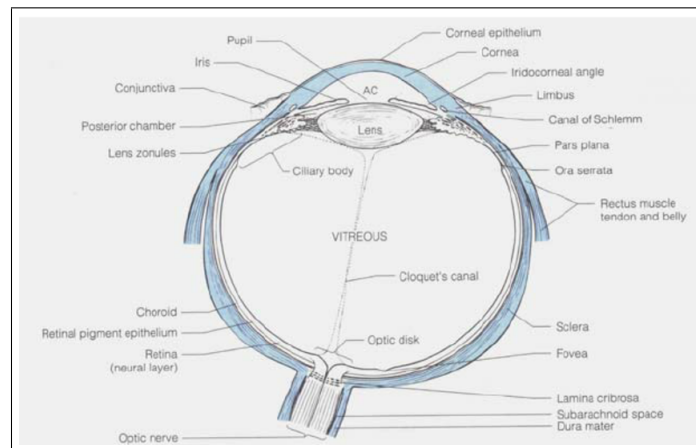


Figure 2-7: Major Parts of Human Eye [5]

### 2.3.3 The Retina

The retina part of the human eye is a thin layer of cells positioning at the interior back and sides of the eye. There are two general classes of light-sensitive cells in the retina; the rods and the cones. Rod cells are responsible on the night-vision due it's high sensitivity to light. However, the cone receptors provide the daylight vision in reasonable light levels. There are about (100-120) million rod cells and (5-6) million cone cells in the human retina. There are more rods than cones because they are used at low light levels and they are desired to collect or gather the incident light [19]. Although there are some 120 million rods and 6 million cone cells in the retina, there are roughly a million optic nerve fibers which connect them to the brain. This means that there cannot be a single one-to-one connection between the photo-receptors and the nerve fibers. The number of receptors connecting to each fiber is location dependent. In other words, the light information will be gathered in a different way depending on the position of the light photoreceptor. In the periphery part of the retina, as many as 600 rods are connected to each nerve fibers, while, in the fovea there is an almost one-to-one connection between cones and fibers. In addition to those two types of photoreceptors, there are other cell types whose function is to accumulate and process the light data information produced by the photoreceptors. The mechanism by which a neural cell can pass information to multiple cells is through horizontal and amacrine cells, see figure 2-8. A receptor cell can directly pass information to another kind of receptor cell which is a bipolar cell, but to send information to other bipolar cells, that electrical signal has been sent already via horizontal cells. The bipolar cells send electrical pulses to many ganglia through similar cells known as amacrine cells. The ganglion cells perform as terminators for the nerve fibers connecting to the brain. Throughout most of the retina, bipolar cells gather signals from several receptors while the fovea there is usually one for each receptor. The benefit of horizontal cells is to connect the adjacent receptors and the amacrine cells to multiple ganglion. The major three types (receptor, bipolar and ganglia) of neural cells send excitatory signals, and the horizontal and amacrine cells send inhibitory signals.

In addition to the inhibitory nature of horizontal cells and amacrine cells, excitatory effects of bipolar cells and ganglion, cells make the lateral inhibition a common form of data processing which

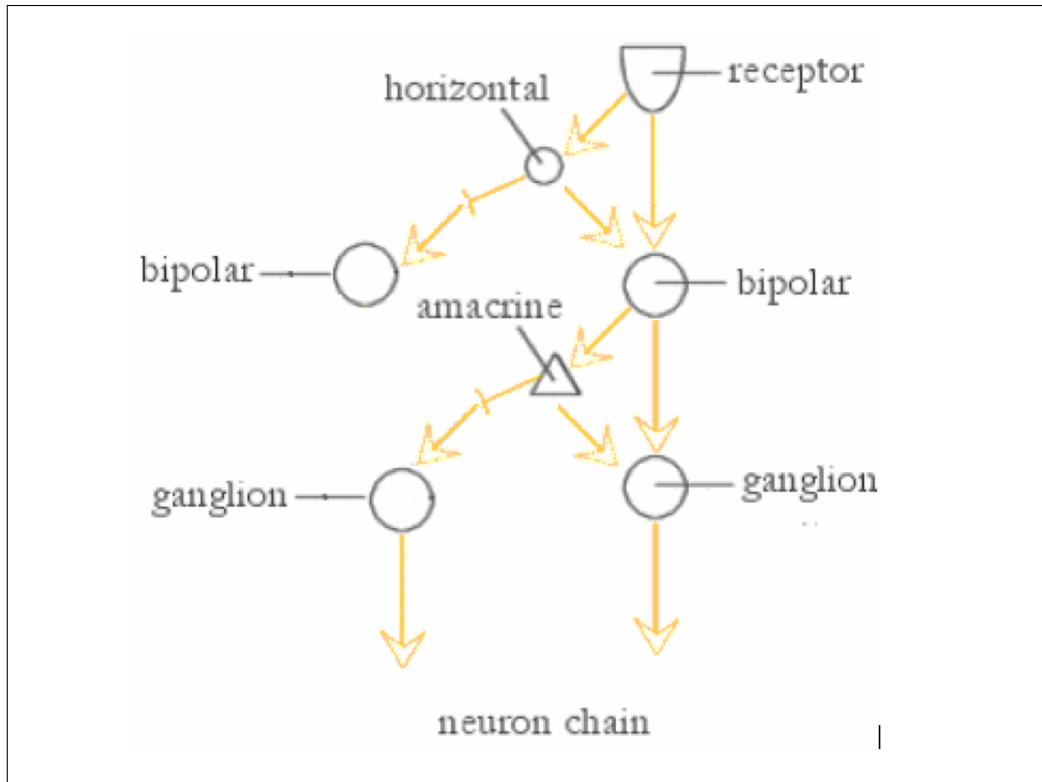


Figure 2-8: Neural Pathway of Visual Stimulus in The Retina [6]

takes place in the retina of the visual system. When a local area of the retina is excited by a fixed input illumination, the cells on the excited part of the retina do not just send the data information to the brain. They also send signals to closest adjacent cells whose effect is to diminish or inhibit the effect of any excitation taking place there. Figure 2-9 shows the effect of a simple model with and without lateral inhibition. In the first part of this figure shown, a uniform input stimulation is applied to an array of sensors. The resultant output is a constant level of production from the sensors. In part (b) the level of stimulation is not continuous it shows a sudden increase. The result also has sudden increase simultaneously. The last part of this figure shows the effect when inhibition is applied to the system. As well as outputting its signal, each sensor has an inhibitory effect on its two neighbors. The resulting sensor output is similar to the second part, however, at the boundary between the two levels of illumination excitatory, the difference in the output is accentuated. In image processing, treating signals in this way is known as edge enhance.

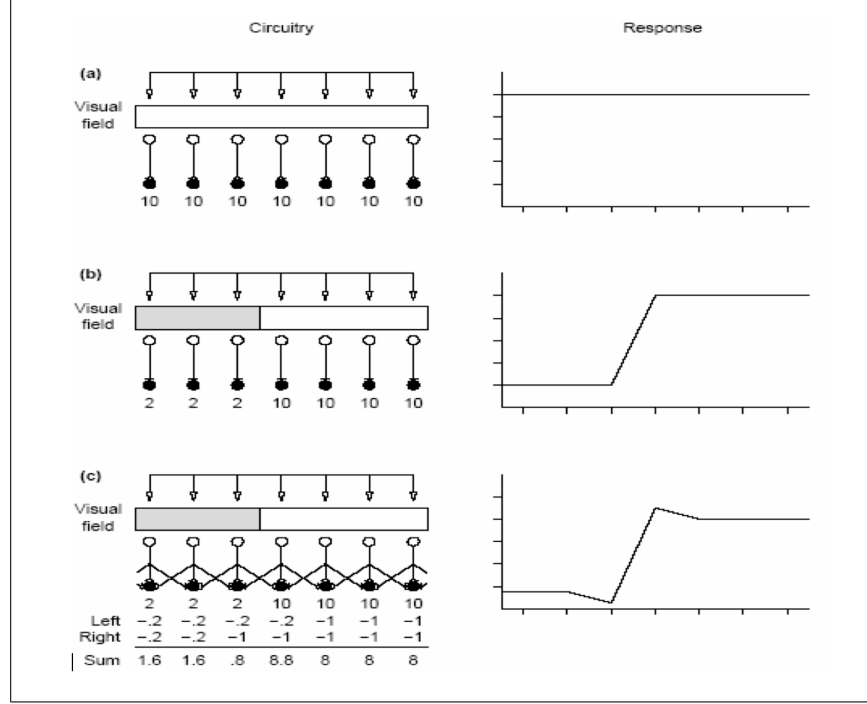


Figure 2-9: The Effects of Lateral Inhibition on Edge Enhancement

## 2.4 Mathematical Formulation of Lateral Inhibition

### 2.4.1 One Dimensional Matrix

The subtractive lateral inhibition occurred when a single receptor was illuminated with a constant level of illumination, and a test signal traveled over a receptor adjacent to the first. This phenomenon has also been observed in the higher level mammals through electro-physiological experiments on the retinas of cats and monkeys[16, 10]. Because of such evidence, the lateral subtractive inhibition has been accepted to occur among the photo-receptors of the Human Visual System. Such inhibition called subtraction because a measure of the activity of any neuron may be obtained by subtracting the inhibitory from the excitatory influences. Thus, the neuron may be totally inhibited if the net inhibition is greater than the excitation. This inhibition influence has been described in equation 2.1:

$$f_i = e_i - \sum_{j=1}^N b_{ij} * f_j \quad (2.1)$$

Whereas,  $e_i$  and  $f_i$  correspond to the input luminance over the receptor field and the output associated with it. And  $b_{ij}$  is the coupling coefficient representing the interaction between the receptors with index  $i$  and  $j$ . This weighting value is usually directly related to the distance between the receptors in a neural network.

In this research work a recurrent model of a lateral subtractive inhibition method will be used as an edge detection and enhancement algorithm and the reason is that this model resembles the biological explanation. The external luminance source over each sensory receptor unit can be considered as an independent excitatory input because of the external luminance itself cannot cause the inhibitory effect. For example, if a machine scans the gray level chart used in the Mach band experiment as shown in figure 2-10 without intelligence, the output will be constant as long as the input is constant. The inhibitory phenomenon is invoked by the biological mechanism of the visual system when each receptor unit is competing for neural firing simultaneously.

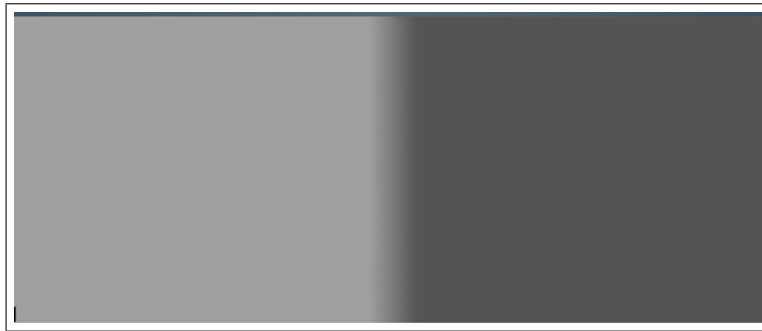


Figure 2-10: Image With Two Intensity level

### 2.4.2 Two Dimensional Matrix

Image signals are typically two dimensional. Therefore, the LSI equation will be extended into the two dimensional form. Each row of receptors can be seen as a group of receptors. Two dimensional form of this biological method can be represented by the equation 2.2:

$$F_{ij} = e_{ij} - \sum_{k=1}^N \sum_{l=1}^N B_{ijkl} * f_{kl} \quad (2.2)$$

Where,  $b_{ijkl}$ , is representing the weighting coefficient matrix; before proceeding further, an explanation of the notation used is necessary matrices, including sub-matrices and vectors as special cases of matrices, are denoted by letters wrapped with brackets,  $[\ ]$ . The elements of a matrix or a vector are denoted by letters along with numeric subscripts indicating their coordinates. To be consistent with the previous expression,  $[E]$  and  $[F]$  correspond to the illumination input and the sensory output respectively in matrix form, while  $[B]$  corresponds to the coupling coefficient matrices. Now we can express the relationship represented in the previous equation in matrix form as shown in equation 2.3:

$$[F] = [E] - [B] * [F] \quad (2.3)$$

For the sake of simplicity, only  $3 - by - 3$  receptor field is being considered as an example.

$$\begin{aligned} [F1] &= [E1] - \left[ [B11][B12][B13] \right] * [F1] \\ [F2] &= [E2] - \left[ [B21][B22][B23] \right] * [F2] \\ [F3] &= [E3] - \left[ [B31][B32][B33] \right] * [F3] \end{aligned}$$

Where,  $[F1] = [f11; f12; f13]$ ,  $[F2] = [f21; f22; f23]$  and  $[F3] = [f31; f32; f33]$ .  $[B_{ik}] = 3 - by - 3$  matrix consisting of the feed-backward coupling coefficients,  $b_{ijkl} = i, k, j$  and  $l$  vary from 1 to 3 respectively in this  $3 - by - 3$  receptor field case. When,  $i = j$  implies intra-row receptor interactions,

which means the two receptors are in the same row.  $i \neq j$  implies inter-row receptor interactions, which mean the two receptors are in different rows. From the previous equation, we have  $[F]$  output variable in both side of the equation. Therefore, we need to do some mathematical conversion in order to simplify the equation 2.3. And an equation 2.4 will be obtained:

$$[F] = S^{-1} * [E] \quad (2.4)$$

Apply this equation above on a  $3 - BY - 3$  matrix:

$$\begin{aligned} [F1] &= \left[ [I + B_{11}][B_{12}][B_{13}] \right] * [E1] \\ [F2] &= \left[ [B_{21}][I + B_{22}][B_{23}] \right] * [E2] \\ [F3] &= \left[ [B_{31}][B_{32}][I + B_{33}] \right] * [E3] \end{aligned}$$

Where,  $[S]$  matrix represents the visual mapping depicted in figure 1-1. Whereas, this matrix is shown to be an inverted version of the weighting coefficients matrix,  $[B]$ , and expressed as a feature extraction filter in visual neuron-physiology, known as the novelty filter [17]. the inverse matrix of the coupling coefficients can be achieved from equation 2.5:

$$[S] = \left[ [I + B_{11}][B_{12}][B_{13}][B_{21}][I + B_{22}][B_{23}][B_{31}][B_{32}][I + B_{33}] \right]^{-1} \quad (2.5)$$

Whereas, the identity matrix  $[I]$  equals to:

$$\begin{bmatrix} 1 & 0 & 0 \\ 0 & 1 & 0 \\ 0 & 0 & 1 \end{bmatrix}$$



And, the Inverse matrix  $[S]$  is :

$$[S_0] = [I + B_{11}] = [I + B_{22}] = [I + B_{33}]$$

$$[S_1] = [B_{12}] = [B_{21}] = [B_{23}] = [B_{32}]$$

$$[S_2] = [B_{13}] = [B_{31}]$$

One of the important characteristics of the matrix  $[S]$  is its symmetry. Let us first look at its sub-matrices. For example,  $[B_{dd}]$ , is a matrix consisting of coefficients describing the coupling among receptors in the  $d_{th}$  row in the two dimensional receptor array. Each receptor unit in row  $d$  may have interaction with any other receptors including itself (in row  $d$ ). This is the intra-row interaction case. For instance, if there are 3 receptors in row  $d$ ,  $3 \times 3$  matrix is needed to represent all these coupling coefficients and is called  $[B_{dd}]$  because the interaction is mutual between any receptors and assuming that it only depends on the distance between them, it follows that  $b_{d1d2}, b_{d2d1}, b_{d2d3}$ , and etc. are all equal. In this case, as long as the difference between the coordinates  $j$  and  $l$  remains constant, the coefficients,  $b_{djd l}$ , will be equal. A similar principle applies to the  $B_{ij}$ , (when  $i = 1, \dots, N, k = 1, \dots, N$ , and  $i \neq j$ ) the inter-row coupling coefficient matrices. They will be identical if the distance separation between the two rows and  $k$ , remains constant. Thus matrix  $[B]$  is symmetric. As we mentioned above,  $[I]$ , is the identity matrix, therefore a matrix  $[S]$  is a symmetric matrix, as well [6].

### 2.4.3 The Exponential Model to Generate the Coupling Coefficients Matrix

The interaction between the receptors is constrained by distance because the receptors always try to draw ions from a nearby region rather than from a remote area when competing for the neuron firing rate and therefore affect other receptors in the neighboring area. However, in the HVS the coupling coefficients,  $b_{ij}$ , are assumed to become exponentially weaker the larger the spatial distance between the receptors [18]. Equation 2.6 is representing the mathematical expression of the mutual interconnection of the neural network:

$$B_{ij} = \alpha * \exp(-\beta * D) \quad (2.6)$$

whereas, alpha  $\alpha$  and beta  $\beta$  are two variables that have a direct impact on the resultant output image via LSI. Therefore, it is crucial to investigate how are they influence on the output image and which numerical value gives them the best representation. In the following chapter, the examination of these two variables impacts and their proper values have shown for both mapping models. The interconnection spatial distances between the neuron receptors have been calculated via the Euclidean equation which is representing by this equation below, see equation 2.7:

$$D = \sqrt{(x - x_0)^2 + (y - y_0)^2} \quad (2.7)$$

As indicated previously, the interconnection spatial distances between the photo-receptors and the way to calculate it is the point of interest in this study. The following chapter will representing the new mapping model based on the Log-Polar Transformation method and a filtration process via Contrast Sensitivity Function (CSF) with the three multiple spatial-frequency channels. In the next chapter the simulation results regarding the new model as well as the conventional one will be shown. Then, the conclusion of this research work and our directions for the future work will be presented in chapter five and chapter six, respectively.

## Chapter 3

# Effect of Lateral Inhibition within Two Different Image Mapping Models

Human visual system is composed of vast neural networks retinal cells to sense light stimulus, neural pathways and visual cortex for high-level visual cognition information processing role at different levels; that is physical level, psychological level and physiological level, as well as a cognitive level. In every level, many rational and well-ordered mechanisms can be found that should be applied in information processing. Such neural computing and generic algorithm are good examples of the application using biological mechanisms [19].

Lateral inhibition which is a physiological level phenomenon of early vision system can be shown as a computational model that improves and enhances the image contrast. Different kind of methods to enhance and improve the image contrast are used such as grayscale transformation (linear, gamma, logarithm, etc. [20]), histogram modification [21] and some filtering or masking techniques [22]. However, these techniques have unsatisfactory results which arise for the following reasons:

1. We have to choose ad hoc one of them to the needs of the moment because they do not adapt themselves to an actual image automatically. .
2. These methods are based on using digital or statistical features of the image, but they lack a consideration of the physiological and psychological behavior of our visual systems. .

The proposed method in this work (image contrast enhancement based on the lateral inhibition), gets over both of the problems mentioned above (1,2) and can show the rationality of human visual system to recognized and detect the important features from wide varieties of visual stimuli. The

lateral inhibition model represents the basis of physiological and psychological levels. Lateral inhibition in retinal cells is a phenomenon that has the effect of making the cells compare the amount of light at one position with the amount at neighboring regions (photo-receptors).

The Lateral Inhibition (LI) comprises two inhibitory modes: Recurrent-Lateral Inhibition (RLI) and Non-Recurrent Lateral Inhibition (N-RLI), and the difference between these two mutual inhibitions is that what caused the inhibition effect. If the network output produced it, then it is the RLI; otherwise, it is N-RLI. The neural network whose connection mode adapts the lateral inhibition mechanism is called Lateral Inhibition Neural Network (LINN). In this research work we have adopted the Recurrent mode of the lateral inhibition since it is much closer to the HVS than an N-RLI and the reason is a biological one.

It is believed that the recurrent (negative) feedback lateral inhibition occurs between the photo-receptors in several different sensory systems, but in particular, Human Visual System. In these optical systems, if one receptor is excitatory after being stimulated, it will inhibit the surrounding neurons through the inhibitory connections; thereby achieve the competition between neurons. This contest among the receptors produces a phenomenon which characterized in enhancing the image contrast in the receptive field. Different models have been investigated to calculate the weighting coefficients matrix of the lateral inhibition algorithm to obtain the contrast enhancement of the processed image, see [6]. However, in this work an exponential model has been used to generate the coupling coefficients of LSI.

Figure 3-1 represents the way to calculate the uniform spatial distances between the center points of the photo-receptors and generating a uniform coupling coefficients for the lateral subtractive inhibition based on the exponential model by using equation 2.6 and equation 2.7.

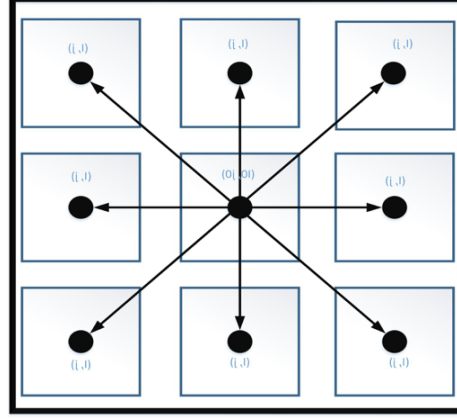


Figure 3-1: This figure Illustrates the Uniform Model of the Recurrent Lateral Inhibition, with neural network size  $[3 \times 3]$ .

The Uniform model introduces the way of how to calculate the spatial distance between the photo-receptors according to the center point (the point of interest). However, this way of calculation produces many difficulties to the pattern recognition process in image processing world. One of these challenges is the size of the output processed image will be same as the input image data, and that needs a large memory space for the data processed to be stored. The second one is the time required to process and detect the features from the entire input image data. While, the real-time operation property is a crucial, especially in vision systems. Therefore, a new mathematical method to sample the image has been introducing to get rid of these difficulties of the conventional model (the Uniform model). This new approach mimics the Human Visual System in a way that it processes the image data in a non-uniform way corresponding to the spatial distribution of the receptive fields. More details about the new model will be presented on the following section. The structure of this research work is representing in figure 3-2 below to illustrate the procedures and the comparison method that we have used to compare the new model with the conventional one which is the Root Mean Square Error (RMSE) quality metric.

### 3.1 The Work Structure:

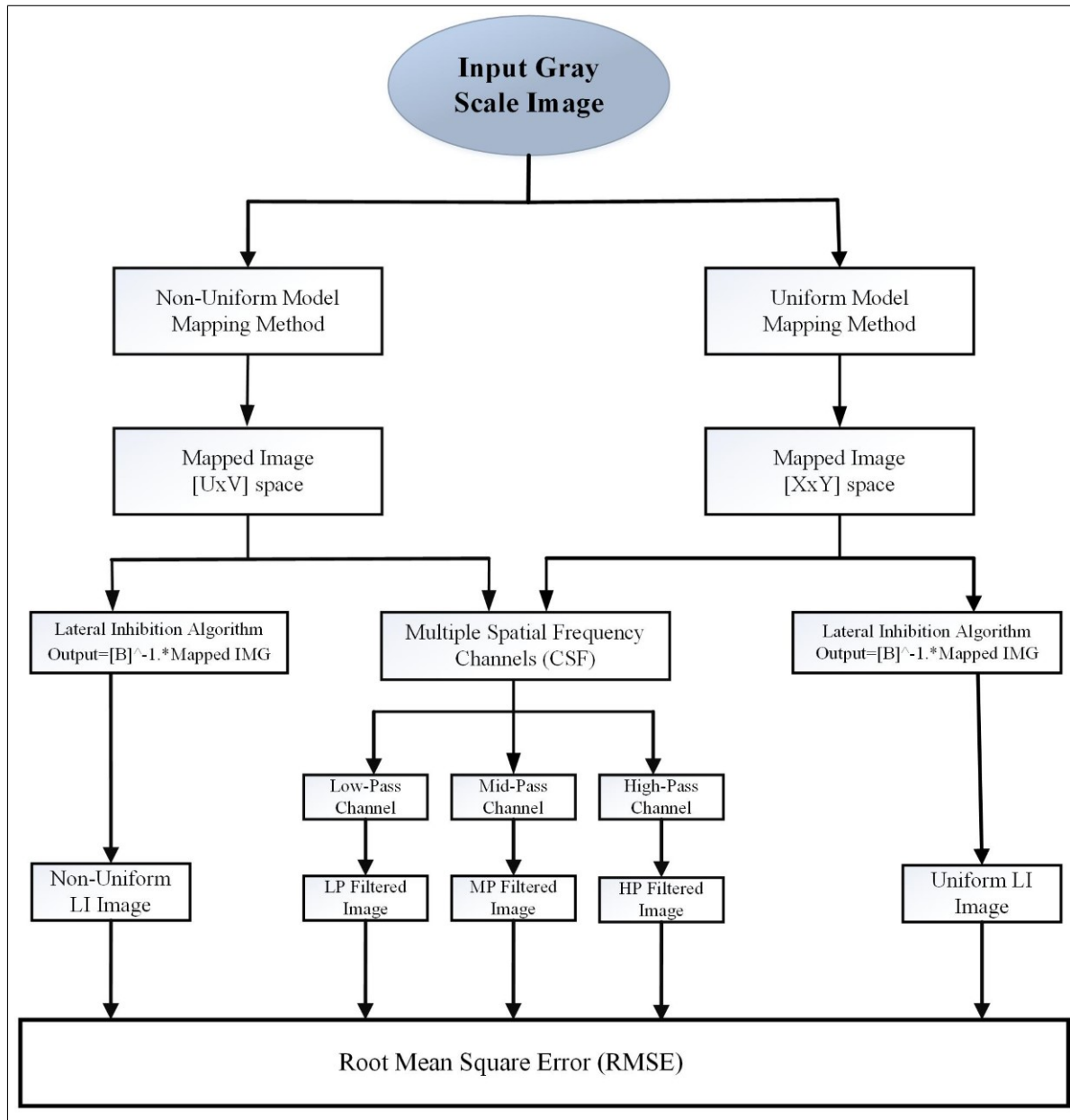


Figure 3-2: The Work Structure Of this Thesis.

## **3.2 The Non Uniform Mapping Model of the coupling coefficients matrix based on the Recurrent Lateral Inhibition Method**

### **3.2.1 Introduction to Log - Polar Transformation Mapping**

At the highest levels of evolution, living beings have developed vision systems that are both active and space-variant. In the vision system of primates and specifically in the human eye, a space-variant image sensor structure exists and characterized by a non-uniform pixel geometry. In biological systems such as these, there are two different areas of resolution can be recognized: the fovea, characterized by a relatively uniform receptor distribution of fine resolution, and the periphery, where the receptor distribution is sparser and is non-uniformly distributed. This mapping method was first motivated by its resemblance with the structure of the retina of mammalian biological vision systems. It has been found that the excitation of the cortex can be approximated by a log-polar mapping of the eye's retinal image. In other words, the real world is projected onto the retinas of our eyes, is reconfigured onto the striate cortex of the brain by a process similar to a log-polar mapping before it is processed by our brains[23]. In the human visual system, the cortical mapping is performed through a space-variant sampling strategy, with the sampling period increasing linearly with the distance from the fovea. Within the fovea, the sampling period becomes almost constant (one-to-one uniform area). The retina-cortical mapping can be described through a transformation from the retinal plane onto the cortical plane[24]. In particular, log-polar mapping algorithm produces an image with less amount of data to be processed, while preserving details in the fovea necessary for robust pattern recognition [25].

### **3.2.2 Background**

In 1866 Max Schultz published an extensive report on the anatomy of the human eye [26]. By carefully raising the sclera on a human eye, removing the choroid and pigment layers, Schultz was able to view the tips of the photo-receptors in situ. He found that the photo-receptors were not organized in a uniform manner, but were denser at the fovea and became less dense as one traversed rays outward from the fovea. From his early work has evolved the exponential model for the cone

density. In other words, as the radial displacement from the center of vision is increased, the cone density decreases in an exponential manner. This physiological fact incited great interest into how the information gathered by the cones is mapped to the corresponding section of the brain. Schwartz in [27, 28], showed that under the conditions that the cortex has unfolded into a cortical plane and the curved retinal surface, within of visual field, is approximated by its tangent plane. Daniel and whitteridge have been introduced the magnification factor, which the cortical magnification factor is defined as a ratio of the distance moved across the surface of the cortex to the corresponding distance moved across the surface of the retina [29]. And this can be approximated by a complex logarithmic mapping model. In his notes, Schwartz has mentioned that this retinal-cortical mapping provides the mechanism for size and rotational invariance in the HVS. The retinal-cortical mapping has the same mathematical insight of a conformal logarithmic model for the projection of the retinal surface onto the striate cortex of the brain. The conformal logarithmic mapping has introduced to the image processing community. The mathematical treatment of the conformal mapping and a suggestion on how to utilize this mapping model in an image processing is described in this study [30], but do not proceed further to develop simulations. The non-uniform structure has investigated regarding the non-uniform sensor arrays with the sensor distributed in such a manner as to preserve chain encoding [31]. However, the human visual system does not require chain encoding preservation and instead of that the physiological evidence for a complex logarithmic retinal-topic mapping has exploited by calculating the logarithmic transformation through a collapsing of a non-uniform (retinal) sampling field onto a uniform (cortical) field [32].

### 3.2.3 Mathematical Representation of Log-Polar Mapping Algorithm

According to the non-uniform distribution of the cone receptors in the human retina, a pattern has been built. Whereas, the non-uniform radial logarithmic sampling of a captured object, produces a uniform homogeneous space as an output which can be expressed as  $(u, v)$ . whereas, the parameter  $(u)$  is equivalent to the natural log radius ( $\log(r)$ ), and  $(v)$  represents the angular position of the receptor  $(\theta)$  in the HVS. This mapping from a non-uniform space  $(r, \theta)$  to a uniform one  $(u, v)$  which preserves angular information, may be decomposed into two steps for simulation purposes.



The first step takes the non-uniform array described in the left side of figure 3-3 below and produces the uniform  $(u, v)$  plane. In the second step, the data will be re-organized in spatial coordinates to reflect the angular information of the original image; this will be shown on the right side of the same figure.

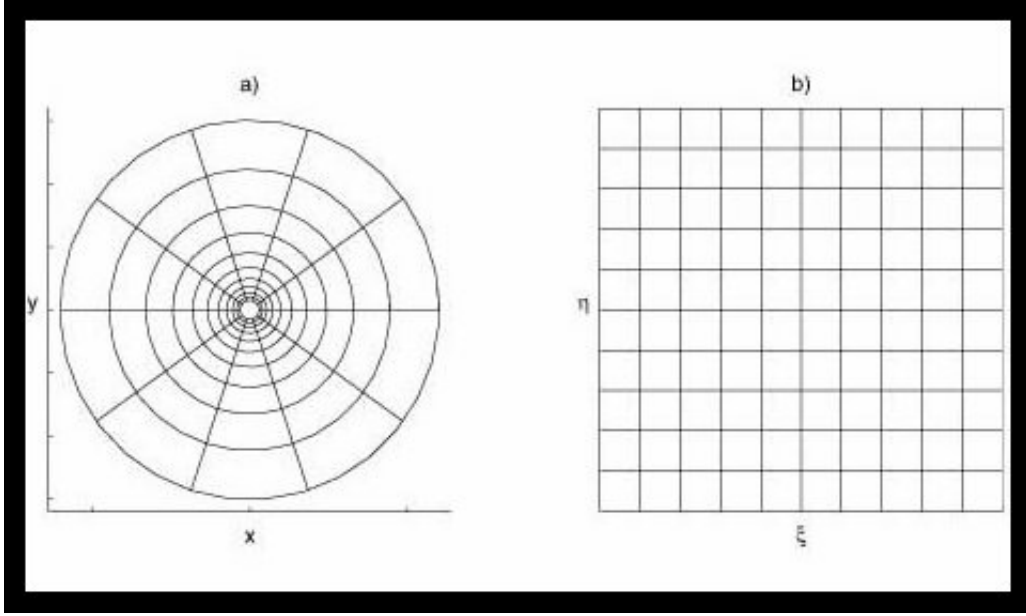


Figure 3-3: The conversion of the Uniform space to the Non-Uniform plane  $(r, \theta)$  in (a). Illustration the transformation of the Non-Uniform Plane to Uniform  $(u, v)$  space (b) [7].

The following equations give the mathematical relationship of these two steps mapping, from the non-uniformly sampling plane to the uniform  $(u, v)$  feature space:

$$r = \sqrt{x^2 + y^2} \quad (3.1)$$

$$\theta = \arctan\left(\frac{y}{x}\right) \quad (3.2)$$

This transformation presents some interesting properties for the scale and rotation invariance about the origin in the Cartesian plane. It can be seen from figure 3-4, that the single circle maps to a single vertical line in the transform space since the radius of the circle at all angles is given by a constant value  $(r)$  coordinates for all  $(\theta)$  coordinates from  $(0$  to  $2\pi)$ . Similarly, an image

of radial lines which have a constant angle but variable radius results in a map of vertical lines in the transform space [33]. These mapping characteristics are well known and are fundamental for many rotation and scaling invariant pattern recognition algorithms. When the input image is rotated that would be translated onto a vertical shift along the  $y$ -axis of the  $(u, v)$  mapped space. However, if the same input image has zoomed in (scaled on the point of view) that will result in only horizontal shift displacement of the mapped space without effecting on the important details of the image itself. This has been explicitly represented and documented by researchers [34] and in figure 3-4 below:

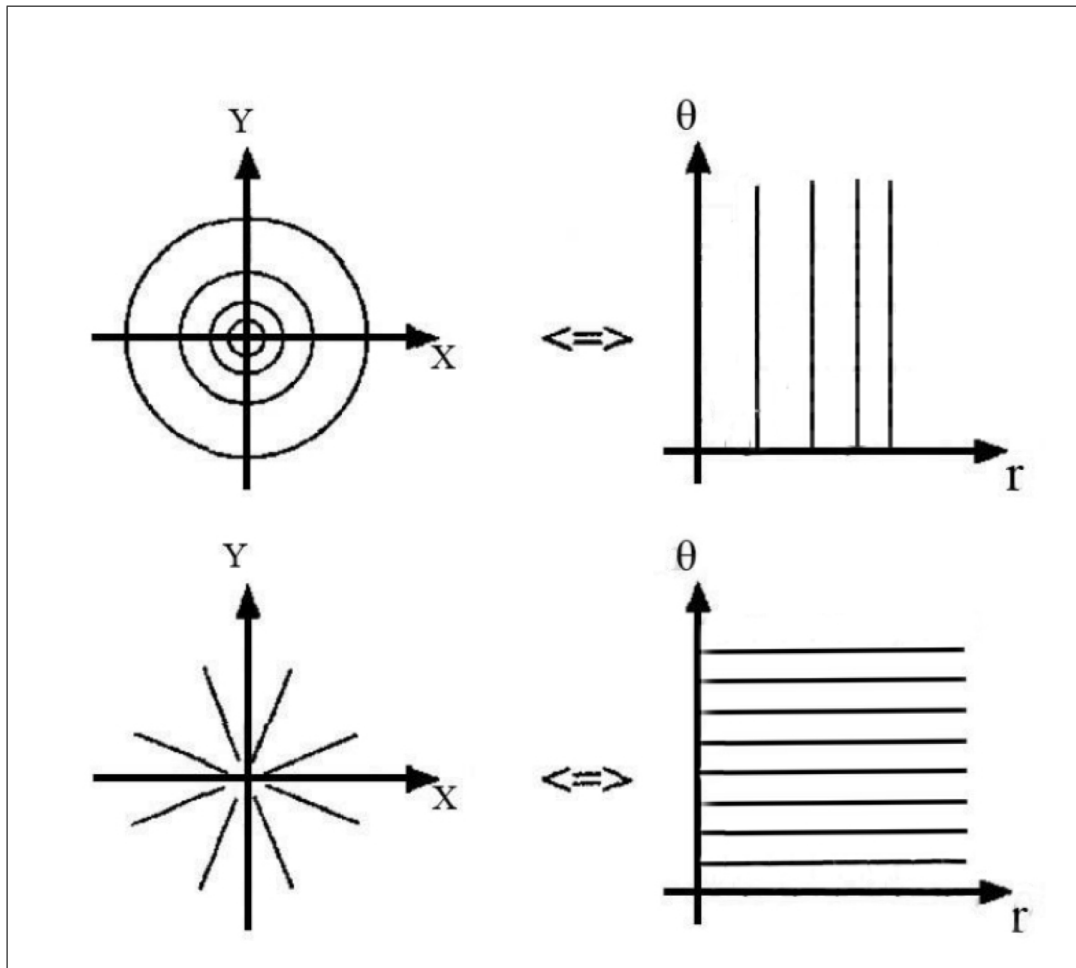


Figure 3-4: The Log-Polar Mapping Applied to Regular Patterns (Concentric Circles and Radial Lines in The Image Plane).

### 3.3 Non-Uniform Model And Lateral Subtractive Inhibition (LSI) Method

The concepts of a non-uniform retinal-like image sampling and log-polar mapping have been widely applied in the area of machine vision and image processing. An extensive research work has been done on log-polar mapping has represented in this study[35]. While, the non-uniform retinotopic image sampling and complex log-mapping applied on face recognition have demonstrated by this work presented here[36]. The lateral inhibition occurs in the frontal pathway of the Human Visual System (HVS) between neuron receptors at different stages of information flow. The explanation of this biological phenomenon. There are only a finite number of ions available for neural firing rates which propagate information from local region of the retina to the corresponding cortex region. This causes an inhibitory influence among the receptors in the neighborhood because they compete for these ions at the ganglion level. As we mentioned earlier, and the mathematical representation of this biological method can be found in equation 2.3 and 2.4.

Non-uniform resolution of the human retina has been found to follow a logarithmic polar law, taking into account the linear increment of the photo-receptor's size with the distance to the center [27]. Combining this with the lateral subtractive inhibition phenomenon, that occurs between the neuron receptors. It is possible to obtain such a robust biological filter model to perform the desired tasks, such as edge-enhancement, without considering all the data contained in uniformly sampled images. Hence, the processing effort can be concentrated in the foveal area. Thereby, less computational cost on the processing data can be achieved. The main advantage of this model is the utilize of geometric properties of the log-polar image to implement lateral inhibition, and hence we can obtain the edge enhancement on the foveal area (the highest resolution part of the LPM pattern) as opposed to the image periphery. And compare that to the uniform Cartesian image, to show that both computational and performance advantages arise from the use of the space-variant systems. The photo-receptors in the human retina are distributing in space with increasing concentration toward the center of the visual field (the fovea) [37]. This model is based on a Log-Polar space variant, and that would produce a non-uniform image sampling. The main advantage of

this kind of sampling is an important data reduction obtained at the cost of reducing the resolution in the periphery of the pictures, but the high settlement in the fovea is sufficient to accomplish most of the visual tasks [38]. As we mentioned earlier, that the structure of the human retina follows the log-polar law and to observe that the figures 3-5 have shown the way that a cone photo-receptors are taken to distributed over the human retina.

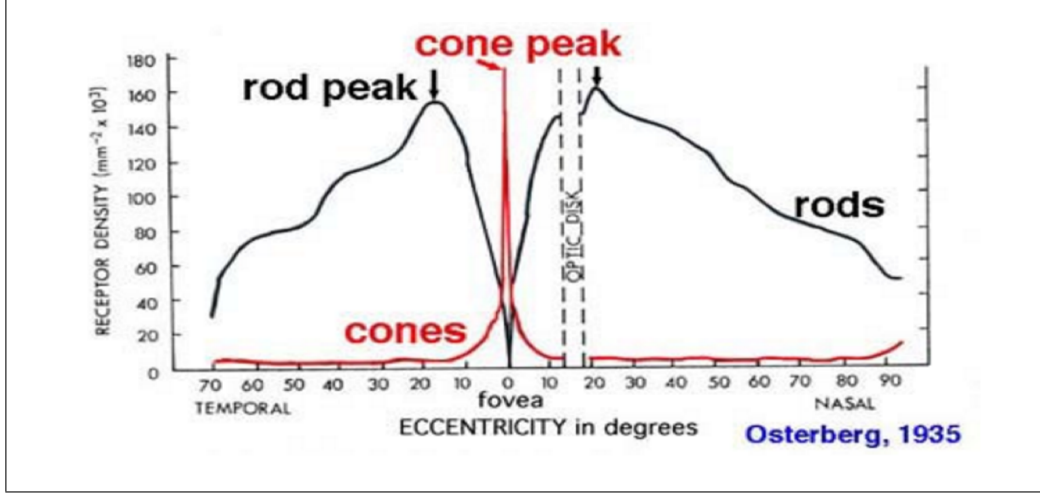


Figure 3-5: the human retina cone-rods distribution.

Figure 3-6, includes the non-uniform distribution of receptors in the human retina. As well as, it shows the inhibition effectiveness between the sub-circles. If we take a particular circle to be our reference sub-circle, then the calculation of the distance and the inhibition competition will be starting from this circle to its neighbors, then the separation distances will be calculated via the Euclidean equation 2.7. From the same figure, the inhibition impact reaches the maximum with the minimum distance between the sub-circles. Therefore, there is an inversely proportional relationship between the inhibition effect and the interconnection spatial distance between the neurons:

$$TheInhibitionImpact = \frac{1}{TheSpatialDistanceBetweenTheNeurons} \quad (3.3)$$

The calculated distances (D) will be re-organized in a uniform space, where the y-axis represents the angular spatial positions for each sub-circle "how it's distributed aver a range from [0 to 360<sup>0</sup>]",

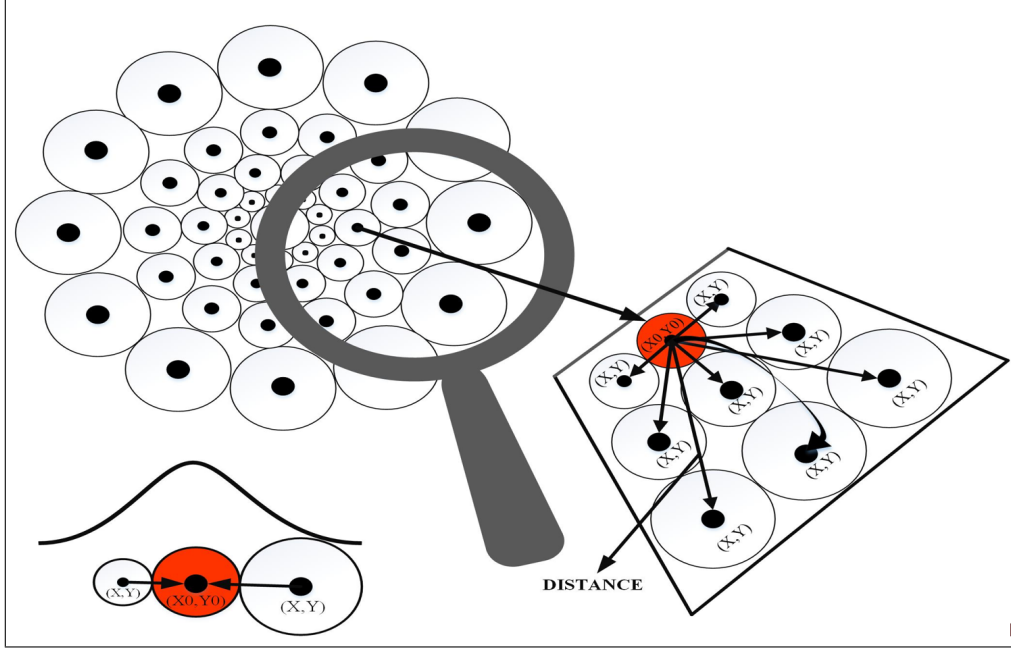


Figure 3-6: Illustrate The Non-Uniform Distribution of the Receptors: Inter-connection Distance Calculation of the Receptors and the inhibition Impact.

and the x-axis represents the non-uniform natural logarithmic increment of the radii, see figure 3-7.

Figure 3-7 illustrates the uniform increment of the y-axis of  $(u, v)$  space, (the angular position regarding  $\theta$ ), due the symmetry. In other words, the difference of the distance between any two angles is constant. However, the x-axis of the same space which represents the non-uniform increment of the radii is asymmetry. Which means, the difference between any two radii is not constant, and it depends on the position of the reference sub-circle, and if we take another sub-circle to be our new reference neuron then, the distances will be different as well as the weighting coefficients according to the new distances. The weighting coefficients matrix will be achieved by applying the same exponential model on the non-uniform distances via the new mapping model, by using the equation in 2.6 . This mathematical expression represents the effect of the Lateral Subtractive Inhibition (LSI) on neuron receptors in the HVS [12]. Each parameter in this equation impacts effectively on the resultant weighting coefficients. More explanation and simulation figures related to this algorithm will be representing on the following chapter.

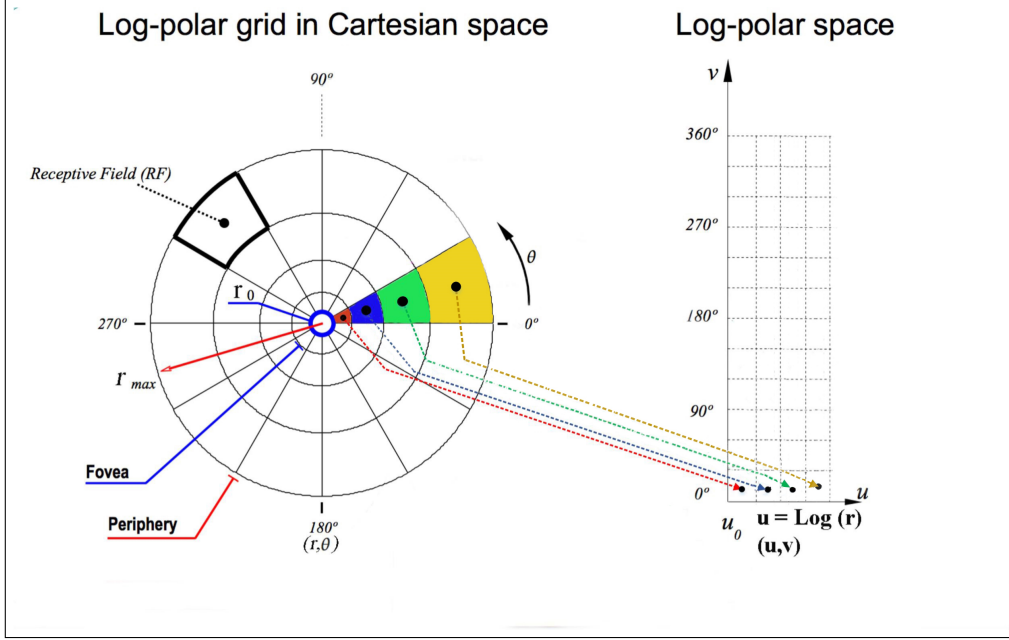


Figure 3-7: Illustration of the Cartesian plane and the Log-Polar plane with non-uniform distance between two radii [8].

### 3.4 The Contrast Sensitivity Function (CSF) of the Human Visual System (HVS)

Evidence that the Human Visual System may be performing some parallel spatial frequency filtration processing is supported by both physiological and psycho-physiological data. Evidence has been found that the cells of the Macaque monkey's visual cortex are spatially selective frequency [39]. The use of multiple, fairly narrowly tuned, spatial frequency channels (presumably cells selectively sensitive to different restricted portions of the spatial frequency spectrum), has been utilized in this research work to show the separation of features in portrait images into different frequency channels. Then, study the possible existence of the Lateral Inhibition between spatially neighboring channels that detect similar spatial frequencies.

### 3.4.1 Contrast Sensitivity

In addition to the anatomical and neurophysiology studies, much insight into human vision has been paid via psycho-physical technique, for example, the HVS can be experimentally characterized by detection the various spatial contrast, most commonly sine-wave gratings, see figure 3-8. The contrast sensitivity threshold for a given stimulus is defined as the minimum contrast necessary for a human to observe the target. Many different measures of contrast have been employed in psycho-physiology studies, such as: Simple Contrast, Weber Contrast, Michelson Contrast and Root-Mean-Squared Contrast (RMS Contrast):

1. *SimpleContrast* is defined as:

$$C_{simple} = \frac{L_{max}}{L_{min}} \quad (3.4)$$

where  $L_{max}$  and  $L_{min}$  denote the target's minimum and maximum luminance, respectively.

2. *WeberContrast* is defined as:

$$C_{weber} = \frac{L_{max} - L_{min}}{L_{min}} \quad (3.5)$$

where  $L_{min}$  and  $L_{max}$  denote the target's minimum and maximum luminance, respectively.

3. *MichelsonContrast* is defined as:

$$C_{michelson} = \frac{L_{max} - L_{min}}{L_{max} + L_{min}} = \frac{1}{2} * \frac{(L_{max} - L_{min})}{\mu(L)} \quad (3.6)$$

where  $L_{min}$  and  $L_{max}$  denote the target's minimum and maximum luminance, respectively;

where  $\mu(L)$  denotes the mean luminance.

4. *RMSCContrast* is defined as:

$$C_{rms} = \frac{1}{\mu(L)} \left( \frac{1}{N} * \sum_{i=0}^N \left[ L_i - \mu(L) \right]^2 \right)^{0.5} = \frac{\sigma(L)}{\mu(L)} \quad (3.7)$$

where  $\mu(L)$  denotes the mean luminance,  $\sigma(L)$  denotes the standard deviation of the target's luminance's,  $L_i$  denotes the target's luminance at spatial location ,  $i$  and  $N$  denotes the total number of spatial locations. Most often, the contrast metric is selected based on the experimental stimuli; e.g., Michelson (peak-to-peak) contrast is commonly used for

targets consisting of sine-wave gratings, whereas RMS contrast is commonly employed for non-periodic targets (noise, textures, images). Note that the luminance values used in all of these definitions of contrast are defined in standard CIE units of candelas/square meter (cd/m<sup>2</sup>).

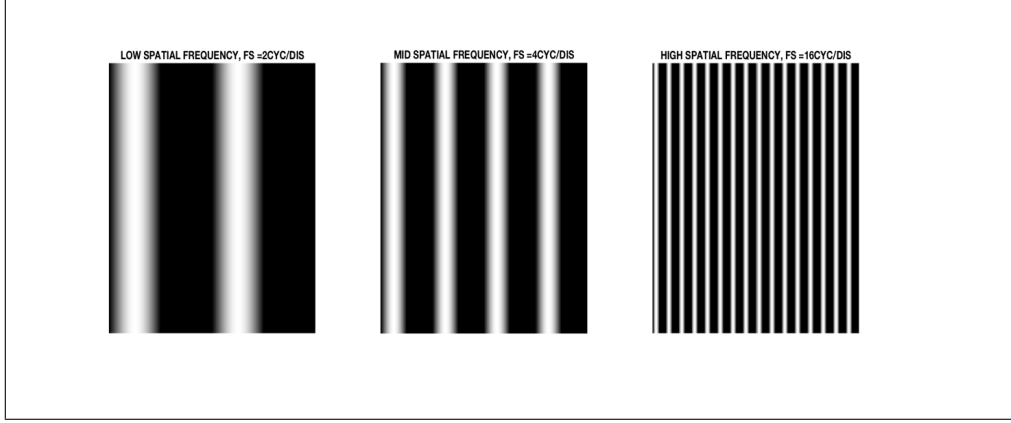


Figure 3-8: three different spatial frequency ranges [2 cycles/mm, 4cycles/mm and 16 cycles/mm.

### 3.4.2 Contrast Sensitivity Function

Contrast is a physical parameter describing the magnitude of the luminance variations around the mean in the scene. According to the previous section, it is not a trivial task to choose the proper metric to measure the contrast, since in any particular scene luminance may change from point to point in complex ways [spatial-temporal contrast]. However, in the visual stimuli always the stimulus is a single of uniform luminance presented against a uniform background or sinusoidal pattern (periodical pattern). If the stimulus is a spatial periodical pattern (or gratings), it defined the spatial frequency which is the number of cycles per unit space. The luminance profile of sinusoidal gratings of frequency ( $f$ ) measured in cycles/ distance,  $cpd$ , oriented along the spatial direction, can be described as:

$$Y(x, y) = Y_0 + A * \sin(2\pi(f_x X + f_y Y)) + \phi \quad (3.8)$$



Where,  $Y_0$ , is the background luminance,  $A$ , is the amplitude and  $(f_x, f_y)$  are the spatial frequencies along  $(x, y)$  orientations, respectively.  $\phi$  is the phase, determine the luminance at the origin of the coordinates  $(x = 0, y = 0)$ . If the phase  $\phi$  is  $\pi rad$  the luminance is zero at the origin the pattern has an odd symmetry. Whereas, if the phase  $\phi$  is  $frac{\pi}{2} rad$ , the luminance is maximum at the origin and the pattern has an even symmetry. The figure shown below illustrates the sinusoidal luminance with different spatial frequencies:  $[2cycles/\pi]$ ,  $[4cyc/\pi]$  and  $[16cyc/\pi]$  to represent the complete frequency bands [Low, Mid, High]. The contrast detection measurement depends on the determination of the minimum contrast required (threshold) to detect sine wave gratings of with different spatial frequencies as the expression in 3.9:

$$CSF = \frac{1}{THRESHOLD CONTRAST} \quad (3.9)$$

Figure 3-9 shows the typical shape of the curve to represent the CSF for a subject with a normal visual system when  $\phi = \frac{\pi}{2} rad$ . This curve is bandpass in nature. In other words, it represents that

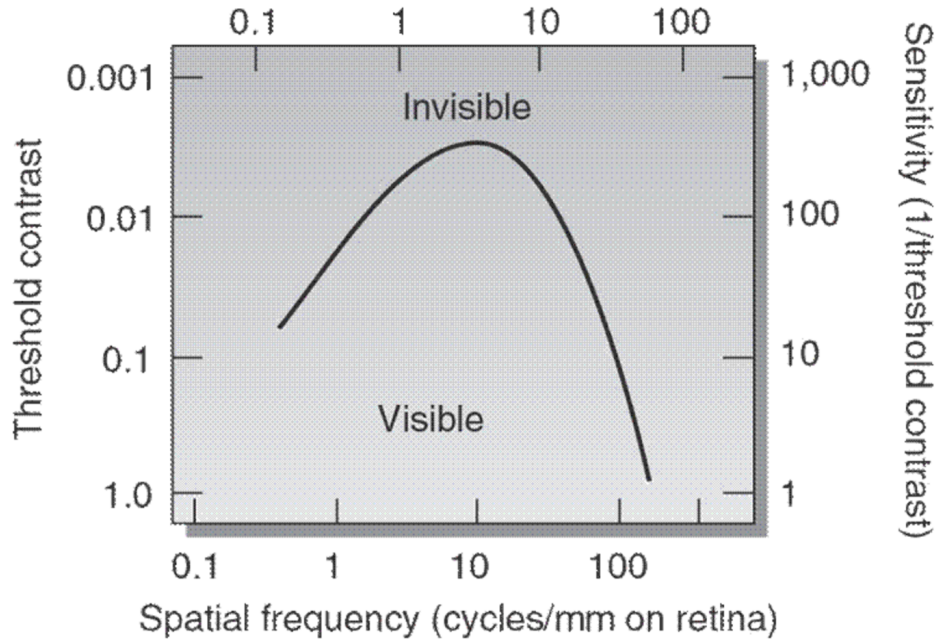


Figure 3-9: Contrast Sensitivity Function Envelope Curve (CSF).

the stimuli are most sensitive to an intermediate range of spatial frequency and less sensitive to the

lower and higher than this range.



Figure 3-10: Sweep Grating

Figure 3-10, displays a pattern that increases in spatial frequency from left to right (the bars get narrower) and decreases in contrast from bottom to top (the bars get fainter). By tracing out the boundary between the visible and invisible you can make out the curved shape of the CSF, which is exactly like the typical curve in the previous figure, see figure 3-9. In the human eye, the reduction in sensitivity at high spatial frequency has been attributed to limitations both in optics of the eye and in receptors spacing, and to quantum noise; whereas at low spatial frequency reduced the sensitivity is believed to occur in part by limited receptive field size[40].

### 3.5 Multiple-Spatial Frequency Channels

The typical curve of the CSF is an envelope of over several underlying mechanisms filter; each corresponds to photo-receptor neurons with differing preferred spatial frequencies, this depends on the evidence has found that the cells of monkey’s visual cortex are spatially selective frequency [41, 42]. Each frequency channel is sensitive to a particular range of frequency, and these channels can be overlapped as well as they are acting like the bandpass filter. According to [42, 43] studies, the HVS has between five and seven spatially-tuned frequency bands. However, for real-time operation, it is necessary to eliminate unnecessary processing or combine several processing tasks into one simultaneous process to reduce the processing time required to accomplish the required task. To do that, we formed the CSF curve to be an envelope over three underlying spatial frequency selective filters. These three bands are thoughts to be useful for pattern identification. All the results simulations for these three groups will be presented in the following chapter.

#### 3.5.1 The Link Between The Contrast Sensitivity Function and The Recurrent Lateral Inhibition of HVS

This section deals with the link between LSI and the Multiple Spatial Frequency Channel HVS Model. According to [18] the Lateral Subtraction Inhibition (LSI) was represented as the process of passing the visual information inputs through the multiple bandpass channel filters. These filters are formed from a difference of Gaussian (DOG) functions under the condition that the coupling coefficient matrix is Gaussian. The difference of Gaussian (DOG) model is a spatial bandpass filter, whereas it describes the characteristics of lateral geniculate nuclei (LGN) receptive fields since the DOG filters show a significant similarity to retinal ganglion cell receptive field. As we mentioned previously, many of physiological researchers have been recorded that the neurons of the retinal ganglion cells signal the spatial differences in light intensity falling upon the retina. This is accomplished by the so-called “center-surround” organization of receptive field, in which it’s excitatory and inhibitory subfields are organized circularly symmetric regions. Therefore, if we want to find the closest function in image processing that can model the receptive field’s properties, we can say that the difference of Gaussian filter function is the one to model the shape of the retinal receptive

field. Whereas, the role of DOG captures reasonably well the “maxi can hat” shape of retinal ganglion cell receptive fields. Of course, the human retina is more complicated than this model in reality; that’s because of the transformation of the visible pixels to retinal ganglion cell outputs is mediated by many other neurons and complex synapses.

There are two major varieties of the center-surround receptive field, which is the main property of the retina and the DOG filter, ON-center/OFF-surround and Off-center/ON-surround, depending on whether the central region is excitatory or inhibitory, respectively. It is widely thought that the reason for having these two varieties is so that both negative and positive changes in intensity can be signaled with positive-only quantities. The figure 3-11 below represents the two types of photo receptors of the human retina:

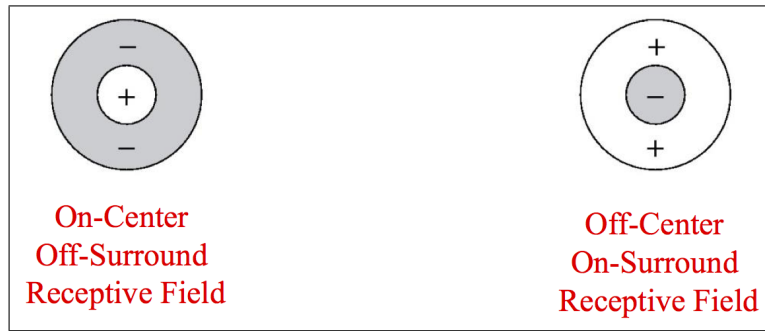


Figure 3-11: The two models of the neurons receptive fields of the HVS.

### 3.5.2 Filtering Entirely In Spatial Domain:

It is known that certain definable features can be shown to be in separate spatial frequency channels [43]. These spatial-frequency channels have generated based on the difference of Gaussian function (DoG). That based on the similarity between the structure of the neuron receptive field and the DoG function. Since the Fourier transformation of a Gaussian is still Gaussian, the filtration process in this research work will be in a spatial domain and that means, a convolution of the original input image with a DOG (difference of Gaussian) where this function can be obtained by subtracting two zero mean Gaussian filters with different sigma parameters. All the mathematical operations

related to these process will be shown below:

In One Dimension:

$$DOG(x) = A * \left( Gaus(\sigma_{high}) - Gaus(\sigma_{low}) \right) \quad (3.10)$$

$$DOG(x) = A1 * \left( \exp \left( -\frac{(x - \mu)^2}{2 * \sigma_{high}^2} \right) - A2 * \left( \exp \left( -\frac{(x - \mu)^2}{2 * \sigma_{low}^2} \right) \right) \right) \quad (3.11)$$

In two Dimension:

$$DOG(x, y) = A1 * \left( \exp \left( -\frac{\left( (x - \mu) + (y - \mu) \right)^2}{2 * (\sigma_{high})^2} \right) \right) - A2 * \left( \exp \left( -\frac{\left( (y - \mu) + (y - \mu) \right)^2}{2 * (\sigma_{low})^2} \right) \right) \quad (3.12)$$

where, A1 and A2 are representing the filter's amplitude. In this work, the spatial domain is the main domain to filter out the mapped images via the following equation to represent the convolution operation regarding this space:

$$FilteredImage = conv2 \left( Mapped_{image}(x, y), DOG(x, y) \right) \quad (3.13)$$

Feature extraction and enhancement can be achieved by using the *DOG* filters. To do that, the filter's parameters should be specified first. As we mentioned earlier, the contrast sensitivity of the captured image is necessary to observe against the constant background and this metric is representing by a typical band-pass envelope curve. To mimic that curve shape with the filters *DOG* as multiple spatial frequency channels, we need to set up parameters in a specific way so that we can achieve the low frequency of the image from the first channel, the middle frequency from the second band as well as the high frequency from the last one. Indeed, the performance of the filter is conditioned by parameter ( $\sigma$ ). The relationship between the first sigma of the first Gaussian low-pass filter to the second sigma of the second filter can be represented by equation 3.14:

$$\sigma2 = k * \sigma1 \quad (3.14)$$

Where,  $k$  is a constant. To test the impact of this parameter on the filtered image based on a *DOG* filter, we have tested a range of numerical values and regarding its output image the best value has chosen. In other words, a Root Mean Square Error quality metric has used to calculate the

difference between a filtered output image regarding different  $k$  parameter to the original one. The following figure, figure 3-12, is illustrating the impact of increasing this parameter on the output image, as we can see that there is no change at all on the output image after a 5.6 value. Therefore, we have used this value to calculate the second sigma  $\sigma_2$  for the second Gaussian filter ( $Gaus_{\sigma_2}$ )

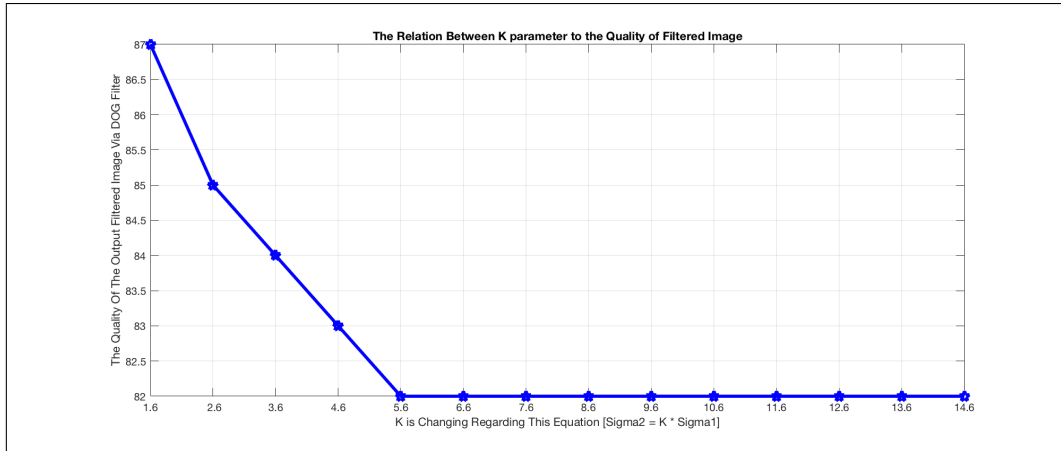


Figure 3-12: Demonstration the Relationship Between the Second Sigma  $\sigma_2$  to the First one  $\sigma_1$ .

According to the figure above, the mathematical expression which will be using to obtain the Gaussian filters for the filtration part of this work will be presenting on the following equation:

$$\sigma_2 = 5.6 * \sigma_1 \quad (3.15)$$

More details about that will be representing on the following chapter of this work. Besides, the amplitude parameter of the kernel has been selected to gives the exact shape of the composite envelope curve; the next figure illustrates all the spatial frequency channels that we have built and used to filter out the images in this work and the envelope curve shape that relates to the CSF of the HVS.

Figure 3-13 illustrates the composite envelope curve that came from adding up all the spatial-frequency channels to represent the Contrast Sensitivity Function (CSF) of the Human Visual System. As we mentioned earlier that these three channels are actually Difference of Gaussian with zero mean and different standard deviations and amplitude to obtain all the important information details from the input image depending on each channel bandwidth. The following figure 3-14, will

be showing the input image as well as the filtered output images via these three spatial frequency bands in grayscale and in color space to let the reader clearly observe the difference between the filtered images.

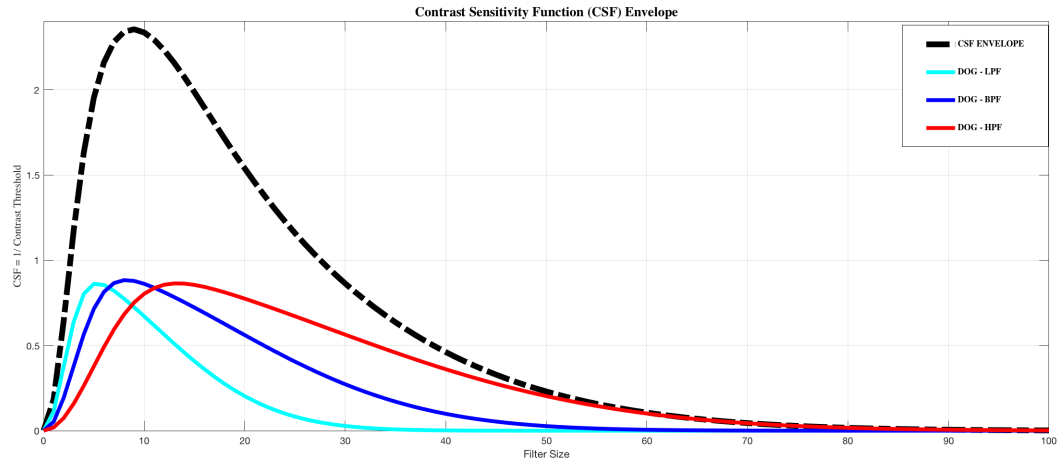


Figure 3-13: The contrast sensitivity function (dashed line) and its underlying spatial frequency channels (solid line). These channels, each of which is sensitive to specific range of frequencies each corresponding to a different size of the receptive fields, by adding up these three channels the Contrast Sensitivity Function envelope curve can be obtained which is the black dashed curve of this figure.

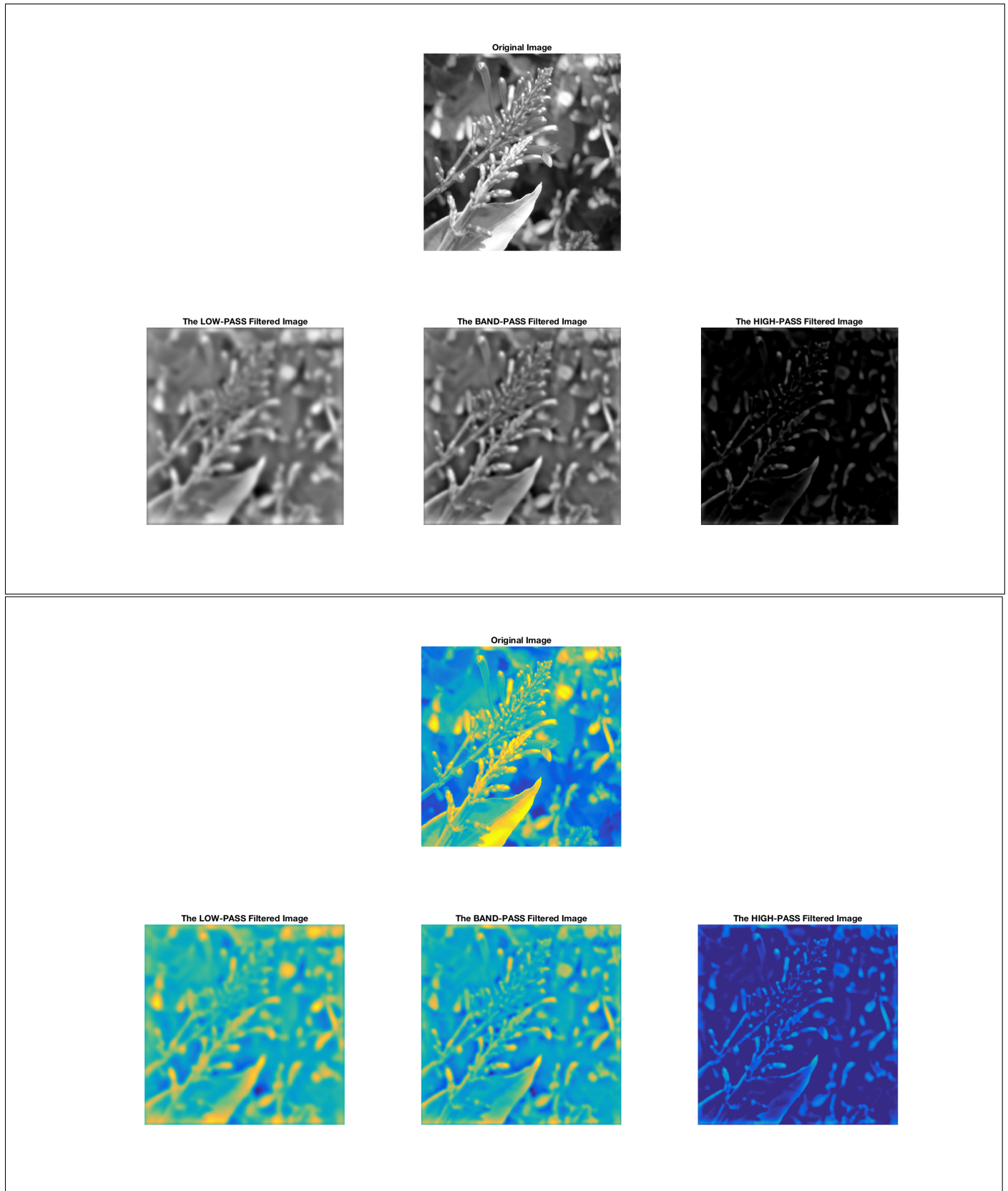


Figure 3-14: Input Image and The Filtered Image based a Three Different Spatial Frequency Bands



# Chapter 4

## The Simulation Output Images

In this chapter, all the output images based on the mapping models and the filtration process via the multiple spatial frequency channels of the CSF will be shown according to figure 4-1. Where, all the related procedures of this chapter have illustrated in the figure below, regarding each particular mapping model. As we mentioned earlier in chapter three, that the difference between a new mapping model (non-uniform mapping model) and a conventional one (which is the uniform model) is the utilizing of a Conformal-Log Mapping method. Whereas, the usefulness of this mapping approach comes from the rotation and size/scale invariance that achieved in the resulting domain making the transform suitable for pattern recognition. The concepts of non-uniform retina-like image sampling and log-polar mapping have been widely applied in the area of machine vision and image processing. An extensive review of biologically motivated data reduction models related to log-polar mapping can be found in [24]. After mapping the input image via these two sampling models, a forward and inverse images will be obtained. Then a lateral inhibition biological algorithm and the multiple spatial frequency channels (CSF) will be applied to these two versions of a mapped image.

A Root Mean Square Error (*RMSE*) quality metric has used to calculated the difference between the filtered image via the Difference-of-Gaussian filter to the lateral inhibition image within the same mapping model in order to measure which output filtered image contains the closest information to the image processed based on the LSI algorithm. All the numerical results will be shown as tables in this chapter [44, 45].

The effectiveness of Lateral Inhibition decreases exponentially with increasing a spatial distance between the adjacent retinal photo-receptors. According to this relationship the weighting coeffi-

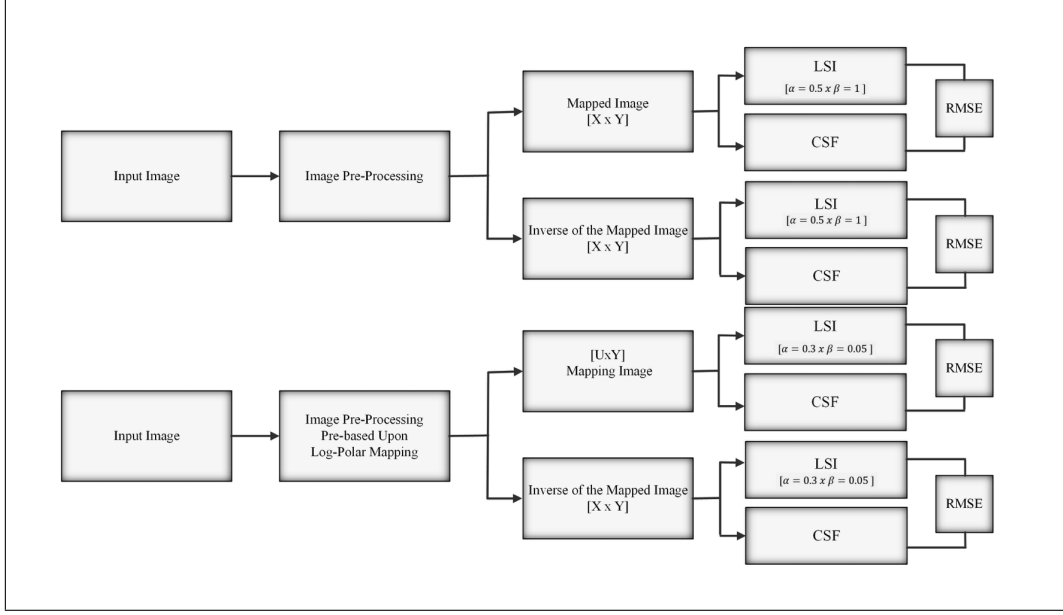


Figure 4-1: Demonstration the Work Procedures of this chapter for both models .

cients for lateral inhibition will be generating depending upon the separation distances between the neurons over the retinal plane for both models. See the equation 2.6. From this equation in 2.6,  $\alpha$  and  $\beta$  are two variables have involved in an exponential model, and they have their impact on the weighting coefficients matrix. A contribution of this research besides generating a new design which mimics the Human Visual System, is specified the best numerical values and the roles of these two parameters. The investigation on these values for the exponential model will be shown firstly for the Uniform model then the non-uniform one, respectively. Then, the comparison by the images between a Lateral Inhibition method and the three spatial-frequency filters image will presenting later.

To identify these two variables for this model, we have used a synthetic pattern image with size  $[100 \times 100]$  and two specific level of intensities which represented by the cross section profile of this image, see figure 4.2 part B. The reason for choosing this picture instead of the real gray-scale image is that the processing results will be easier to observe and compare to determine which parameter value is more suitable for obtaining an accurate result. Also, it conserves a lot of time by working with smaller size images in general; therefore, we've preferred to work with  $[100 \times 100]$ . MATLAB computer language with version (R2016a), has been used to process the images and obtain the

simulation results.

## **4.1 The Exponential Model's variables for the Uniform Mapping Image:**

A synthetic image has used for this model with image size equals to  $[100 \times 100]$ , to make this study more general. To clearly understand the impact of these two variables on the processed image, one of them has to be set as a constant while changing the other variable within a particular range of numerical values. And depending on the overshooting and the undershooting edges of the cross section profile of the resultant image as well as the preserved information beyond the edges, we can notice the impact of these two variables and investigate the best numerical value which gives the desired LSI image. According to two important criteria that are representing in the cross section profile of the LSI image that is shown in figure 4.1, where these criteria are: first: the degree of the edge enhancement which can be calculated by subtracting the peak of the overshooting edge (P) from the setting of the overshooting area (S1). Second: the preserved information beyond edges, and this can be calculated by subtracting the setting of the overshooting are (S) from the setting of the undershooting part of the LSI image (S2).

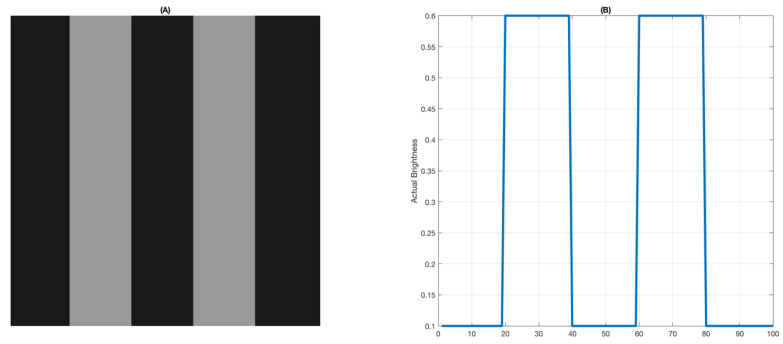


Figure 4-2: (A)Input Synthetic Image. (B)Cross Section Profile

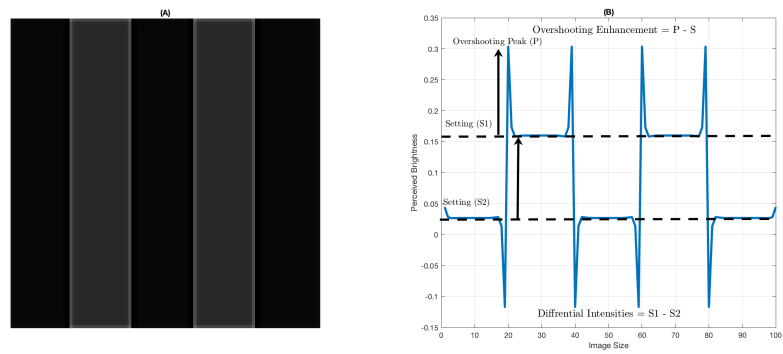


Figure 4-3: (A)Lateral Inhibition Uniform Mapping Image. (B)Cross Section Profile

#### 4.1.1 The $\alpha$ Variable of the Exponential Model

Alpha  $\alpha$  variable will be tested and verified in this section using a synthetic image with two specific region of intensities. According to the Overshooting edges and the differential of the intensities between the Overshooting and Undershooting of the processed image based on lateral subtractive inhibition, the best numerical value will be specified. The following simulation figures are representing all the results related to this investigation. Figure 4.4 illustrates the minimum value of an alpha  $\alpha$  parameter, 0.03, has been used as the minimum value to represent an alpha variable for the uniform mapping model because that (0.01 and 0.02) values are giving an image which is exactly similar to the original image and the first changing on the information of the processed image is starting to be seen when alpha equals to 0.03, then the following figures will be showing the rest of the numerical values within a range of values starting from 0.03 to 1.2:

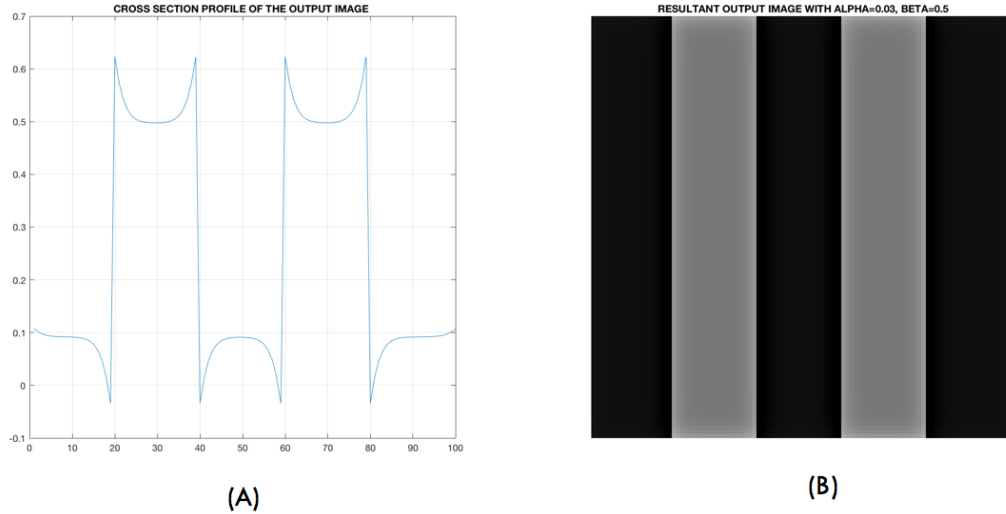
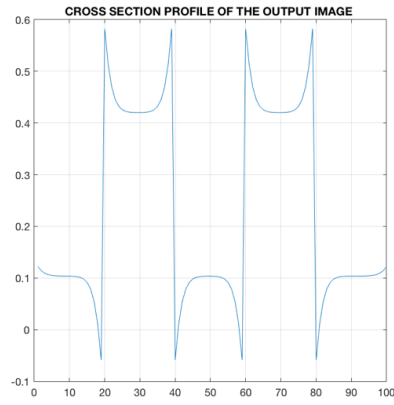
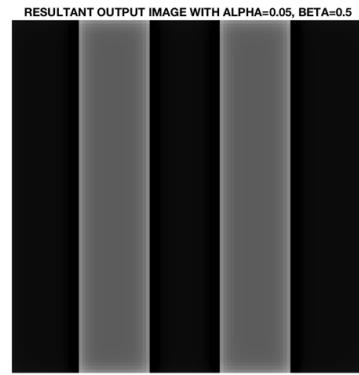


Figure 4-4: (A) The Cross Section Profile of The LSI Image. (B) The LSI Image With  $\alpha=0.03$  and  $\beta=0.5$ .

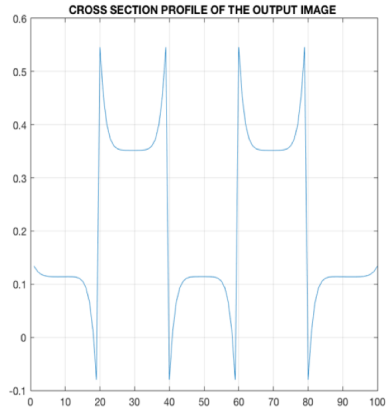


(A)

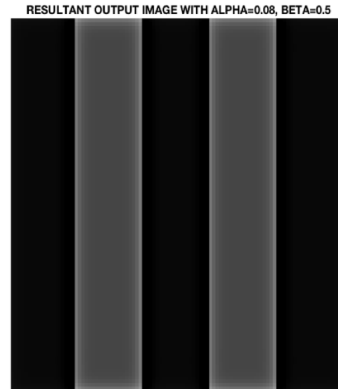


(B)

Figure 4-5: (A) The Cross Section Profile of The LSI Image. (B) The LSI Image With  $\alpha=0.05$  and  $\beta=0.5$ .

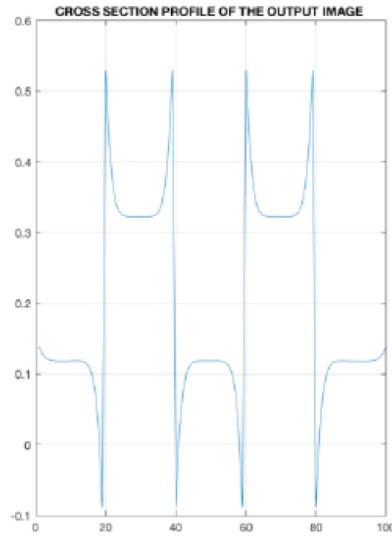


(A)

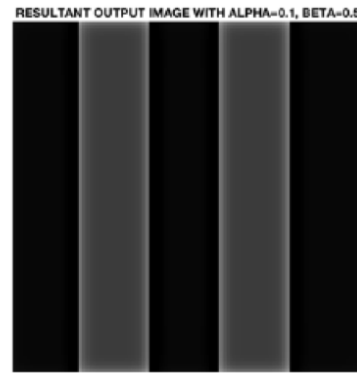


(B)

Figure 4-6: (A) The Cross Section Profile of The LSI Image. (B) The LSI Image With  $\alpha=0.08$  and  $\beta=0.5$ .

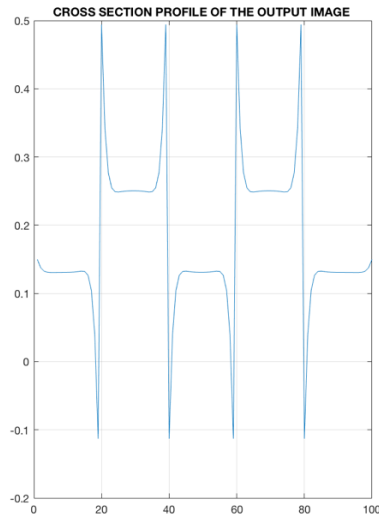


(A)

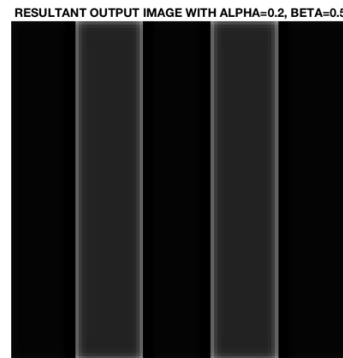


(B)

Figure 4-7: (A) The Cross Section Profile of The LSI Image. (B) The LSI Image With  $\alpha=0.1$  and  $\beta=0.5$ .

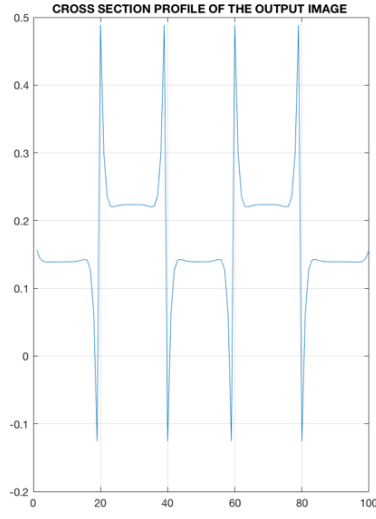


(A)



(B)

Figure 4-8: (A) The Cross Section Profile of The LSI Image. (B) The LSI Image With  $\alpha=0.2$  and  $\beta=0.5$ .

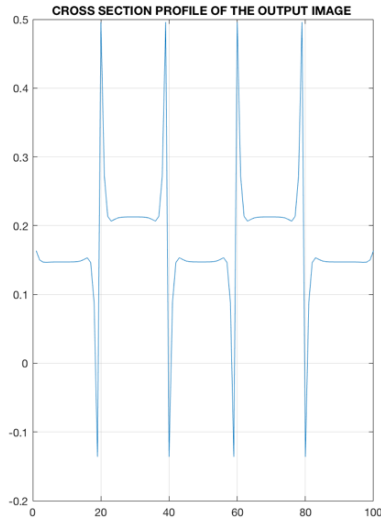


(A)

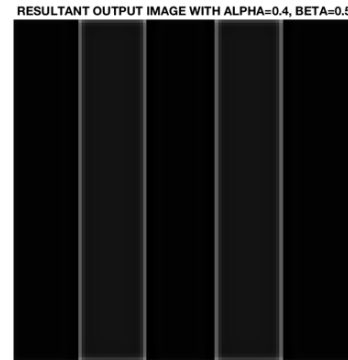


(B)

Figure 4-9: (A) The Cross Section Profile of The LSI Image. (B) The LSI Image With  $\alpha=0.3$  and  $\beta=0.5$ .



(A)



(B)

Figure 4-10: (A) The Cross Section Profile of The LSI Image. (B) The LSI Image With  $\alpha=0.4$  and  $\beta=0.5$ .



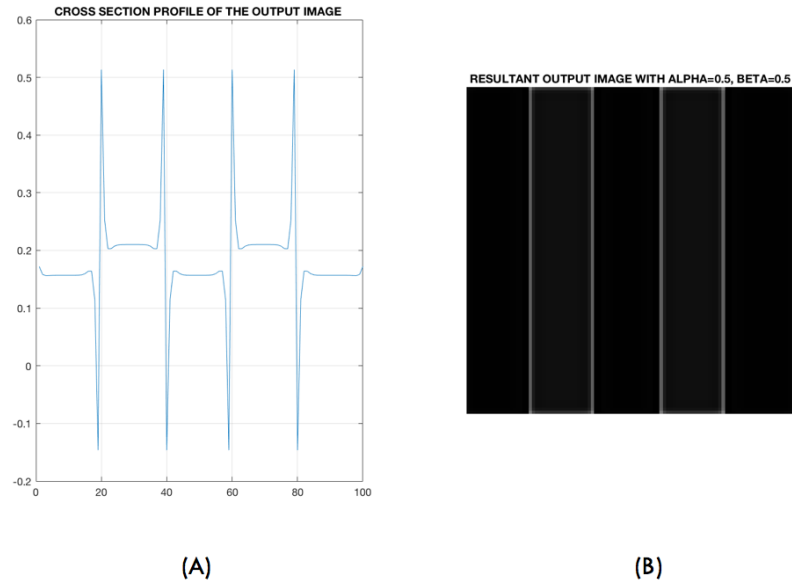


Figure 4-11: (A) The Cross Section Profile of The LSI Image. (B) The LSI Image With  $\alpha=0.5$  and  $\beta=0.5$ .

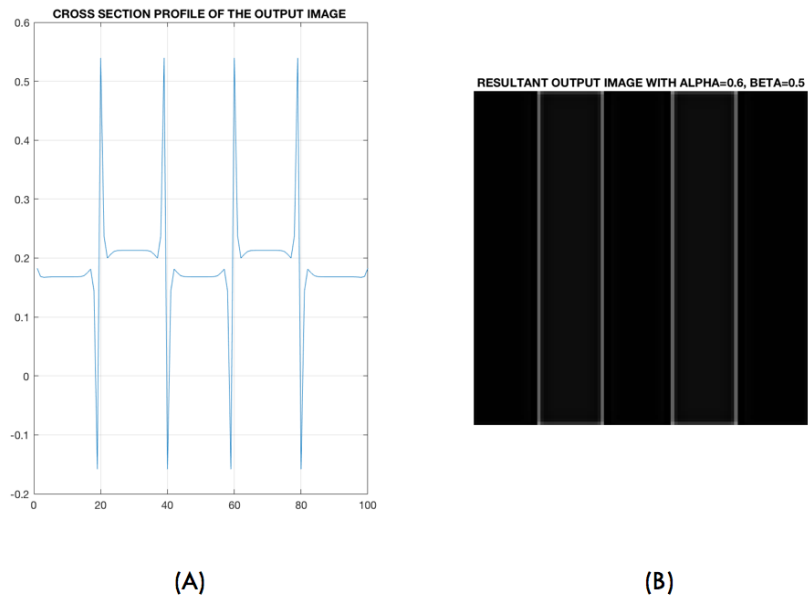


Figure 4-12: (A) The Cross Section Profile of The LSI Image. (B) The LSI Image With  $\alpha=0.6$  and  $\beta=0.5$ .

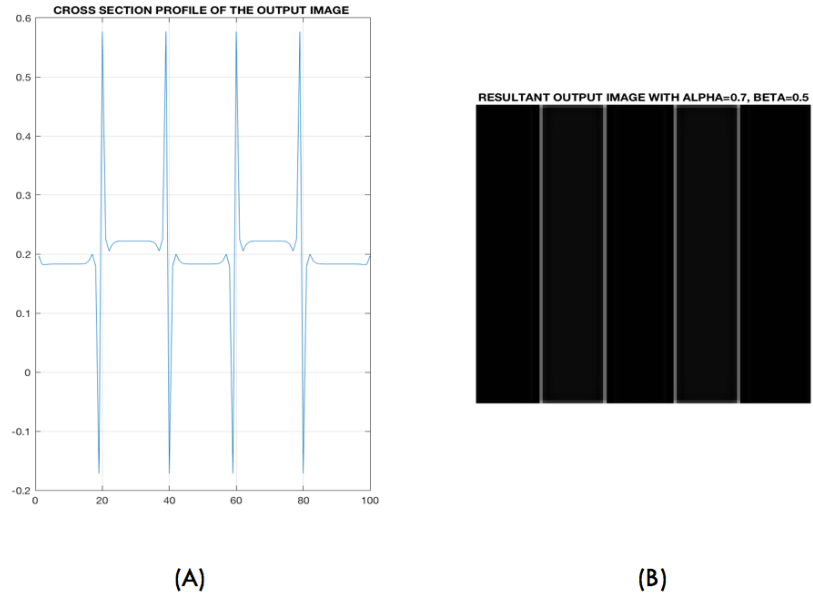


Figure 4-13: (A) The Cross Section Profile of The LSI Image. (B) The LSI Image With  $\alpha=0.7$  and  $\beta=0.5$ .

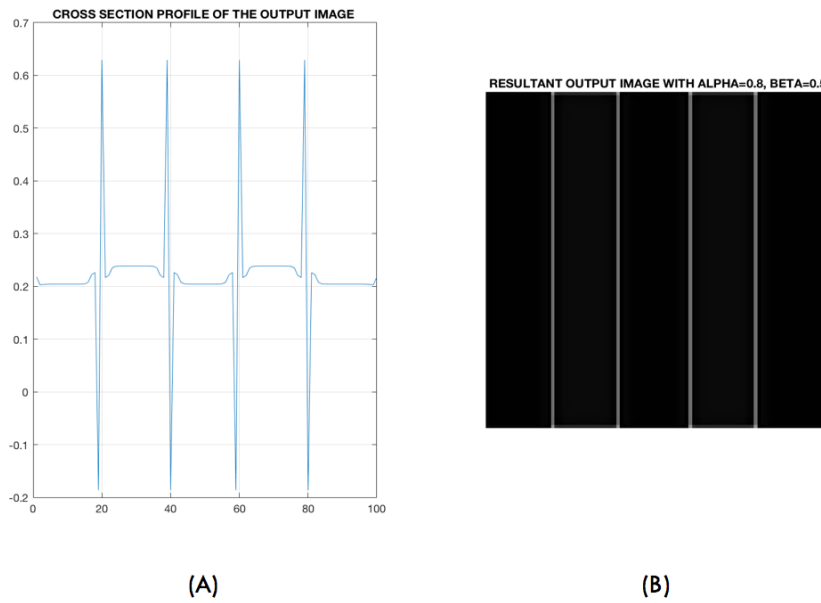


Figure 4-14: (A) The Cross Section Profile of The LSI Image. (B) The LSI Image With  $\alpha=0.8$  and  $\beta=0.5$ .

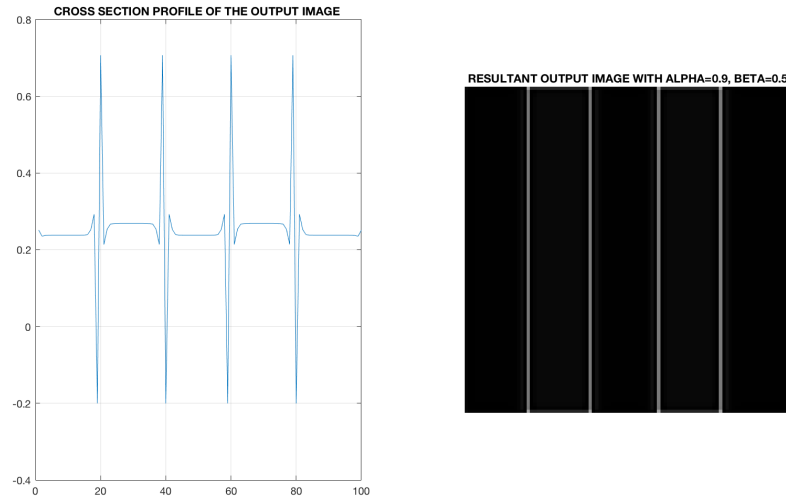


Figure 4-15: (A) The Cross Section Profile of The LSI Image. (B) The LSI Image With  $\alpha=0.9$  and  $\beta=0.5$ .

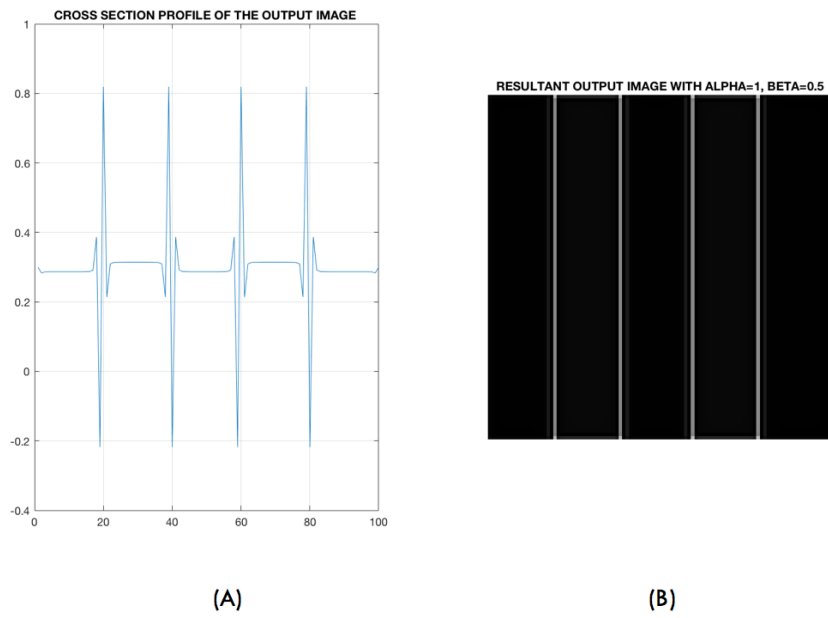


Figure 4-16: (A) The Cross Section Profile of The LSI Image. (B) The LSI Image With  $\alpha=1$  and  $\beta=0.5$ .

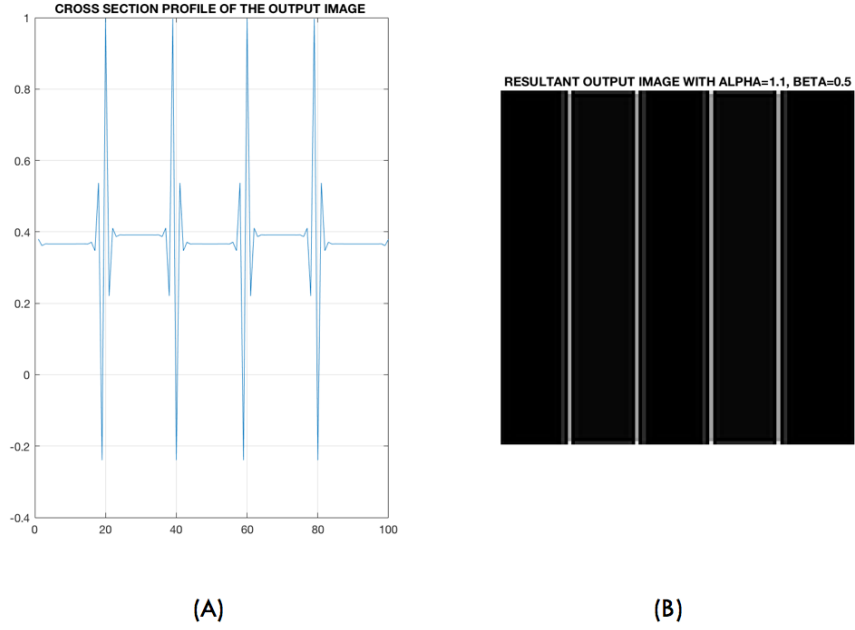


Figure 4-17: (A) The Cross Section Profile of The LSI Image. (B) The LSI Image With  $\alpha=1.1$  and  $\beta=0.5$ .

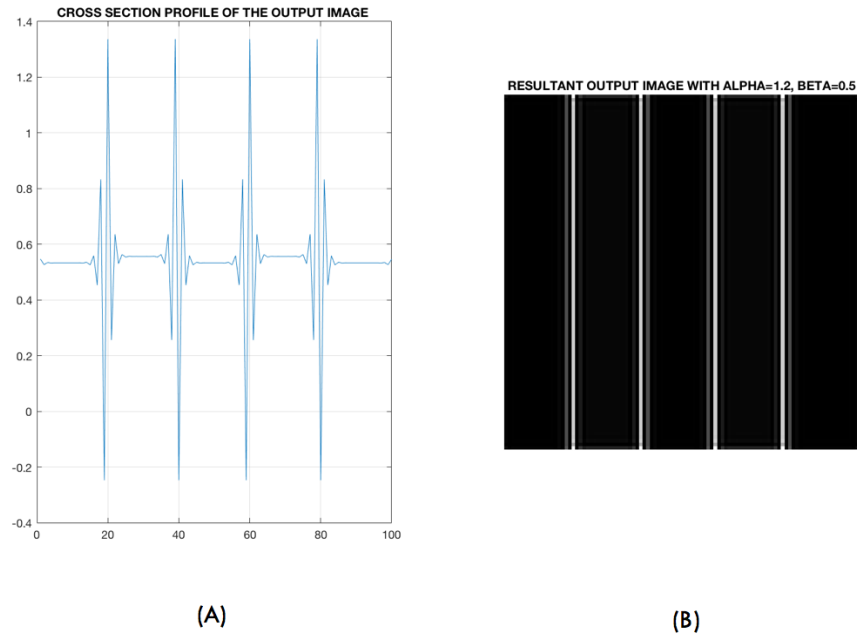


Figure 4-18: (A) The Cross Section Profile of The LSI Image. (B) The LSI Image With  $\alpha=1.2$  and  $\beta=0.5$ .

From the previous simulation figures, we have concentrated on the overshooting edges of the cross section profiles since it represents the edge enhancement of the output image. As we can see that by increasing an alpha parameter, the overshooting peak increases linearly. However, this increment of the alpha parameter reduces the differential intensities of the same image. In other words, the separation distance between the overshooting and the undershooting peaks of the cross section profile image is decreasing when alpha is increasing. And that means if we increasing the alpha parameter we will achieve the edge enhancement of the processed image but the relevant information beyond these edges will be missing. Therefore, a numerical value need to be chosen to represent an alpha parameter on the exponential model which gives the desired results according to the edge enhancement as well as improving the important information beyond these contrast.

Figure 4-19 represents the relationship between an alpha parameter  $\alpha$  and the edge enhancement (Overshooting peaks) of the image that treated via LSI method:

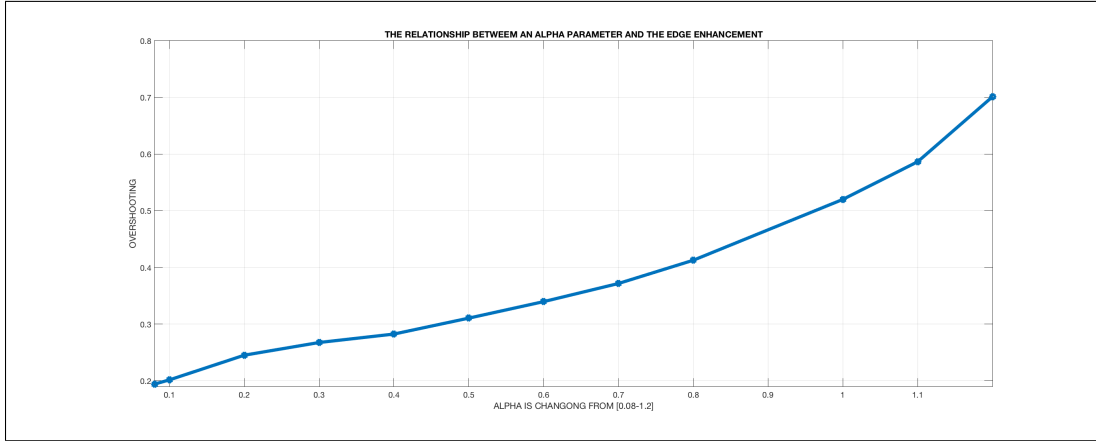


Figure 4-19: Illustrates the relationship between the overshooting edges of the lateral inhibition image and  $\alpha$  parameter. when alpha  $\alpha$  changes from  $[0.08 - 1.2]$ , while beta  $\beta = 0.5$ .

And the following figure 4-20 is representing the relationship between the alpha variable  $\alpha$  while fixing beta  $\beta$  to the relevant information beyond the image enhancement in order to study the impact of this parameter on the whole image (the edges and the important information between the edges):

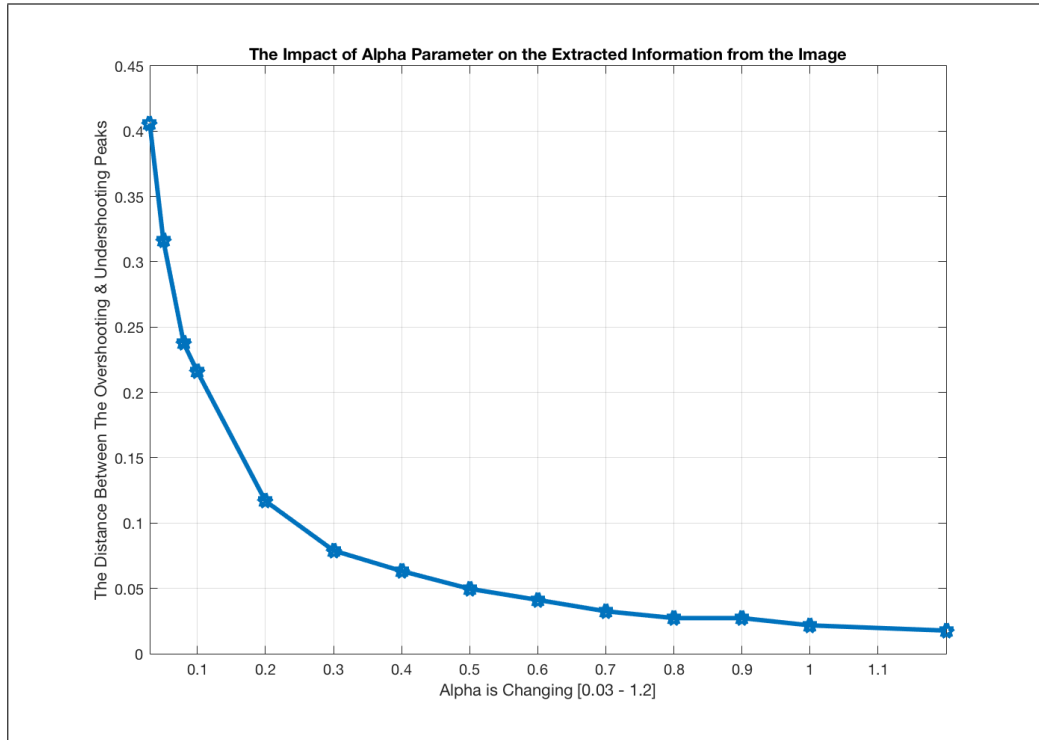


Figure 4-20: Represents the Impact of  $\alpha$  Parameter on the Differential of The Intensities of the Resultant Output Image.

From these two figures above, we can observe that there is a linearly proportional relationship between an alpha parameter to the edge enhancement of the LSI image. While an inversely proportional relationship between the same parameter to the differential intensities which representing the preserved information beyond the edges of the same image. In other words, as an alpha parameter increasing the important information between the overshooting and undershooting edges decreases until we almost lose all the image data [see figure 4-18].

Before proceeding to choose the best numerical value of an alpha parameter, we need to study the

impact of the other parameter of an exponential model which is a beta  $\beta$  variable. In order to complete this investigation and obtain the big picture of the operation function of these two variable and what is exactly their influence on the processed image and which number is giving us the best result regarding the edge enhancement as well as the improvement of the relevant information beyond these edges.

#### 4.1.2 The $\beta$ Variable:

The same procedures will be used as the previous section, in order to the other variable of an exponential model which beta  $\beta$ . To do that we have set an alpha  $\alpha$  parameter to be as (0.5) by default while changing beta within specific range of numbers from 0.1 until 1.5, figures (4.21 - 4.34) are showing the output images when alpha=0.5 and beta changes to represent the impact of a beta variable on the edge enhancement and the perceived information of the lateral inhibition image results.

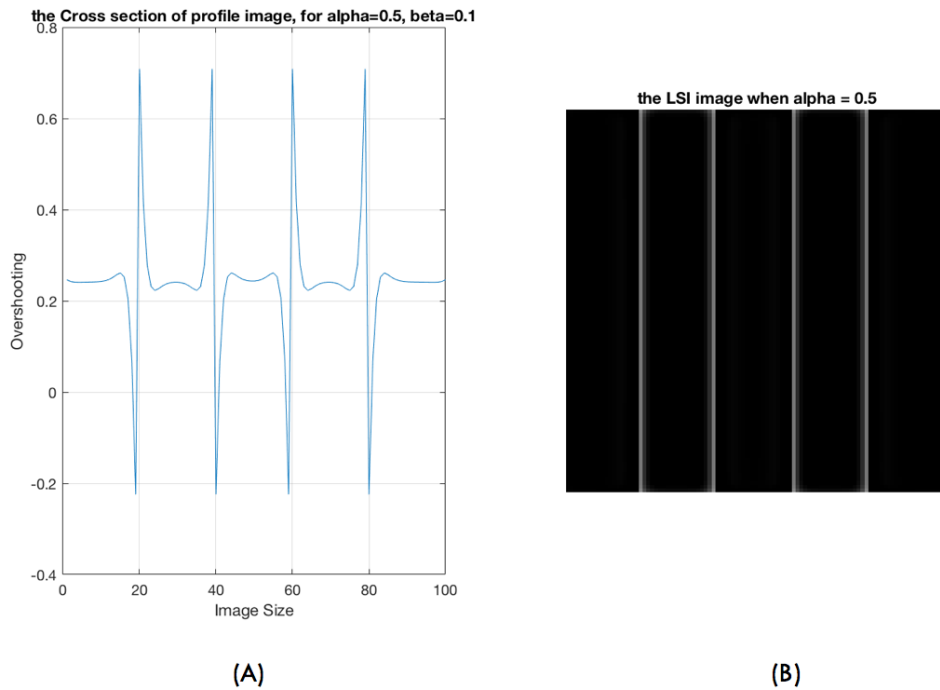


Figure 4-21: (A) The Cross Section Profile of The LSI Image. (B) The LSI Image With  $\beta=0.1$  and  $\alpha=0.5$ .

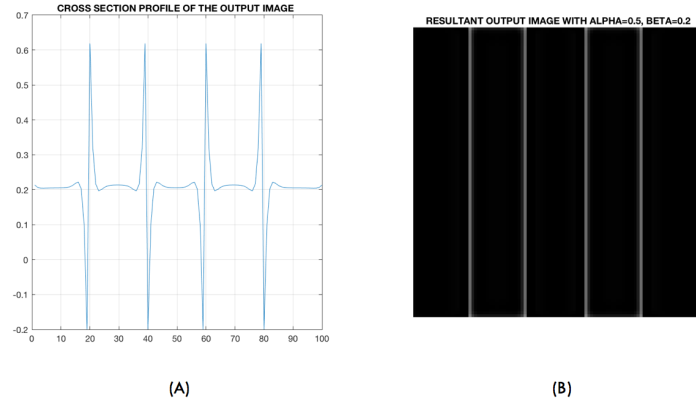


Figure 4-22: (A) The Cross Section Profile of The LSI Image. (B) The LSI Image With  $\beta=0.2$  and  $\alpha=0.5$ .

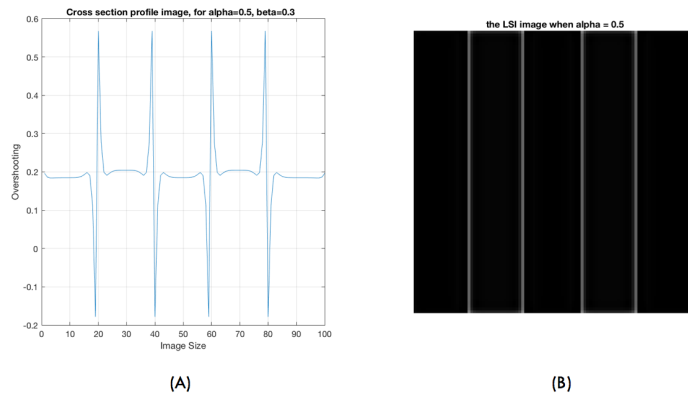
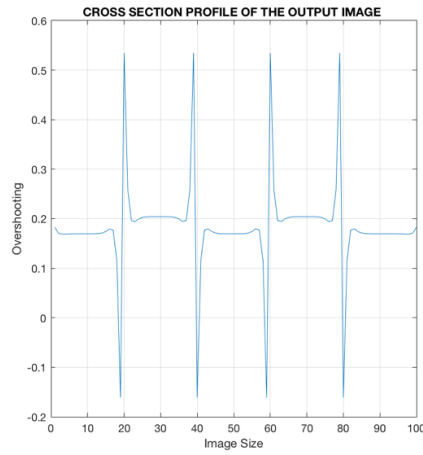


Figure 4-23: (A) The Cross Section Profile of The LSI Image. (B) The LSI Image With  $\beta=0.3$  and  $\alpha=0.5$ .



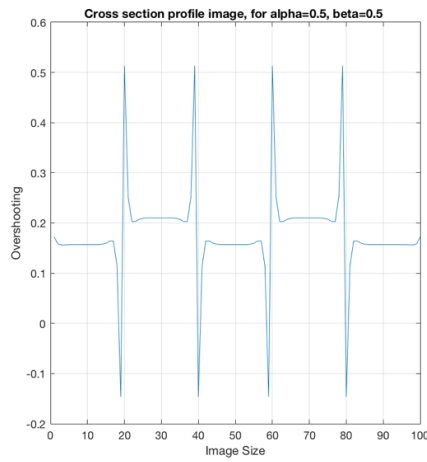


(A)

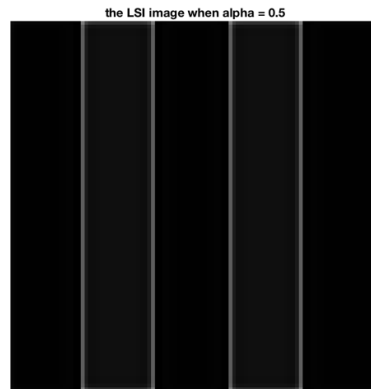


(B)

Figure 4-24: (A) The Cross Section Profile of The LSI Image. (B) The LSI Image With  $\beta=0.4$  and  $\alpha=0.5$

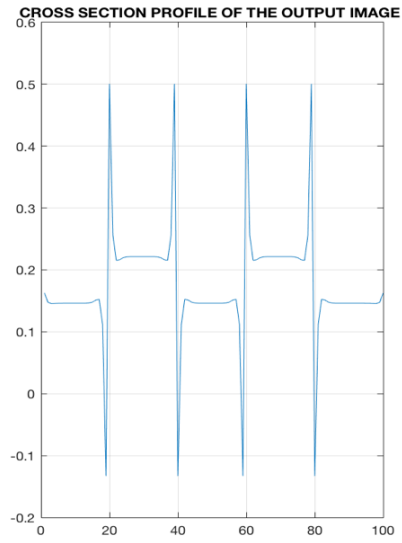


(A)



(B)

Figure 4-25: (A) The Cross Section Profile of The LSI Image. (B) The LSI Image With  $\beta=0.5$  and  $\alpha=0.5$



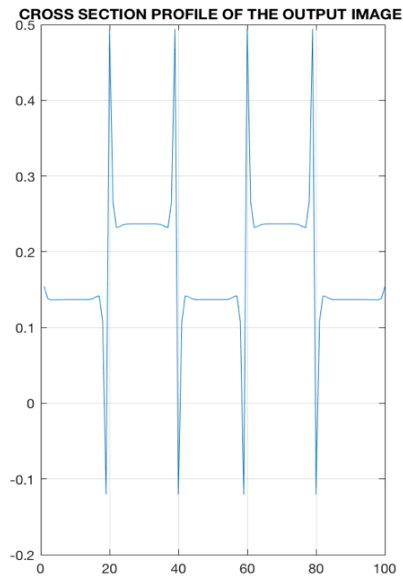
(A)

RESULTANT OUTPUT IMAGE WITH ALPHA=0.5, BETA=0.6



(B)

Figure 4-26: (A) The Cross Section Profile of The LSI Image. (B) The LSI Image With  $\beta=0.6$  and  $\alpha=0.5$



(A)

RESULTANT OUTPUT IMAGE WITH ALPHA=0.5, BETA=0.7



(B)

Figure 4-27: (A) The Cross Section Profile of The LSI Image. (B) The LSI Image With  $\beta=0.7$  and  $\alpha=0.5$

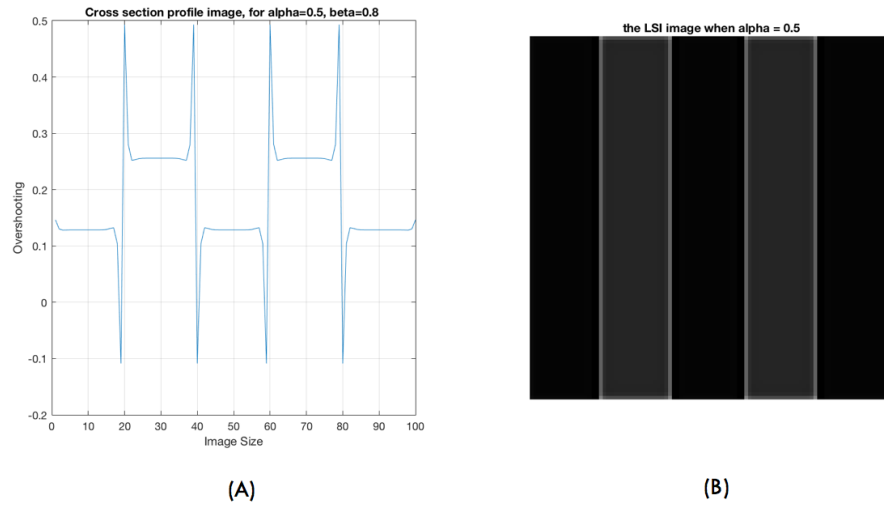


Figure 4-28: (A) The Cross Section Profile of The LSI Image. (B) The LSI Image With  $\beta=0.8$  and  $\alpha=0.5$

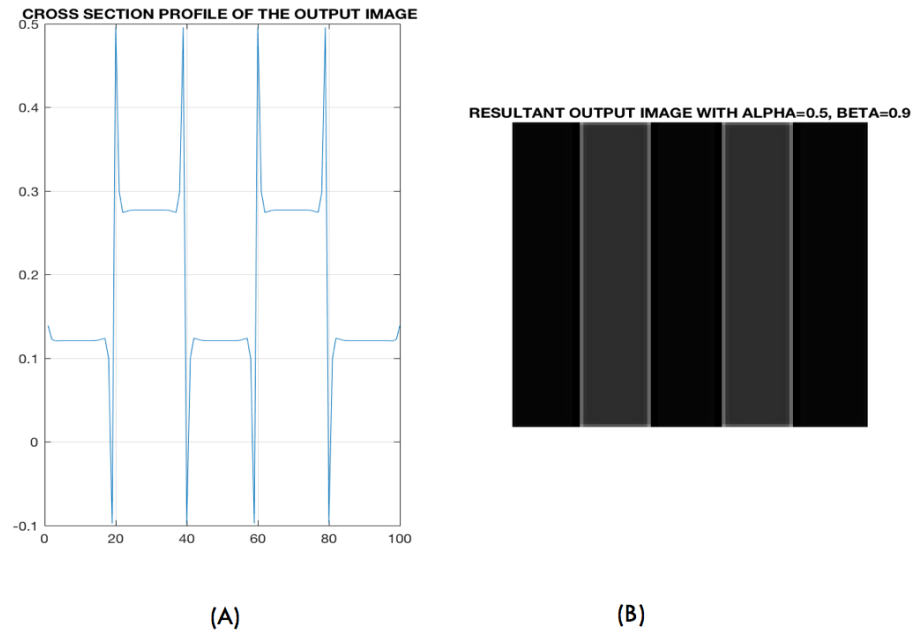
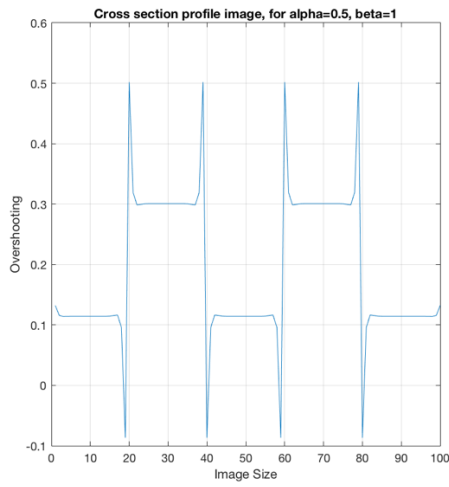
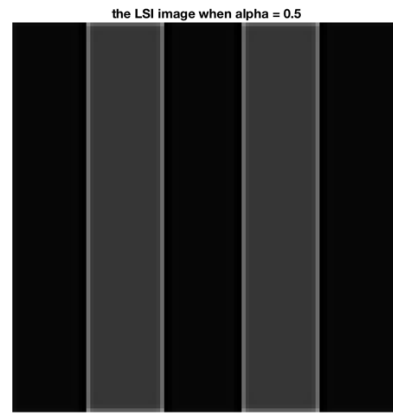


Figure 4-29: (A) The Cross Section Profile of The LSI Image. (B) The LSI Image With  $\beta=0.9$  and  $\alpha=0.5$

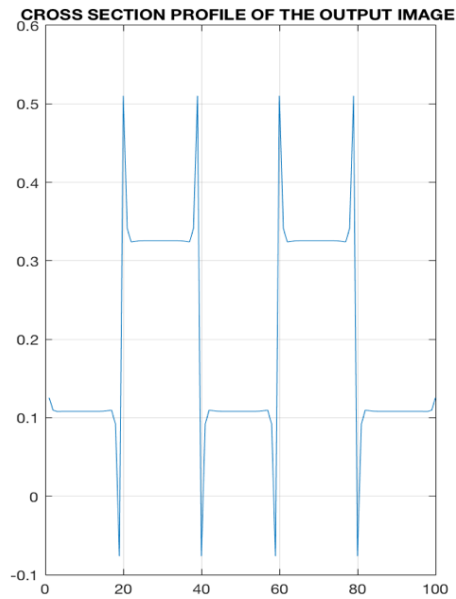


(A)

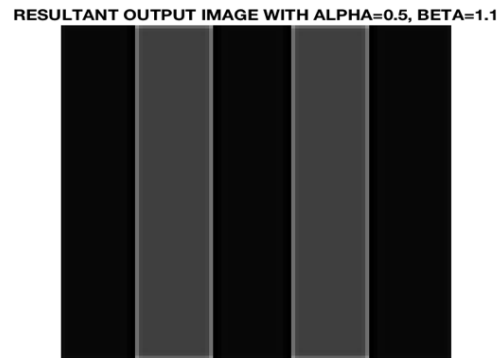


(B)

Figure 4-30: (A) The Cross Section Profile of The LSI Image. (B) The LSI Image With  $\beta=1$  and  $\alpha=0.5$

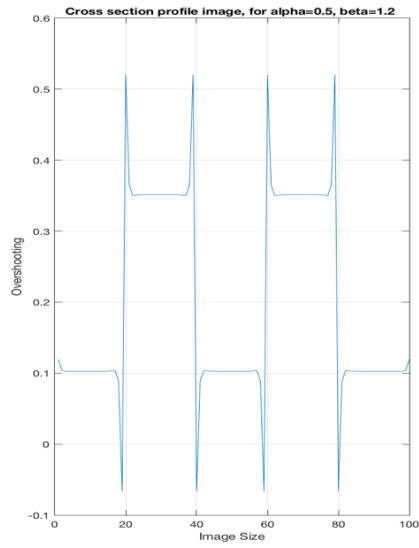


(A)

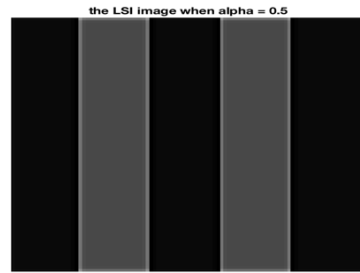


(B)

Figure 4-31: (A) The Cross Section Profile of The LSI Image. (B) The LSI Image With  $\beta=1.1$  and  $\alpha=0.5$

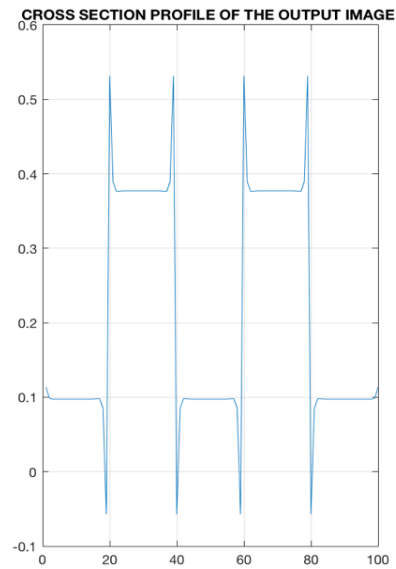


(A)

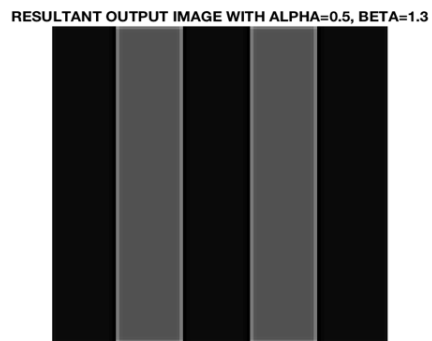


(B)

Figure 4-32: (A) The Cross Section Profile of The LSI Image. (B) The LSI Image With  $\beta=1.2$  and  $\alpha=0.5$



(A)



(B)

Figure 4-33: (A) The Cross Section Profile of The LSI Image. (B) The LSI Image With  $\beta=1.3$  and  $\alpha=0.5$

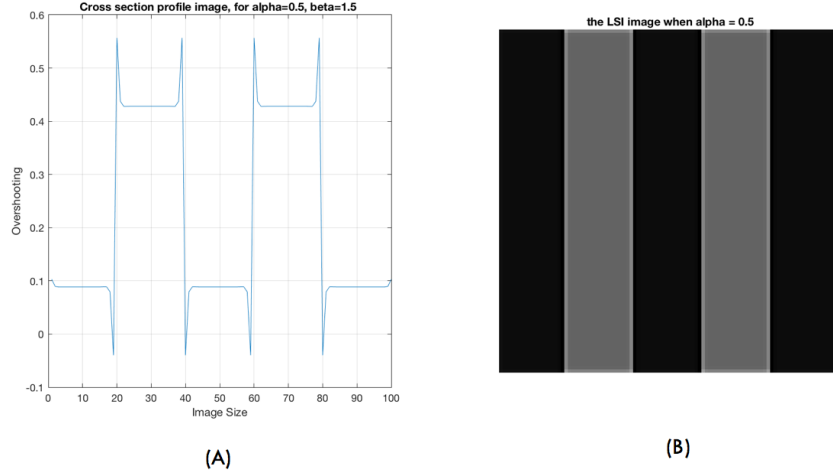


Figure 4-34: (A) The Cross Section Profile of The LSI Image. (B) The LSI Image With  $\beta=1.5$  and  $\alpha=0.5$

As we can see from all the figures above, that the relative information beyond the overshooting and undershooting edges of the lateral subtractive inhibition image is improving linearly as the value of beta variable is increasing while the enhancement of the image contrast reduces. The following figures 4-35 and 4-36 are representing the relationship between the beta parameter of an exponential model (while fixing an alpha variable as 0.5 by default) to the edge enhancement of the processed image and the perceived information beyond the edges. We can observe that there is an inverse relationship between the edge enhancement to the distance between these edges. Therefore, to specify the numerical values for these two variables that are giving the desired output images a brief comparison between these two variables is made and presented in figure 4-37 and figure4-38.

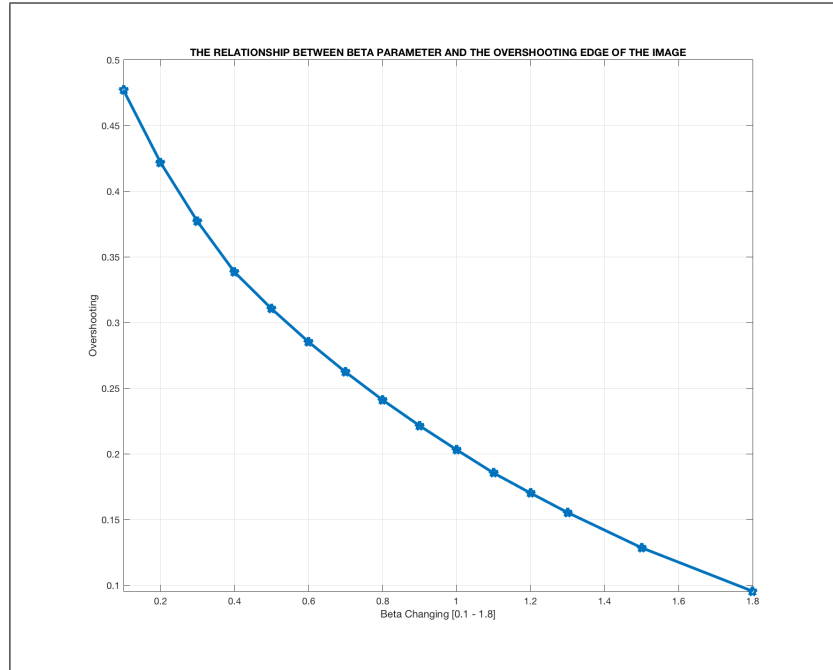


Figure 4-35: Illustration The Impact of Beta parameter  $\beta$  on the Overshooting Peak of the LSI Image

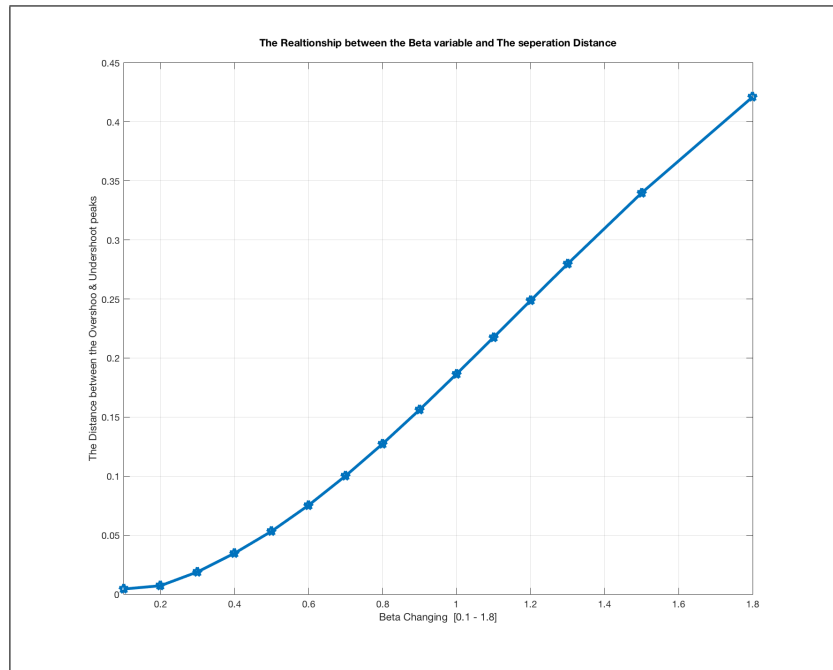


Figure 4-36: The Relationship between the separation Distance between the Overshooting and the Undershooting and the beta  $\beta$  parameter of LSI Image

From all the above simulation results related to this investigation of beta and alpha impact over the LSI image. An inversely proportional relationship between an alpha parameter to the beta parameter within an exponential model has observed. In other words, when an alpha variable increasing the overshooting edges increases as well while the differential distance between the edges is dropping. However, when a beta variable is rising the edge enhancement decreases while the differential distance between the edges improves. The following figures 4-37 and 4-38 illustrate the operation functions for these two parameters over the LSI image briefly to choose which case is giving the desired output image via LSI method.

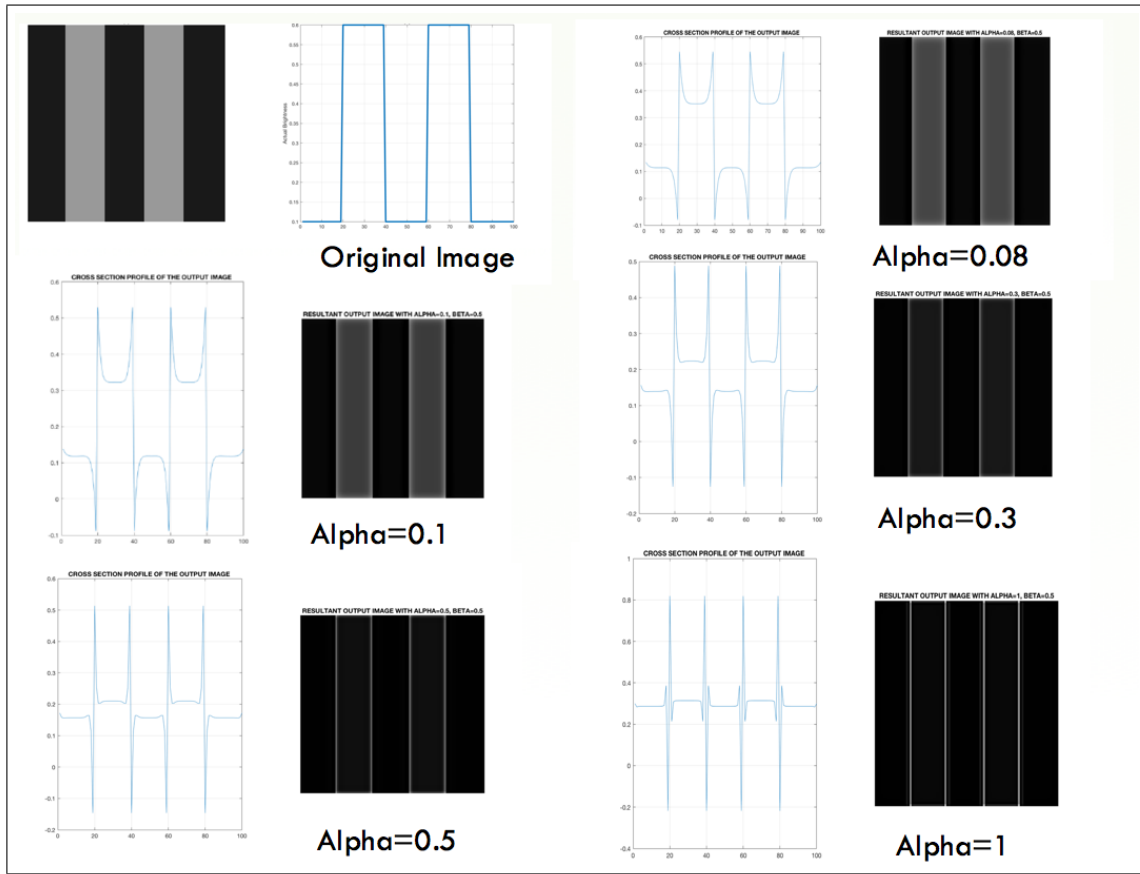


Figure 4-37: Different Cases of Alpha from [0.08 to 1] While Beta =0.5.



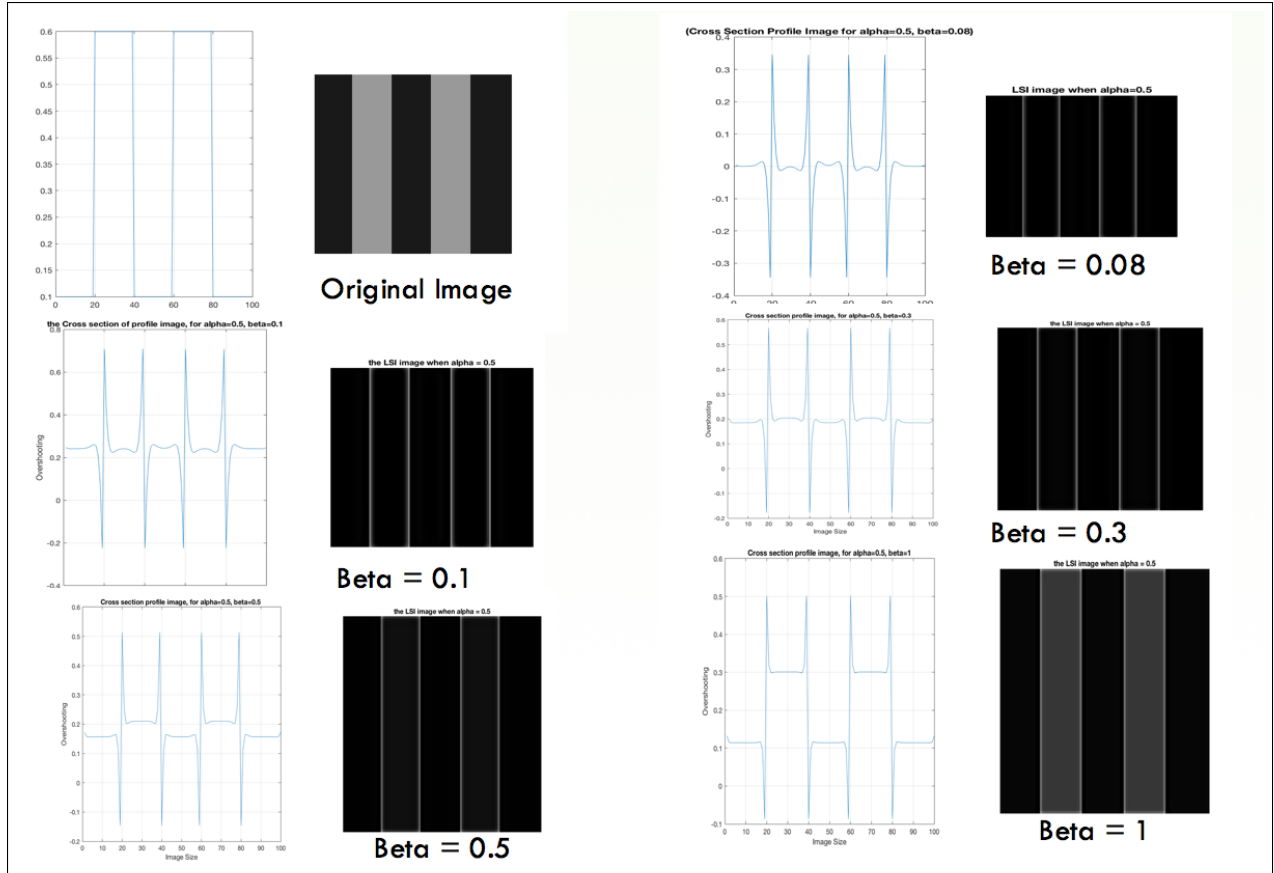


Figure 4-38: Different Cases of Beta from [0.08 to 1] While Alpha =0.5.

According to the data in figure 4-37 and 4-38, the desired situation is obtained when beta is higher than alpha [more details regarding the relation between these two variables will be shown in chapter five]. In other words, the desired output image with the edge enhancement and perceived information is achieved when an alpha  $\alpha$  equals to (0.5) and beta  $\beta$  is (1).

## 4.2 The Simulation Results of the Uniform model via the LSI Method

In this section, the numerical values that have obtained from the previous experiment for an alpha and beta variables to generate the coupling coefficient matrix via an exponential equation for this mapping model will tested on a different synthetic and real images. The result output images will shown in this section according to figure 4-1.

All the experiments in this work were performed on the images, (synthetic or real), with particular image size  $[100 \times 100]$  for the Uniform Model and  $[128 \times 64]$  for the Non-Uniform Model, that's because of the inverse matrix  $[S]$  which is corresponding to the RLI method. Matrix inversion can be easily done by a function call in the MATLAB; however, different versions of MATLAB running on different platforms have different capabilities of handling large size matrix inversion. For example, MATLAB with Simulink for Windows running on a PC platform is capable of performing matrix inversion by a direct function call up to order  $[16384 \times 16384]$ . Beyond that size, "out of memory" errors occur. Therefore, the following simulations will have one particular size which is  $[100 \times 100]$  for this image mapping model. Firstly, the synthetic Uniform mapped image, for this research work we have built two types of synthetic images, a staircase image and a stripped image with two gray level scales, see figure 4-39 part A and B. While, the real image is presenting on the following figure, in figure 4-40 part A, B, C, and D.

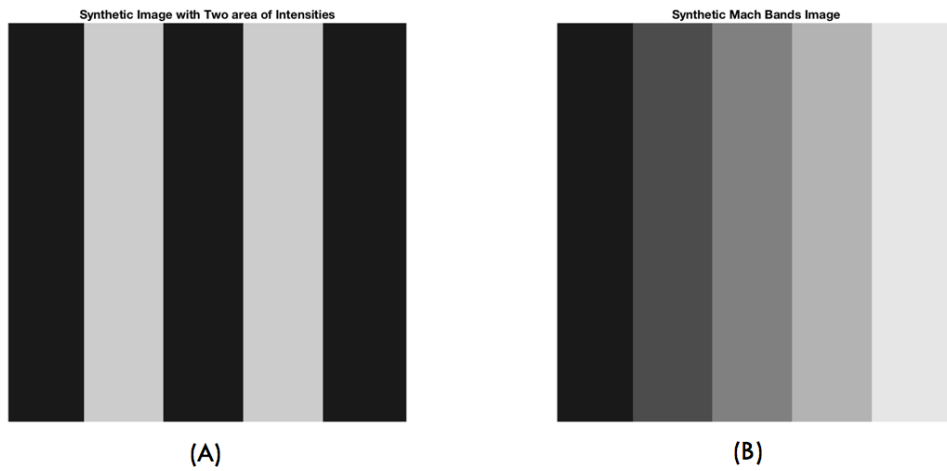


Figure 4-39: (A):A Stripped Image with Size  $[100 \times 100]$ . (B)A Synthetic Staircase Images with size  $[100 \times 100]$  .

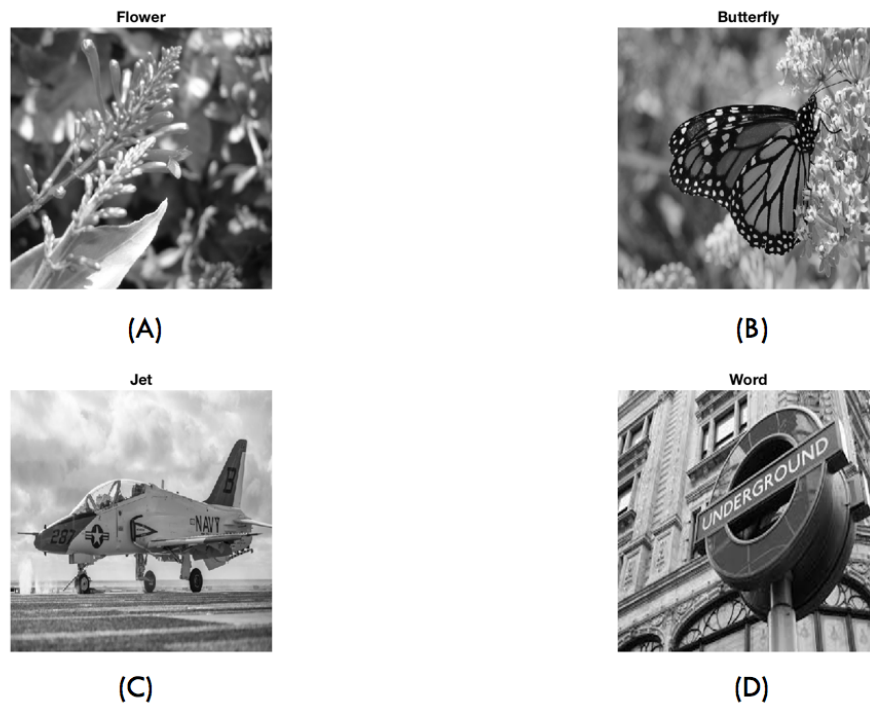


Figure 4-40: The Input Real images with size  $[100 \times 100]$  with Four Different Types: (A): Flower. (B):Butterfly. (C):Jet. (D): Word.

The lateral inhibition method is applied to the input image directly regarding this model. Therefore, the interconnection spatial distances will be calculating uniformly via the Euclidean equation, see equation 2.7.

The circular version of this image will be obtained via a pattern that constructed from number circles that is equivalent to the image size and increasing linearly (uniformly). The reason for obtaining this type of the image is because that the new design has two type of the pictures; the forward mapped image as well as the reverse one (wrapped back image) which comes from a circular pattern that is similar to this pattern in figure 4-41. However, the non-uniform circular pattern is including concentric circles that are increasing in a non-linear way (logarithmically) [more details regarding this model will be illustrating in the following section of this chapter].

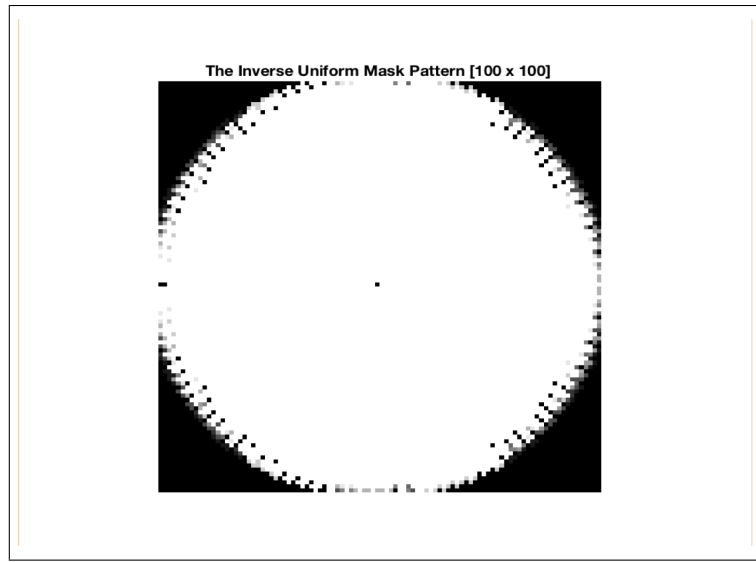


Figure 4-41: Circular Pattern To inverse the Uniform Mapped Image with size [100 ring x 100 wedge] .

Figure 4-42 represents the synthetic image with size [100x100] before and after applying the lateral subtractive inhibition method with an  $\alpha = 0.5$  and  $\beta = 1$ , for an exponential model.

In the following figures, the second type of the synthetic image will be treated by the (LSI)

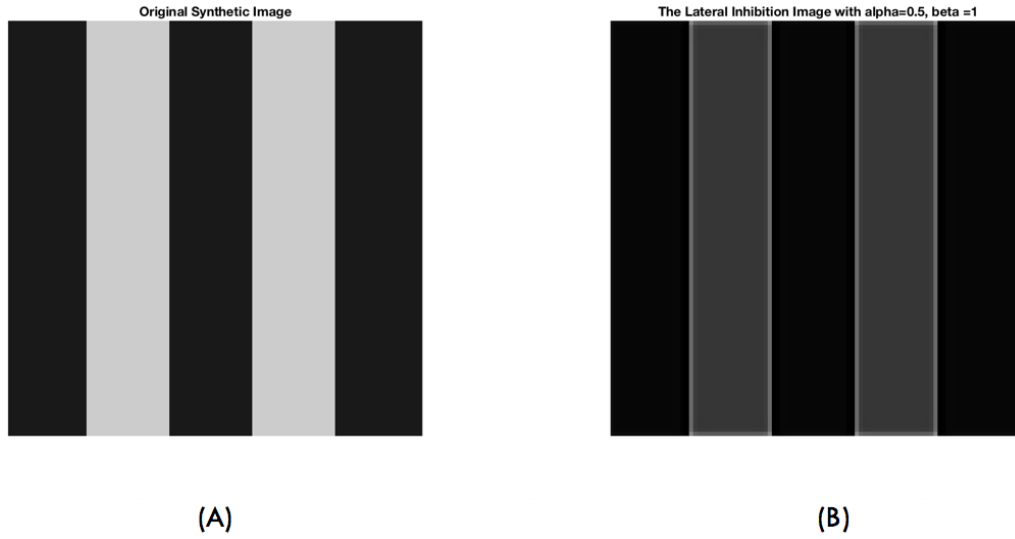


Figure 4-42: (A)The Synthetic Input Image. (B)The Lateral Inhibition Image with  $\alpha = 0.5$  and  $\beta = 1$ .

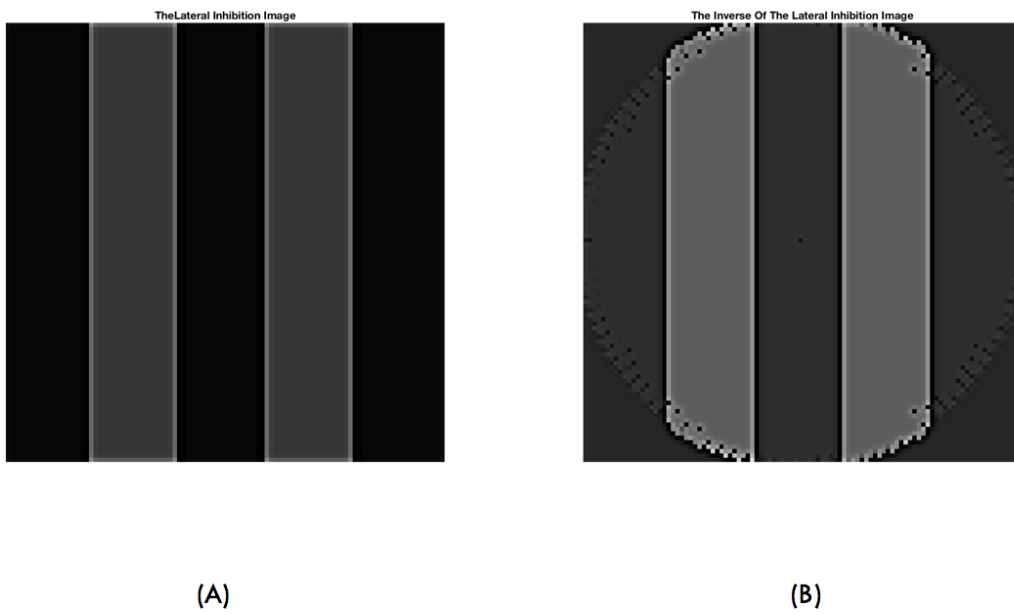


Figure 4-43: (A)The LSI of Synthetic Input Image.(B) the LSI Wrapped Back Image with  $\alpha = 0.5$  and  $\beta = 1$ .

biological method to study the characteristics of the resultant output image. However, the output image will be too dark to visualize the changes occurred after applying the recurrent lateral inhibition to it. Therefore, the colored version of the input and the output image will be presenting right next to this figure to illustrate the edge enhancement of the output image based LSI.

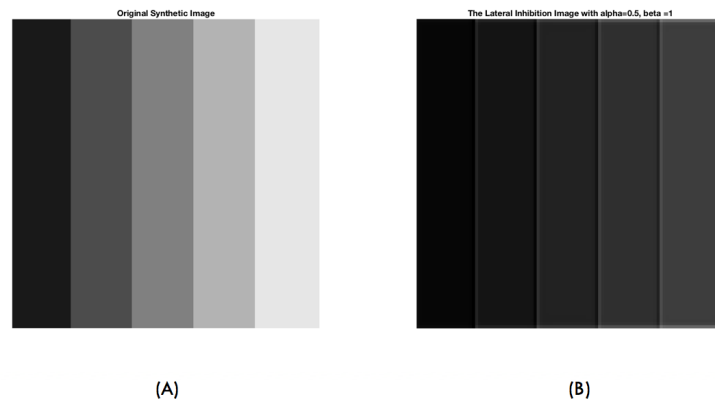


Figure 4-44: (A)The Synthetic Mach Bands Input Image. (B) the Lateral Inhibition Image with  $\alpha = 0.5$  and  $\beta = 1$ .

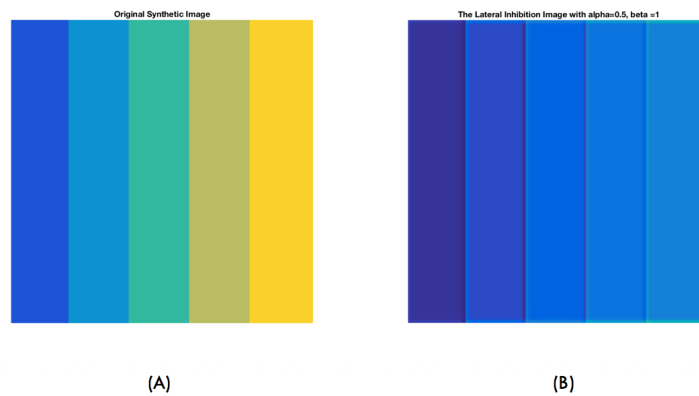


Figure 4-45: (A)The Colored Version of the Synthetic Mach Bands Input image. (B)The Colored Version of the Lateral Inhibition Image.

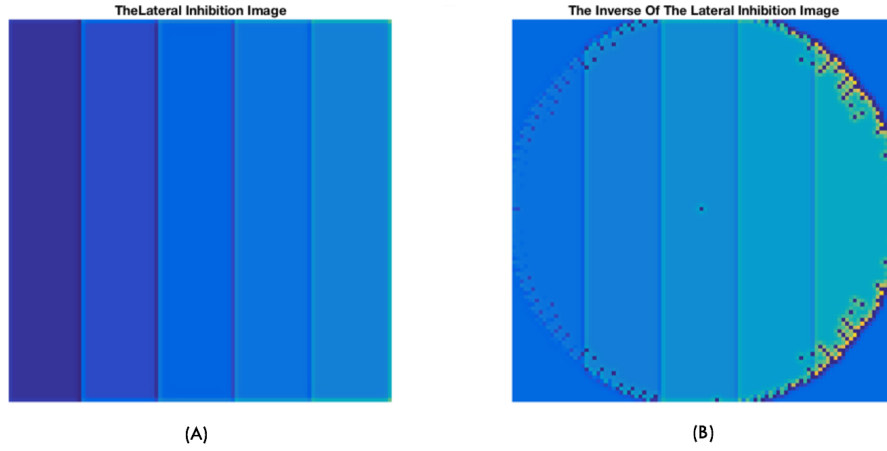


Figure 4-46: (A)The Colored Version of the Synthetic Mach Bands Input image. (B)The Colored Version Wrapped Back LSI Image with  $\alpha = 0.5$  and  $\beta = 1$ .

As we can see from the previous simulation figures, that the feature enhancement (the edges or the discontinuities regions in the image) were successfully obtained by using this biological phenomenon for the Uniform Mapped image and the Inverse mapped image. The colored images have presented above to visualized the enhanced edges based the Lateral Inhibition image for Mach Bands image. The following result images is related to a four real images in order to examine the performance of the lateral subtractive inhibition over a real grayscale pictures, see figures 4-47 to 4-54 .



Figure 4-47: (A)The Real Image with Size [100x100]. (B)The Lateral Inhibition Image with alpha  $\alpha=0.5$  and beta  $\beta=1$ .

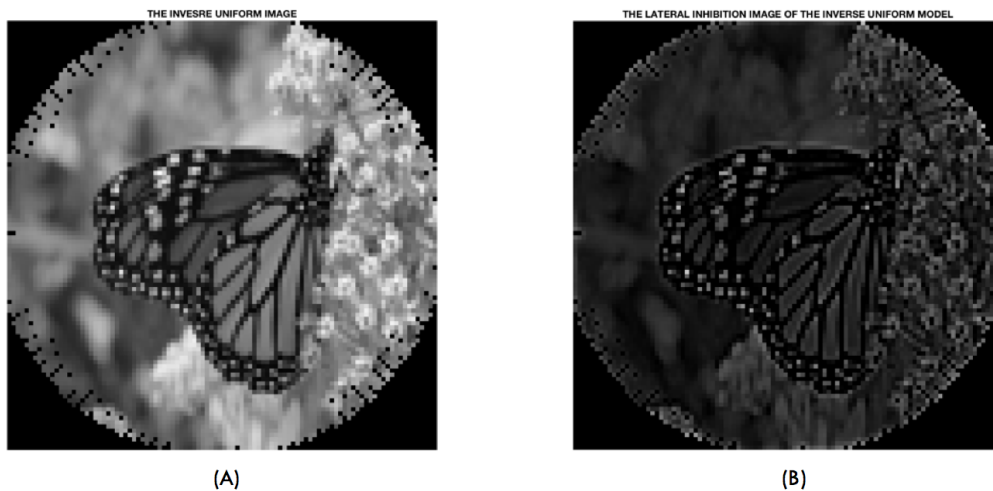


Figure 4-48: (A)The Inverse of Real Image with Size [100x100]. (B)The Lateral Inhibition Image with alpha  $\alpha=0.5$  and beta  $\beta=1$ .



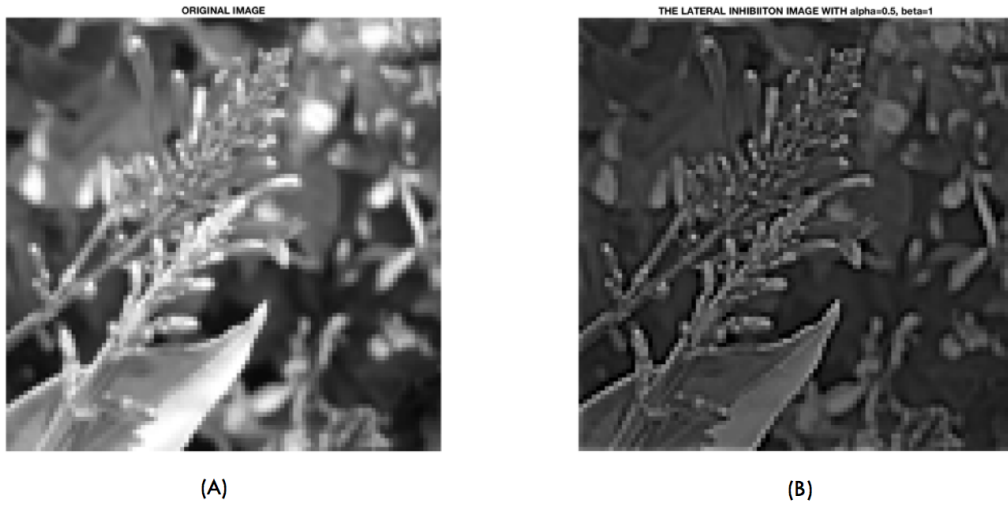


Figure 4-49: (A)The Real Image with Size [100x100]. (B)The Lateral Inhibition Image with alpha  $\alpha=0.5$  and beta  $\beta=1$ .

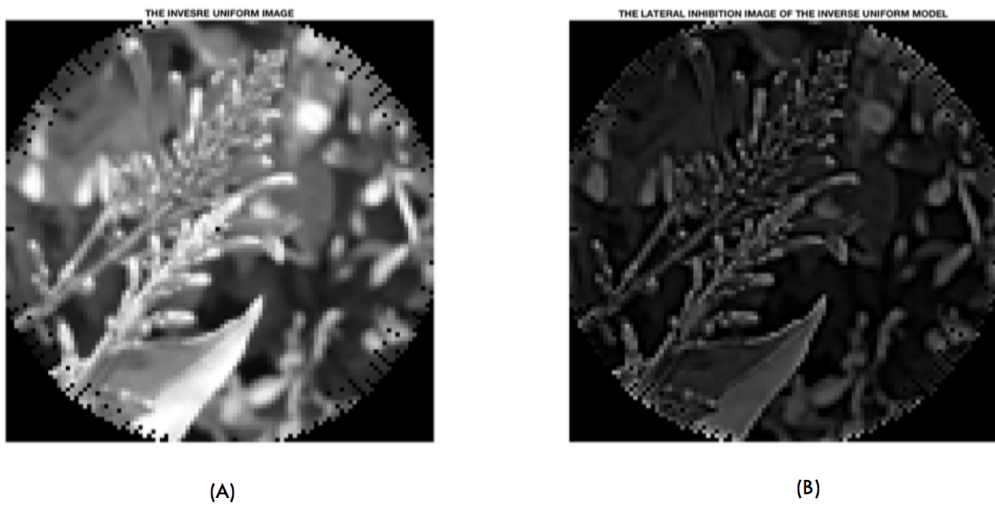


Figure 4-50: The Inverse Real Image with Size [100x100] and the Lateral Inhibition Image with alpha  $\alpha=0.5$  and beta  $\beta=1$



Figure 4-51: (A)The Real Image with Size [100x100]. (B) The Lateral Inhibition Image with alpha  $\alpha=0.5$  and beta  $\beta=1$ .

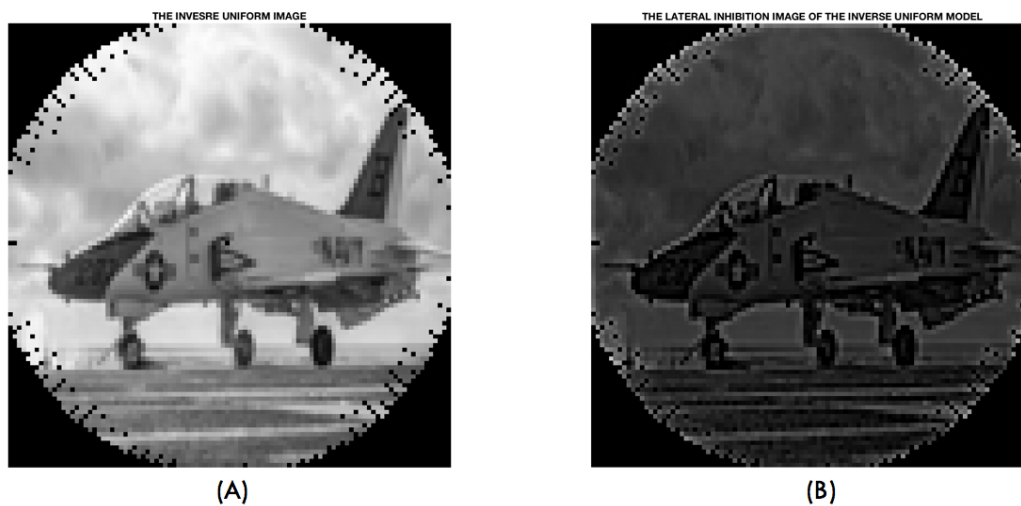


Figure 4-52: (A)The Inverse Real Image with Size [100x100] (B) The Lateral Inhibition Image with alpha  $\alpha=0.5$  and beta  $\beta=1$ .



Figure 4-53: (A)The Real Image with Size [100x100]. (B)The Lateral Inhibition Image with alpha  $\alpha=0.5$  and beta  $\beta=1$ .

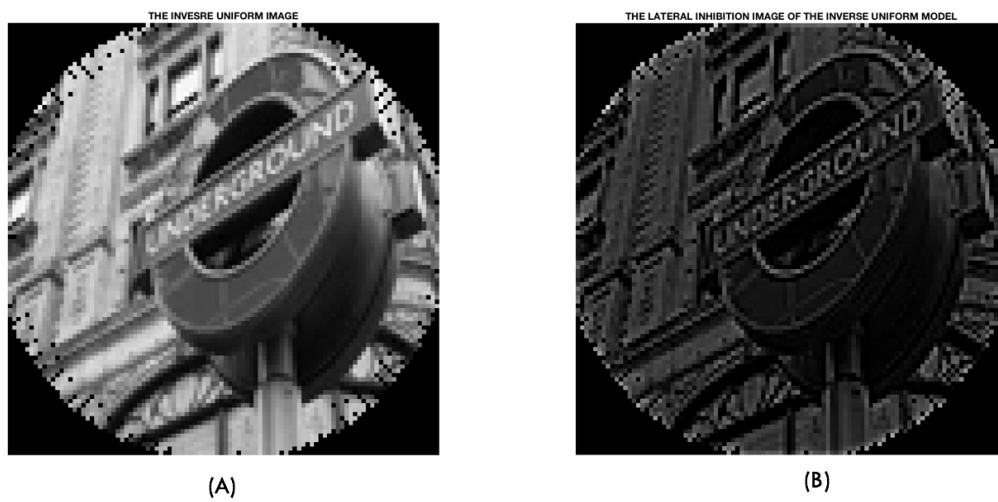


Figure 4-54: (A)The Inverse Real Image with Size [100x100].(B)The Lateral Inhibition Image with alpha  $\alpha=0.5$  and beta  $\beta=1$ .

### 4.3 Filtering the Uniform Mapping Image via Multiple Spatial Frequency Channels (CSF)

The feature extraction image processing can be done by using a separate spatial-frequency bands [43]. These bands can be created as shown previously by performing a difference of Gaussian operation in the spatial domain. In this simulation, three spatial-frequency bands were formed to mimic the Contrast Sensitivity Function envelop (CSF), see figure 3-13. As we mentioned earlier, the HVS has between five and seven spatially-tuned frequency bands [46]. However, in our case and because the processing time is critical, we have eliminated an unnecessary processing or combine several processing tasks into one simultaneous process to reduce the processing time required to accomplish the required task. Therefore, in this research work, three spatially-tuned channels which cover the range of detectable visual spatial frequencies have generated. These spatially tuned channels can be created by taking the difference of two successive zero mean Gaussian low pass filters with different standard deviation parameters ( $\sigma$ ), using the same equations provided in 3.10, 3.11 and 3.12. According to the mathematical expressions in equation 3.14 and 3.15. These mathematical representations are illustrating the relationship between the first Gaussian filter to the second one. Note that the difference of two low pass Gaussian filters with various width and spatial frequency ranges implies that this process can be viewed as a successive approximation to the Lateral Inhibition model, when the coupling coefficient matrix, [B], is, respectively, Gaussian or low-pass [47]. The spatial domain is our filtering processing space to filter out the image since a Fourier transform of the Gaussian in a frequency domain is still Gaussian. Therefore, the convolution operation will used to obtain the filtered image relative details regarding each frequency band.

Different studies such as [48] and [49] have presented the lateral subtractive inhibition method as an edge detection preprocessing image; which means it detects and enhances the high-frequency information of the picture only (acts like High-Pass Filter). Moreover, from [50] the effect of lateral inhibition (as in the retinal ganglion cell receptive field) may be seen mathematically as a second derivative operator  $\frac{d^2}{dx^2}$  which is equivalent to the Laplacian of Gaussian (LoG). Whereas, a LoG

performs as a high pass filter, which means it enhances the edges of the image only. However, in this research work the edge enhancement as well as the perceived information beyond the edges have achieved by using the lateral inhibition. Therefore, we need to examine the difference between the image treated via LSI (Lateral Subtractive Inhibition biological phenomenon that is occurring between the photo-receptors of the human retinal eye) to the filtered image based on LoG (approximation using Difference of Gaussian (DoG)). The LOG can be approximated by a Difference of two Gaussian (DoGs) at different scales. Where, that separability and scalability of Gaussian apply to the DoG so that we can achieve an efficient implementation of the LoG operator. The equations from 4.1 to 4.4 are representing the mathematical expressions regarding the Difference of Gaussian filters.

$$\partial^2 DOG \approx A * (G_{\sigma 2} - G_{\sigma 1}) \quad (4.1)$$

Where, A represents the amplitude of the Difference of Gaussian curve, and  $\sigma 2 = 5.6\sigma 1$ , see figure 3-12. whereas, the Fourier Transform of the second derivative operator will be as following:

$$F(u) = \int_{-\inf}^{\inf} \left( f(x) * \exp(-2\pi * x) \right) dx \quad (4.2)$$

The first derivative operator of the Fourier function is given by:

$$F\left(\frac{\partial f(x)}{\partial x}\right) = i2\pi F(u) \quad (4.3)$$

and the second derivative is given by:

$$F\left(\frac{\partial^2 f(x)}{\partial x^2}\right) = -(2\pi u)^2 F(u) \quad (4.4)$$

the contrast enhancement effect can be divided into three ranges [50]. At the low contrast range, there is no edge enhancement at all, where the grating is visible but the contrast is invisible. However, at the very high spatial frequency range, the contrast of the grating is visible and enhanced right down to the contrast sensitivity threshold curve, see figure 3-14. Lastly, the intermediate spatial frequency range, the edges did not appear brighter than the other information within the same image; in fact, it may seem less bright. Figures from 4-55 to 4-57, are showing the three Difference of Gaussian channels in 3D [the upper row] and 2D [lower row]. While the Composite

filter that comes from adding up all the three channels to mimic the Modulation Transfer Function curve of the Human Visual System 4-58.

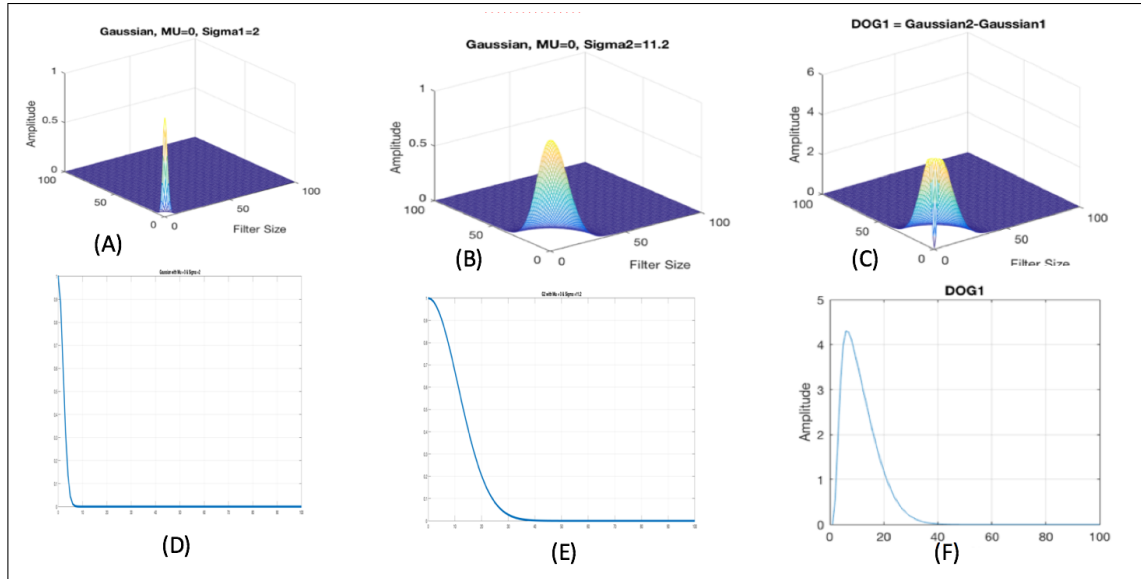


Figure 4-55: Difference of Gaussian Filter (DOG) acts like Low-Pass Filter where: (A) First Gaussian with  $\mu = 0$  and  $\sigma = 2$ . (B) First Gaussian with  $\mu = 0$  and  $\sigma = 11.2$ . (C) The Difference-of-Gaussian Filter. (D) Profile of The First Low-Pass Gaussian Filter. (E) Profile of The Second Low-Pass Gaussian Filter. (F) Profile of The Difference of Gaussian Filter.

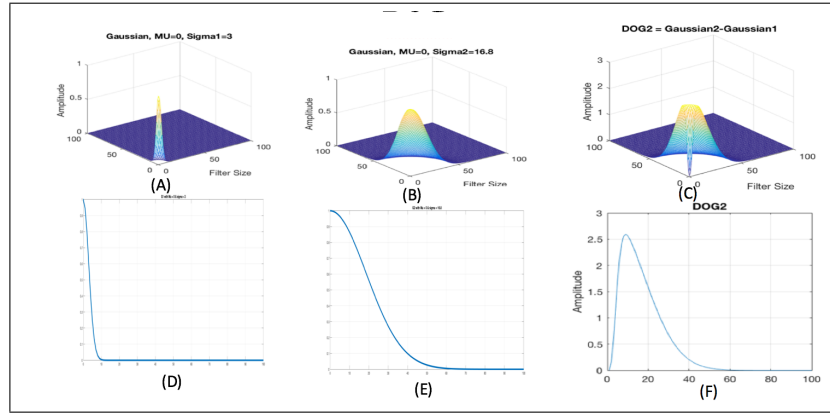


Figure 4-56: Difference of Gaussian Filter (DOG) acts like Band-Pass Filter where: (A) First Gaussian with  $\mu = 0$  and  $\sigma = 3$ . (B) First Gaussian with  $\mu = 0$  and  $\sigma = 16.8$ . (C) The Difference-of-Gaussian Filter. (D) Profile of The First Low-Pass Gaussian Filter. (E) Profile of The Second Low-Pass Gaussian Filter. (F) Profile of The Difference of Gaussian Filter.

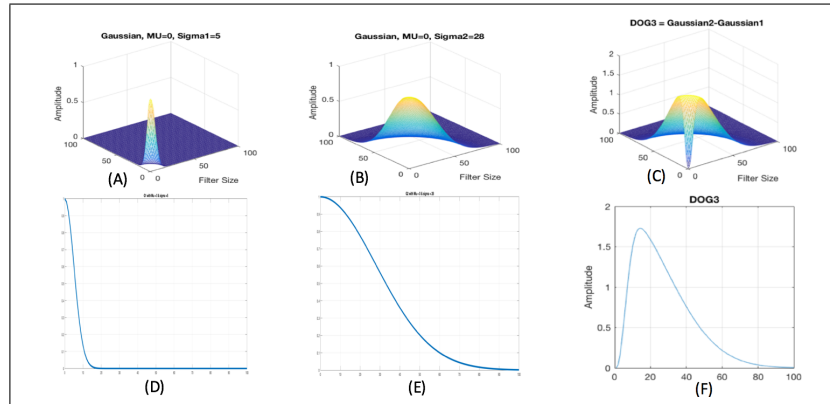


Figure 4-57: Difference of Gaussian Filter (DOG) acts like High-Pass Filter where: (A) First Gaussian with  $\mu = 0$  and  $\sigma = 5$ . (B) First Gaussian with  $\mu = 0$  and  $\sigma = 28$ . (C) The Difference-of-Gaussian Filter. (D) Profile of The First Low-Pass Gaussian Filter. (E) Profile of The Second Low-Pass Gaussian Filter. (F) Profile of The Difference of Gaussian Filter.

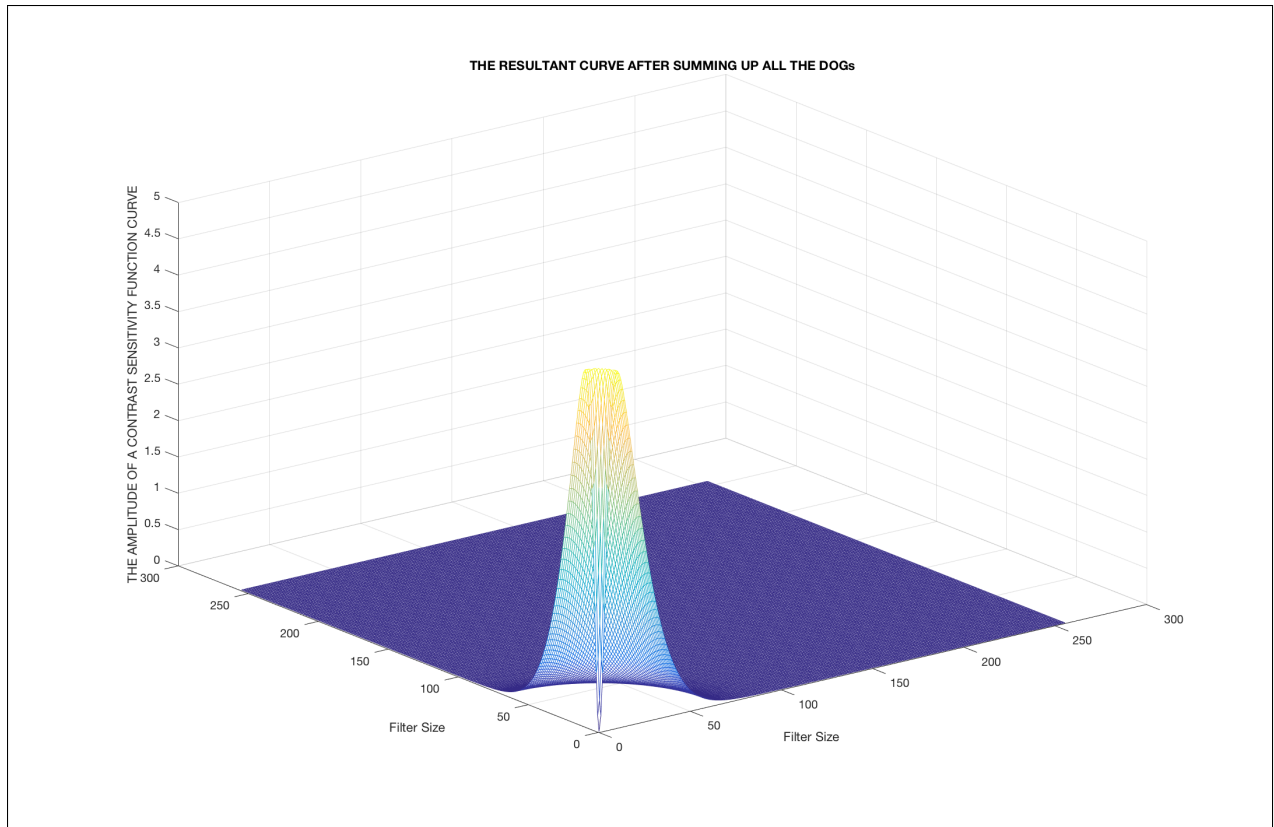


Figure 4-58: The Composite Envelop Figure Which Represents The Result of Summing Up All The Three Channels Above.

The following section of this chapter will represent the simulation results based on the multiple spatial-frequency channels (which mimics the Contrast Sensitivity Function curve of the Human Visual System). Then, a comparison will be made via the quality metric (RMSE) between the image processed via the biological method (Lateral Subtractive Inhibition) to the filtered image based on these three spatial-frequency bands. The benefit of this comparison is to identify which spatial-frequency channel produces an image data that is closest to the lateral inhibition image. In other words, which DoG filter is most similar to this biological phenomenon. Where, all the results related to this comparison is shown in table 4.1 and table 4.2 for the uniform and non-uniform models, respectively.



#### 4.3.1 The Simulation Results of The Filtration Process of The Uniform Model:

Figure 4-59 is representing the first real image before and after filtration process in gray scale:

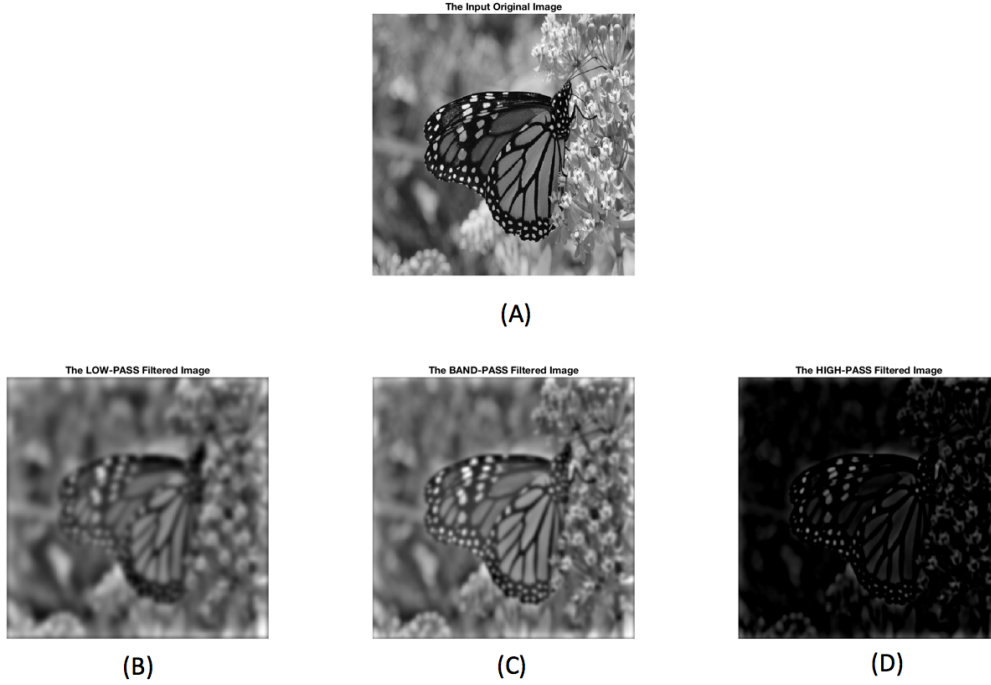


Figure 4-59: (A)Butterfly Image in Gray scale. (B)Butterfly Image After DOG-LPF. (C)Butterfly Image After DOG-BPF.(D)Butterfly Image After DOG-HPF.

In order to visualize the difference between theses three filtered image, we have colorized the figure above, and the colored version is shown in figure 4-61. To transform the grayscale image to color space image, we have used a MATLAB command function called (*colormap(parula)*). Figure 4-60 represents the range of colors regarding this color map function, where the dark blue color represents the dark gray color of the grayscale image while the yellow color corresponds to the bright gray of that image. Then, the following figures from 4-62 to 4-67 are shown all the resultant output images based on the filtration process via the Difference of Gaussian filters.



Figure 4-60: This Figure is Representing the Gray Scale Image and The Color Space Version of Lena Image.

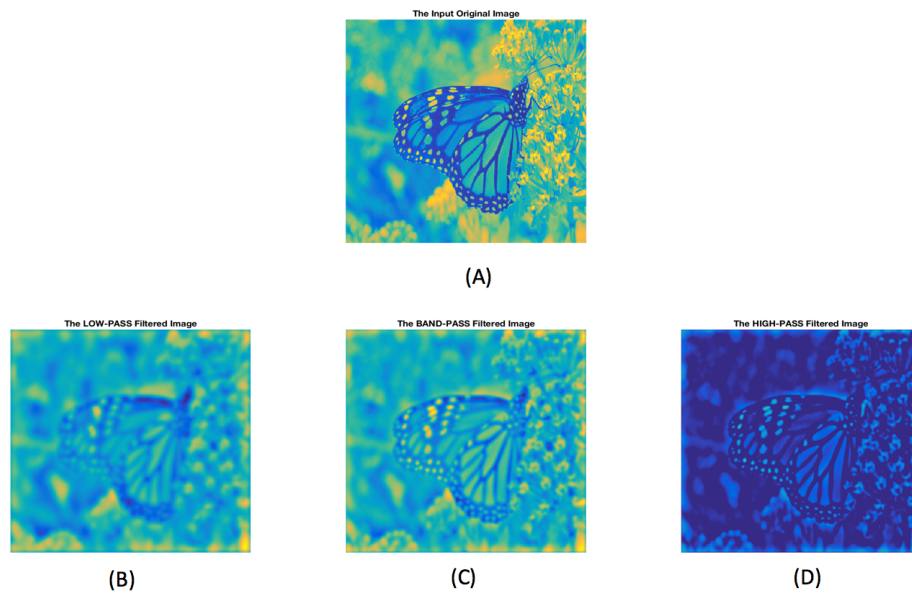


Figure 4-61: (A)Butterfly Image in Color Space. (B)Butterfly Image After DOG-LPF. (C)Butterfly Image After DOG-BPF.(D)Butterfly Image After DOG-HPF.

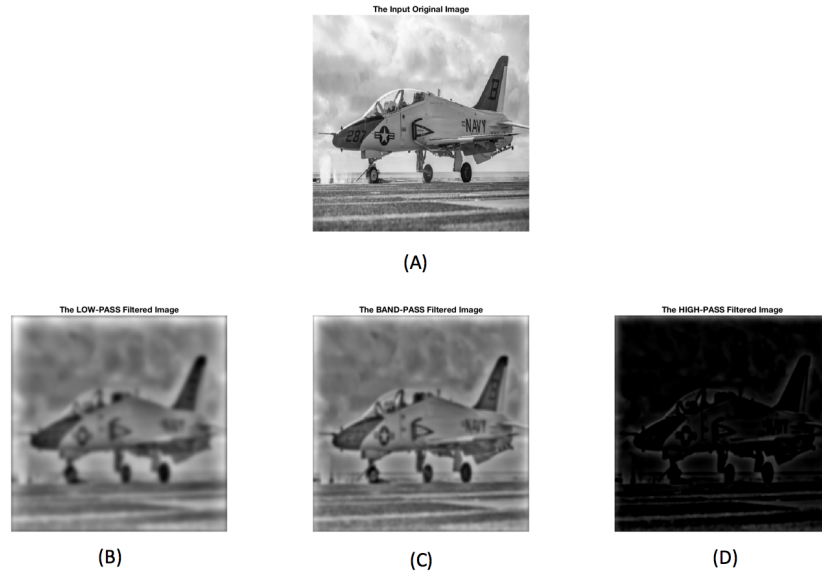


Figure 4-62: (A)Jet Image in Grayscale. (B)Jet Image After DOG-LPF. (C)Jet Image After DOG-BPF.(D)Jet Image After DOG-HPF.

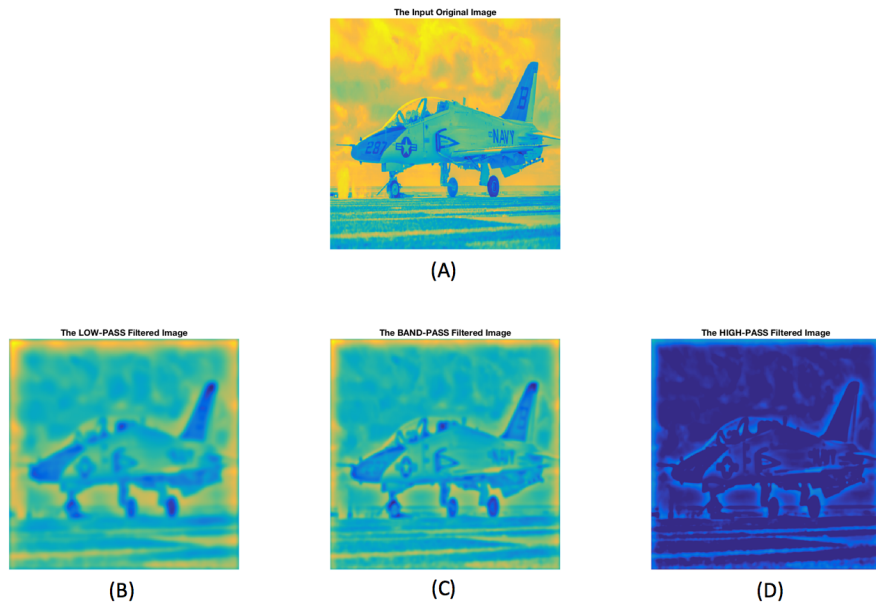


Figure 4-63: (A)Jet Image in Color Space. (B)Jet Image After DOG-LPF. (C)Jet Image After DOG-BPF.(D)Jet Image After DOG-HPF.

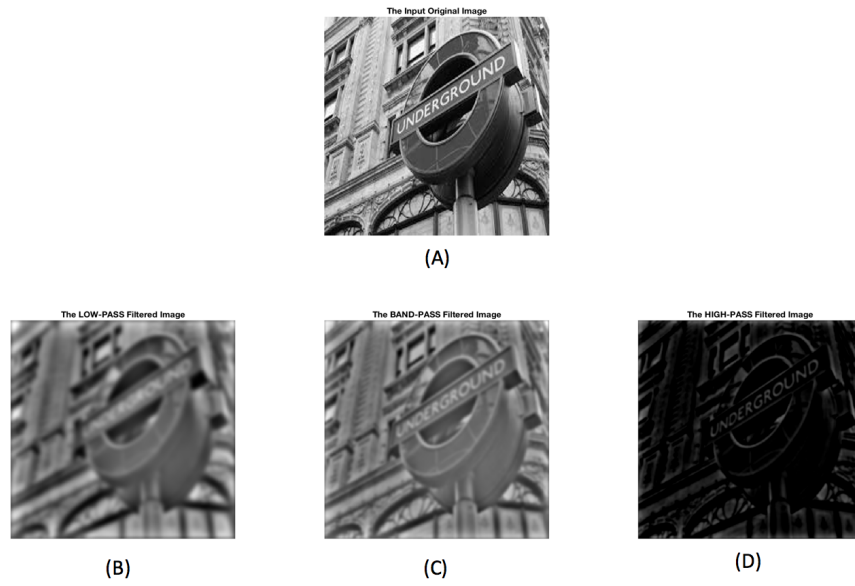


Figure 4-64: (A)Word Image in Grayscale. (B)Word Image After DOG-LPF. (C)Word Image After DOG-BPF.(D)Word Image After DOG-HPF.

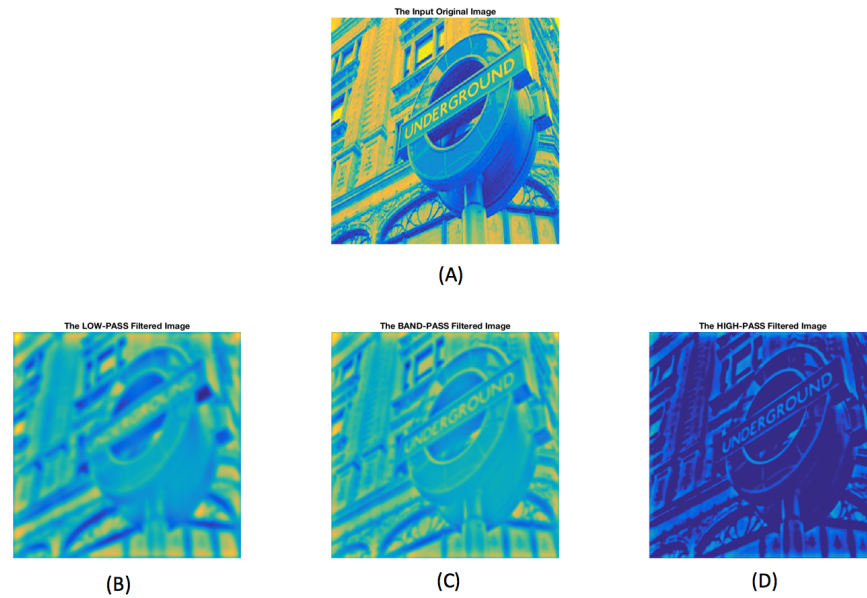


Figure 4-65: (A)Word Image in Color Space. (B)Word Image After DOG-LPF. (C)Word Image After DOG-BPF.(D)Word Image After DOG-HPF.

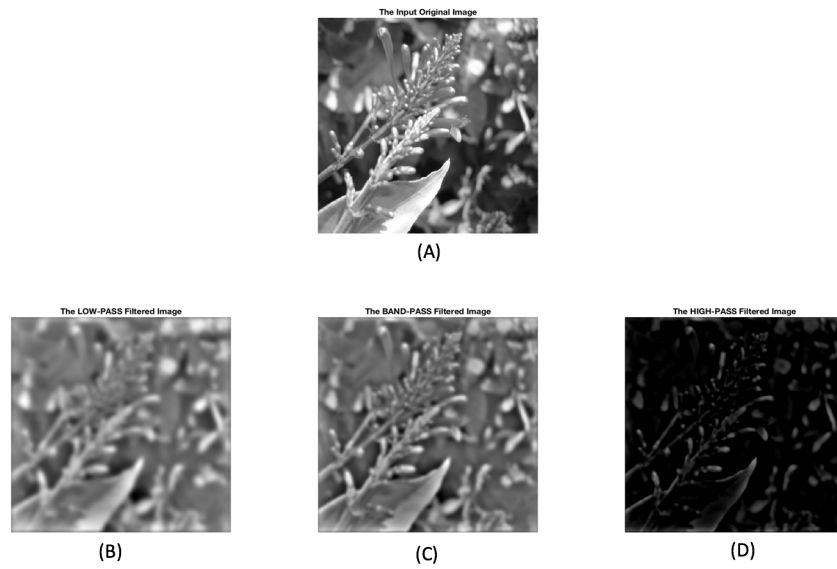


Figure 4-66: (A) Flower Image in Grayscale. (B) Flower Image After DOG-LPF. (C) Flower Image After DOG-BPF. (D) Flower Image After DOG-HPF.

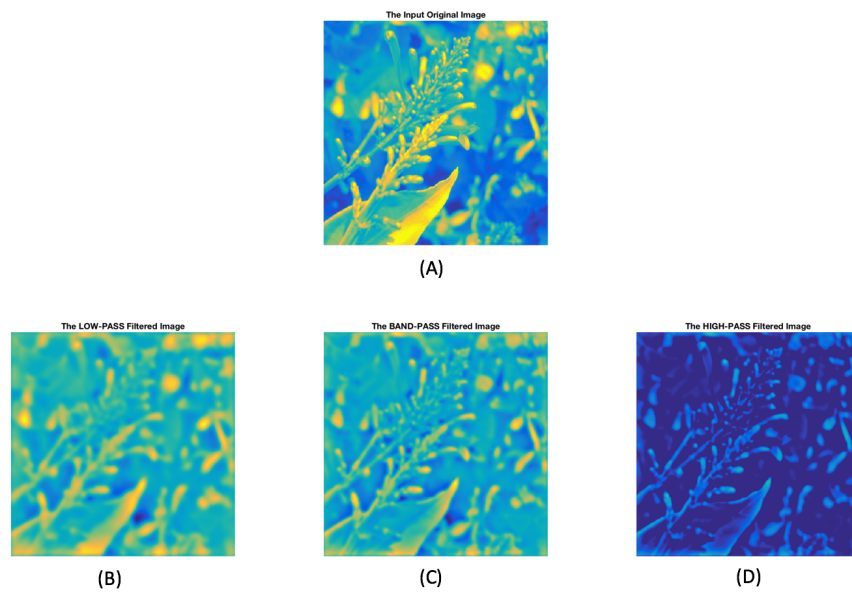


Figure 4-67: (A) Flower Image in Color Space. (B) Flower Image After DOG-LPF. (C) Flower Image After DOG-BPF. (D) Flower Image After DOG-HPF.

The figures above, from 4-62 to 4-67, have shown the filtered images based on the three spatial-frequency channels (DOG-LPF, DOG-BPF, and DOG-HPF) in grayscale and color space, as well. However, the objective of this simulation is to find out which filtered image contains the closest information as the biological image (lateral inhibition image), we have re-generated the same images above however in this time the LSI image will included too.

#### **4.3.2 The Simulation Results of The Lateral Inhibition Method and the Multiple Spatial Frequency channels (CSF):**

The comparison between an image processed via lateral inhibition biological method to the filtered image based the multiple spatial frequency channels (CSF), has established under this section. The following figures will represented all the uniform mapping images from both methods to find out which spatial frequency channel that produces an image similar to the lateral inhibition model see the figure 4-1. As we mentioned earlier, each mapping model includes two type of images, Forward and Inverse images. For this section the Forward Uniform mapping image represents after applying the lateral subtractive inhibition algorithm with  $[\alpha=0.5 \text{ and } \beta=1]$ , and the three different Band-Pass spatial-frequency channels. Then, the differences between the filtered image via the three multiple spatial-frequency to the picture processed based on the biological method will calculated based on the Root Mean Square Error (RMSE) quality metric regarding this mapping model. The following figures from 4-68 to 4-75 represent the resultant images via each method in grayscale and color space as well. While the figures from 4-76 to 4-81 are shown the difference between the LI image to the filtered image based on each spatial frequency channel in both scales, the gray and colored one.

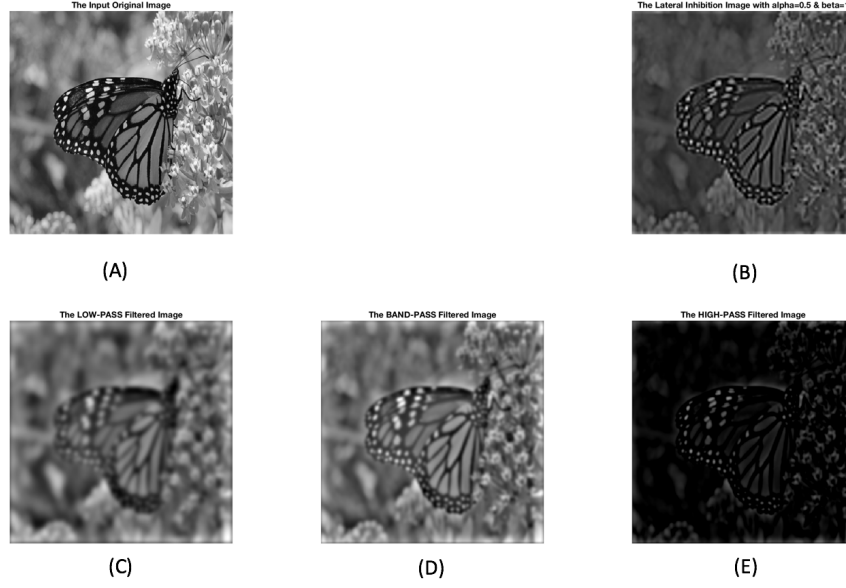


Figure 4-68: The Comparison Between LSI Image to The Filtered image: (A)The Original Image.(B)The Lateral Inhibition Image with  $[\alpha = 0.5$  and  $\beta = 1]$ .(C)The Filtered Image via DOG-LPF.(D)The Filtered Image via DOG-BPF.(E)The Filtered Image via DOG-HPF.

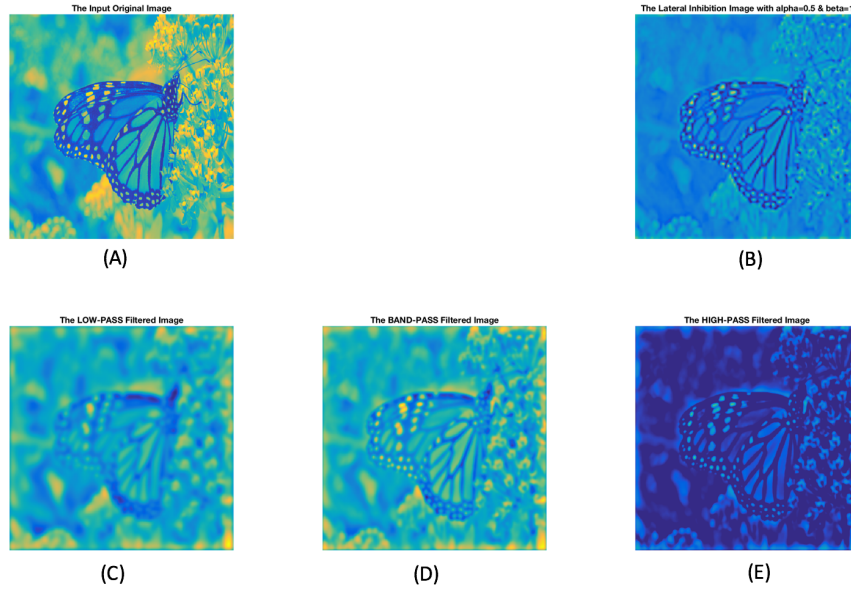


Figure 4-69: The Comparison Between LSI Image to The Filtered image: (A)The Original Image.(B)The Lateral Inhibition Image with  $[\alpha = 0.5$  and  $\beta = 1]$ .(C)The Filtered Image via DOG-LPF.(D)The Filtered Image via DOG-BPF.(E)The Filtered Image via DOG-HPF.



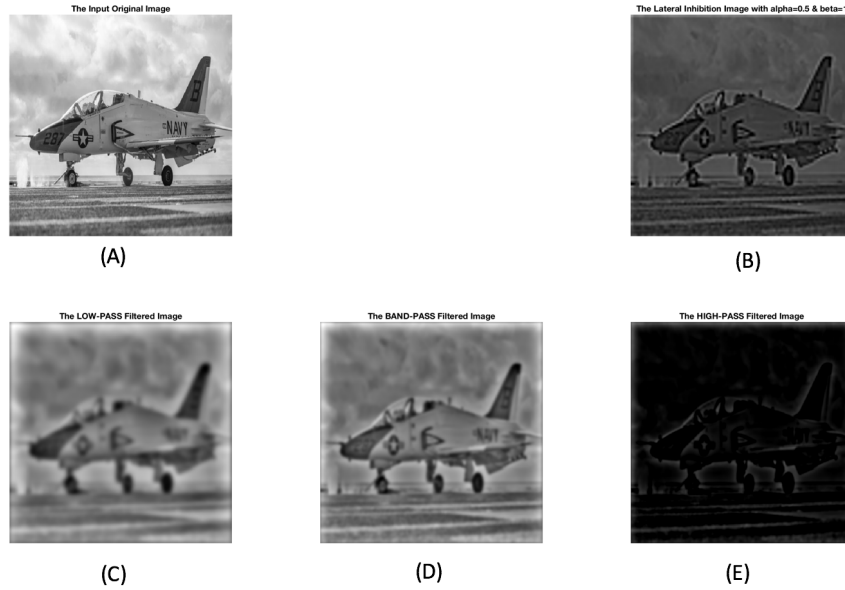


Figure 4-70: The Comparison Between LSI Image to The Filtered image: (A)The Original Image.(B)The Lateral Inhibition Image with  $[\alpha = 0.5 \text{ and } \beta = 1]$ .(C)The Filtered Image via DOG-LPF.(D)The Filtered Image via DOG-BPF.(E)The Filtered Image via DOG-HPF.

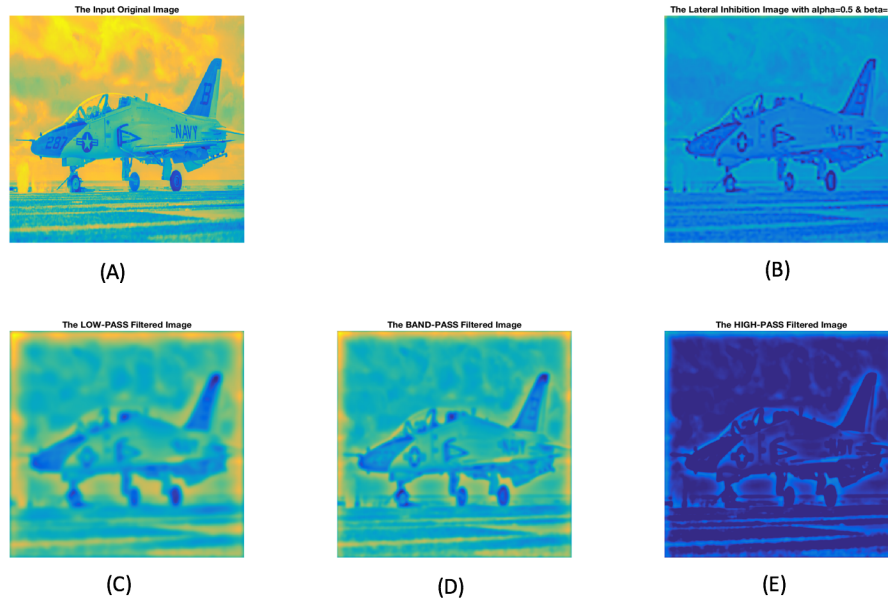


Figure 4-71: The Comparison Between LSI Image to The Filtered image: (A)The Original Image.(B)The Lateral Inhibition Image with  $[\alpha = 0.5 \text{ and } \beta = 1]$ .(C)The Filtered Image via DOG-LPF.(D)The Filtered Image via DOG-BPF.(E)The Filtered Image via DOG-HPF.



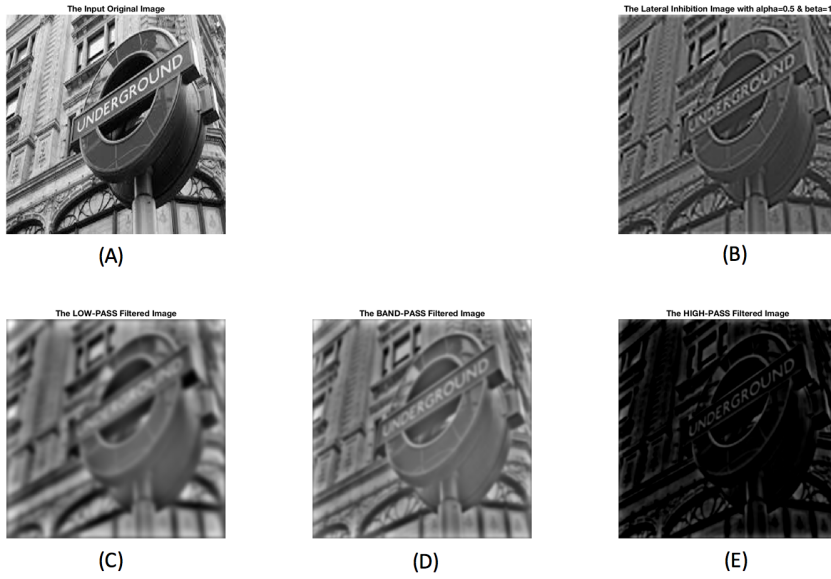


Figure 4-72: The Comparison Between LSI Image to The Filtered image: (A)The Original Image.(B)The Lateral Inhibition Image with  $[\alpha = 0.5 \text{ and } \beta = 1]$ .(C)The Filtered Image via DOG-LPF.(D)The Filtered Image via DOG-BPF.(E)The Filtered Image via DOG-HPF.

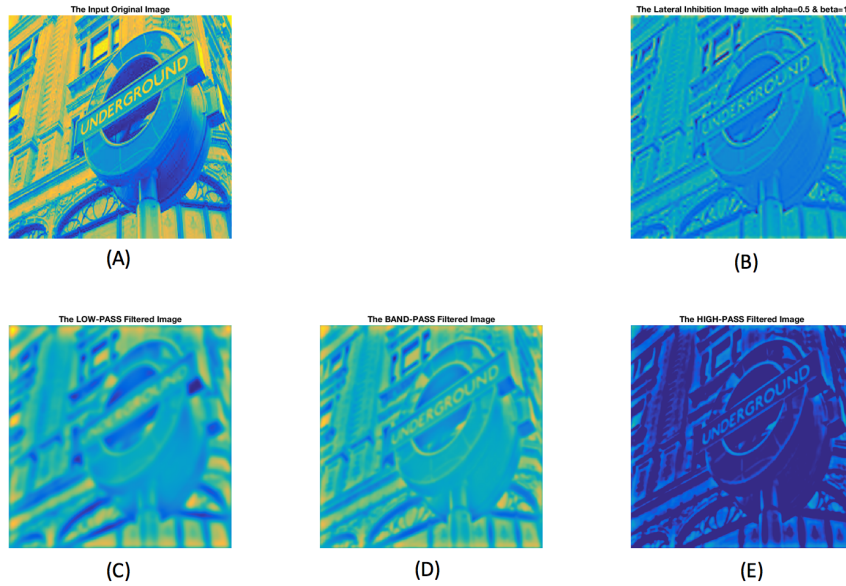


Figure 4-73: The Comparison Between LSI Image to The Filtered image: (A)The Original Image.(B)The Lateral Inhibition Image with  $[\alpha = 0.5 \text{ and } \beta = 1]$ .(C)The Filtered Image via DOG-LPF.(D)The Filtered Image via DOG-BPF.(E)The Filtered Image via DOG-HPF.

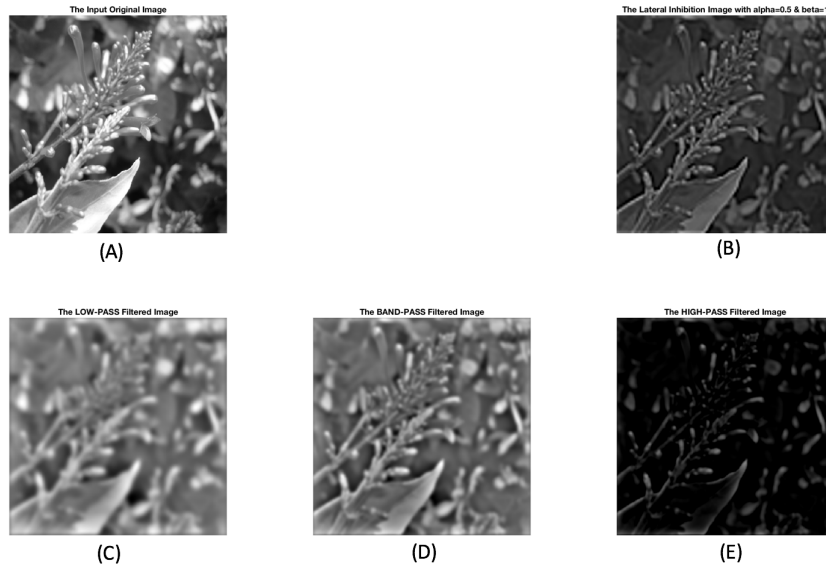


Figure 4-74: The Comparison Between LSI Image to The Filtered image: (A)The Original Image.(B)The Lateral Inhibition Image with  $[\alpha = 0.5 \text{ and } \beta = 1]$ .(C)The Filtered Image via DOG-LPF.(D)The Filtered Image via DOG-BPF.(E)The Filtered Image via DOG-HPF.

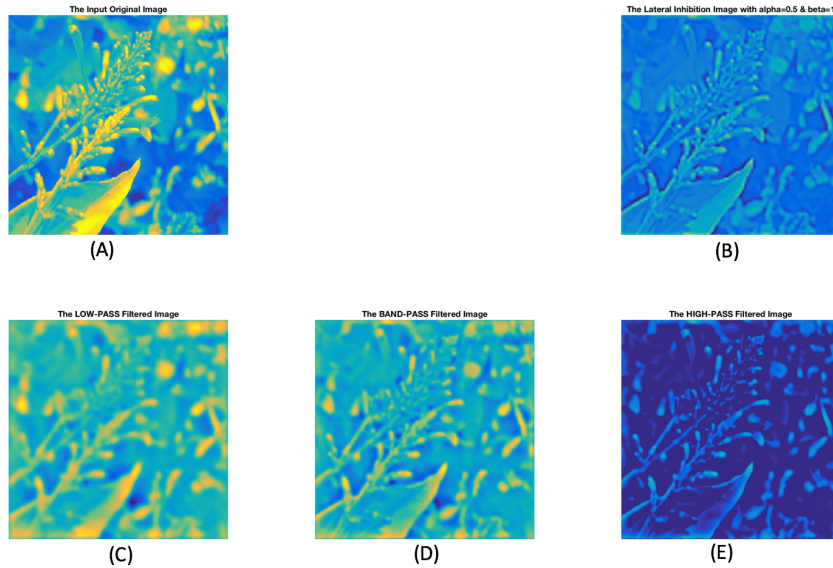


Figure 4-75: The Comparison Between LSI Image to The Filtered image: (A)The Original Image.(B)The Lateral Inhibition Image with  $[\alpha = 0.5 \text{ and } \beta = 1]$ .(C)The Filtered Image via DOG-LPF.(D)The Filtered Image via DOG-BPF.(E)The Filtered Image via DOG-HPF.

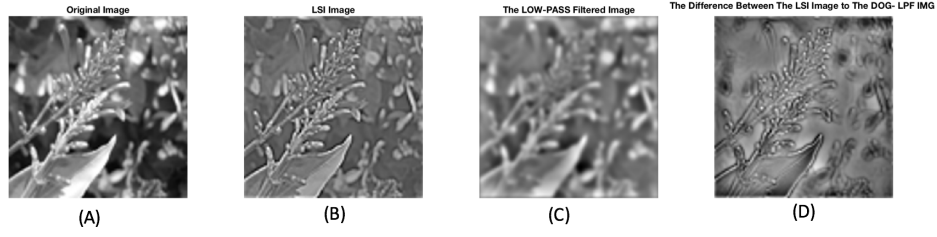


Figure 4-76: (A)The Flower original input image.(B) Lateral Inhibition image with  $\alpha=0.5$  and  $\beta=1$ (C) DOG-LPF Filtered image with  $\mu=0$  and  $\sigma=9.2$ .(D)The Test image  $[LSI_{img} - LPF_{img}]$ .

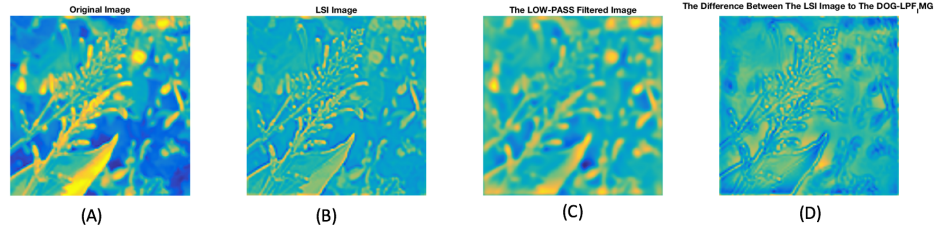


Figure 4-77: (A)The Flower original input image.(B) Lateral Inhibition image with  $\alpha=0.5$  and  $\beta=1$ (C) DOG-LPF Filtered image with  $\mu=0$  and  $\sigma=9.2$ .(D)The Test image  $[LSI_{img} - LPF_{img}]$ .

As we can see from figure 4-76 and 4-77, that after subtracting the low-pass filtered image from the lateral subtractive inhibition image. The remaining details will be basically: the edges (which is the high-frequency information) in addition to the relative information between the low and high frequencies, see part D of these two figures above.

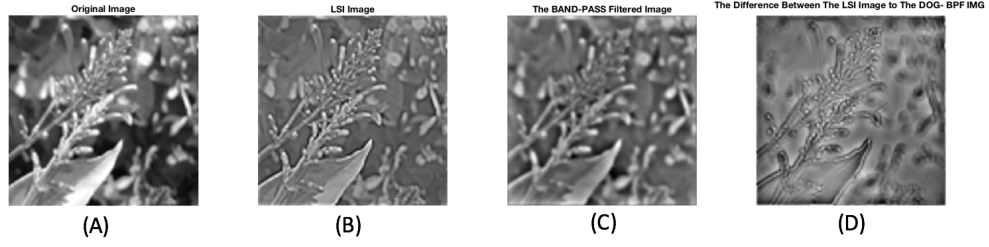


Figure 4-78: (A)The Flower original input image.(B) Lateral Inhibition image with  $\alpha=0.5$  and  $\beta=1$ (C) DOG-BPF Filtered image with  $\mu=0$  and  $\sigma=13.8$ .(D)The Test image  $[LSI_{img} - BPF_{img}]$ .

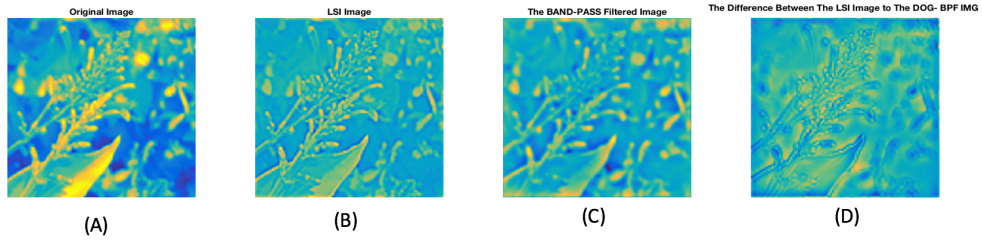


Figure 4-79: (A)The Flower original input image.(B) Lateral Inhibition image with  $\alpha=0.5$  and  $\beta=1$ (C) DOG-BPF Filtered image with  $\mu=0$  and  $\sigma=13.8$ .(D)The Test image  $[LSI_{img} - BPF_{img}]$ .

However, after subtracting the band-pass filtered image from the lateral inhibition image the resultant details, as illustrated in figure 4-78D and in 4-79D, only the contrast that is remaining besides a blurry details from the original image.

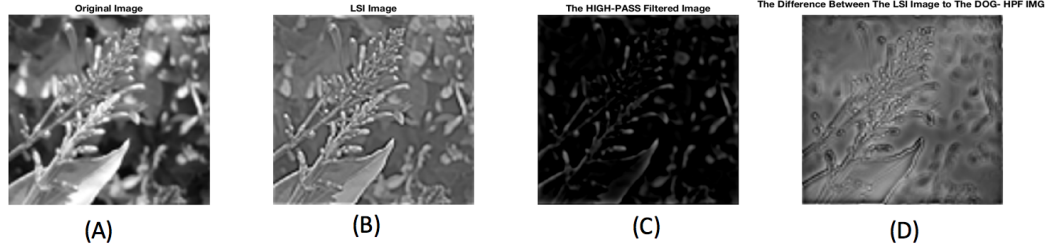


Figure 4-80: (A)The Flower original input image.(B) Lateral Inhibition image with  $\alpha=0.5$  and  $\beta=1$ (C) DOG-HPF Filtered image with  $\mu=0$  and  $\sigma=23$ .(D)The Test image  $[LSI_{img} - HPF_{img}]$ .

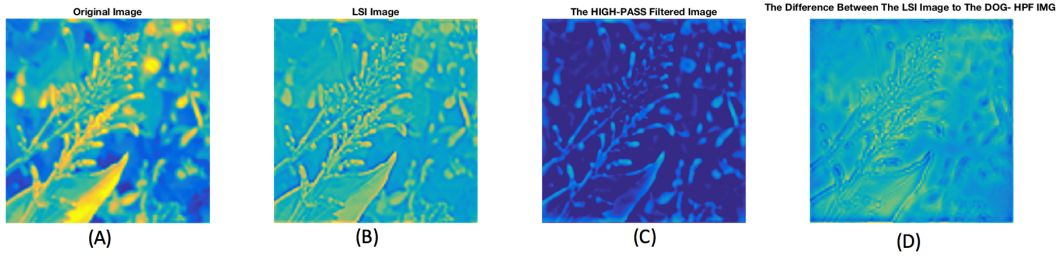


Figure 4-81: (A)The Flower original input image.(B) Lateral Inhibition image with  $\alpha=0.5$  and  $\beta=1$ (C) DOG-HPF Filtered image with  $\mu=0$  and  $\sigma=23$ .(D)The Test image  $[LSI_{img} - HPF_{img}]$ .

While the resultant output image in, 4-80part D and 4-81 part D, which is the resultant output image of subtracting the high pass filtered image from the lateral inhibition image has a blurry edges and there is a few details related to the relative information beyond the edges comparing to the previous figures.

To complete all the image results regarding this model, we need to add the Inverse of this model too. Therefore, the next part of this section will be concentrating on the inverse image of a Uniform mapped model.

### 4.3.3 The Simulation results of the Inverse Uniform Model Based on the Multiple Spatial Frequency Channels (MTF):

In this section, the wrapped back version of the uniform mapped image will be obtaining based on a circular mapping model within that same size as the original input image. This pattern has constructed based on a number of circles and wedges that are equivalent to the scale of the entry picture. Whereas, these circles are extending linearly as the distance from the center point increases. That contradicts to the non-uniform mapping model, where the circles are growing logarithmically as we move further from the fovea. Therefore, the resultant output image has the same resolution at the center and the periphery area. The reason of generating this type of uniform mapped image is to complete the comparison between the uniform mapping model to the novel model in both image patterns [the foreword and inverse pattern]. See figures from 4-82 to figure 4-89.

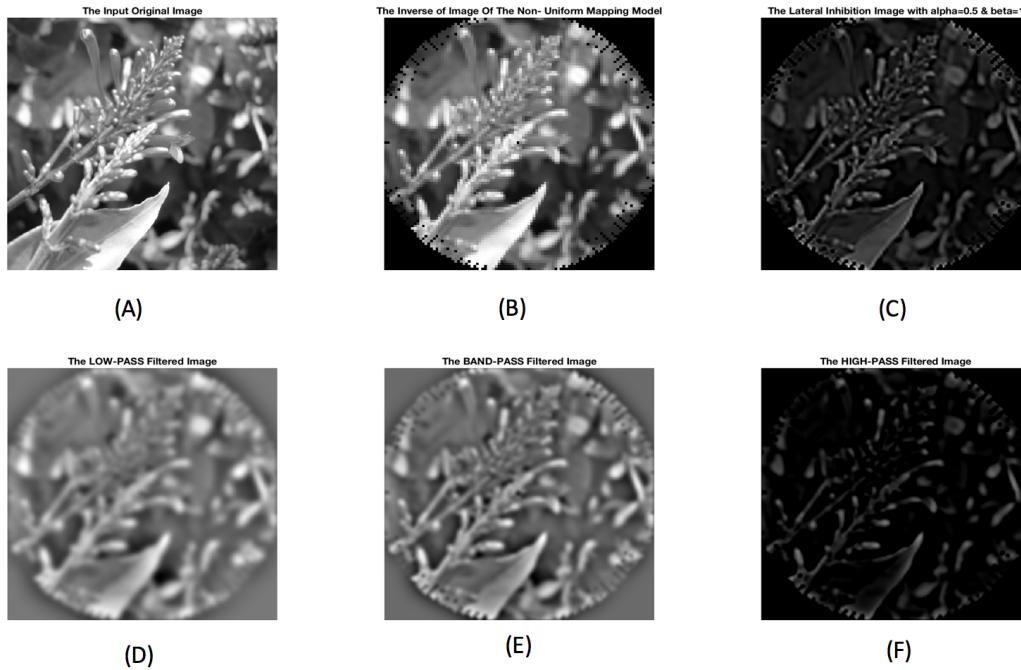


Figure 4-82: (A)The Original Image. (B) THE Wrapped Back Version of the Uniform Mapped Image with Size [100 x 100]. (C) LSI Image with [ $\alpha = 0.5$  and  $\beta = 1$ ]. (D)The Filtered Image via DOG-LPF.(E)The Filtered Image via DOG-BPF.(F)The Filtered Image via DOG-HPF.



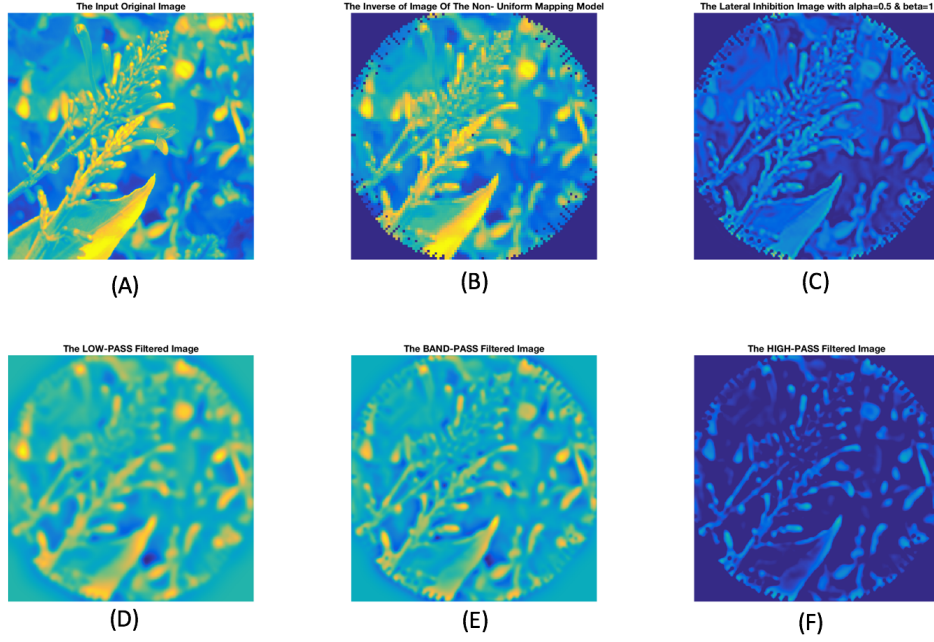


Figure 4-83: (A)The Original Image. (B) The Wrapped Back Version of the Uniform Mapped Image with Size  $[100 \times 100]$ . (C) LSI Image with  $[\alpha = 0.5 \text{ and } \beta = 1]$ . (D)The Filtered Image via DOG-LPF.(E)The Filtered Image via DOG-BPF.(F)The Filtered Image via DOG-HPF.

From the figure 4-83, we can notice that the wrapped back image has a uniform resolution over the entire picture and the Lateral subtractive inhibition model has the same frequency band as the high-pass filtered image see part (C) and (F) of the same figure above. However, the lateral inhibition image has information more than the DOG-high pass filtered image. In other words, the lateral inhibition does improve the relative information beyond the contrasts beside enhancing the edges of the picture. And that contradicts the idea in [50] where the lateral inhibition method is only a second derivative operator. But before drawing any conclusion, we need to test the rest of the real images regarding this model and the new one and observe if that's applicable on the other images or no!

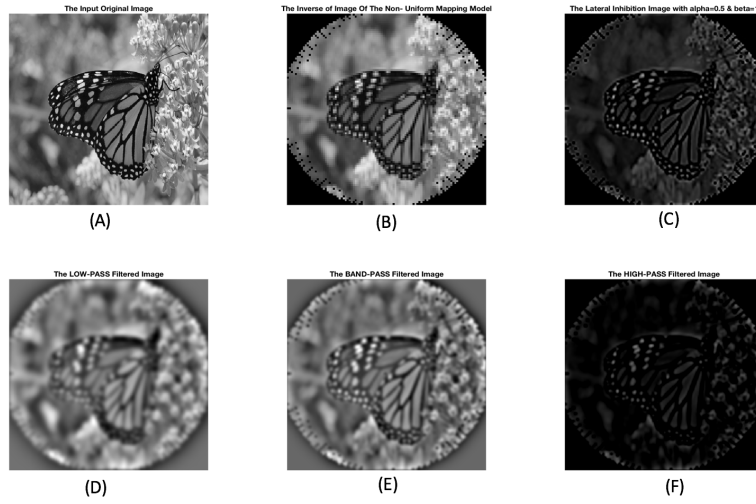


Figure 4-84: (A)The Original Image. (B) The Wrapped Back Version of the Uniform Mapped Image with Size  $[100 \times 100]$ . (C) LSI Image with  $[\alpha = 0.5 \text{ and } \beta = 1]$ . (D)The Filtered Image via DOG-LPF.(E)The Filtered Image via DOG-BPF.(F)The Filtered Image via DOG-HPF.

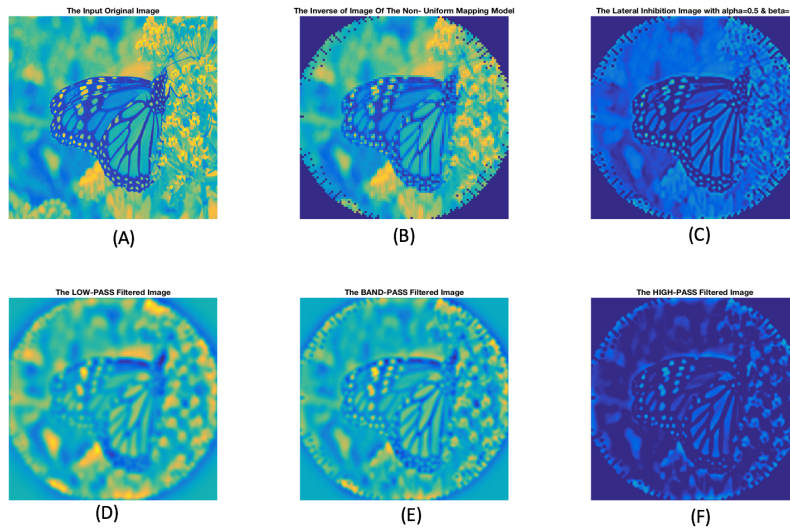


Figure 4-85: (A)The Original Image. (B) The Wrapped Back Version of the Uniform Mapped Image with Size  $[100 \times 100]$ . (C) LSI Image with  $[\alpha = 0.5 \text{ and } \beta = 1]$ . (D)The Filtered Image via DOG-LPF.(E)The Filtered Image via DOG-BPF.(F)The Filtered Image via DOG-HPF.



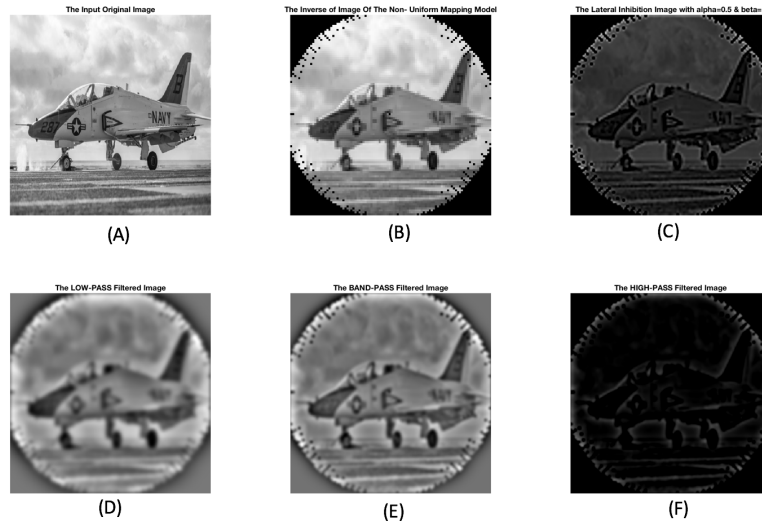


Figure 4-86: (A)The Original Image. (B) The Wrapped Back Version of the Uniform Mapped Image with Size  $[100 \times 100]$ . (C) LSI Image with  $[\alpha = 0.5 \text{ and } \beta = 1]$ . (D)The Filtered Image via DOG-LPF.(E)The Filtered Image via DOG-BPF.(F)The Filtered Image via DOG-HPF.

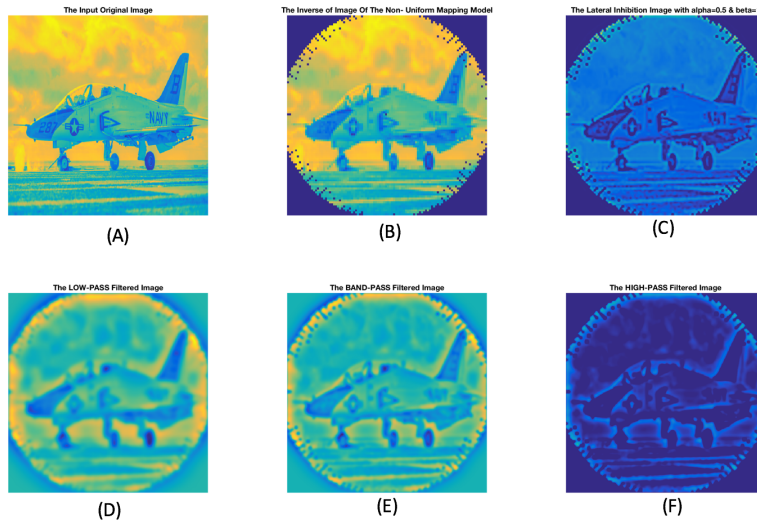


Figure 4-87: (A)The Original Image. (B) The Wrapped Back Version of the Uniform Mapped Image with Size  $[100 \times 100]$ . (C) LSI Image with  $[\alpha = 0.5 \text{ and } \beta = 1]$ . (D)The Filtered Image via DOG-LPF.(E)The Filtered Image via DOG-BPF.(F)The Filtered Image via DOG-HPF.

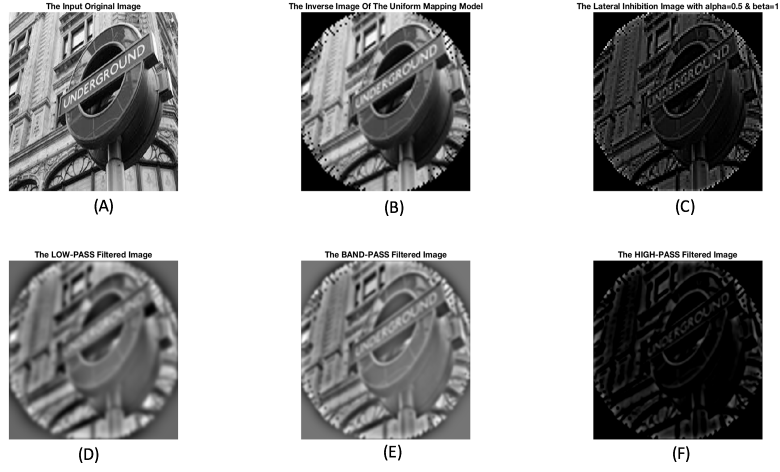


Figure 4-88: (A)The Original Image. (B) The Wrapped Back Version of the Uniform Mapped Image with Size  $[100 \times 100]$ . (C) LSI Image with  $[\alpha = 0.5 \text{ and } \beta = 1]$ . (D)The Filtered Image via DOG-LPF.(E)The Filtered Image via DOG-BPF.(F)The Filtered Image via DOG-HPF.

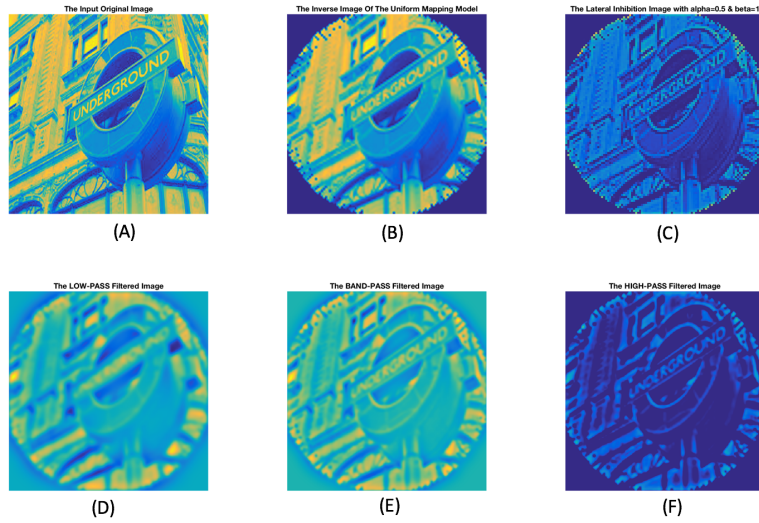


Figure 4-89: (A)The Original Image. (B) The Wrapped Back Version of the Uniform Mapped Image with Size  $[100 \times 100]$ . (C) LSI Image with  $[\alpha = 0.5 \text{ and } \beta = 1]$ . (D)The Filtered Image via DOG-LPF.(E)The Filtered Image via DOG-BPF.(F)The Filtered Image via DOG-HPF.

The following figures are representing the remaining details after subtracting the filtered image via the three multiple spatial frequency channels from the lateral inhibition image regarding this version of the uniform mapping model.

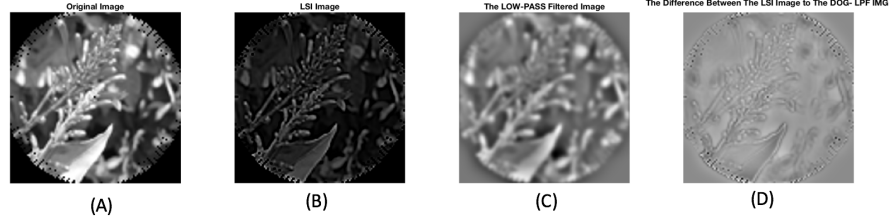


Figure 4-90: (A)The Flower original input image.(B) Lateral Inhibition image with  $\alpha=0.5$  and  $\beta=1$ (C) DOG-LPF Filtered image with  $\mu=0$  and  $\sigma=9.2$ .(D)The Test image  $[LSI_{img} - LPF_{img}]$ .

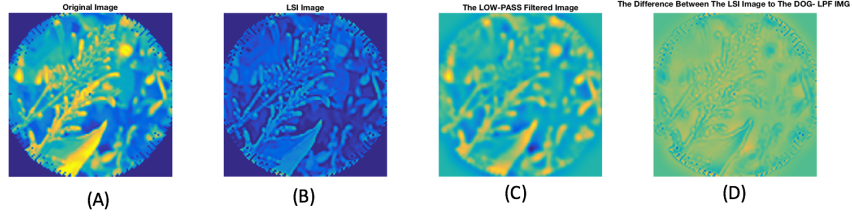


Figure 4-91: (A)The Flower original input image.(B) Lateral Inhibition image with  $\alpha=0.5$  and  $\beta=1$ (C) DOG-LPF Filtered image with  $\mu=0$  and  $\sigma=9.2$ .(D)The Test image  $[LSI_{img} - LPF_{img}]$ .

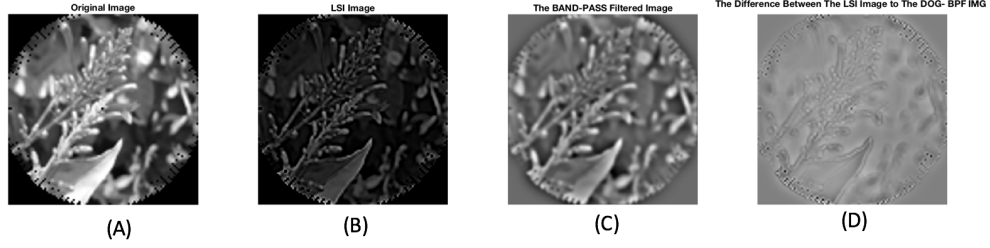


Figure 4-92: (A)The Flower original input image.(B) Lateral Inhibition image with  $\alpha=0.5$  and  $\beta=1$ (C) DOG-BPF Filtered image with  $\mu=0$  and  $\sigma=13.8$ .(D)The Test image  $[LSI_{img} - BPF_{img}]$ .

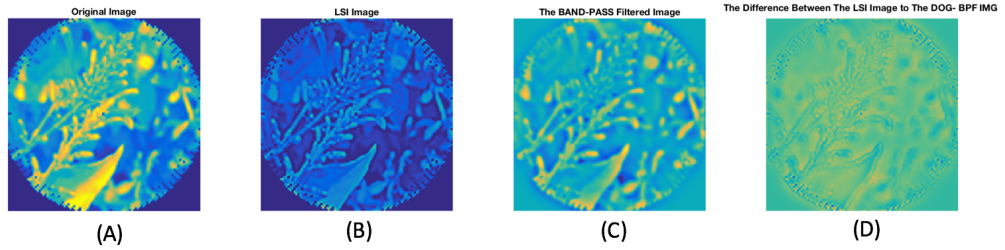


Figure 4-93: (A)The Flower original input image.(B) Lateral Inhibition image with  $\alpha=0.5$  and  $\beta=1$ (C) DOG-BPF Filtered image with  $\mu=0$  and  $\sigma=13.8$ .(D)The Test image  $[LSI_{img} - BPF_{img}]$ .

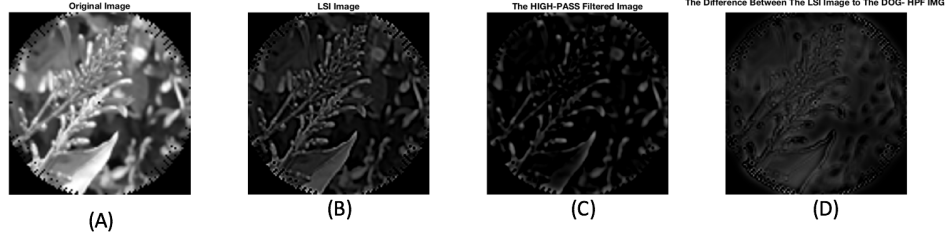


Figure 4-94: (A)The Flower original input image.(B) Lateral Inhibition image with  $\alpha=0.5$  and  $\beta=1$ (C) DOG-HPF Filtered image with  $\mu=0$  and  $\sigma=23$ .(D)The Test image  $[LSI_{img} - HPF_{img}]$ .

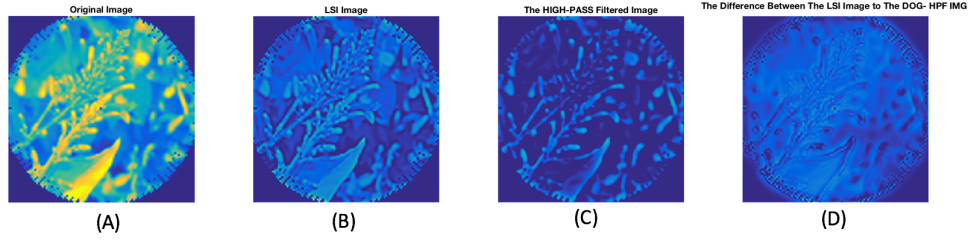


Figure 4-95: (A)The Flower original input image.(B) Lateral Inhibition image with  $\alpha=0.5$  and  $\beta=1$ (C) DOG-HPF Filtered image with  $\mu=0$  and  $\sigma=23$ .(D)The Test image  $[LSI_{img} - HPF_{img}]$ .

## 4.4 The Non-Uniform Model

For this model, we have used the Log-Polar Mapping method to mimic the non-uniform distribution of the receptors in the human visual system. Whereas, this pattern gives us two different regions of resolution (spatially variant pattern), and because of the way that the neuron receptors are taking to distribute over the retina. In other words, the retinal receptors are densely packed at the fovea, and their density decreases as the radial distance from the fovea increases. These characteristics result in data reduction and wide field of view while preserving the detailed information at the point of interest. The diameter of the receptive field size increases linearly with eccentricity. According to that we have built this model with specific dimensions to represent different radii and different angles, ([number of rings (Radii)-by-number of wedges (angles), NR x NW]). To sample the input grayscale image, we need to overlay our new pattern on the image of entry. Whereas, each sub-circle from the non-uniform pattern will be centered on a particular point of the picture and gathered all the information data underneath it. The average value of this information will be calculated, then will be mapped into a uniform ([U x V]) space. For example, the figure below represents the non-uniform pattern with size equals to  $[NR \times NW]$ , where  $NR$  equals two and  $NW$  equals to 4. The central circle represents the fovea part of the retinal area, where the uniform sampling is occurring. Thus, if we want to perform only the non-uniform sampling of the image, we need to remove this part (the fovea area) from the pattern, and that's what the following figures are illustrating, see figure 4-96. After, these points (the center-points) have set up on the image using the following expression. The Non-Uniform Mapping model with size  $[numberofringsnumbersofangles]$  have overlaid the input image, then all the information that positioning underneath each sub-circle will be extracted, see figure 4-97. As we mentioned earlier, the Foveal area will be removed from this model, to represent only the Retinal Mapping space (Th Non-Uniform Mapping Plane). The mean of these information from each sub-circle will be calculated and the result value will be placed on a Uniform  $[U \times V]$  plane, see the figure 4-98:

$$TheCentralPointoftheSubCircle = \frac{(Radius2 - Radius1)}{2} \quad (4.5)$$

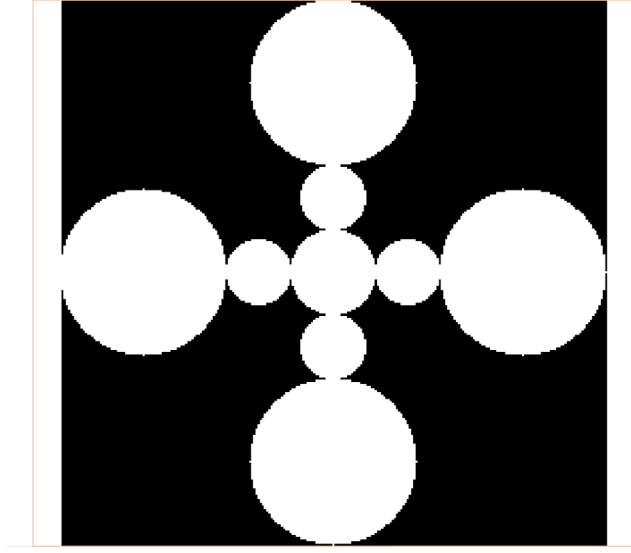


Figure 4-96: Illustration the Non-Uniform Circular Pattern with  $NRXNW = 2X4$ .

The spatial variant geometry of the sampling points is obtained through this space-variant sampling structure which is similar to the human retina. where this grid is formed by concentric circles with  $N_{ang} = 2 * N_{radii}$ . However, the fovea radius could be chosen equal to the minimum sampling period to cover all the image center without generate oversampling in the retinal plane [51]. If we want to obey to this constraint, then the radius of fovea equals to:

$$\rho_{Fovea} \geq \frac{N_{ang}}{2\pi} \quad (4.6)$$

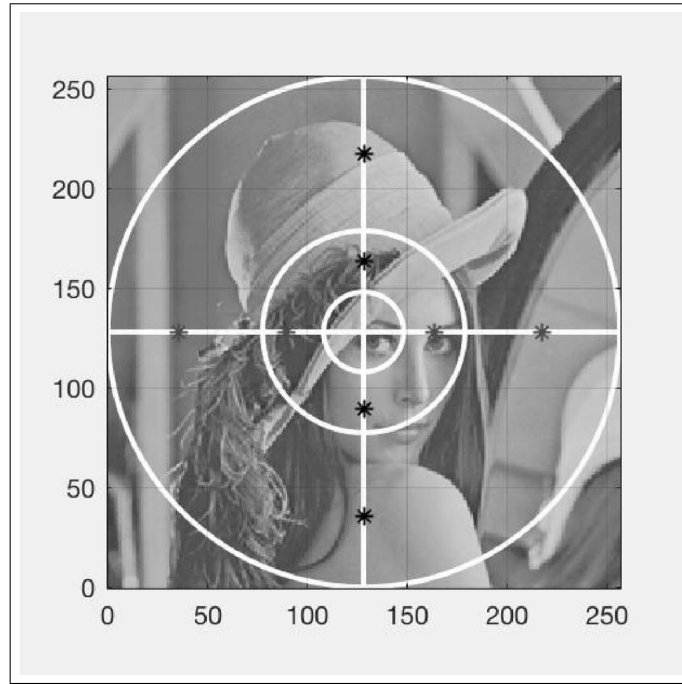


Figure 4-97: Lena Image after assigning the center-points of each Sub-Circle of the Previous Pattern.

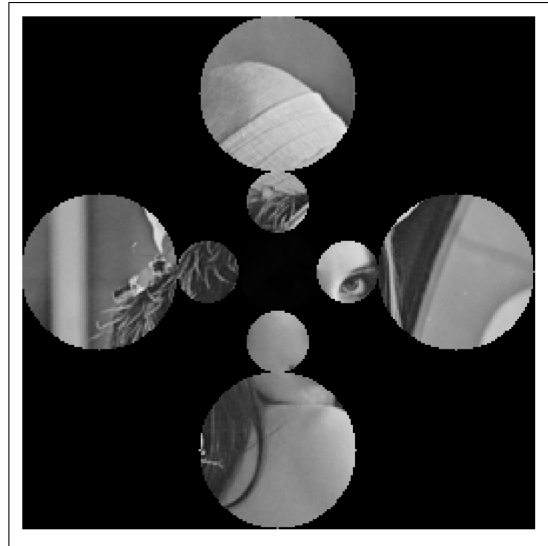


Figure 4-98: The Extracted Information from the Input Image based the Non-Uniform Mapping Model with size  $[2 \times 4]$ , Where, the Fovea Area has removed using equation 4.6 .



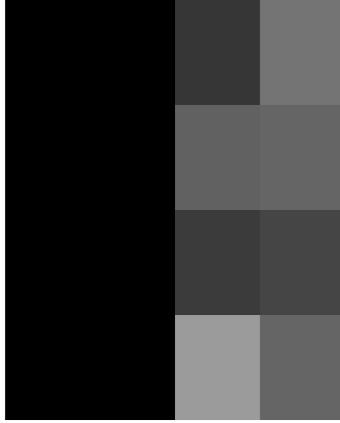


Figure 4-99: The Mean Value of each sub-circle has been calculated and placed on the exact position according to the Log-Polar Mapping Mathematical Representation see equations (3.1) and (3.2). The black part is representing the removed area of the nonuniform model (Fovea).

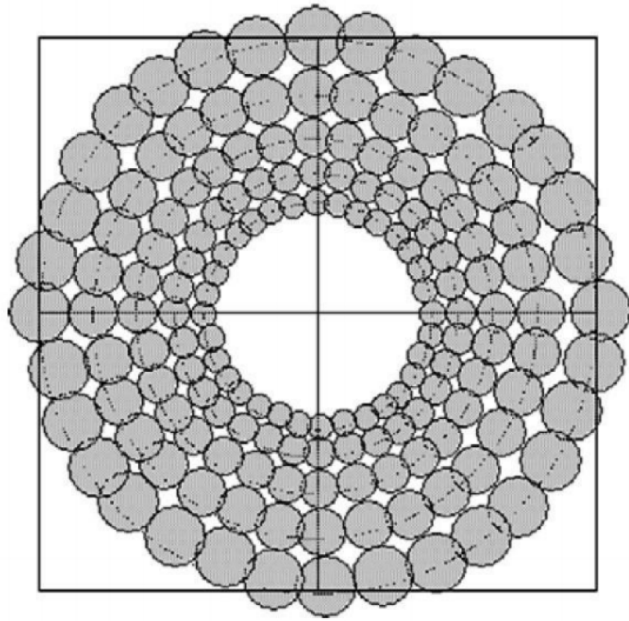


Figure 4-100: Illustration the distribution of the cone receptive fields along a concentric rings with different Radii in the HVS, [8].

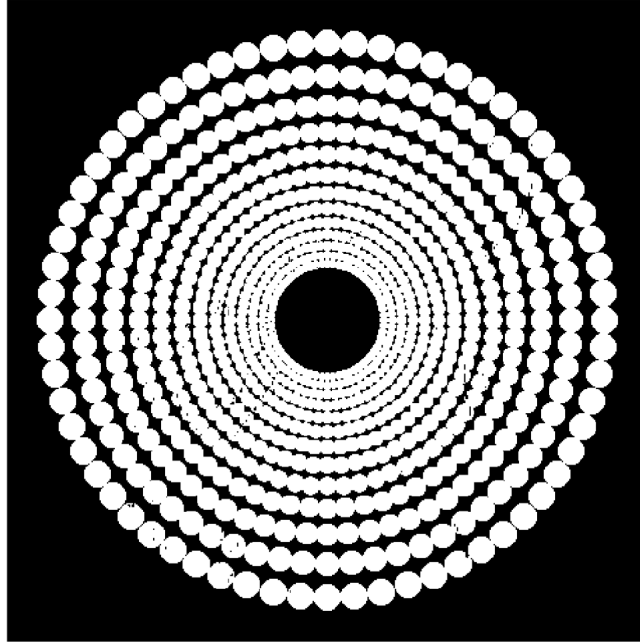


Figure 4-101: The Non-uniform Model to Mimic the HVS with size= $[numberofRings \times numberofangles = 32 \times 64]$ .

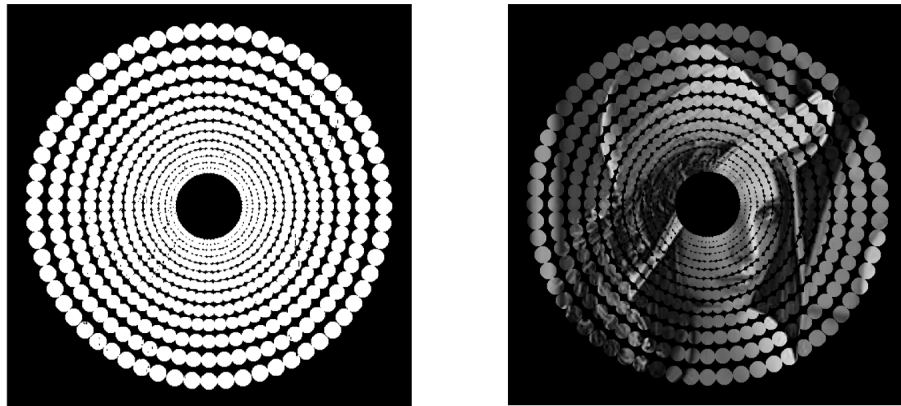


Figure 4-102: Representation of the relationship between the number of rings and the number of wedges  $[NR \times NW]$  to the fovea's radius depending upon the equation 4.6.

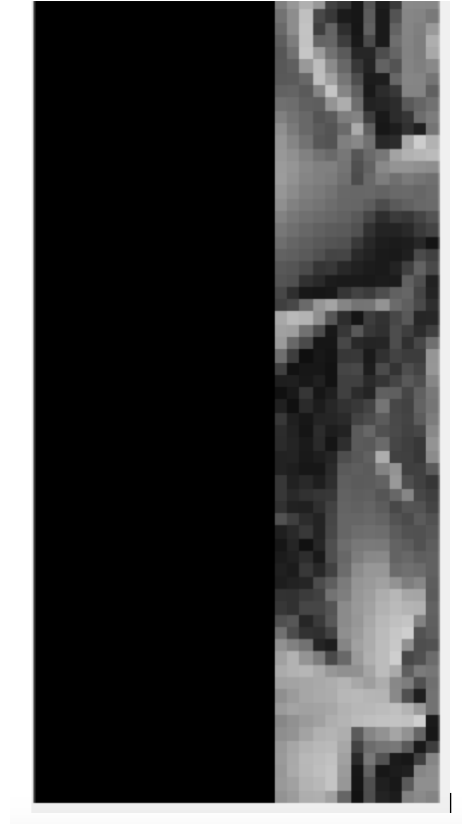


Figure 4-103: The Resultant output image with the Mean Values via the Non-Uniform Mapping, with size =  $[128 \times 64]$ .

The distinct functional advantages of the nonlinear (space variant) structure of the human visual system are that a wide range of visual resolution is provided, without massive cost that would be incurred by a spatially uniform high-resolution system. Since cortical magnification factor decreases by as much as 1.5-2 orders of magnitude from central fovea to far periphery, thus the foveal resolution was utilized, [23].

## 4.5 The Exponential Model's variables for the NON-Uniform Mapping Image:

In this section, Lateral Subtractive Inhibition phenomenon has been applied to non-uniform grayscale images. In other words, there are two processing tasks should be done before implementing this biological method on the model. First, obtain and read a symmetrical image, then insert it to the Log-Polar Mapping Transformation Method to sample the image non-uniformly. The sampled image within size equals to  $[nr \times nw]$ , has treated by the LSI mechanism for feature extraction and edge enhancement processing. [52] has introduced the sequence of these operations in his work, starting with mapping the image via log-polar transformation method then apply the lateral inhibition biological method to the mapped image. This sequence is most reasonable to represent the human visual system, where the retinal photo-receptors have sampled the captured scene then the retinal neurons are start competing to achieve the maximum amount of light intensity by inhibit the neighboring neurons and hence the lateral inhibition impact occurs. The simulation results via the LSI method will be represented in this section including the inverse image of the non-uniform model, as well. Since the spatial distance between the adjacent photo-receptors on the human retinal plane is exponentially increasing, thus we will use the same exponential model as the previous mapping model to calculate the the coupling coefficient matrix regarding a non-uniform interconnection distances between the photo-receptors. In order to apply the lateral inhibition method on the non-uniform mapped image, the numerical values for alpha  $\alpha$  and beta  $\beta$  variables regarding the mathematical expression in 2.6 have to identified first to obtain the desired lateral inhibition output image with the edge enhancement and perceived information beyond the edges, same as the previous model. Since the spatial distances between the neuron photo-receptors of this Model are different, definitely the impact of Lateral Inhibition biological method is different too.

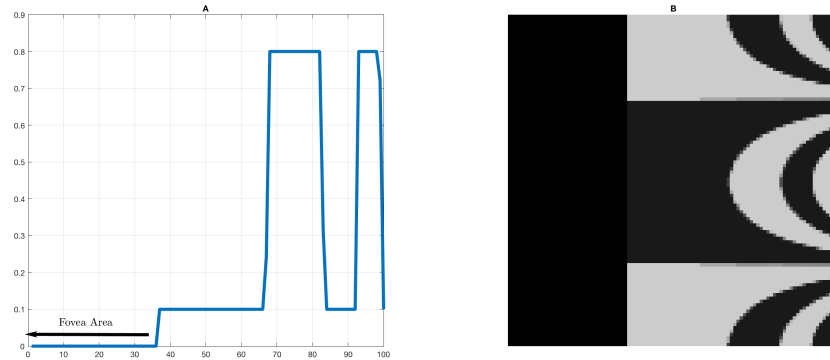


Figure 4-104: (A) The Cross Section Profile of The Original Image. (B) The Original Synthetic Image.

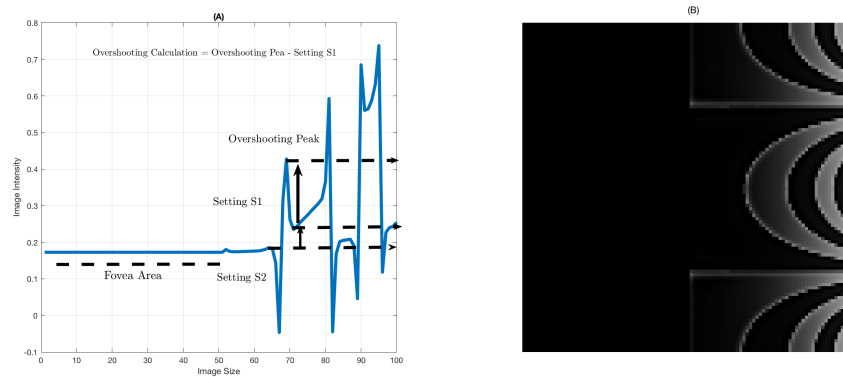


Figure 4-105: (A) The Cross Section Profile of The LSI Image. (B) The LSI Image.

In order to identify these two variables the same synthetic image as the uniform model will be used. However in this time, the log-polar mapping pattern (non-uniform model) will be applied to that synthetic image within specific dimension, then the calculation will be made depending on the overshooting peaks and the differential distance between the two settings (represents the differential between two intensity levels of the image). Figure 4-104 represents the original mapped image. Since the distribution of the photo-receptors is different in this model, definitely the exponential model's variables will be different too since they are directly related to interconnection distances

between these receptors. The following section will illustrate how is an alpha parameter impact on the resultant LSI image and which numerical value gives the most desirable image based on the overshooting edges and the relative information enhancement as well.

#### 4.5.1 Alpha ( $\alpha$ ) parameter for the NON-Uniform Model:

For consistency purposes with the Uniform model, we have assigned (0.5) by default for beta  $\beta$  variable while alpha will changed within specific range of numbers, see the following figures from 4-106 to figure 4-114. As we can see from the figure 4-106, the output image is not affected by the

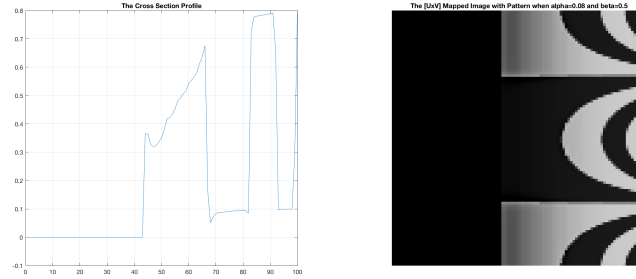


Figure 4-106: (A) The Cross Section Profile of The LSI Image. (B) The LSI Image With  $\beta=0.5$  and  $\alpha=0.08$ .

lateral inhibition method, this is because of the exponential model's parameters. In order to find out which variable we should change one of them to obtain the actual impact of lateral inhibition method (edge enhancement). We have reduced a beta  $\beta$  parameter first to be equals to (0.05) and maintaining the same value of alpha. Then a reasonable output image will obtained in the following figure, see figure 4-107. According to this figure above, we will consider (0.05) value to represent beta  $\beta$  variable in the exponential model for this mapping model and changing alpha  $\alpha$  parameter to find out a good value to obtain the reasonable image regarding this model.

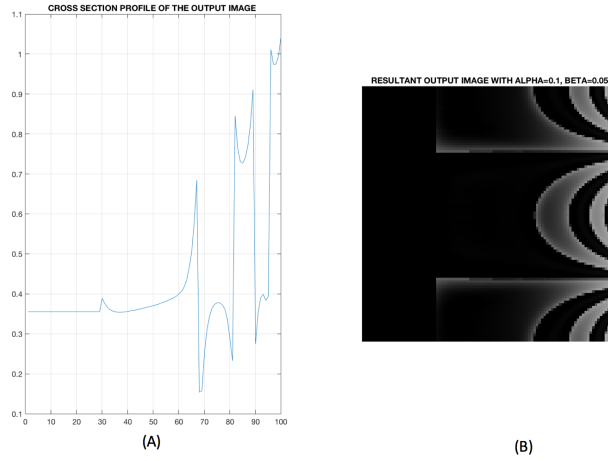


Figure 4-107: (A) The Cross Section Profile of The LSI Image. (B) The LSI Image With  $\beta=0.05$  and  $\alpha=0.1$ .

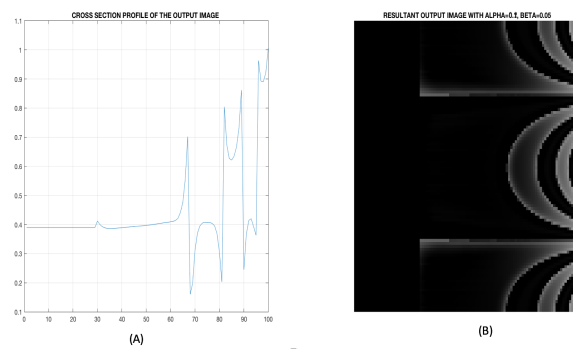


Figure 4-108: (A) The Cross Section Profile of The LSI Image. (B) The LSI Image With  $\beta=0.05$  and  $\alpha=0.2$ .

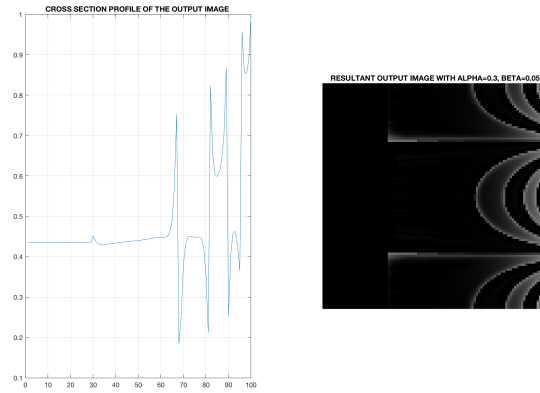


Figure 4-109: (A) The Cross Section Profile of The LSI Image. (B) The LSI Image With  $\beta=0.05$  and  $\alpha=0.3$ .

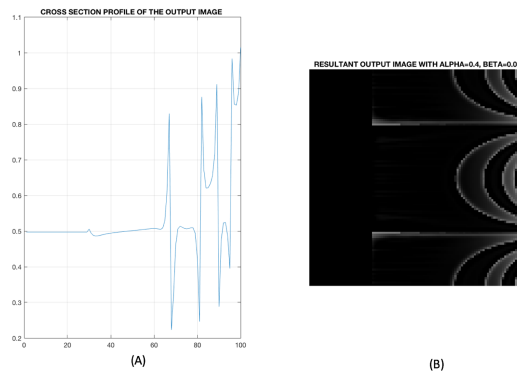


Figure 4-110: (A) The Cross Section Profile of The LSI Image. (B) The LSI Image With  $\beta=0.05$  and  $\alpha=0.4$ .

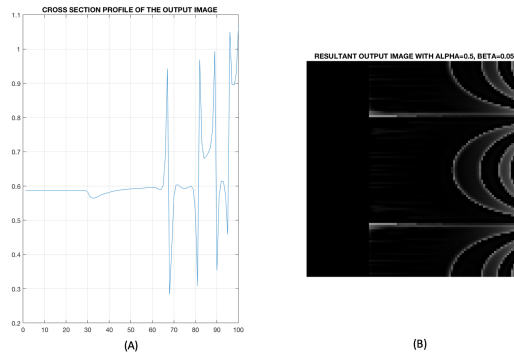


Figure 4-111: (A) The Cross Section Profile of The LSI Image. (B) The LSI Image With  $\beta=0.05$  and  $\alpha=0.5$ .



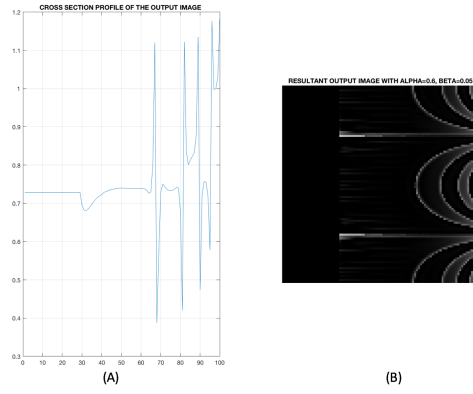


Figure 4-112: (A) The Cross Section Profile of The LSI Image. (B) The LSI Image With  $\beta=0.05$  and  $\alpha=0.6$ .

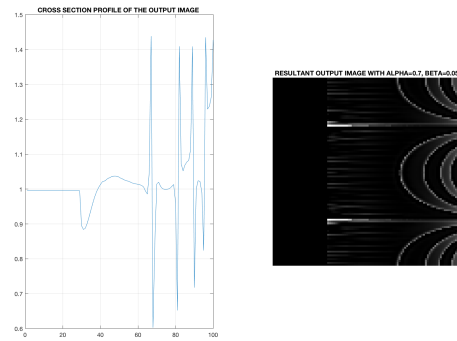


Figure 4-113: (A) The Cross Section Profile of The LSI Image. (B) The LSI Image With  $\beta=0.05$  and  $\alpha=0.7$ .

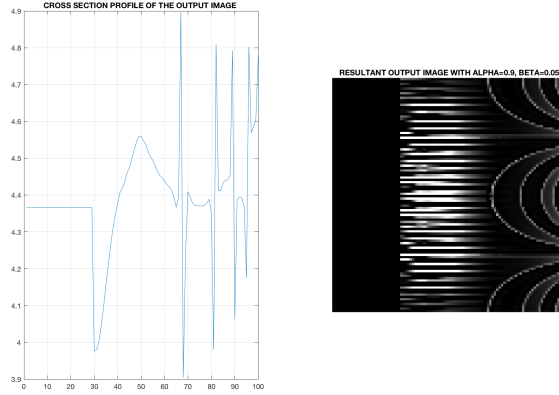


Figure 4-114: (A) The Cross Section Profile of The LSI Image. (B) The LSI Image With  $\beta=0.05$  and  $\alpha=0.9$ .

An observation has made according to all these figures shown above regarding this section, which is that an alpha parameter ( $\alpha$ ), has a direct impact on the edge enhancement (Overshooting peaks) and that similar to what we had in the uniform model. However, for this mapping model a beta parameter ( $\beta$ ), should be lower than an alpha parameter in order to achieve a desired output image based on a lateral inhibition biological method with the edge enhancement and the perceived information. In this experiment, different numerical values have been tested to represent an alpha parameter while a beta is being constant to investigate the effect of this particular variable on the resultant image. The following two curves in figure 4-115 and 4-116, have been generated to illustrate the relationship between an alpha parameter with the enhancement of an overshooting peaks as well as to the differential intensities between these two peaks of the image which represents the perceived information beyond the edges based on a lateral inhibition biological method. From these two figures, we have noticed that an alpha parameter has a direct impact on the overshooting edges. In other words, the contrast enhancement is rising when an alpha parameter is increasing as well. However, that would decrease the relative information beyond these boundaries until we almost lost all the important details from the original image, see figure 4-114, where it represents the highest value of an alpha variable regarding this mapping model. Therefore, the proper numerical value has to be chosen according to the edge enhancement as well as maintaining the necessary

information that is related to these contrasts to obtain the desire LSI image. Depending on all these results of this section,  $\alpha = 0.3$ , value has chosen to represent an alpha parameter in an exponential model for this mapping design.

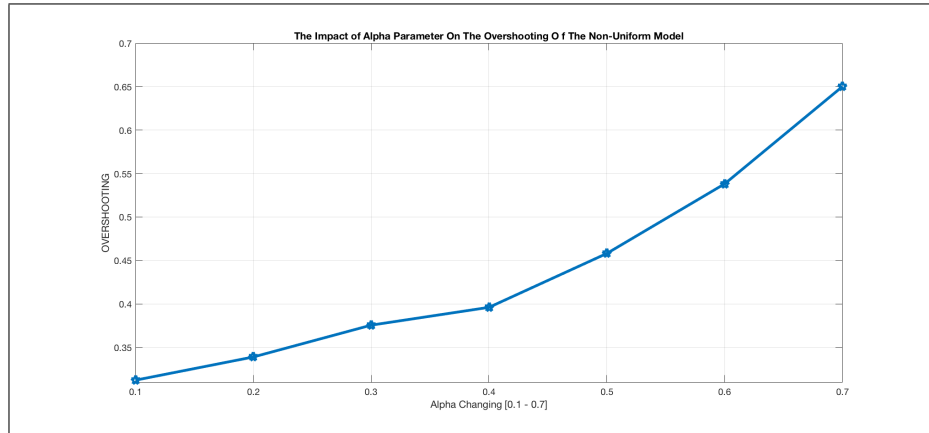


Figure 4-115: Illustrating The Relationship Between an Alpha Parameter  $\alpha$  to the Overshooting Peak Enhancement. When Beta  $\beta=0.05$  and Alpha  $\alpha$  is changing within the range of  $[0.1 - 0.7]$ .

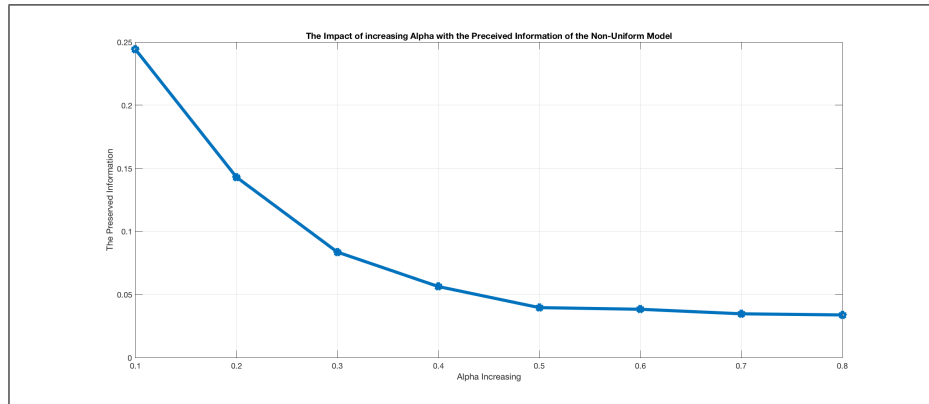


Figure 4-116: Represents The Impact of  $\alpha$  Parameter on the Differential of the Intensities of the Resultant Output Image with Changing Alpha  $[0.1-0.7]$ .

### 4.5.2 Beta ( $\beta$ ) parameter for Non-Uniform Model:

The same procedures and image will be used to test the second variable of an exponential model which a beta  $\beta$  and to make sure that a(0.05) is the numerical value that gives a proper lateral inhibition resultant image. In this section we have fixed an alpha parameter  $\alpha$  and make it equals to (0.3) depending on the previous section and changing a beta  $\beta$  variable within specific range of numbers starting from (0.01) until (0.1).

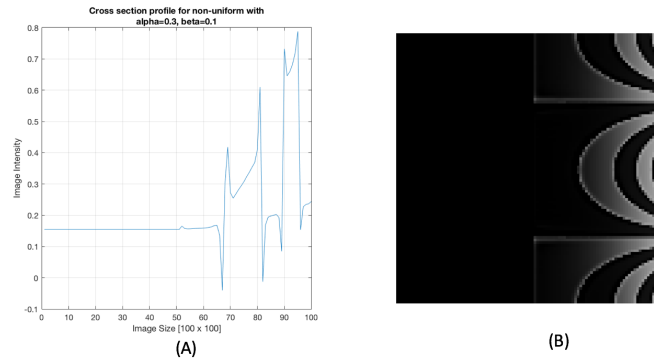


Figure 4-117: (A) The Cross Section Profile of The LSI Image. (B) The LSI Image With  $\beta=0.1$  and  $\alpha=0.3$ .

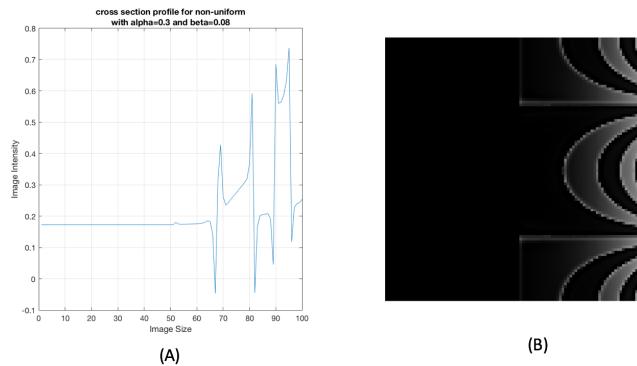


Figure 4-118: (A) The Cross Section Profile of The LSI Image. (B) The LSI Image With  $\beta=0.08$  and  $\alpha=0.3$ .

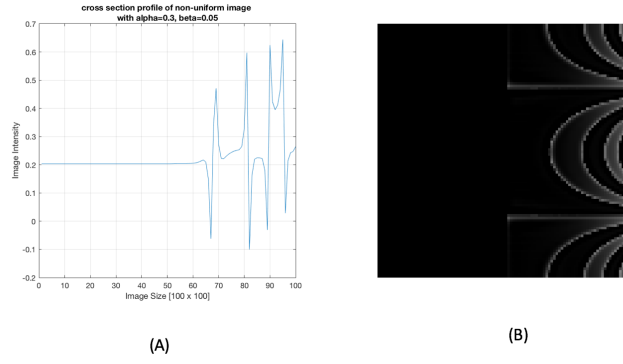


Figure 4-119: (A) The Cross Section Profile of The LSI Image. (B) The LSI Image With  $\beta=0.05$  and  $\alpha=0.3$ .

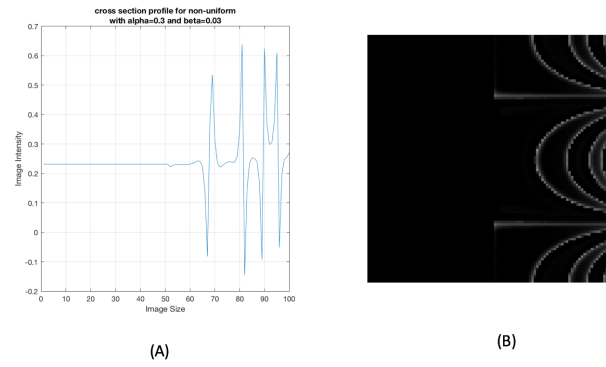


Figure 4-120: (A) The Cross Section Profile of The LSI Image. (B) The LSI Image With  $\beta=0.03$  and  $\alpha=0.3$ .

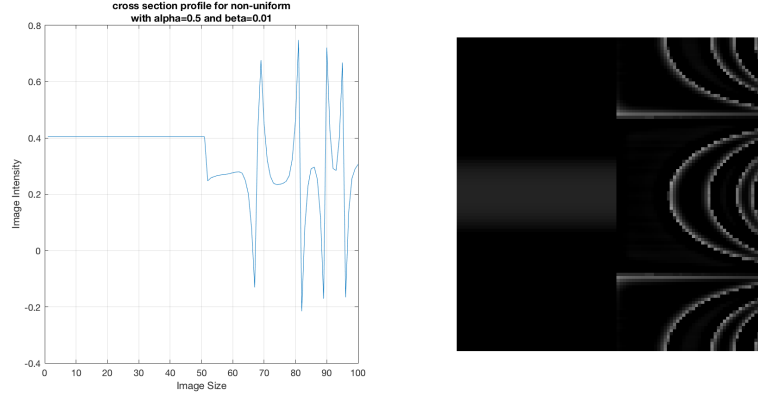


Figure 4-121: (A) The Cross Section Profile of The LSI Image. (B) The LSI Image With  $\beta=0.01$  and  $\alpha=0.3$ .

According to all the previous figures of this section, an observation has made, that a beta parameter should always be lower than an alpha variable to obtain the desired edge enhancement and perceived information via the Lateral Inhibition. Additionally, the increment of a beta parameter will reduce the overshooting and undershooting peaks of the output image, see figure 4-122. Therefore, a value of (0.05) has used to represent a beta ( $\beta$ ) variable in the exponential equation for this model since it gives a good results regarding the information extracted beyond the boundaries as well improving the edge, see figure 4-123. The following two figures are shown below, figure 4-124 and 4-125, represent the impact of a beta variable on the edge enhancement as well as the preserved information beyond the contrast. As we can see from these two curves below, that as beta increases the enhancement of the image contrast decreases. While this increment improves the relevant data between the edges.

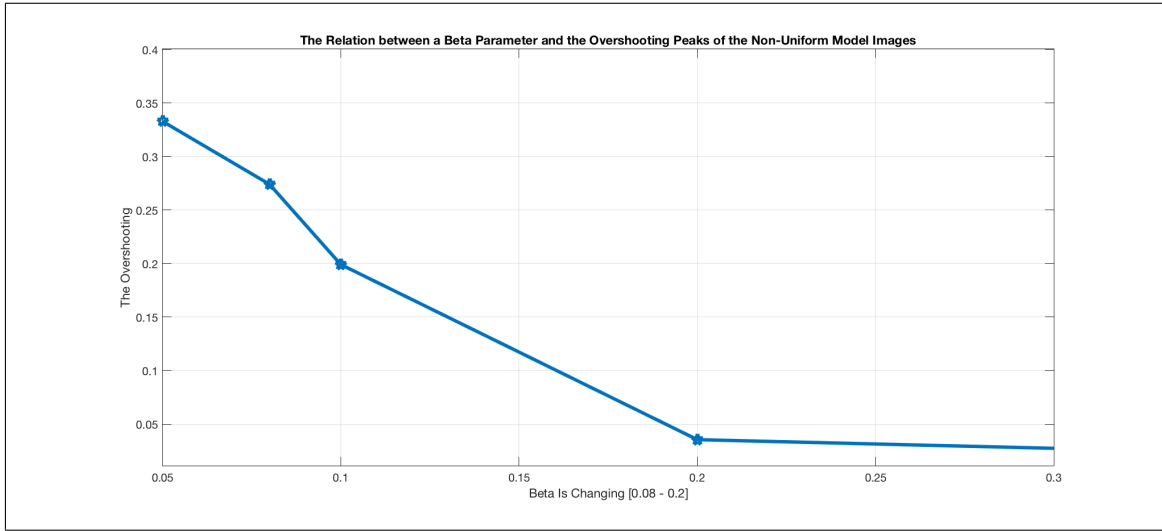


Figure 4-122: The Impact of Beta  $\beta$  parameter on the Overshooting Peaks of the Lateral Inhibition Image when Alpha  $\alpha = 0.3$ .

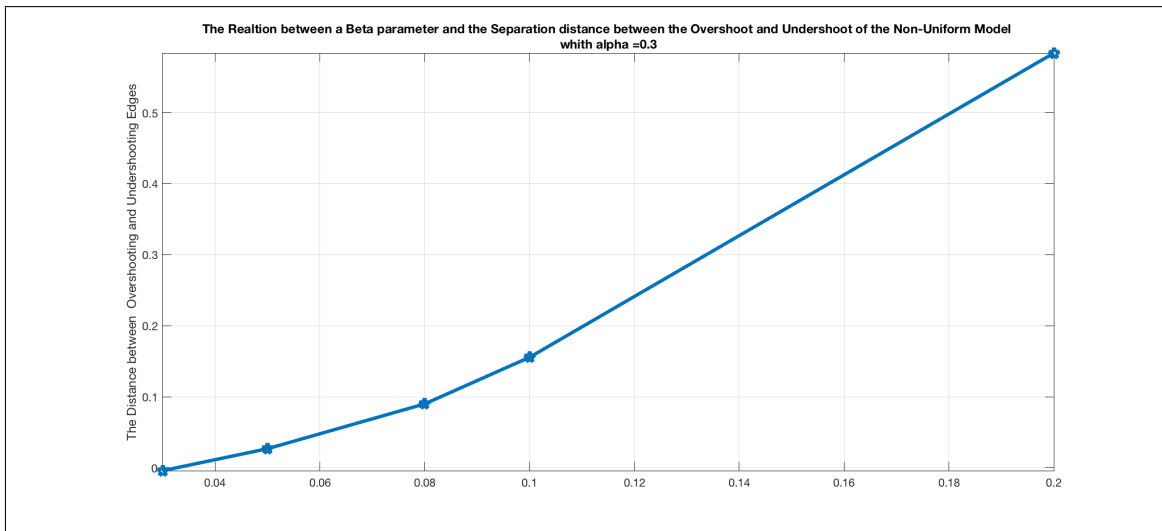


Figure 4-123: The Impact of Beta  $\beta$  parameter on the Differential Intensities of the Lateral Inhibition Image when Alpha  $\alpha=0.3$ .

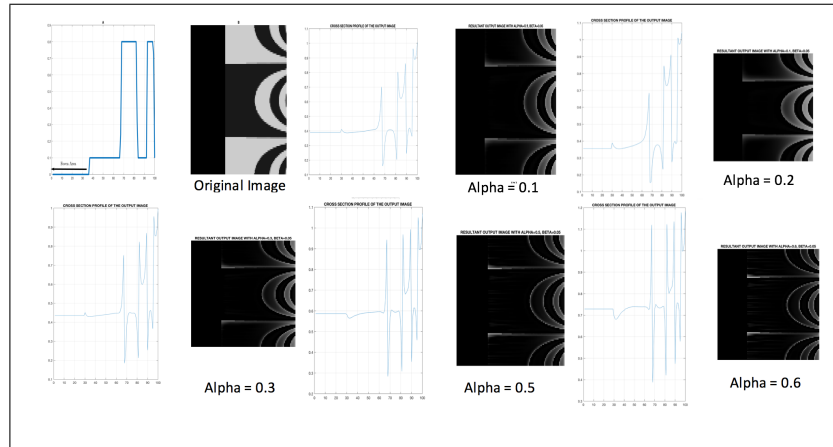


Figure 4-124: Different Cases of Alpha from [0.1 to 0.6] While Beta = 0.05.

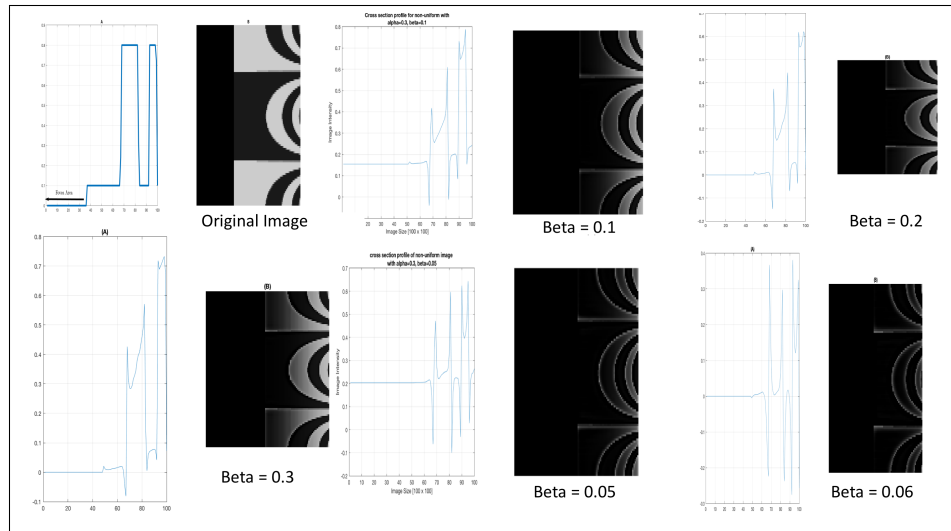


Figure 4-125: Different Cases of Beta While Alpha = 0.3.



## 4.6 The Simulation Results of the Non-Uniform Model Based Lateral Inhibition

According to figure 4-1, the new pattern has started with Log-Polar Mapping Transformation method to obtain the non-uniformly distribution of the photo-receptors. A uniform mapped image is achieved by taking the average value of each sub-circle of the new design and reorganizing them in a consistent way. The lateral Inhibition biological will be applied on the mapped image to investigate its effect on the new model. As we mentioned earlier, the spatial distance between the adjacent photo-receptors increases in an exponential way and the inhibition effect between these receptors decrease in the same way as we go farther from the center point of the pattern (the Fovea area). To be consistent with the uniform model, we shall start our simulation regarding this model with the synthetic images; then the real pictures will be represented. For the Synthetic image, where the size of an input image is  $[500 \times 500]$ , while the scale of the output Mapped image will be depending on the number of rings versus the number of angles,  $[64 \times 128]$ . Then the inverse of the mapped image has been presented to compare the original image efficiently, [ the inverse mapped image and the Lateral Inhibition Inverse Mapped image]. As mentioned earlier, the fovea part of the retinal plane perform the Uniform sampling on the picture. However, the purpose of this section is to show the advantage of the non-uniform sampling only. Therefore, the fovea area will be removed, and only the retina region will be represented in this new pattern. The fovea radius has been calculated via a particular mathematical relationship which we have already explained earlier in this chapter, see the mathematical description in 4.6. The following Images illustrating the effectiveness of Lateral Inhibition biological phenomenon on the Non-Uniform model via Synthetic Images. The black section of the nonuniform pattern is representing the removed fovea.

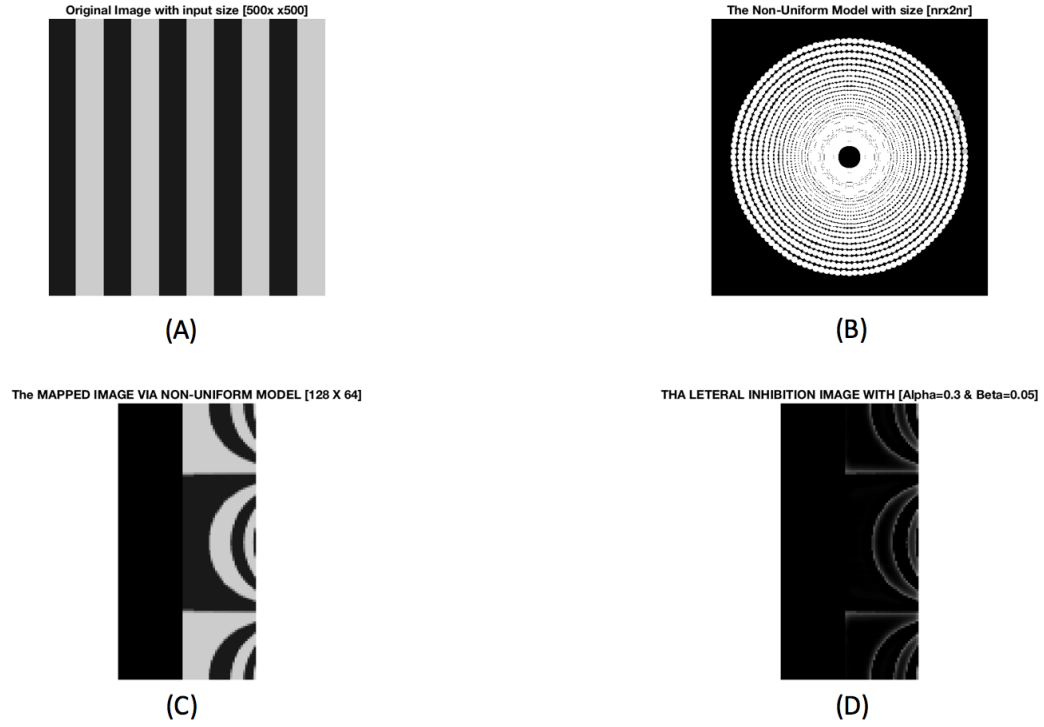


Figure 4-126: (A) The Synthetic Input Image of Two Gray Intensity Levels with Size [500 x 500]. (B) The Non-uniform Mapping Model via LPT Method with Size [64 x 128]. (C) The Uniform [UxV] Mapped Image via LPT Method. (D) The Lateral Inhibition Method with Alpha  $\alpha=0.3$  and Beta  $\beta=0.05$ .

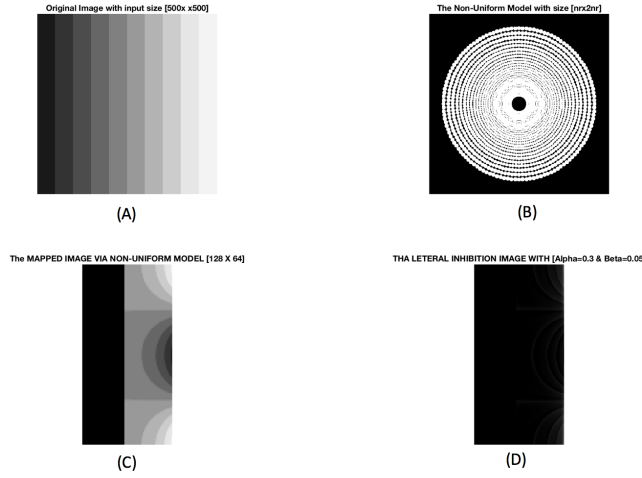


Figure 4-127: (A)The Synthetic Staircase grayscale Input Image with with Size [500 x 500]. (B) The Non-uniform Mapping Model via LPT Method with Size [64 x 128]. (C)The Uniform  $[UxV]$  Mapped Image via LPT Method. (D) The Lateral Inhibition Method with Alpha  $\alpha=0.3$  and Beta  $\beta=0.05$ .

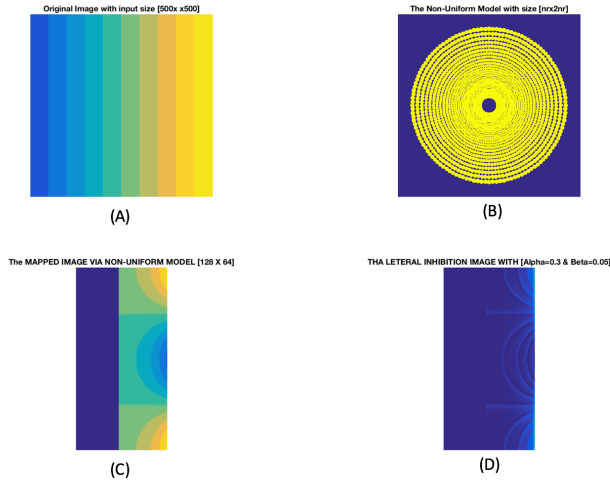


Figure 4-128: (A)The Colored Version of Synthetic Staircase grayscale Input Image with with Size [500 x 500]. (B) The Non-uniform Mapping Model via LPT Method with Size [64 x 128]. (C)The Uniform  $[UxV]$  Mapped Image via LPT Method. (D) The Lateral Inhibition Method with Alpha  $\alpha=0.3$  and Beta  $\beta=0.05$ .

The wrapped back version of the mapped image will be obtaining by using a log-polar circular grid within a number of circles that increasing logarithmically and the number of wedges increases uniformly. Then, the sampled image via the LPT method and resultant mean value of each particular sub-circle, see figure 4-103, will be re-organized in a circular pattern depending on their coordinates (x and y position on the  $uxv$  mapped image). For more explanation see the figure 4-129 below. As we can see from this figure, that the sub-circle of the wrapped back circular pattern, (4-129C), is containing the mean value of the image data related to the same sub-circle within a same location of the forward circular pattern, (4-129A). As we mentioned earlier, that the advantage of this design is providing a wide field of view while maintaining the necessary details from the point of interest. In other words, as we move farther from the center point of the circular pattern (the fovea area where is the uniform sampling occurred), the detailed information will be less and less, and the mean value of each sub-circle will be shrinking too while the radius of the sub-circles is increasing in an exponential way thus a blurry image detailed can be achieved at the periphery region of this pattern ( we can't visualize that from this figure below, because of the dimension size of this pattern is too small [20x40]. However, we shall observe this difference of the resolution on the following figures.

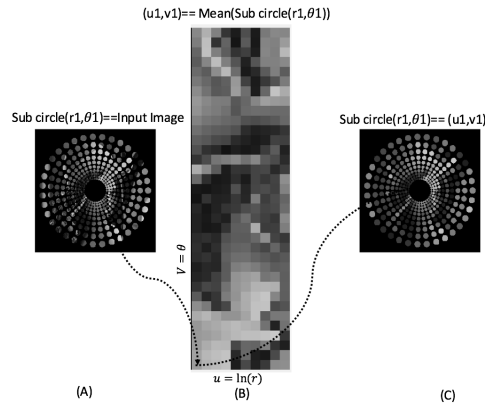


Figure 4-129: (A)The Image after Combining The non-uniform Mapping Model and The Original Image. (B).The Mean Value Image After Mapping The Original One with size  $[NR \times NW]$ . (C) The Wrapped Back Image with The Mean Values From the  $[U \times V]$  Mapped Image With The Same Size As The Non-uniform Circular Pattern.

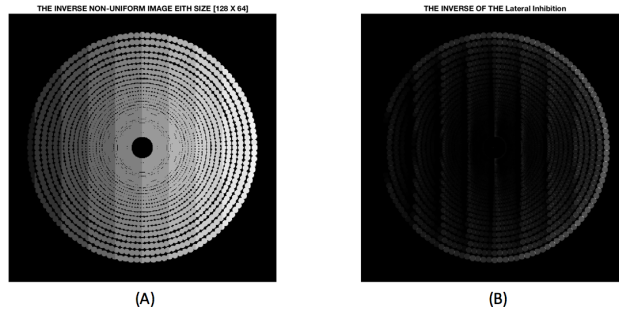


Figure 4-130: (A)The Wrapped Back Version of Synthetic Staircase Input Image. (B)The Lateral Inhibition Image of The Reverse Non-uniform Mapped image.

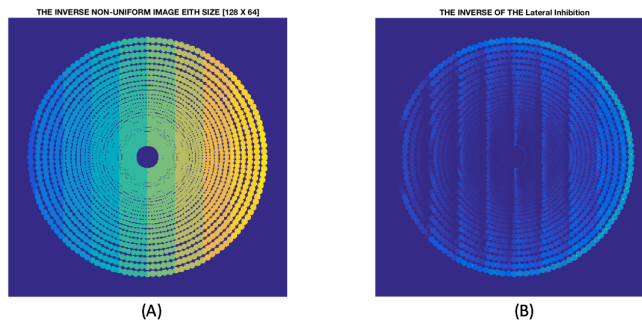


Figure 4-131: (A)The Wrapped Back Version of Synthetic Staircase Input Image. (B)The Lateral Inhibition Image of The Reverse Non-uniform Mapped image.

The real image with input size equals to  $[500 \times 500]$  will be processed based on log-polar mapping method in order to sample the image non-uniformly with in two area of resolutions, see the following image results. Then the new coupling coefficient matrix for the lateral inhibition biological algorithm will be obtained based on an exponential model with specific numerical values for an alpha and beta. The output mapped image size will be same as the mapped synthetic image which is equals to  $[nr = 64 \times nw = 128]$  and the radius of Fovea =  $\frac{NW}{2\pi}$ . While the reversed version of the mapped image will be the same size as the original one.

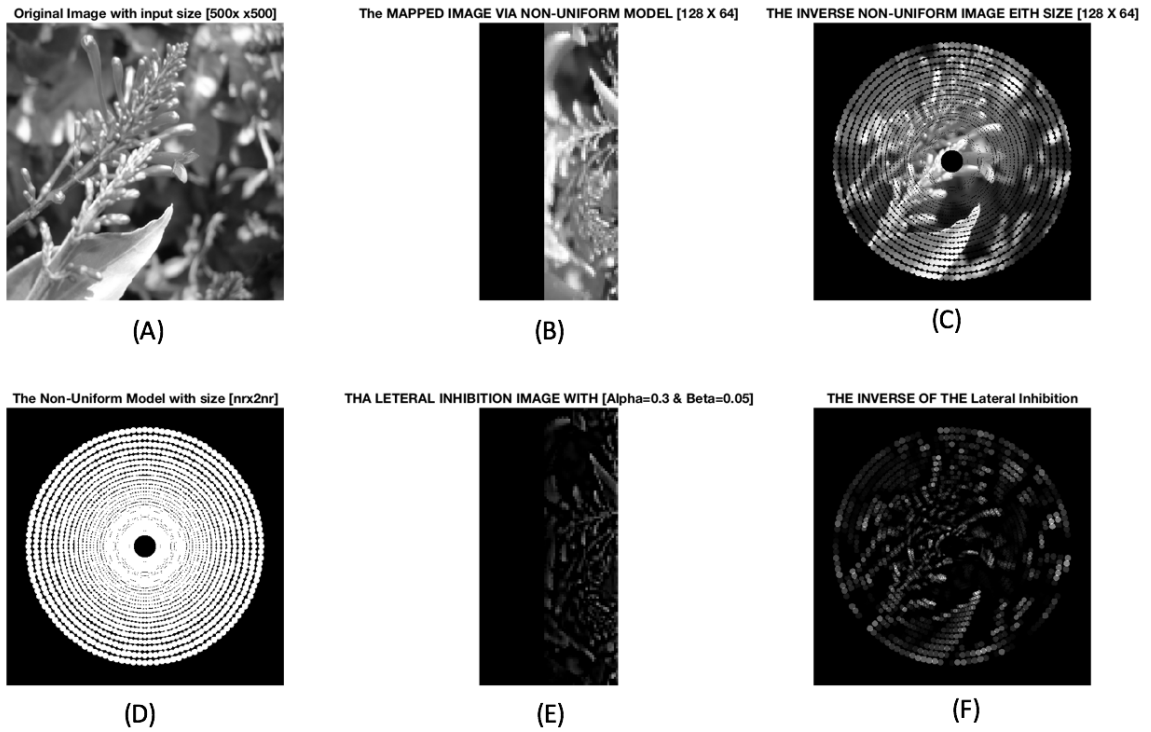


Figure 4-132: (A)The Flower Input Image with Size  $[500 \times 500]$ . (B) The  $[UxV]$  Mapped Image Based on Log-Polar Mapping Method. (C) The Wrapped Back Image with Size  $[500 \times 500]$ . (D)The Non-Uniform Mapped Pattern with Dimension  $[128 \times 64]$ . (E)The Lateral Inhibition Method of the Forward Image with size  $[128 \times 64]$ . (F)The Lateral Inhibition Image of the Reversed mapped image.

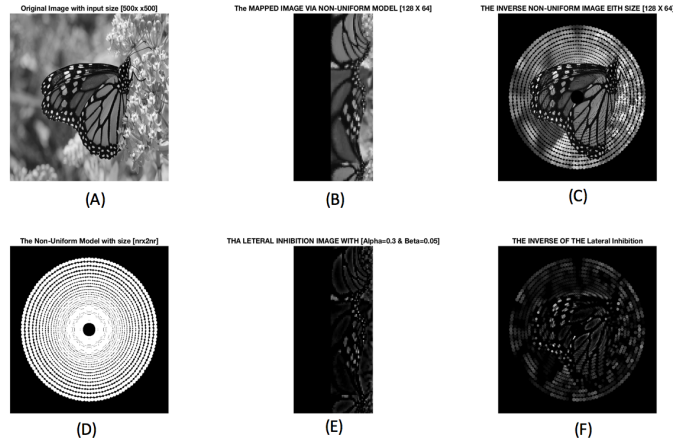


Figure 4-133: (A)The Butterfly Input Image with Size [500x500].(B) The  $[UxV]$  Mapped Image Based on Log-Polar Mapping Method.(C) The Wrapped Back Image with Size [500x500]. (D)The Non-Uniform Mapped Pattern with Dimension [128 x 64].(E)The Lateral Inhibition Method of the Forward Image with size [128x64]. (F)The Lateral Inhibition Image of the Reversed mapped image.

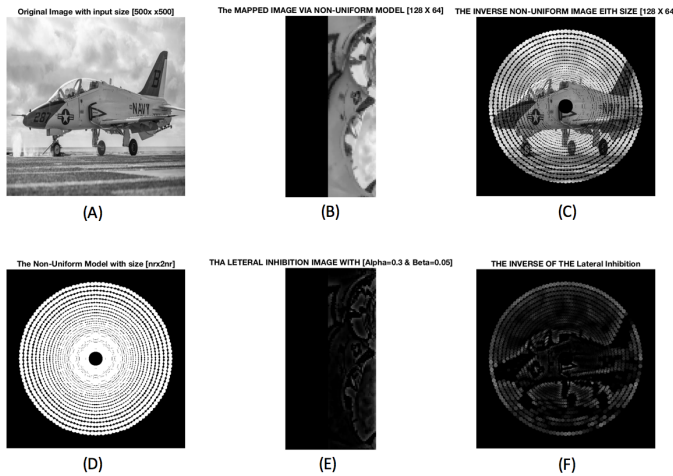


Figure 4-134: (A)The Jet Input Image with Size [500x500].(B) The  $[UxV]$  Mapped Image Based on Log-Polar Mapping Method.(C) The Wrapped Back Image with Size [500x500]. (D)The Non-Uniform Mapped Pattern with Dimension [128 x 64].(E)The Lateral Inhibition Method of the Forward Image with size [128x64]. (F)The Lateral Inhibition Image of the Reversed mapped image.

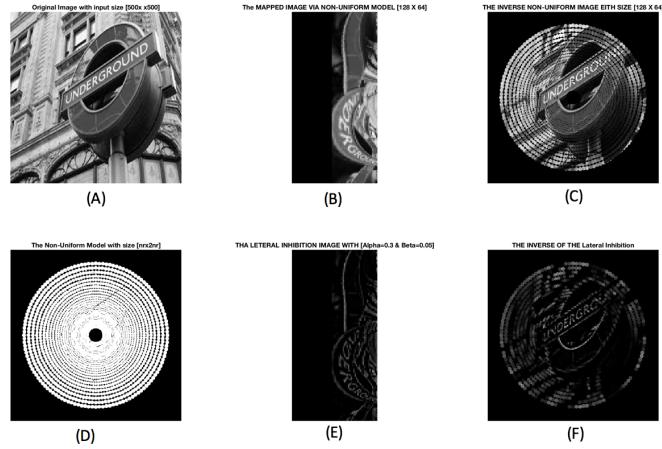


Figure 4-135: (A)The Word Input Image with Size [500x500].(B) The  $[UxV]$  Mapped Image Based on Log-Polar Mapping Method.(C) The Wrapped Back Image with Size [500x500]. (D)The Non-Uniform Mapped Pattern with Dimension [128 x 64].(E)The Lateral Inhibition Method of the Forward Image with size [128x64]. (F)The Lateral Inhibition Image of the Reversed mapped image.

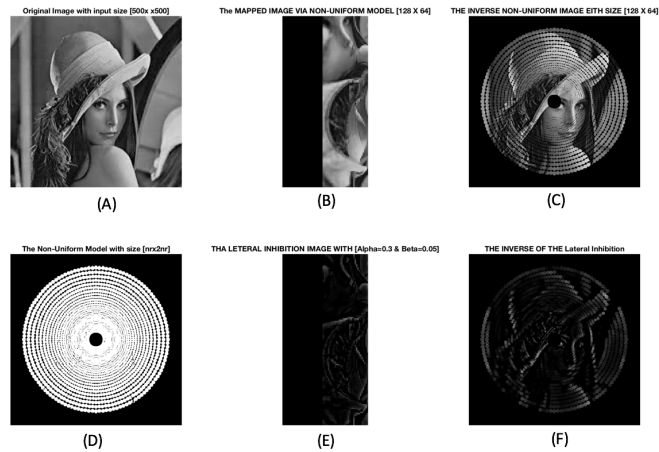


Figure 4-136: (A)The Lena Input Image with Size [500x500].(B) The  $[UxV]$  Mapped Image Based on Log-Polar Mapping Method.(C) The Wrapped Back Image with Size [500x500]. (D)The Non-Uniform Mapped Pattern with Dimension [128 x 64].(E)The Lateral Inhibition Method of the Forward Image with size [128x64]. (F)The Lateral Inhibition Image of the Reversed mapped image.



## 4.7 The Filtration Process of the Non-Uniform Model based on the Multiple Spatial Frequency Channels (CSF):

As we mentioned in figure 3-2, the next step will be the filtration process via the Multiple Spatial Frequency channels applied to the non-uniform Mapped image and to the wrapped back version of the mapped image, respectively. Then, the Comparison between the resultant image via the natural method to the picture processed by the three spatial-frequency filters will be illustrated as a picture figures in grayscale and the color space as well, see the figures from 4-137 to figure 4-145. The purpose of this calculation is to calculate the difference information between the Lateral Inhibition image and the Filtered image. The same frequency range of the multiple spatial-frequency channels that has been used for the previous model will be employed here in this mapping model too. The following figures illustrate the simulation results regarding the Forward nonuniform  $[UV]$  mapped image.

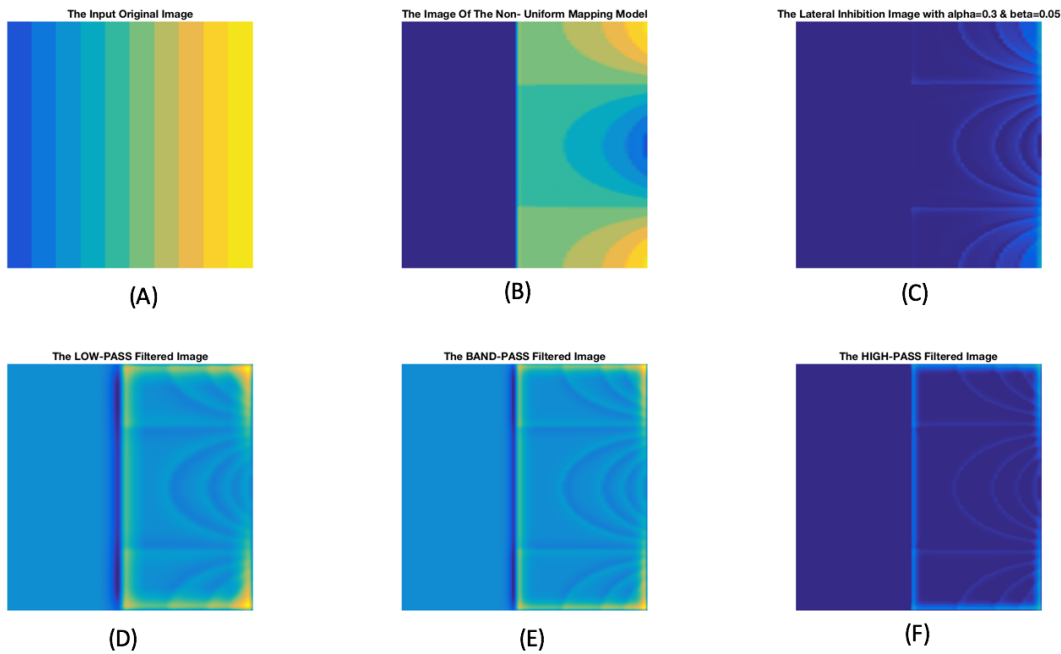


Figure 4-137: (A)The Original Input Image. (B) The Non-Uniform Sampling of Synthetic Staircase Image. (C) The Lateral Inhibition Synthetic Image with  $[\alpha = 0.3 \text{ and } \beta = 0.05]$ . (D) The Filtered Image via DOG-LPF. (E) The Filtered Image via DOG-BPF. (F) The Filtered Image via DOG-HPF.

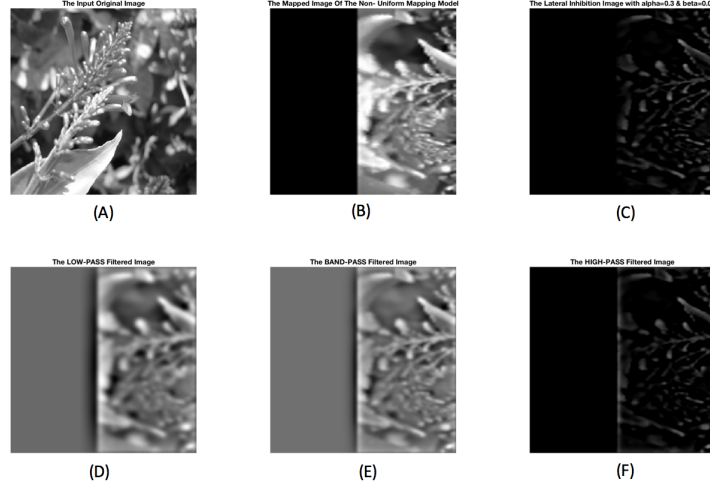


Figure 4-138: (A)The Original Input Image. (B) The Non-Uniform Sampling of Synthetic Staircase Image. (C) The Lateral Inhibition Synthetic Image with  $[\alpha = 0.3 \text{ and } \beta = 0.05]$ . (D) The Filtered Image via DOG-LPF. (E)The Filtered Image via DOG-BPF. (F)The Filtered Image via DOG-HPF.

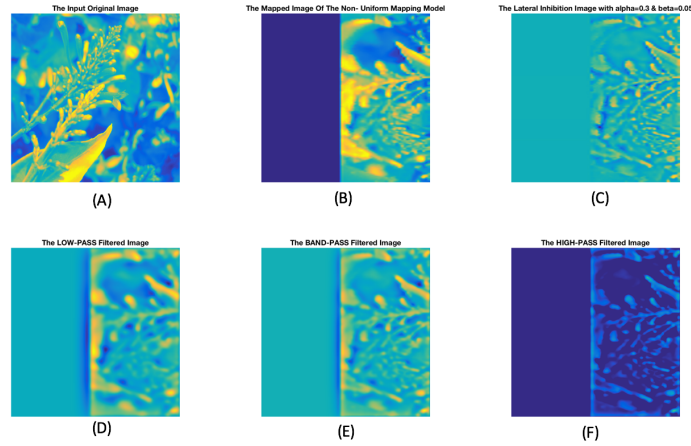


Figure 4-139: (A)The Original Input Image. (B) The Non-Uniform Sampling of Synthetic Staircase Image. (C) The Lateral Inhibition Synthetic Image with  $[\alpha = 0.3 \text{ and } \beta = 0.05]$ . (D) The Filtered Image via DOG-LPF. (E)The Filtered Image via DOG-BPF. (F)The Filtered Image via DOG-HPF.

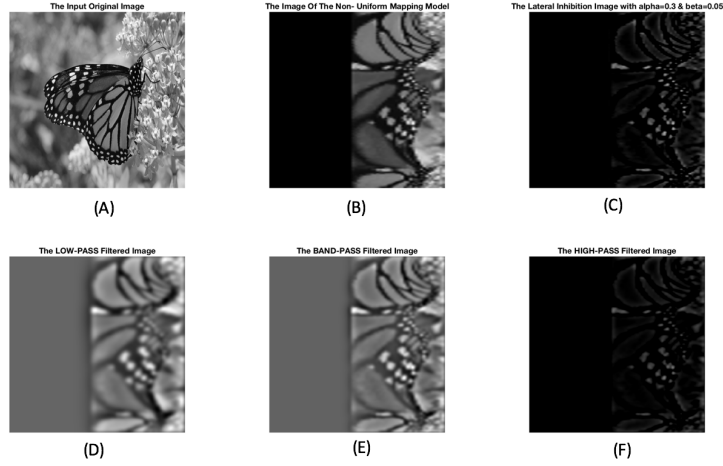


Figure 4-140: (A)The Original Input Image. (B) The Non-Uniform Sampling of Butterfly Real Image. (C) The Lateral Inhibition Real Image with  $[\alpha = 0.3 \text{ and } \beta = 0.05]$ . (D) The Filtered Image via DOG-LPF. (E)The Filtered Image via DOG-BPF. (F)The Filtered Image via DOG-HPF.

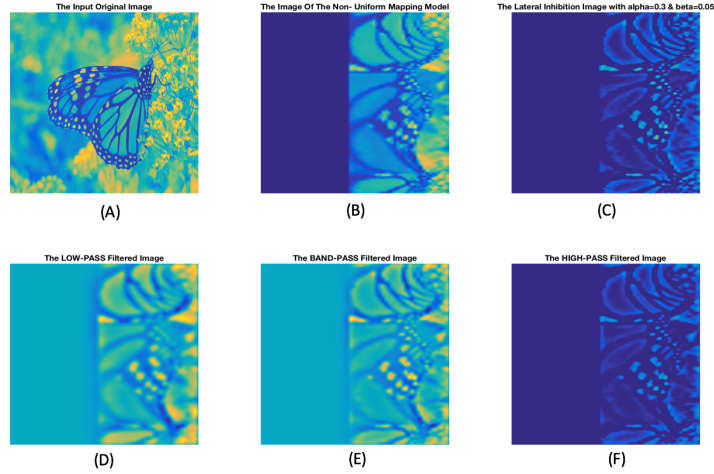


Figure 4-141: (A)The Original Input Image. (B) The Non-Uniform Sampling of Butterfly Real Image. (C) The Lateral Inhibition Real Image with  $[\alpha = 0.3 \text{ and } \beta = 0.05]$ . (D) The Filtered Image via DOG-LPF. (E)The Filtered Image via DOG-BPF. (F)The Filtered Image via DOG-HPF.

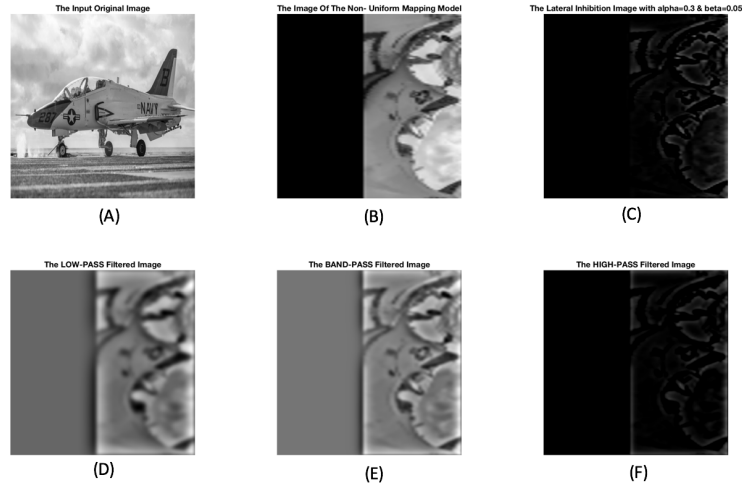


Figure 4-142: (A)The Original Input Image. (B) The Non-Uniform Sampling of Jet Real Image. (C) The Lateral Inhibition Real Image with  $[\alpha = 0.3 \text{ and } \beta = 0.05]$ . (D) The Filtered Image via DOG-LPF. (E)The Filtered Image via DOG-BPF. (F)The Filtered Image via DOG-HPF.

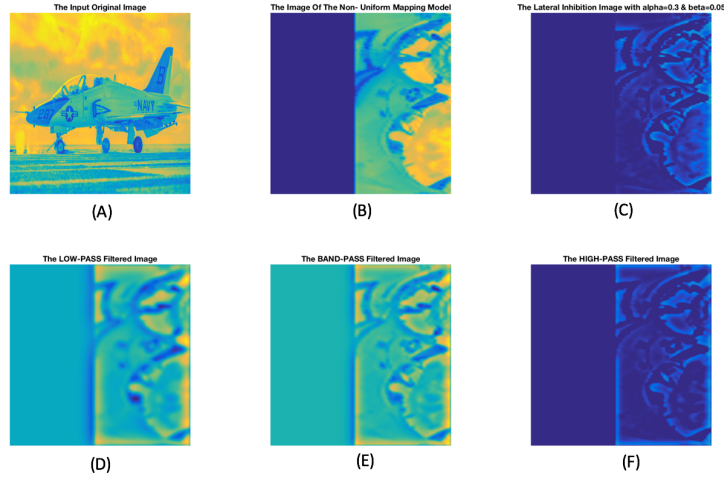


Figure 4-143: (A)The Original Input Image. (B) The Non-Uniform Sampling of Jet Real Image. (C) The Lateral Inhibition Real Image with  $[\alpha = 0.3 \text{ and } \beta = 0.05]$ . (D) The Filtered Image via DOG-LPF. (E)The Filtered Image via DOG-BPF. (F)The Filtered Image via DOG-HPF.

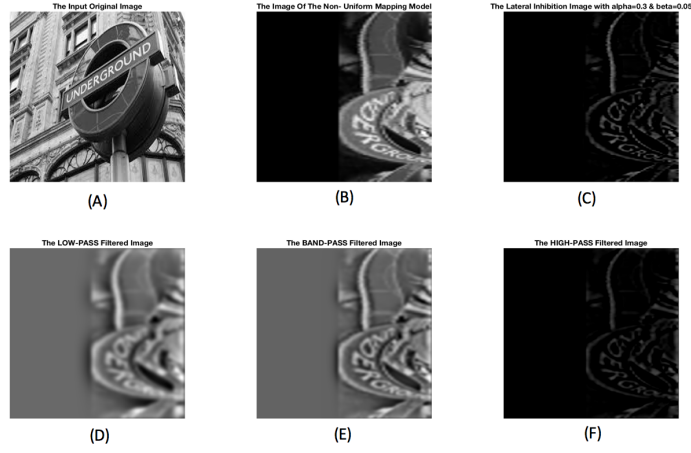


Figure 4-144: (A)The Original Input Image. (B) The Non-Uniform Sampling of Word Real Image. (C) The Lateral Inhibition Real Image with  $[\alpha = 0.3 \text{ and } \beta = 0.05]$ . (D) The Filtered Image via DOG-LPF. (E)The Filtered Image via DOG-BPF. (F)The Filtered Image via DOG-HPF.

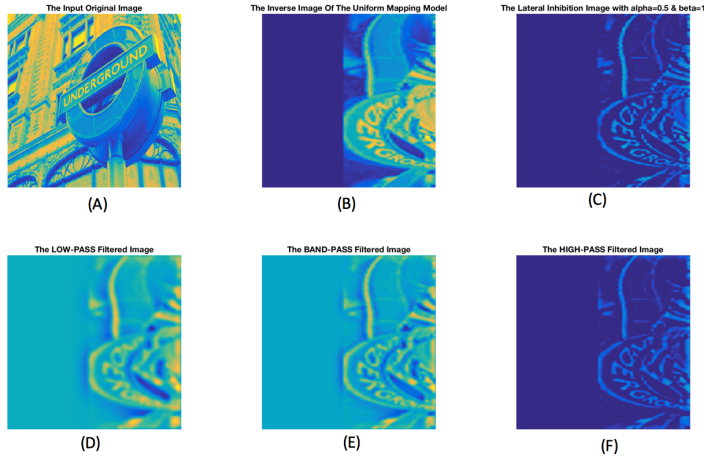


Figure 4-145: (A)The Original Input Image. (B) The Non-Uniform Sampling of Word Real Image. (C) The Lateral Inhibition Real Image with  $[\alpha = 0.3 \text{ and } \beta = 0.05]$ . (D) The Filtered Image via DOG-LPF. (E)The Filtered Image via DOG-BPF. (F)The Filtered Image via DOG-HPF.

The following figures are illustrating the remaining information details after subtracting the filtered image via difference of Gaussian filters from the image processed via the biological lateral inhibition image regarding this version of the non-uniform mapping model:

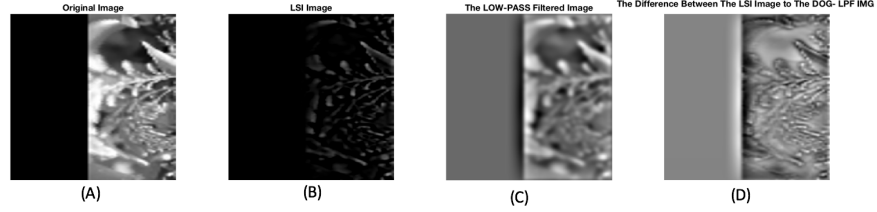


Figure 4-146: (A)The Non-Uniform Mapping Flower original input image.(B)Lateral Inhibition image with  $\alpha = 0.3$  and  $\beta = 0.05$ .(C)DOG-LPF Filtered image with  $\mu = 0$  and  $\sigma = 9.2$ .(D) The Test Image image  $[LI_{img} - LPF_{img}]$ .

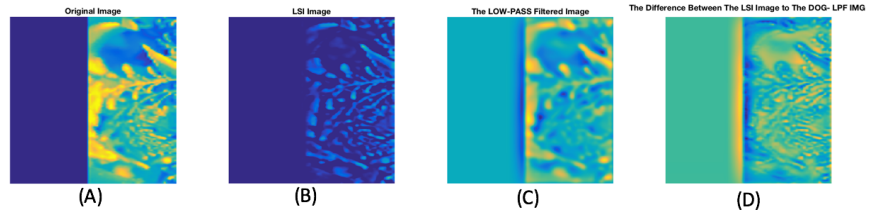


Figure 4-147: (A)The Non-Uniform Mapping Flower original input image.(B)Lateral Inhibition image with  $\alpha = 0.3$  and  $\beta = 0.05$ .(C)DOG-LPF Filtered image with  $\mu = 0$  and  $\sigma = 9.2$ .(D) The Test Image image  $[LI_{img} - LPF_{img}]$ .

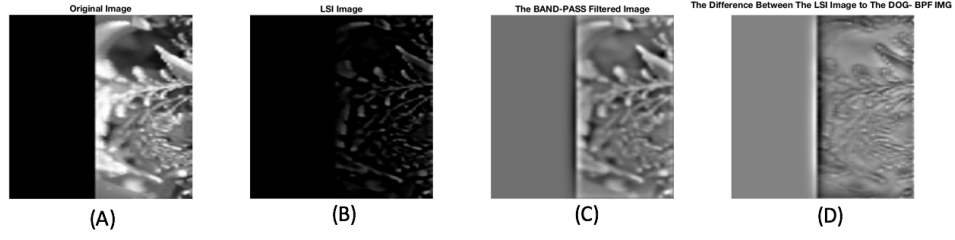


Figure 4-148: (A)The Non-Uniform Mapping Flower original input image.(B)Lateral Inhibition image with  $\alpha = 0.3$  and  $\beta = 0.05$ . (C)DOG-BPF Filtered image with  $\mu = 0$  and  $\sigma = 13.8$ . (D) The Test Image image  $[LI_{img} - BPF_{img}]$ .

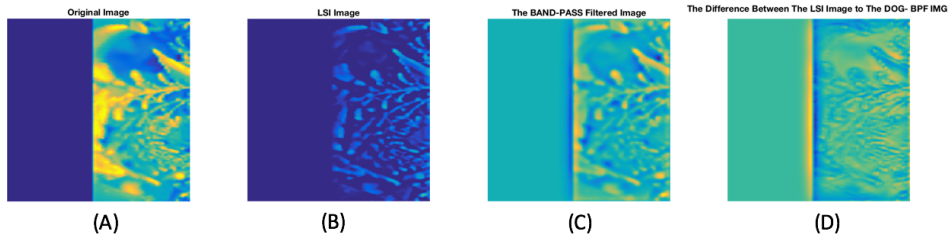


Figure 4-149: (A)The Non-Uniform Mapping Flower original input image.(B)Lateral Inhibition image with  $\alpha = 0.3$  and  $\beta = 0.05$ . (C)DOG-BPF Filtered image with  $\mu = 0$  and  $\sigma = 13.8$ . (D) The Test Image image  $[LI_{img} - BPF_{img}]$ .

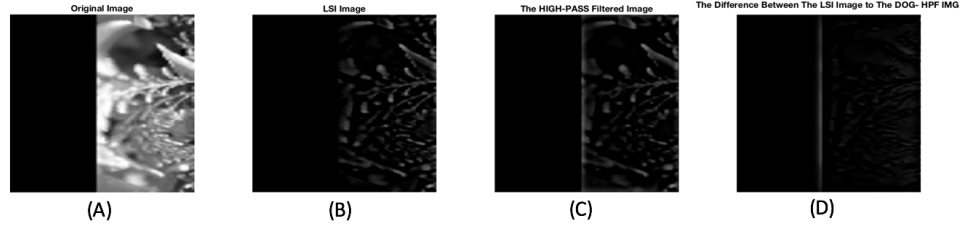


Figure 4-150: (A)The Non-Uniform Mapping Flower original input image.(B)Lateral Inhibition image with  $\alpha = 0.3$  and  $\beta = 0.05$ . (C)DOG-HPF Filtered image with  $\mu = 0$  and  $\sigma = 23$ . (D) The Test Image image  $[LI_{img} - HPF_{img}]$ .

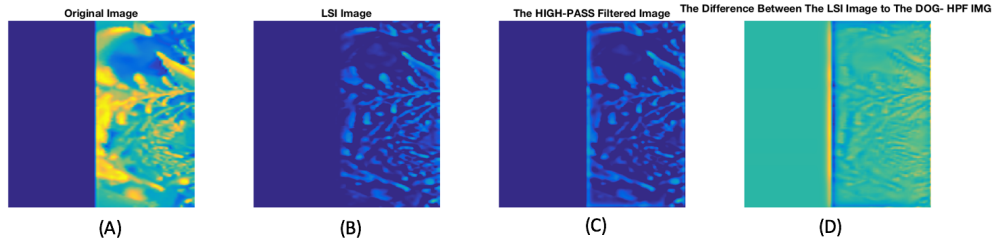


Figure 4-151: (A)The Non-Uniform Mapping Flower original input image.(B)Lateral Inhibition image with  $\alpha = 0.3$  and  $\beta = 0.05$ . (C)DOG-HPF Filtered image with  $\mu = 0$  and  $\sigma = 23$ . (D) The Test Image image  $[LI_{img} - HPF_{img}]$ .



#### 4.7.1 The Simulation results of the Inverse Non-Uniform Model

In this section, the inverse of the non-uniform mapping image will be presenting to validate the comparison between the new model to the conventional one. The lateral inhibition image has been generated based on non-uniform weighting coefficients that are created by log-polar mapping method, and the size of the output image will be equivalent to the original picture. The following figures will including the projected image with size equals to  $[500 \times 500]$ , then the inverse form of the mapped image based upon the log-polar transformation method will be obtained. Then, the lateral inhibition image has achieved after applying the numerical values for an alpha and a beta variables in the exponential model that have specified from the previous experiments regarding this mapping model to calculate the non-uniform weighting coefficient. An enhancement on the contrast and the related information can be observed in the lateral inhibition image, which means that this method is providing details exceeds the edge enhancement and the idea of second derivative operator which presented in [50]. The other three images of the same figure are presenting the output filtered pictures via multiple spatial-frequency channels. Whereas the first image is showing the filtered image based upon the difference of Gaussian low-pass filter, as we can see the blurry details in that picture as we go further from the fovea, while the filtered image via difference of Gaussian high-pass filter is containing only the image contrasts of the original image, which is similar to the negative second derivative of Laplacian. Then, the centered image of the same figure will be representing the filtered output image by the difference of Gaussian band-pass filter, as we can see that this image it does have some information related to the contrasts as well as some low frequency details. The goal of this simulation is to compare and study the similarity in performance between the lateral inhibition image and the three filtered image regarding the three difference of Gaussian filters of this version image of the non-uniform mapping model.

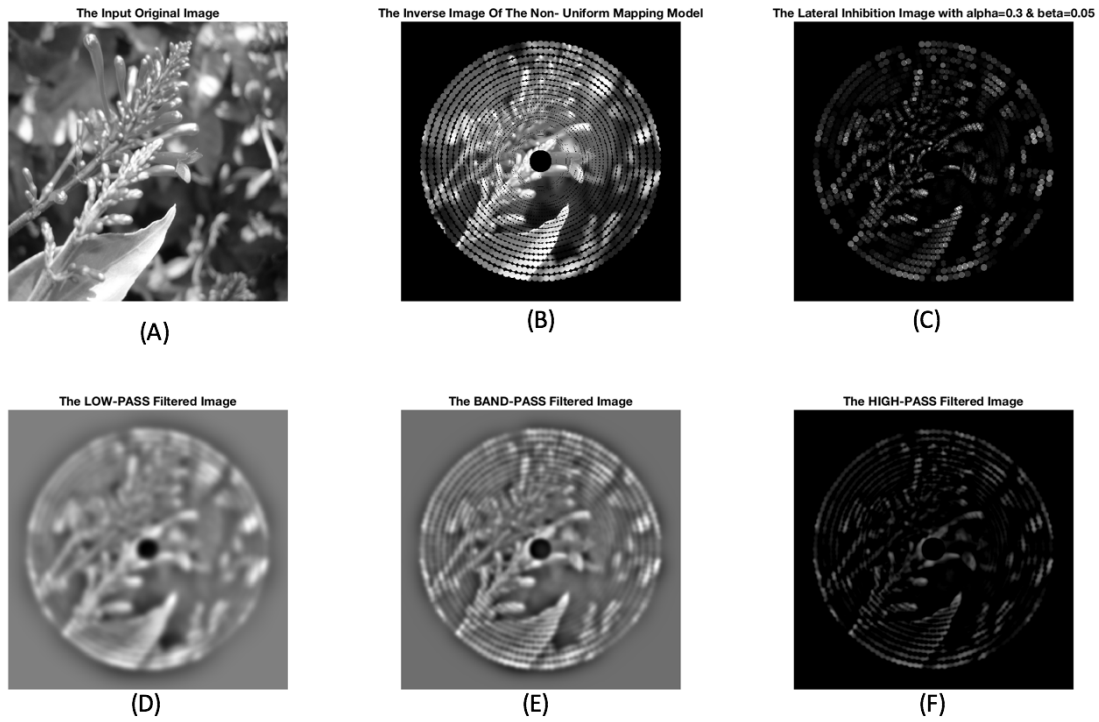


Figure 4-152: (A)The Flower Input Image with Size  $[500 \times 500]$ . (B) The  $[XY]$  Wrapped Back Image Based on Log-Polar Mapping Method. (C) The LSI Wrapped Back Image. (D)The Wrapped Back Non-Uniform Filtered Image Based on DOG-LPF. (E)The Wrapped Back Non-Uniform Filtered Image Based on DOG-BPF. (F)The Wrapped Back Non-Uniform Filtered Image Based on DOG-HPF.

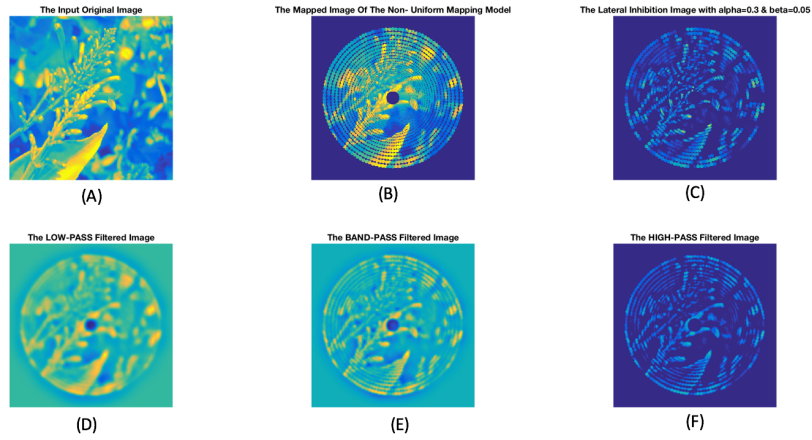


Figure 4-153: (A)The Flower Input Image with Size [500x500].(B) The  $[XxY]$  Wrapped Back Image Based on Log-Polar Mapping Method.(C) The LSI Wrapped Back Image. (D)The Wrapped Back Non-Uniform Filtered Image Based on DOG-LPF.(E)The Wrapped Back Non-Uniform Filtered Image Based on DOG-BPF. (F)The Wrapped Back Non-Uniform Filtered Image Based on DOG-HPF.

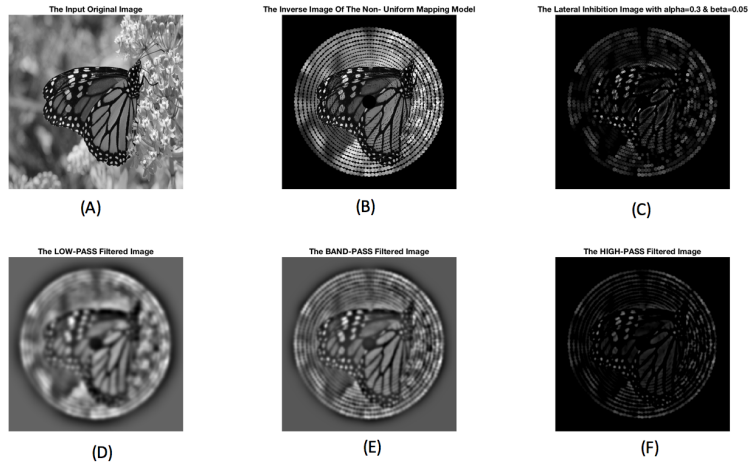


Figure 4-154: (A)The Butterfly Input Image with Size [500x500].(B) The  $[XxY]$  Wrapped Back Image Based on Log-Polar Mapping Method.(C) The LSI Wrapped Back Image. (D)The Wrapped Back Non-Uniform Filtered Image Based on DOG-LPF.(E)The Wrapped Back Non-Uniform Filtered Image Based on DOG-BPF. (F)The Wrapped Back Non-Uniform Filtered Image Based on DOG-HPF.

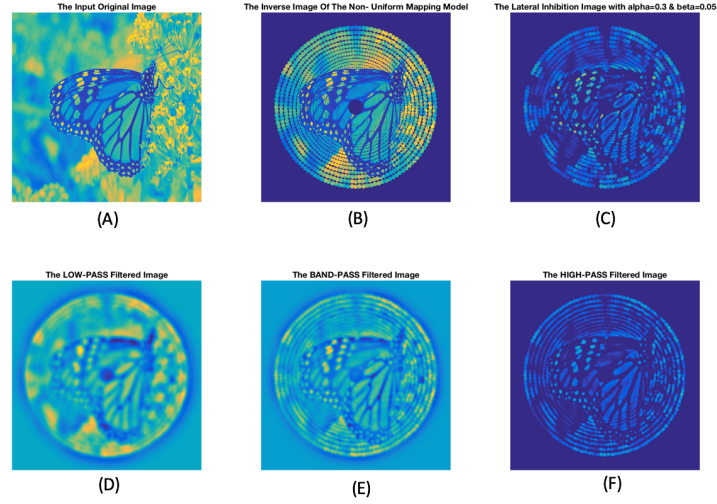


Figure 4-155: (A)The Butterfly Input Image with Size  $[500 \times 500]$ . (B) The  $[XxY]$  Wrapped Back Image Based on Log-Polar Mapping Method. (C) The LSI Wrapped Back Image. (D)The Wrapped Back Non-Uniform Filtered Image Based on DOG-LPF. (E)The Wrapped Back Non-Uniform Filtered Image Based on DOG-BPF. (F)The Wrapped Back Non-Uniform Filtered Image Based on DOG-HPF.

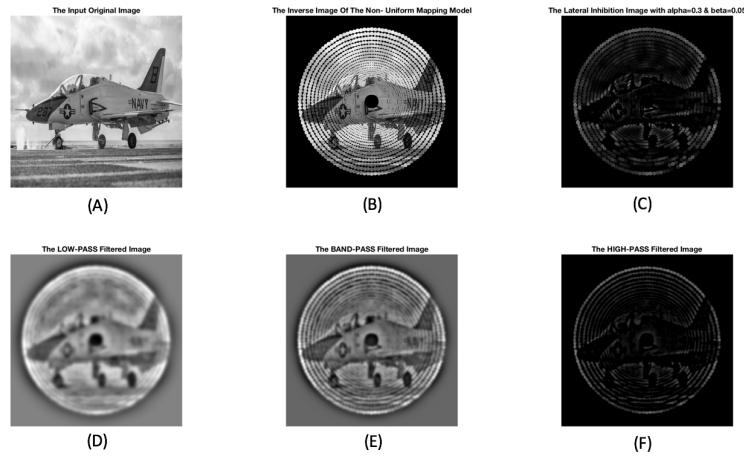


Figure 4-156: (A)The Jet Input Image with Size  $[500 \times 500]$ . (B) The  $[XxY]$  Wrapped Back Image Based on Log-Polar Mapping Method. (C) The LSI Wrapped Back Image. (D)The Wrapped Back Non-Uniform Filtered Image Based on DOG-LPF. (E)The Wrapped Back Non-Uniform Filtered Image Based on DOG-BPF. (F)The Wrapped Back Non-Uniform Filtered Image Based on DOG-HPF.

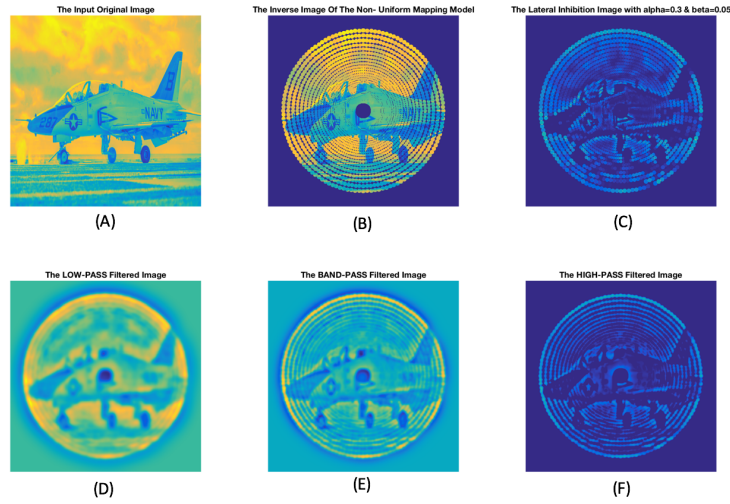


Figure 4-157: (A)The Jet Input Image with Size  $[500 \times 500]$ . (B) The  $[XxY]$  Wrapped Back Image Based on Log-Polar Mapping Method. (C) The LSI Wrapped Back Image. (D)The Wrapped Back Non-Uniform Filtered Image Based on DOG-LPF. (E)The Wrapped Back Non-Uniform Filtered Image Based on DOG-BPF. (F)The Wrapped Back Non-Uniform Filtered Image Based on DOG-HPF.

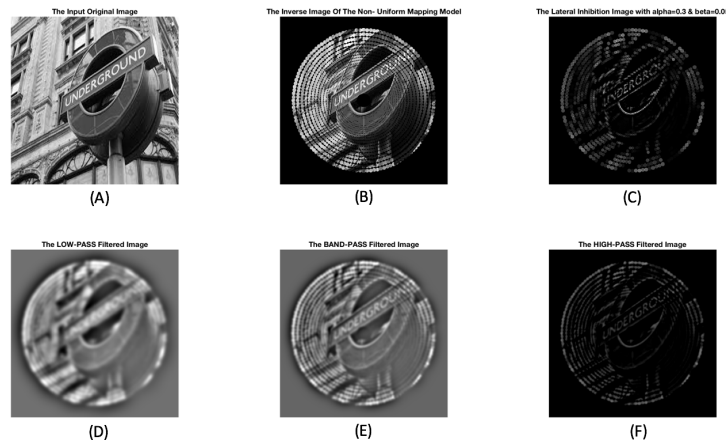


Figure 4-158: (A)The Word Input Image with Size  $[500 \times 500]$ . (B) The  $[XxY]$  Wrapped Back Image Based on Log-Polar Mapping Method. (C) The LSI Wrapped Back Image. (D)The Wrapped Back Non-Uniform Filtered Image Based on DOG-LPF. (E)The Wrapped Back Non-Uniform Filtered Image Based on DOG-BPF. (F)The Wrapped Back Non-Uniform Filtered Image Based on DOG-HPF.

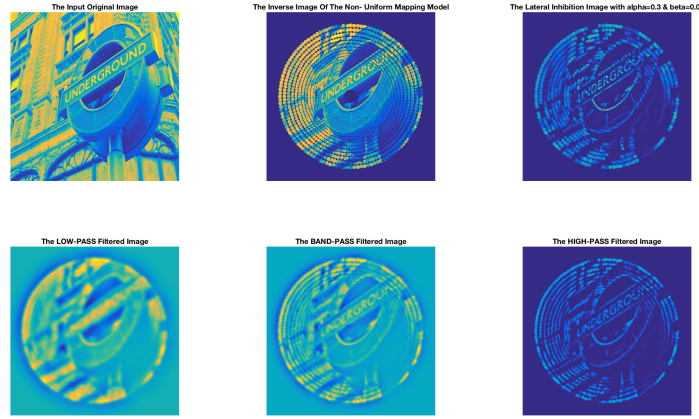


Figure 4-159: (A)The Word Input Image with Size [500x500].(B) The  $[XxY]$  Wrapped Back Image Based on Log-Polar Mapping Method.(C) The LSI Wrapped Back Image. (D)The Wrapped Back Non-Uniform Filtered Image Based on DOG-LPF.(E)The Wrapped Back Non-Uniform Filtered Image Based on DOG-BPF. (F)The Wrapped Back Non-Uniform Filtered Image Based on DOG-HPF.

## 4.8 The Comparison Between The Uniform Model and The Non-Uniform Model:

To conclude this chapter, a comparison between the new mapping model [Non-Uniform Model] and a conventional one [Uniform Model] will be represented below. Whereas, this comparison demonstrates the fact that the new mapping design processes the input image [in any size] within the minimum amount of time comparing to the uniform layout. And that is because of the non-uniform distribution of visual sensors (sub-circles) in the retina (Circular Mapping model) corresponds to the spatially variant sampling strategy of the Human Visual System (HVS). Where, the retinal receptors are densely packed at the fovea, and their density decreases as the radial distance from the fovea increases (Exponentially). This directly effects on the time required to process the input information since this model is characterized in a spatial way to calculate its dimension to mimic

the human retina,  $nr \times nw$  where  $nw = 2nr$ . While the conventional (Uniform) mapping model maps the entire input image uniformly and the resultant output image size will be similar to the original image,  $[X \times Y]$ . Therefore, the last one needs a long time to process such an image with high resolution comparing to the nonuniform model. See the following figure which explains this comparison regarding the degree of complexity or the time required for mapping the image, figure 4-160.

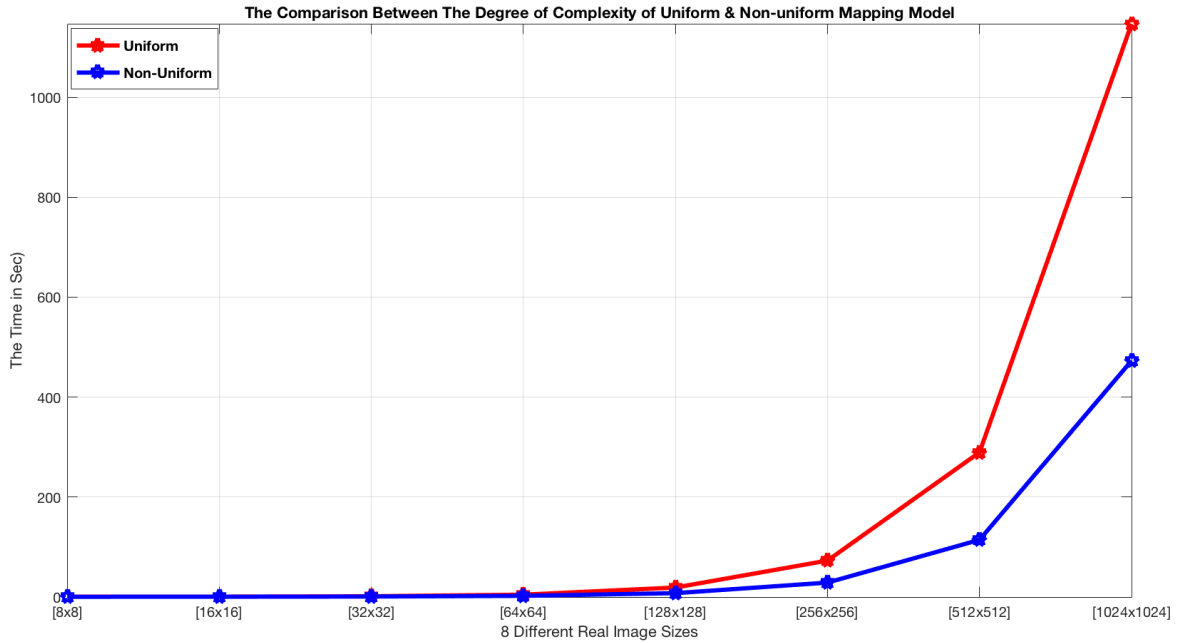


Figure 4-160: The Comparison Between the Uniform to the Non-uniform Model Regarding Time Required to Sample The Input Image within Different Image Sizes.

As we can see, that the non-uniform model exhibits better performance regarding a degree of complexity. Where this superiority of a non-uniform mapping model can be precisely characterized as the picture size is increased.

According to figure 3-2, the Root Mean Square Error quality metric will be used to compare the image processed based on (LSI) natural method to the filtered image based on Difference of Gaussian filters. Since the remaining details of subtracting these two images for all both models have shown

that the closest filtered image to the lateral inhibition image is the picture treated via the DOG-HPF, see figure4-151 regarding the new model and figure 4-80 which represents the uniform one. To assure this observation with a practical calculation the RMSE quality metric will be used to determine precisely by values what is the difference between these two methods (the biological and DOG filtration). Therefore, the following tables are representing these determination via the equation 4.7 for both models regarding by testing eight different real images with one specific size, for the uniform model is [100x100], see Table 4.1. And [128x64] for the new mapping model, see table 4.2.

$$RMSE = \sqrt{\frac{1}{MN} * \sum (LateralInhibitionImage - FilteredImage)^2} \quad (4.7)$$

Where, MN represent the number of elements of the filtered image. And the "Lateral Inhibition Image" is the output image via the natural method after calculating the interconnection distances between the neurons and obtain the coupling coefficients based on the exponential model for each mapping model. Then, the LSI algorithm will be applied to that mapped image. And the "Filtered Image" represents the output image via the three Difference-of-Gaussian spatial-frequency channels within different standard deviation parameter,  $\sigma$ . To provide three separate information details from a picture depending on the range of frequency of each particular channel. Theses calculations are revealing numerical values that are describing how different are these two processed images, in other words, as these numerical results decrease it reveals the degree of similarity between the image processed by the lateral inhibition biological method to the filtered image based on the three multiple spatial frequency channels. As we can observe from these two tables below, Table4.1 and 4.2, that the DOG-HP filtered image is the closest image to the biological picture for both models.

The following table is illustrating the numerical results for each particular spatial frequency channel regarding the uniform and non-uniform mapping model:



Uniform Img	RMSE-LPF	RMSE-BPF	RMSE-HPF
Flower	38	31	20
Jet	48	42	32
Word	44	38	33
Butterfly	33	31	31
Lena	38	27	17
Peppers	33	32	32

Table 4.1: The Root Mean Square Error Numerical Results Regarding The Uniform Model

Non-Uniform	RMSE-LPF	RMSE-BPF	RMSE-HPF
Flower	23	17	13
Jet	18	12	10
Word	17	12	10
Butterfly	18	14	11
Lena	18	13	10
Peppers	18	13	11

Table 4.2: The Root Mean Square Error Numerical Results Regarding The Non-Uniform Model

# Chapter 5

## Conclusions

It is worth mentioning that the non-uniform mapping model collaborating with a lateral inhibition natural method is a novel way to treat the visual information in the same way as a human retinal eye, and there is no previous study similar to the work presented here. However, the idea of using log-polar mapping method to mimic the distribution of the retinal cone cells has first presented and explained by Richard Messner in [13]. The objective of this research is, to create a computationally efficient, biologically inspired, image processing framework suitable for pattern recognition that can be utilized on an inexpensive PC platform. Where the benefits of such model are: the first one is maintaining a large field of view while preserving the detailed critical information from the captured scene at the point of interest. The second one is providing the capability of the system to process an enormous amount of data at a very fast rate. These advantages are directly correlated with the way human, and many other organisms process the visual information depending on the non-uniform distribution of visual sensors in the retina corresponds to the spatially variant sampling strategy of the Human Visual System (HVS). The response of a given retinal ganglion cell depends on the light intensity falling on the photo-receptors within the small, more or less, circular area of the retina called the ganglion cell receptive field. The retinal receptors over the non-uniform sampling model are densely packed at the fovea (the central part of the pattern), and their density decreases as the radial distance from the fovea increases. This directly allows for data reduction and wide field of view while preserving the detailed information at the gaze point. As reported by chapter three and four, the diameter of the receptive fields (the concentric circles on the non-uniform pattern) increases linearly with the eccentricity. The distribution of ganglion cells has been reported to be similar to the cone distribution [35]. At the fovea, there are at least three ganglion

cells per one cone, while at the periphery there is one ganglion cell per two cones. Obvious data reduction performed at the retinal sensory level through non-uniform sampling is only one aspect of information processing occurring in frontal stages of the HVS. Early discoveries have shown that the inverse of cortical magnification factor is linearly dependent on eccentricity [29]. This leads to the introduction of a conformal logarithmic mapping (log-polar mapping) as the model that agrees well with the rearrangement of retinal signals in the visual cortex (this signal rearrangement is usually referred as retinal-cortical projection). Additionally, the lateral inhibition mechanism is known to occur in the early stages of visual information processing in biological systems. This is especially seen in the retina, lateral geniculate nucleus (LGN) and certain areas of the visual cortex. The importance of lateral inhibitory connectivity in the context of the visual process is very often perceived as edge enhancement or even interpreted as Mach-band effect. As mentioned in previous studies that the effect of lateral inhibition (as in the retinal ganglion cell receptive field) can be seen mathematically as a negative second derivative operator ( $-\frac{\partial^2}{\partial x^2}$ ). In particular, such an area will not respond to uniform or to uniformly graded illumination stimuli, for which a second derivative is zero. After Fourier transformation, in the spatial frequency ( $f$ ) domain, the negative second derivative operator becomes equivalent to multiplication by  $f^2$  [50]. Where the negative second derivative (or the Laplacian of Gaussian) operator is used in enhancing or detecting the edges from the captured image (as High-Pass Filter). However, the lateral inhibitory sensory function exhibits better than merely edge detection processor, see the resultant images via lateral inhibition for both uniform and non-uniform mapping models in the previous chapter. Where, the inhibition impact is shrinking when the radial distance increases in an exponential way. As explained previously in this thesis, that this exponential model included two variables that effect directly on the resultant output image via lateral subtractive inhibition. from the previous chapter, we have identified the numerical values for these two variables that give a reasonable lateral inhibition image regarding each mapping models depending on the edge enhancement of an input image and the differential of the intensities between the edges of the same image as well which represents the perceived information beyond the edges. In this part of research, the relation between the output image to the input image corresponding to an exponential model will be presenting based on these two

variables ( $\alpha$  and  $\beta$ ) and the relationship between these parameters themselves for both models. To find out the adequate mathematical expression for these two variables. First, we shall relay on our investigation study from the previous chapter on the search for the numerical value of beta and alpha. Then, different mathematical equations will be tested to find the description of this relationship depending on the characteristics of the resultant image. Since a (0.5) has confirmed to be the value for an alpha  $\alpha$  parameter for the uniform pattern, in this section the same value will be used. The following three figures below are showing the resultant output images based on different mathematical relationships between an alpha and beta parameters for the lateral inhibition method regarding the uniform model:

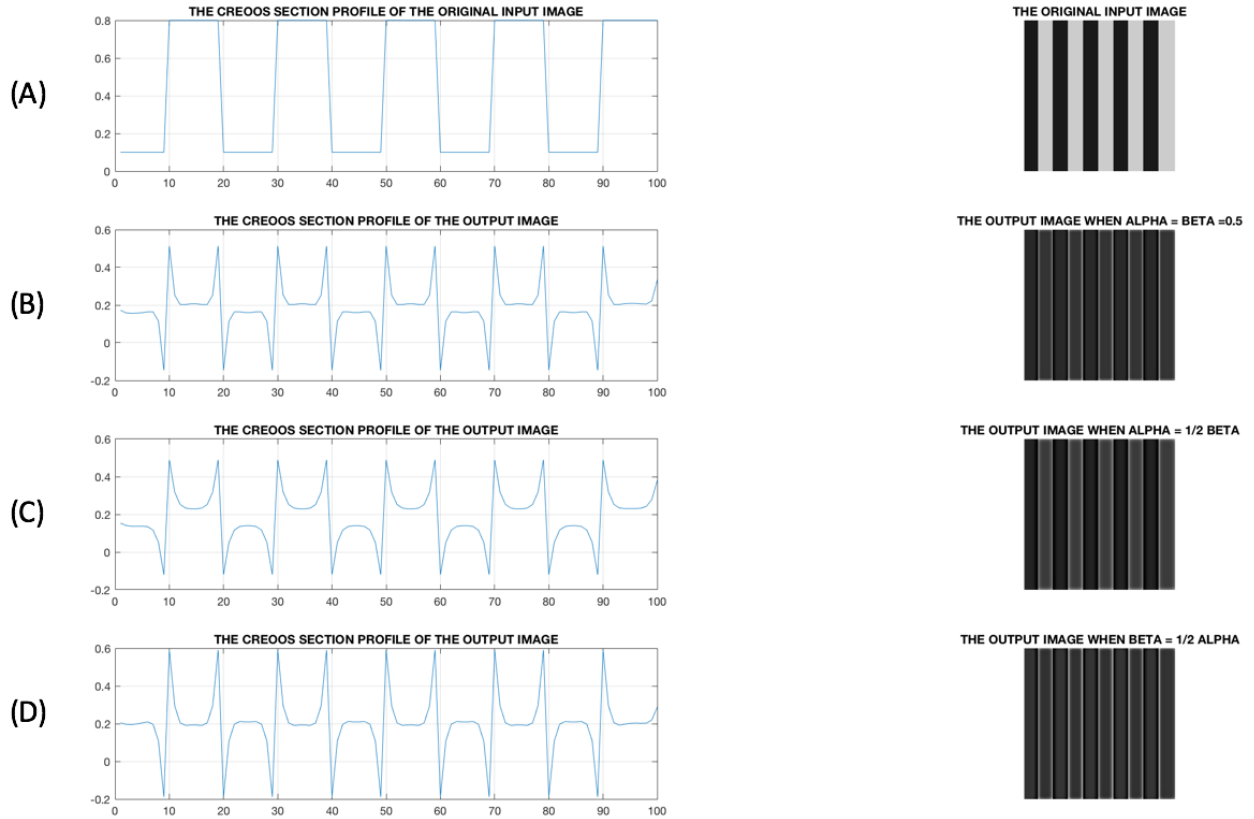


Figure 5-1: The Identification of the Mathematical Relationship Between an Alpha and Beta Variables [ $\alpha$  and  $\beta$ ] for the Unifrom Model: (A)The Original Image.(B)LSI Image When  $\alpha=\beta$  (C)LSI Image When  $\alpha=\frac{1}{2}*\beta$  (D) LSI Image When  $\beta=\frac{1}{2}*\alpha$ .

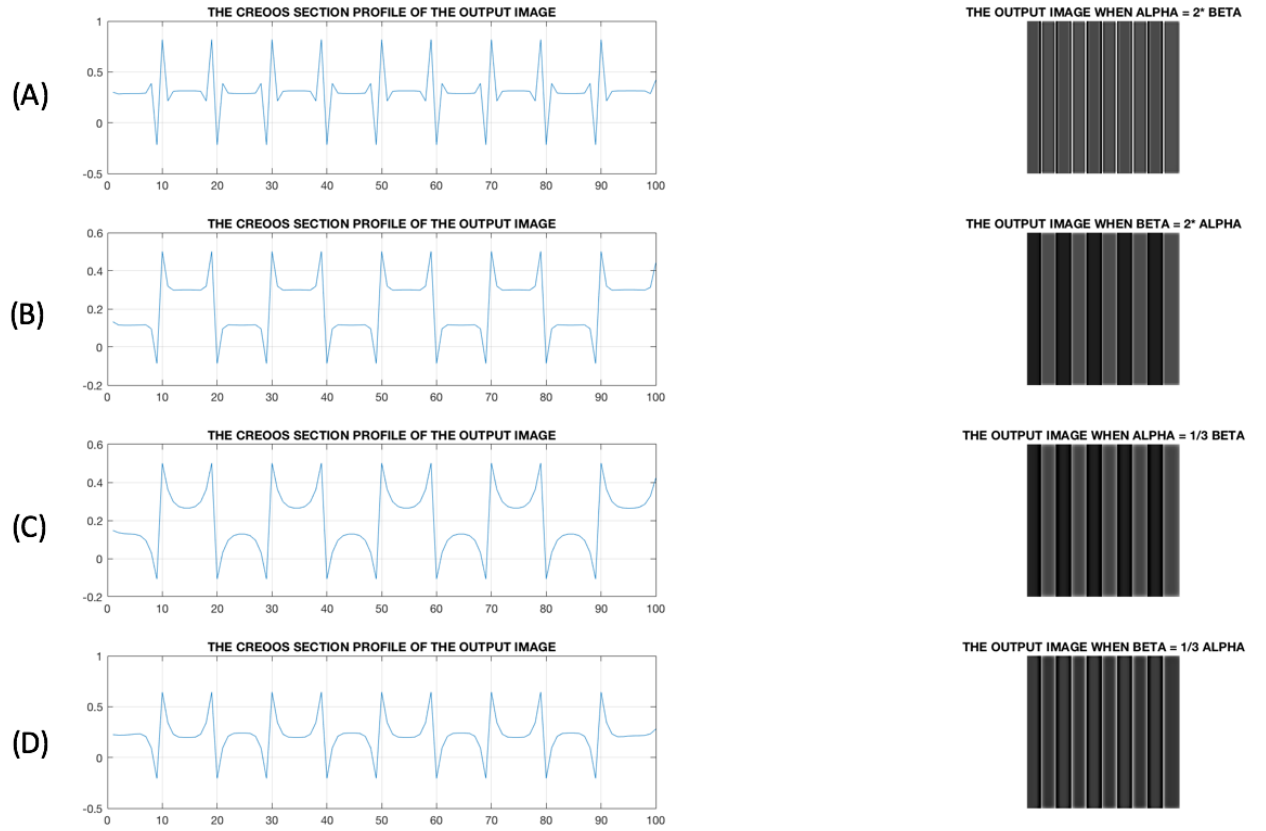


Figure 5-2: The Identification of the Mathematical Relationship Between an Alpha and Beta Variables  $[\alpha$  and  $\beta]$  for the Uniform Model: (A)LSI Image When  $\alpha=2*\beta$ (B)LSI Image When  $\beta=2*\alpha$  (C)LSI Image When  $\alpha=\frac{1}{3}*\beta$  (D) LSI Image When  $\beta=\frac{1}{3}*\alpha$ .

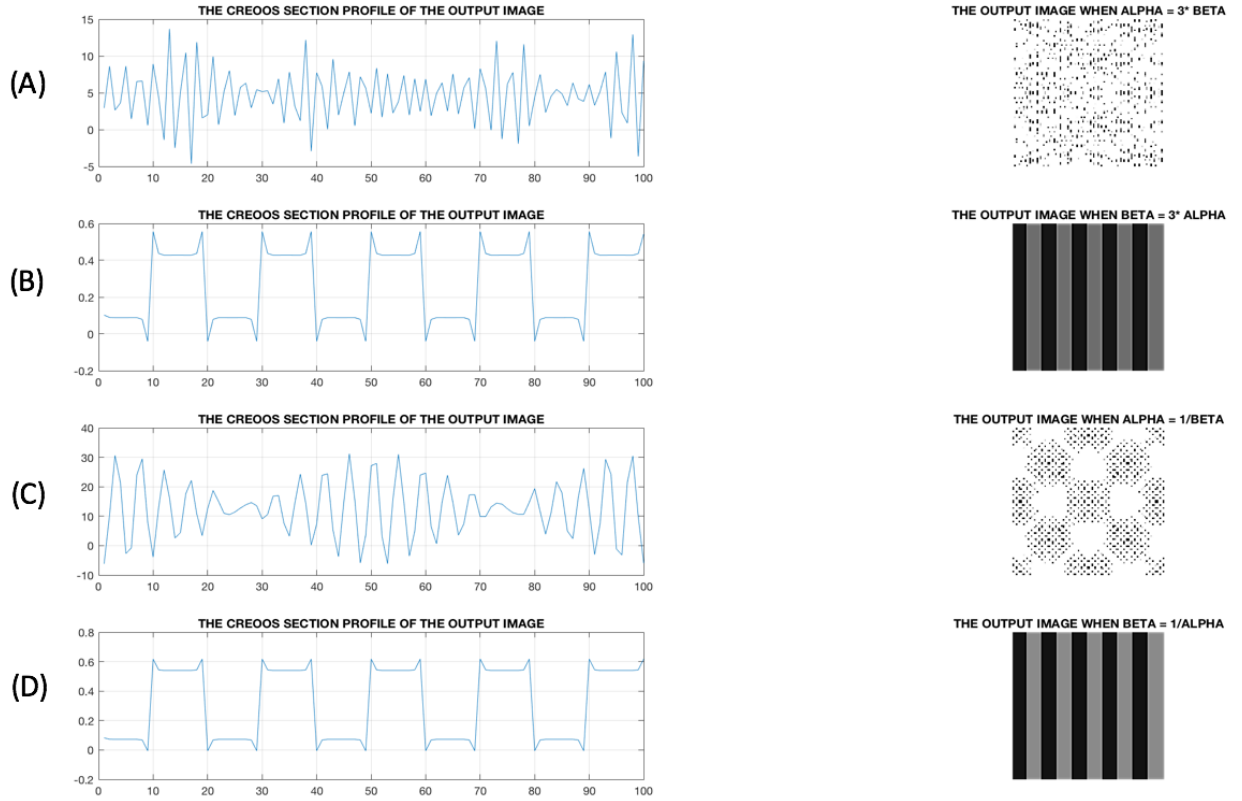


Figure 5-3: The Identification of the Mathematical Relationship Between an Alpha and Beta Variables [ $\alpha$  and  $\beta$ ] for the Uniform Model: (A)LSI Image When  $\alpha=3*\beta$ (B)LSI Image When  $\beta=3*\alpha$  (C)LSI Image When  $\alpha=\frac{1}{\beta}$  (D) LSI Image When  $\beta=\frac{1}{\alpha}$ .

According to these three figures above, figure 5-1, 5-2, and 5-3, we can notice that: when alpha equals beta, see figure (5-1B), the related output image has an enhanced edges (that is almost similar to the negative of the second derivative operator which is we think that the LSI can give more than that). Because, we are almost losing the relative information between these edges. While, when an alpha parameter is higher than beta, we won't achieve the desired output image or in other words, we will be missing all the important information of the captured image, see the images in figure 5-1D, 5-2A,5-2D, and 5-3A. According to all these results we can say that an alpha parameter should always be lower than beta to obtain the desired lateral inhibition image with the edge enhanced as well as the information beyond the boundaries of this mapping model. Different numerical values will be testing on the following figures within a particular range of numbers [starting from 1 to 10], to identify by how much an alpha should be lower than beta. Then, a conclusion with the specified mathematical relationship between an alpha  $\alpha$  parameter to beta  $\beta$  for the exponential model regarding the uniform format will be introduced right after these figures below:

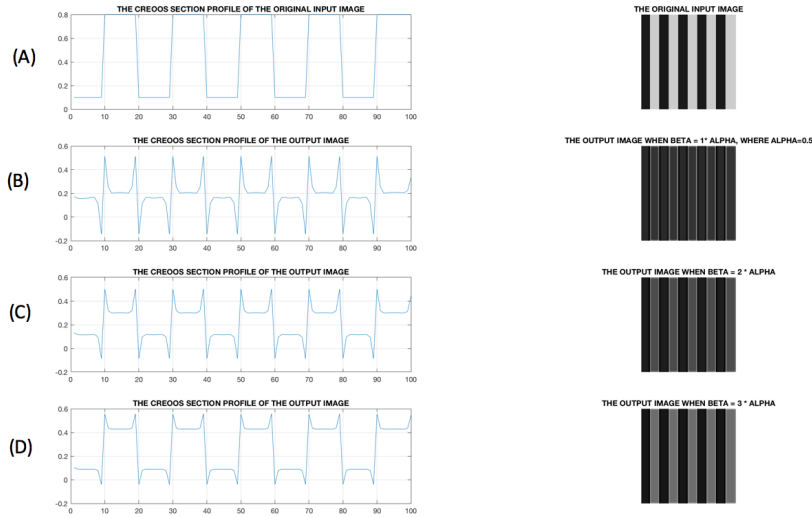


Figure 5-4: Illustration the Best Expression of Alpha  $\alpha$  parameter and Beta  $\beta$  for the Uniform Model. (A)The Original Image (B)LSI Image  $\beta = 1 * \alpha$ . (C)LSI Image  $\beta = 2 * \alpha$ . (D)LSI Image  $\beta = 3 * \alpha$ .

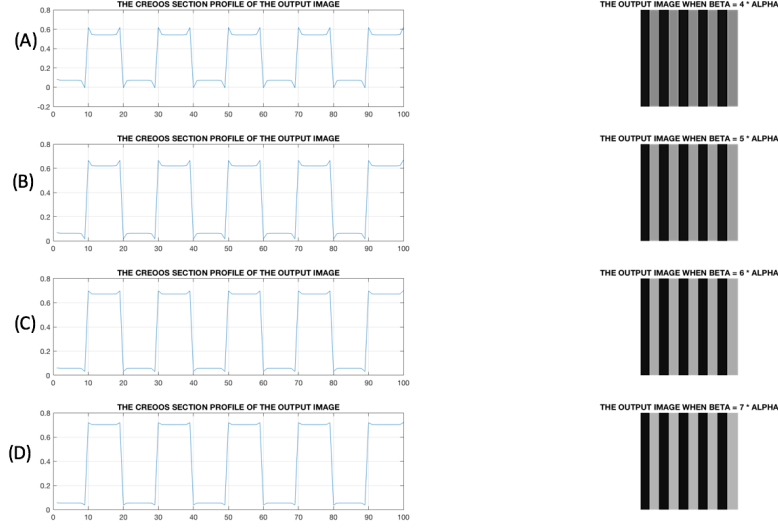


Figure 5-5: Illustration the Best Expression of Alpha  $\alpha$  parameter and Beta  $\beta$  for the Uniform Model. (A)LSI Image  $\beta = 4 * \alpha$  (B)LSI Image  $\beta = 5 * \alpha$ . (C)LSI Image  $\beta = 6 * \alpha$ . (D)LSI Image  $\beta = 7 * \alpha$ .

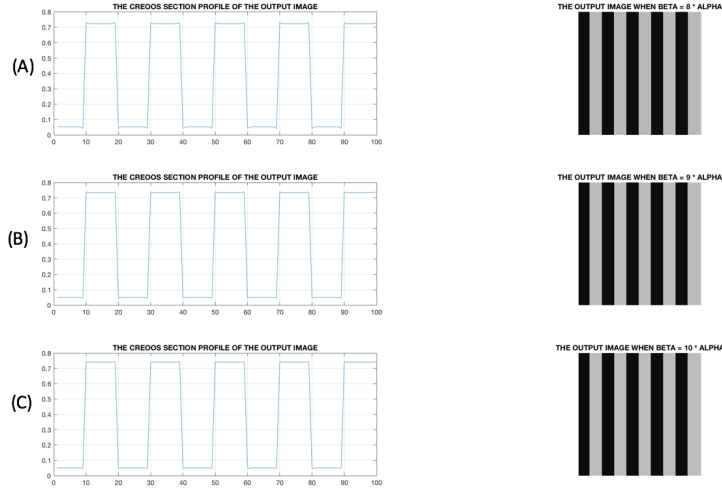


Figure 5-6: Illustration the Best Expression of Alpha  $\alpha$  parameter and Beta  $\beta$  for the Uniform Model. (A)LSI Image  $\beta = 8 * \alpha$  (B)LSI Image  $\beta = 9 * \alpha$ . (C)LSI Image  $\beta = 10 * \alpha$ .



According to the above figures, the best mathematical relationship between  $[\alpha$  and  $\beta]$  variables have been investigated and confirmed that beta always should be higher than alpha by a numerical value. From the above three figures particularly, figure 5-4, 5-5, and figure 5-6, we can notice that this value should be less than 4 to achieve the edge enhancement and the information beyond the edges. In this thesis work, the following relation has been used to form the lateral inhibition coupling coefficient matrix:

$$\beta = 2 * \alpha \quad (5.1)$$

Then, the final description of the exponential model regarding this model will be as follows in the equation 5.2:

$$B = \left(\frac{\beta}{2}\right) * \exp(-\beta * D) \quad (5.2)$$

And the relationship between an original input image to the output lateral inhibition image will be illustrated on the equation below 5.3

$$OutputLateralInhibitionImage = B^{-1} * OriginalImage \quad (5.3)$$

However, for the non-uniform mapping model based on the log-polar transformation method, we need to identify the mathematical expression of the exponential model's variables to obtain the desired weighting coefficients matrix for the output image via the natural method (lateral inhibition). The same mathematical relationships that have used for the uniform model will be using in this pattern too. For consistency purposes, we shall use the same procedure of identifying the mathematical relationship between an alpha and beta variables of the exponential model  $[\alpha$  and  $\beta]$ , from the conventional model in the new design. To see how are these variables acting on the new paradigm and which mathematical description gives the reasonable LSI image output, to do that the same numerical value for an alpha will apply here which is (0.3), see the following figures below:

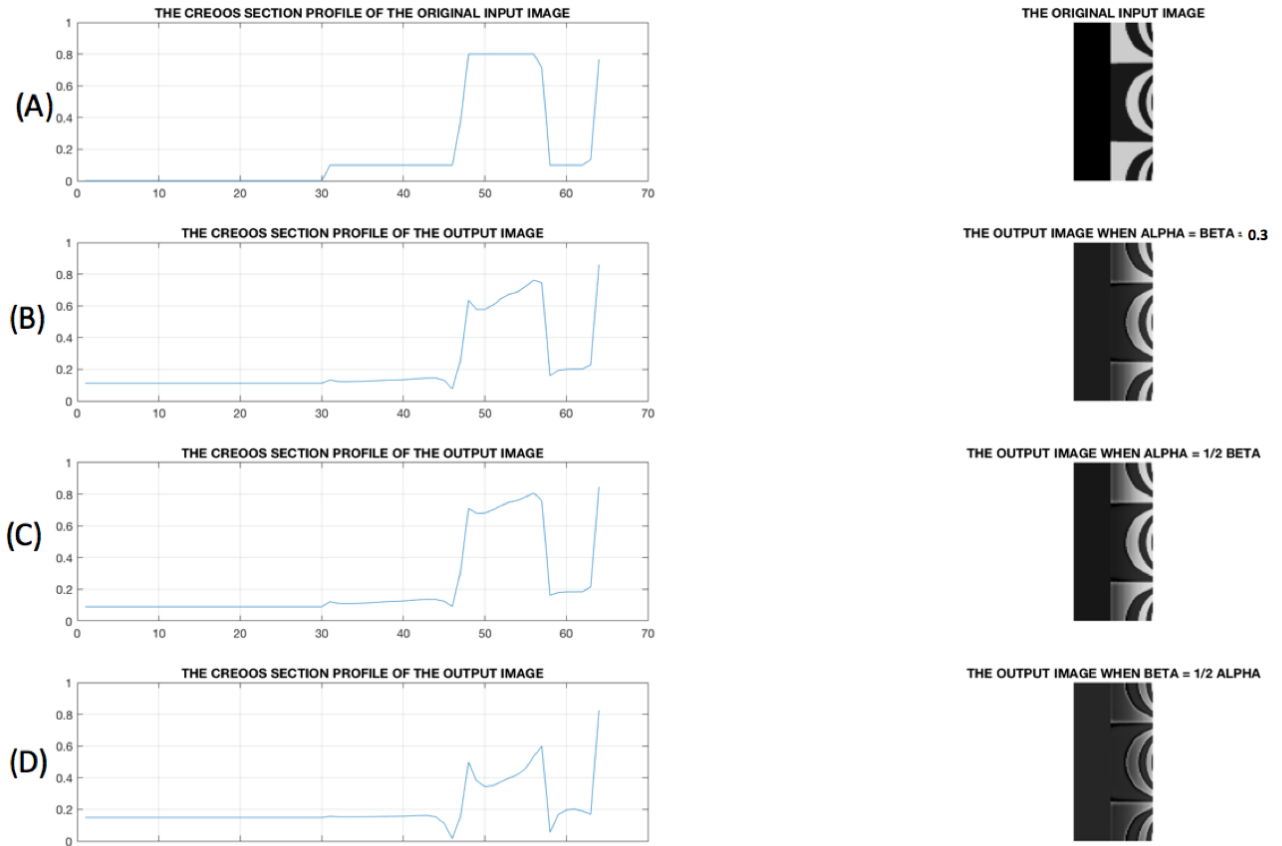


Figure 5-7: The Identification of the Mathematical Relationship Between Alpha and Beta Variables  $[\alpha \text{ and } \beta]$  for the Non-uniform Model. (A) The Original Image. (B) LSI Image when  $\alpha = \beta = 0.3$ . (C) LSI Image when  $\alpha = \frac{1}{2} * \beta$ . (D) LSI Image when  $\beta = \frac{1}{2} * \alpha$ .

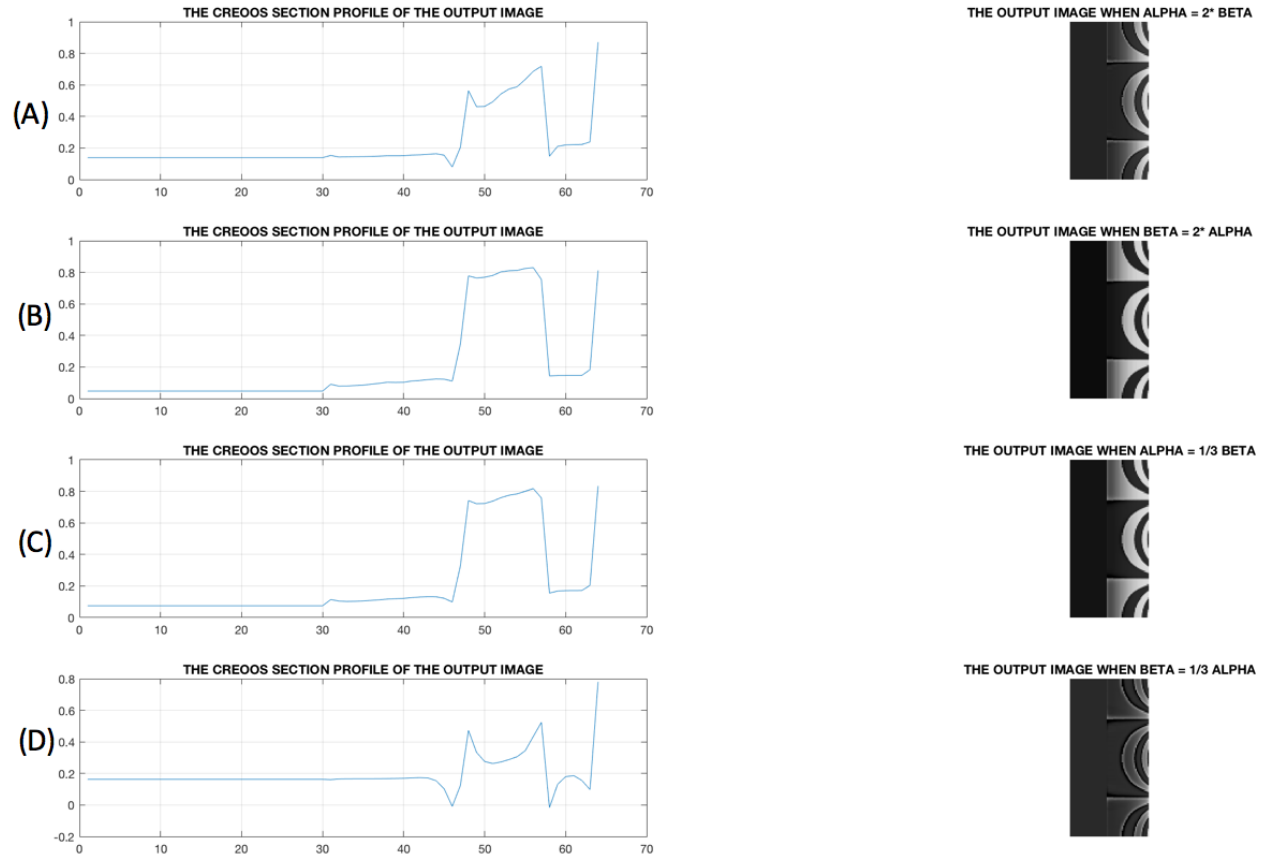


Figure 5-8: The Identification of the Mathematical Relationship Between Alpha and Beta Variables  $[\alpha \text{ and } \beta]$  for the Non-uniform Model. (A) LSI Image when  $\alpha = 2 * \beta$ . (B) LSI Image when  $\beta = 2 * \alpha$ . (C) LSI Image when  $\alpha = \frac{1}{3} * \beta$ . (D) LSI Image when  $\beta = \frac{1}{3} * \alpha$ .

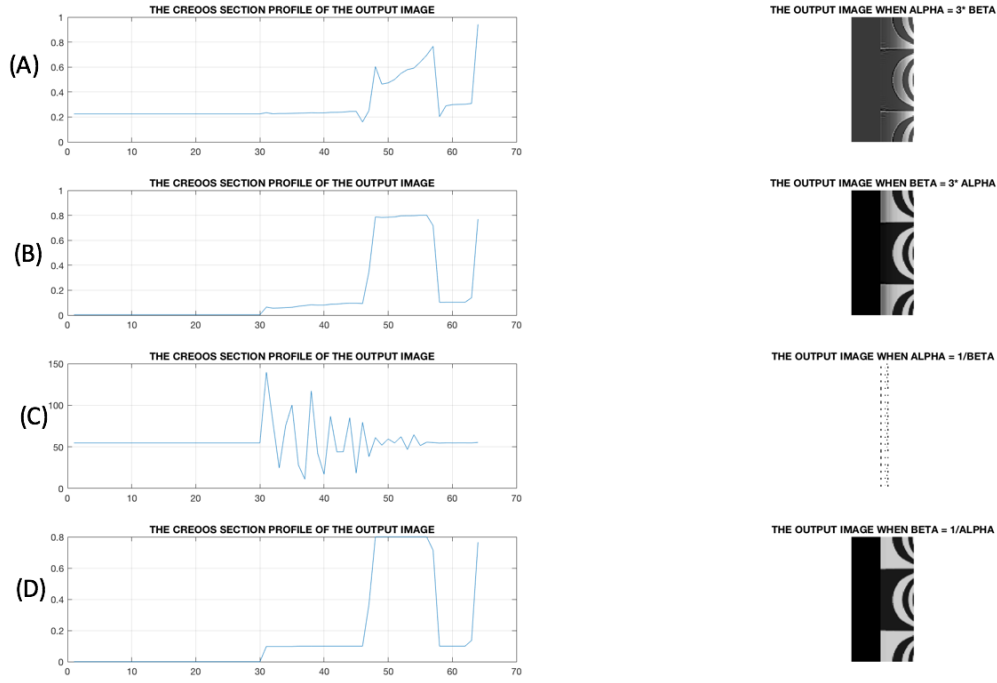


Figure 5-9: The Identification of the Mathematical Relationship Between Alpha and Beta Variables  $[\alpha \text{ and } \beta]$  for the Non-uniform Model. (A) LSI Image when  $\alpha = 3\beta$ . (B) LSI Image when  $\beta = 3\alpha$ . (C) LSI Image when  $\alpha = \frac{1}{\beta}$ . (D) LSI Image when  $\beta = \frac{1}{\alpha}$ .

According to these results above, we can observe that when beta parameter  $\beta$  is higher than alpha variable  $\alpha$  the output image will be exactly as the original image, in other words, the LSI natural method won't impact on the processed image. However, when an alpha parameter  $\alpha$  is higher than beta  $\beta$ , the desired image will be achieved. To verify this observation and extract a mathematical expression that represents the relationship between these two variables with the input and output image the following figure has been made to illustrate precisely "by how much an alpha parameter should be higher than a beta variable" within an exponential model to generate non-uniform coupling coefficient matrix for the lateral inhibition method.

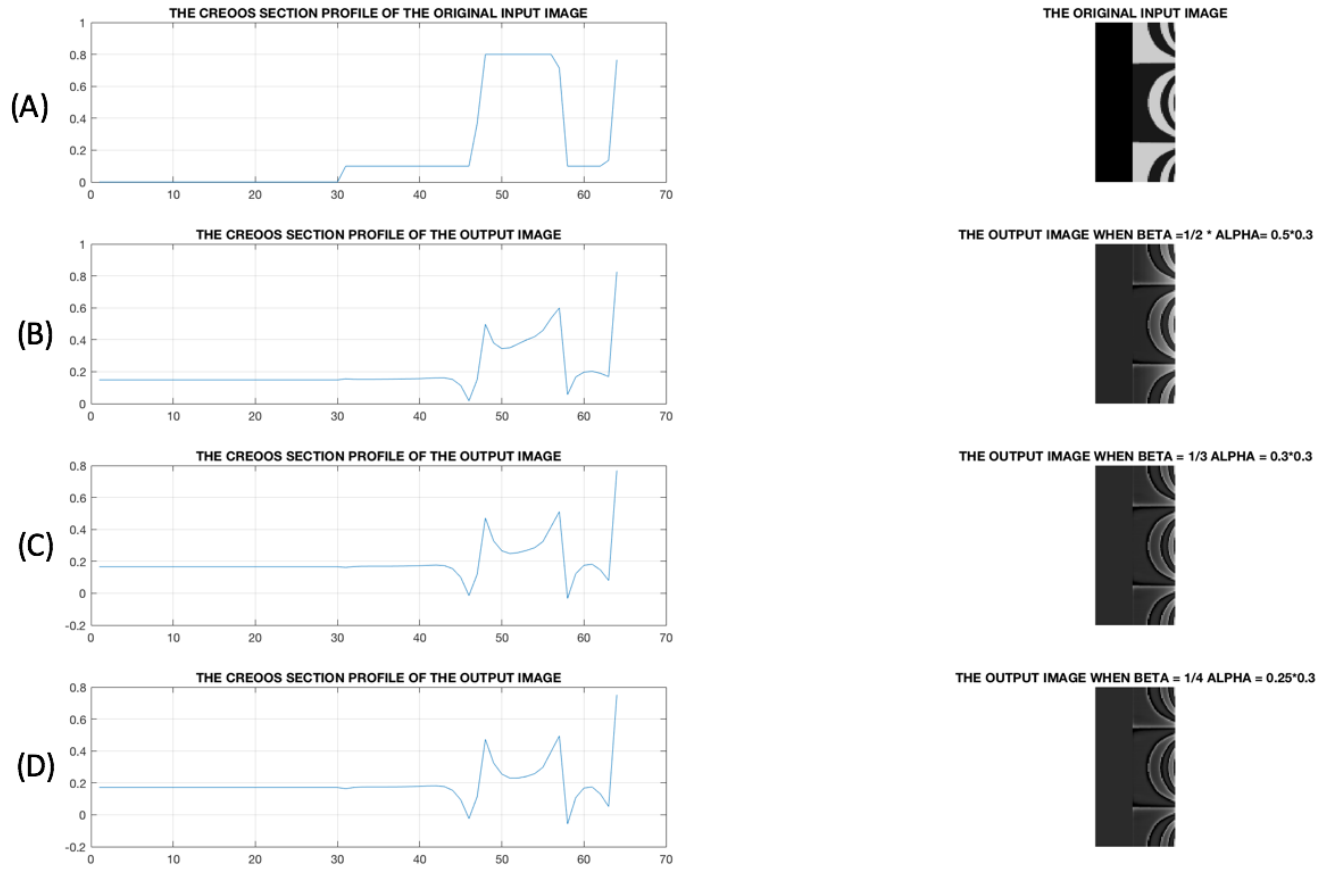


Figure 5-10: Illustration the Best Expression of Alpha  $\alpha$  parameter and Beta  $\beta$  for the Non-uniform Model. (A)The Original Image. (B)LSI Image when  $\beta = \frac{1}{2} * \alpha$ . (C)LSI Image when  $\beta = \frac{1}{3} * \alpha$ . (D)LSI Image when  $\beta = \frac{1}{4} * \alpha$ .

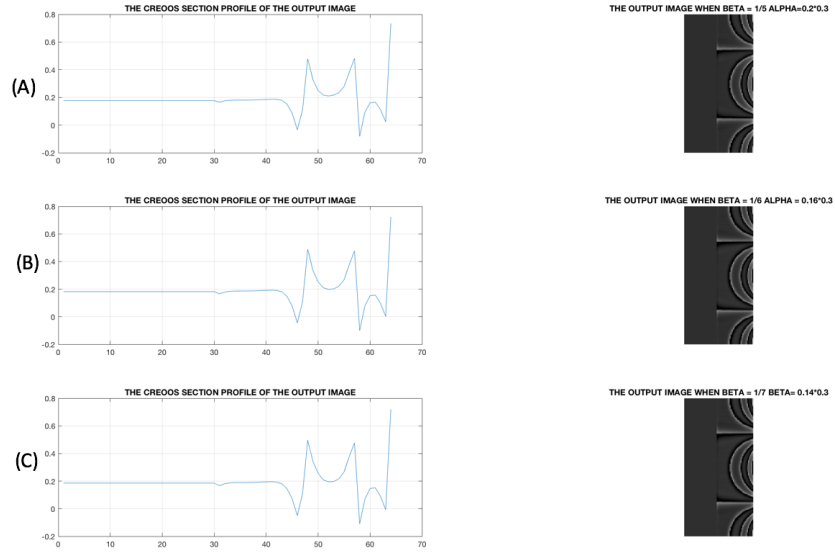


Figure 5-11: Illustration the Best Expression of Alpha  $\alpha$  parameter and Beta  $\beta$  for the Non-uniform Model. (A)LSI Image when  $\beta=\frac{1}{5}*\alpha$ .(B)LSI Image when  $\beta=\frac{1}{6}*\alpha$ .(C)LSI Image when  $\beta=\frac{1}{7}*\alpha$ .

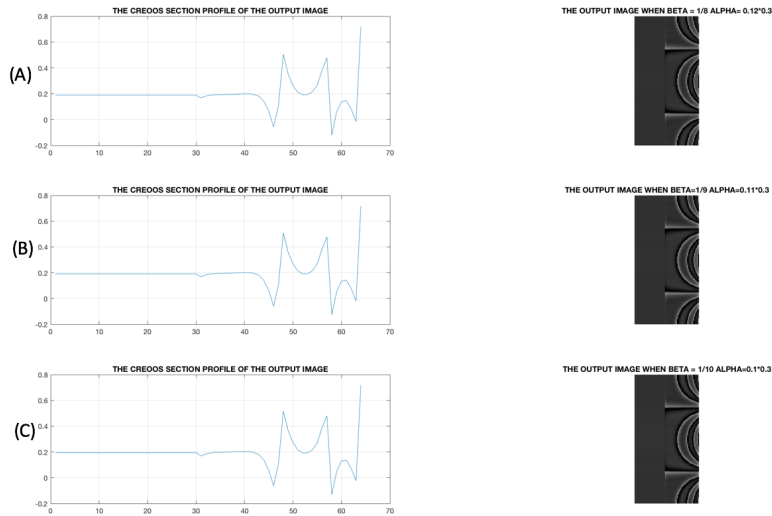


Figure 5-12: Illustration the Best Expression of Alpha  $\alpha$  parameter and Beta  $\beta$  for the Non-uniform Model. (A)LSI Image when  $\beta=\frac{1}{8}*\alpha$ .(B)LSI Image when  $\beta=\frac{1}{9}*\alpha$ .(C)LSI Image when  $\beta=\frac{1}{10}*\alpha$ .

As we can see from the previous results above, that beta should always be less than an alpha parameter to obtain the desired images based on lateral inhibition biological method. However, by how much beta should be lower than alpha, to answer that question we have made these three figures above. According to these simulation results, if a beta is less than alpha by more than 2, the desired output image will be achieved, in this thesis work we have taken ( $\beta = 0.05$ ) which is almost to ( $\frac{1}{6}$ ) of alpha (when  $\alpha = 0.3$ ), see figure (5-11B). Therefore, the mathematical expression which represents the relationship between these two variables to the input and the desired output image will be as the following expression in equation 5.4:

$$\beta = \frac{1}{6} * \alpha \quad (5.4)$$

Then, the final mathematical description to generate the non-uniform coupling coefficients via the log-polar mapping transformation method will be illustrating in the equation 5.5:

$$B = (6 * \beta) * \exp(-\beta * D) \quad (5.5)$$

Lastly, the mathematical relationship between these two variables from the exponential model to the original image and the resultant output image via the lateral inhibition method will be explained on the following equation 5.6:

$$OutputImage = B^{-1} * InputImage \quad (5.6)$$

To mimic the lateral inhibition biological phenomenon, Laplacian of Gaussian or (Difference of Gaussian) filters have been generated by subtracting two zero mean Gaussian filters with different standard deviation parameters and applied the resultant filter to the mapped image. This filtration process is classified into three categories; the first one is a DoG-Low-Pass filter to attenuate the high-frequency details then a blurry output image will be achieved. The second one is a DoG-High-Pass filter to enhance all the edges and get rid of the low-frequency image information. The third category is a DoG-Band-Pass filter to extract all the relative information between the high and low-frequency details. A particular quality metric has been used which is Root Mean Square Error (RMSE) to test the performance of these filters and investigate which filtered image has the closest information details as the picture processed via the natural method. The numerical results via the RMSE quality metric have been proposed as tables, see tables in 4.1 and 4.2, regarding the forward version of the mapped image from each mapping model. From these two tables as well as the resultant images after subtracting the filtered image from LSI image we have observed that the output image via a lateral inhibition method contains all the essential information from the original image such as the edges (the high-frequency details) and the data beyond these boundaries (almost the mid frequency details). Therefore, the filtered image via DoG-BPF and DoG-HPF are the closest images to the LSI image more than the blurry image that is processed based on the DoG-LPF. Besides that, a comparison between the conventional mapping model to the non-uniform one has made from another perspective which is the time required to map the input image with different dimension sizes. Whereas, the new sampling design was indicating the superiority in performance over the conventional one as the picture size increases.

The following chapter will represent our directions and suggestions to expand this work in the future.



# Chapter 6

## Future Work

Although the research results presented in this work are satisfactory, they are still only the beginning of the study related to the Lateral Inhibition biological phenomenon and its application. In other words, there is another type of the lateral inhibition interaction among receptors called shunting [53]. Both subtractive and shunting type of lateral inhibition are capable of enhancing image contrast in the sensory field of the receptors and neurons, more details regarding the comparison between these type of lateral inhibition method is presenting in [12]. As has been indicated, only the subtractive type of lateral inhibition has been investigated in this research work. it might be worthwhile to explore the shunting type of inhibition on the new mapping model (non-uniform) and compare the resultant images via these two neural connectivity types.

As has been presented in this work, we have concentrated on the Sensory Mapping method [S] by proposing a new model to map the visual information in a way similar to the human retinal eye, see figure 1-1. However, the HVS does not stop at this point, though. The neural firing rate information is then mapped into the internal memory world of the brain via associative memory mapping, representing by the matrix  $[M]$  of the same figure to generate a set of memory information. Whereas the associative memory mapping coefficient matrix  $[M]$  is such a fascinating research topic in the neural network world, see [54] for further study. Additionally, we have taken only one mapping platform to mimic the human visual system, whereas, in reality, the human visual system is characterized as a Binocular field of view. In other words, there are two eyes to visualize the captured object. Therefore, to complete this work, another sampling mapping pattern has to add to this non-uniform platform, where this extension will enhance the depth of the view. Then, the

proper correlation and collaboration process between these two platforms will be in the cortical part of the visual system. Then, the memory world will obtain the information from the whole projected scene (from both sides) at the cortex within less amount of time comparing to the visual system with only one sampling pattern.

Another idea that might be of interest, which is changing the location of the gaze point. In other words, here in this study, we have considered the point of interest to be in the middle of the mapping model,  $[x/2 \text{ and } y/2]$ . Then the interconnection distances between the photo-receptors have been calculated regarding that point, and the weighting coefficient matrix has obtained for the lateral inhibition biological method based on an exponential model as we stated previously in this work, see chapter three. However, this reference point can be changing to a different location (since the human visual system has the full flexibility to moving the eye at various spots within a minimum amount of processing time). This means that a new spatial inter-connection distances (new coordinates) will be calculated according to the new gaze point and thus new coupling coefficients will be achieved corresponding to these new coordinates. Therefore, we think that it would be great to expand this work and make it more flexible on changing the position of our gaze point.

The Contrast Sensitivity Function (CSF) which is constructed by three multiple spatial frequency channels, is now scaled of cycles per unit distance. However, the more biological flavored scale for this function is cycles per degree. This can be a good point to start design a system that has a parameter determine the distance from the sensor site to the object in degree scale, for more details see [55].

The matrix inversion limitation could be a real point of study to enhance the resolution of the output images via the non-uniform model of the LSI method and increase the dimension size of the processing images to reach the  $[2048 \times 2048]$  pixels double precision. Also, if a color-space image is added to this research since the human eye can visualize the object in a gray and color scales. Therefore, we believe that adding color-space images is a very necessary aspect of representing this study in a perfect way.

# Bibliography

- [1] Dennis Dacey, Orin S Packer, Lisa Diller, David Brainard, Beth Peterson, and Barry Lee. Center surround receptive field structure of cone bipolar cells in primate retina. *Vision research*, 40(14):1801–1811, 2000.
- [2] Anıl Coşkun. *Contrast enhancement by lateral inhibition in a sensory network*. PhD thesis, Citeseer, 2006.
- [3] H KEFFER Hartline and Floyd Ratliff. Inhibitory interaction of receptor units in the eye of limulus. *The Journal of general physiology*, 40(3):357–376, 1957.
- [4] Christopher L Passaglia, Frederick A Dodge, and Robert B Barlow. Cell-based model of the limulus lateral eye. *Journal of neurophysiology*, 80(4):1800–1815, 1998.
- [5] Michael J Hogan and JE JA Weddell. Histology of the human eye: an atlas and textbook. 1971.
- [6] Li Mu. *The lateral subtractive inhibition algorithm: simulation and application in image processing*. 1995.
- [7] Massimo Tistarelli and Giulio Sandini. On the advantages of polar and log-polar mapping for direct estimation of time-to-impact from optical flow. *IEEE Transactions on Pattern Analysis and Machine Intelligence*, 15(4):401–410, 1993.
- [8] Pavlo Melnyk. *Biologically inspired composite image sensor for deep field target tracking*. University of New Hampshire, 2008.
- [9] H Keffer Hartline and Floyd Ratliff. Inhibitory interaction of receptor units in the eye of limulus. *The Journal of general physiology*, 40(3):357–376, 1957.

- [10] David H Hubel and Torsten N Wiesel. Receptive fields of single neurones in the cat's striate cortex. *The Journal of physiology*, 148(3):574–591, 1959.
- [11] J Anthony Movshon, ID Thompson, and DJ Tolhurst. Receptive field organization of complex cells in the cat's striate cortex. *The Journal of physiology*, 283:79, 1978.
- [12] GG Furman. Comparison of models for subtractive and shunting lateral-inhibition in receptor-neuron fields. *Kybernetik*, 2(6):257–274, 1965.
- [13] Richard A Messner. Smart visual sensors for real-time image processing and pattern recognition based upon human visual system characteristics, 1984.
- [14] Xiaohui Xie, Richard HR Hahnloser, and H Sebastian Seung. Learning winner-take-all competition between groups of neurons in lateral inhibitory networks. *Advances in Neural Information Processing Systems*, pages 350–356, 2001.
- [15] H K Hartline, Henry G Wagner, and Floyd Ratliff. Inhibition in the eye of limulus. *The Journal of general physiology*, 39(5):651–673, 1956.
- [16] Colin Blakemore and Elisabeth A Tobin. Lateral inhibition between orientation detectors in the cat's visual cortex. *Experimental Brain Research*, 15(4):439–440, 1972.
- [17] Teuvo Kohonen. *Self-organization and associative memory*, volume 8. Springer Science & Business Media, 2012.
- [18] William H Merigan and John HR Maunsell. How parallel are the primate visual pathways? *Annual review of neuroscience*, 16(1):369–402, 1993.
- [19] Colin Blakemore, Roger H Carpenter, and Mark A Georgeson. Lateral inhibition between orientation detectors in the human visual system. *Nature*, 1970.
- [20] Edward H Adelson, Charles H Anderson, James R Bergen, Peter J Burt, and Joan M Ogden. Pyramid methods in image processing. *RCA engineer*, 29(6):33–41, 1984.

- [21] Tarik Arici, Salih Dikbas, and Yucel Altunbasak. A histogram modification framework and its application for image contrast enhancement. *IEEE Transactions on image processing*, 18(9):1921–1935, 2009.
- [22] Andrea Polesel, Giovanni Ramponi, V John Mathews, et al. Image enhancement via adaptive unsharp masking. *IEEE transactions on image processing*, 9(3):505–510, 2000.
- [23] Eric L Schwartz. Anatomical and physiological correlates of visual computation from striate to infero-temporal cortex. *IEEE Transactions on Systems, Man, and Cybernetics*, (2):257–271, 1984.
- [24] V Javier Traver and Alexandre Bernardino. A review of log-polar imaging for visual perception in robotics. *Robotics and Autonomous Systems*, 58(4):378–398, 2010.
- [25] Frédéric Jurie. A new log-polar mapping for space variant imaging.: Application to face detection and tracking. *Pattern Recognition*, 32(5):865–875, 1999.
- [26] Max Schultze. Zur anatomie und physiologie der retina. *Archiv für mikroskopische Anatomie*, 2(1):175–286, 1866.
- [27] Eric L Schwartz. Spatial mapping in the primate sensory projection: analytic structure and relevance to perception. *Biological cybernetics*, 25(4):181–194, 1977.
- [28] Eric L Schwartz. Computational anatomy and functional architecture of striate cortex: a spatial mapping approach to perceptual coding. *Vision research*, 20(8):645–669, 1980.
- [29] PM Daniel and D Whitteridge. The representation of the visual field on the cerebral cortex in monkeys. *The Journal of physiology*, 159(2):203–221, 1961.
- [30] Carl FR Weiman and George Chaikin. Logarithmic spiral grids for image processing and display. *Computer Graphics and Image Processing*, 11(3):197–226, 1979.
- [31] LF Pau. Detector layout and scanning for an infrared source classification system. In *24th Annual Technical Symposium*, pages 160–166. International Society for Optics and Photonics, 1980.

- [32] FJ Tolkmitt. A computer simulation of the afferent part of the visual foveation system. *Biological cybernetics*, 25(4):195–203, 1977.
- [33] Bala Krishna Vadapally and Zia-ur Rahman. Image registration using conformal log polar mapping. In *SPIE Defense, Security, and Sensing*, pages 73410G–73410G. International Society for Optics and Photonics, 2009.
- [34] Giulio Sandini and Vincenzo Tagliasco. An anthropomorphic retina-like structure for scene analysis. *Computer Graphics and Image Processing*, 14(4):365–372, 1980.
- [35] Marc Bolduc and Martin D Levine. A review of biologically motivated space-variant data reduction models for robotic vision. *Computer vision and image understanding*, 69(2):170–184, 1998.
- [36] Fabrizio Smeraldi and Josef Bigun. Retinal vision applied to facial features detection and face authentication. *Pattern recognition letters*, 23(4):463–475, 2002.
- [37] Cheon Woo Shin and Seiji Inokuchi. A new retina-like visual sensor performing the polar transform. *MVA*, 94:52–56, 1994.
- [38] Alexandre Bernardino and José Santos-Victor. Vergence control for robotic heads using log-polar images. In *Intelligent Robots and Systems’ 96, IROS 96, Proceedings of the 1996 IEEE/RSJ International Conference on*, volume 3, pages 1264–1271. IEEE, 1996.
- [39] Michael Davidson. Perturbation approach to spatial brightness interaction in human vision. *JOSA*, 58(9):1300–1308, 1968.
- [40] Frank Schaeffel. Processing of information in the human visual system. *Handbook of machine vision*, pages 1–33, 2007.
- [41] Russell L De Valois, Duane G Albrecht, and Lisa G Thorell. Spatial frequency selectivity of cells in macaque visual cortex. *Vision research*, 22(5):545–559, 1982.
- [42] HR Wilson. Psychophysical evidence for spatial channels. In *Physical and biological processing of images*, pages 88–99. Springer, 1983.

- [43] Arthur P Ginsburg. Visual information processing based on spatial filters constrained by biological data. Technical report, DTIC Document, 1978.
- [44] PV Sudeep, P Palanisamy, Chandrasekharan Kesavadas, and Jeny Rajan. Nonlocal linear minimum mean square error methods for denoising mri. *Biomedical Signal Processing and Control*, 20:125–134, 2015.
- [45] Amin Zollanvari and Edward R Dougherty. Moments and root-mean-square error of the bayesian mmse estimator of classification error in the gaussian model. *Pattern recognition*, 47(6):2178–2192, 2014.
- [46] HR Wilson. Psychophysical evidence for spatial channels. In *Physical and biological processing of images*, pages 88–99. Springer, 1983.
- [47] JG Robson. Frequency domain visual processing. In *Physical and biological processing of images*, pages 73–87. Springer, 1983.
- [48] Zi Fang, Zhao Dawei, and Zhang Ke. Image pre-processing algorithm based on lateral inhibition. In *Electronic Measurement and Instruments, 2007. ICEMI’07. 8th International Conference on*, pages 2–701. IEEE, 2007.
- [49] Xiaohua Wang, Haibin Duan, and Delin Luo. Cauchy biogeography-based optimization based on lateral inhibition for image matching. *Optik-International Journal for Light and Electron Optics*, 124(22):5447–5453, 2013.
- [50] Dov Sagi and Shaul Hochstein. Lateral inhibition between spatially adjacent spatial-frequency channels? *Perception & Psychophysics*, 37(4):315–322, 1985.
- [51] Kazuhiro Hotta, Takio Kurita, and Taketoshi Mishima. Scale invariant face detection method using higher-order local autocorrelation features extracted from log-polar image. In *Automatic Face and Gesture Recognition, 1998. Proceedings. Third IEEE International Conference on*, pages 70–75. IEEE, 1998.

- [52] Matthew G Luniewicz and Richard A Messner. Effects of lateral subtractive inhibition within the context of a polar-log spatial coordinate mapping. In *1988 Robotics Conferences*, pages 58–67. International Society for Optics and Photonics, 1989.
- [53] Gary R Holt and Christof Koch. Shunting inhibition does not have a divisive effect on firing rates. *Neural computation*, 9(5):1001–1013, 1997.
- [54] Bai-Ling Zhang, Haihong Zhang, and Shuzhi Sam Ge. Face recognition by applying wavelet subband representation and kernel associative memory. *IEEE Transactions on neural networks*, 15(1):166–177, 2004.
- [55] Ivan Bodis-Wollner. Visual acuity and contrast sensitivity in patients with cerebral lesions. *Science*, 178(4062):769–771, 1972.